

**Evolution of (bio-)geochemical processes in deep subseafloor sediments
from the Nankai Trough along the tectonic migration of ocean floor and
related changes in depositional and thermal conditions**

Dissertation zur Erlangung des akademischen Doktorgrades der Naturwissenschaften
- Dr. rer. nat. -

Im Fachbereich Geowissenschaften
der Universität Bremen

vorgelegt von
Male Köster

Bremen, März 2022



Gutachterinnen:

Prof. Dr. Sabine Kasten
Universität Bremen
Fachbereich Geowissenschaften
Klagenfurter Straße 2
28359 Bremen
Deutschland

Prof. Dr. Marta Torres
Oregon State University
College for Earth, Ocean, and Atmospheric Sciences
Weniger Hall 543
103 SW Memorial Place
Corvallis, OR 97331
USA

Datum des Promotionskolloquiums: 08. Juli 2022

*Science and peace will triumph
over ignorance and war.*

– Louis Pasteur

PREFACE

This doctoral thesis is submitted to achieve the doctoral degree in natural sciences (Dr. rer. nat.) at the Faculty of Geosciences, University of Bremen, Germany. This study was performed within the project “*Examining the role of biotic iron reduction as a life-sustaining process at the potential temperature limit of the deep seafloor biosphere (IODP Expedition 370) (RESPIRE)*”, funded by the German Research Foundation (DFG) in the framework of the Priority Programme “Bereich Infrastruktur - International Ocean Discovery Program (IODP)” (SPP 527). The Alfred Wegener Institute Helmholtz Centre for Polar and Marine Research (AWI), Bremerhaven, Germany, provided additional financial support. The research described herein was conducted under the supervision of Prof. Dr. Sabine Kasten and Dr. Susann Henkel (both AWI) and the outcome is compiled in the presented cumulative doctoral thesis.

The doctoral thesis begins with a general overview of the deep biosphere and (bio-)geochemical processes within deep seafloor sediments as well as a brief introduction to the study area and the motivation and objectives of this study (Chapter I). The scientific objectives were addressed in three first-authorship manuscripts, which represent the main part of this thesis (Chapter II, IV and V). A co-authorship contribution is presented in Chapter III. The manuscripts are published (Chapter II and III), submitted (Chapter IV) or in preparation (Chapter V) for the submission to international peer-reviewed journals. The manuscripts are arranged in chronological order of submission and presented to the full extend with the supplementary materials to be found collectively in the appendix. Chapter VI summarizes the main findings and conclusions of this thesis and provides an outlook for future research.

The studies presented in this thesis are based on samples and data obtained during IODP Expedition 370 (Temperature Limit of the Deep Biosphere off Muroto) onboard *D/V Chikyu* in September – November 2016. The analyses were mainly performed in the laboratories of the Alfred Wegener Institute Helmholtz Centre for Polar and Marine Research in Bremerhaven as well as in close collaboration with project partners at the MARUM – Center for Marine Environmental Sciences, University of Bremen, and the Center for Advanced Marine Core Research, Kochi University, in Japan.

TABLE OF CONTENTS

ABSTRACT	i
ZUSAMMENFASSUNG	iv
LIST OF FIGURES AND TABLES	viii
CHAPTER I:	1
1.1 The deep seafloor biosphere.....	1
1.2 Main drivers of (bio-)geochemical processes in deep seafloor sediments	2
1.3 Iron cycling and interactions with sulfur in seafloor sediments.....	5
1.4 Stable iron isotopes as indicator for microbial iron cycling	7
1.5 Non-steady state diagenesis in the deep seafloor biosphere.....	9
1.6 Temperature limit of microbial life in the deep seafloor biosphere	10
1.7 Geological setting of the Nankai Trough subduction zone.....	11
1.8 Motivation and objectives.....	13
1.9 Declaration of (co)-author contributions	14
References.....	16
CHAPTER II: Evolution of (bio-)geochemical processes and diagenetic alteration of sediments along the tectonic migration of ocean floor in the Shikoku Basin off Japan.....	26
CHAPTER III: Influence of early low-temperature and later high-temperature diagenesis on magnetic mineral assemblages in marine sediments from the Nankai Trough	70
CHAPTER IV: Uniquely low stable iron isotopic signatures in deep marine sediments caused by Rayleigh distillation	102
CHAPTER V: Fading of a sulfate-methane transition in deep and hot seafloor sediments from the Nankai Trough	122
CHAPTER VI: Conclusions and outlook.....	139
APPENDIX	144
APPENDIX OF CHAPTER II.....	145
APPENDIX OF CHAPTER III	151
APPENDIX OF CHAPTER IV	163
APPENDIX OF CHAPTER V	170
ACKNOWLEDGEMENTS	190

ABSTRACT

Deep seafloor sediments represent the largest reservoir of organic carbon on Earth. The degradation of organic matter is the driving force of microbial activity within this realm, linking the (bio-)geochemical cycles of carbon, sulfur and iron. (Bio-)geochemical processes in deep sediments can notably change over geological timescales due to variations in oceanographic, climatic or depositional conditions, which can have significant impacts on global element cycles and the carbon sequestration in marine sediments. Thus, it is crucial to improve the understanding of long-term variations in the deep biosphere.

An ideal setting to study (bio-)geochemical processes under the influence of strongly changing environmental and depositional conditions is the Nankai Trough subduction zone offshore Japan in the northwestern Pacific Ocean, which marks the subduction boundary between the Philippine Sea plate and the Eurasian plate. The sediment cores that were investigated in the framework of this cumulative doctoral thesis were taken from a 1,180 m deep hole (Site C0023) drilled during International Ocean Discovery Program Expedition 370 in the Nankai Trough off Cape Muroto, Japan, in the northwestern Pacific Ocean, which aimed at exploring the temperature limit of microbial life in the deep seafloor biosphere. At present, the temperature increases from 2°C at the seafloor up to 120°C at the sediment-basement interface. Over the past 15 million years, the sediments at Site C0023 have moved several hundreds of kilometers – relative to its present-day position – from the central Shikoku Basin to the Nankai Trough due to tectonic motion of the Philippine Sea plate. During this tectonically induced migration, the sediments at Site C0023 have experienced significant changes in depositional, geochemical and thermal conditions.

This doctoral thesis focuses on the evolution of (bio-)geochemical processes, especially the cycling of iron, along the tectonic migration of ocean floor at Site C0023. By combining comprehensive geochemical and rock magnetic analyses, we reconstructed the potential succession of (bio-)geochemical processes and the associated diagenetic alteration of the sediments over the past 15 million years. In a next step, the resulting evolution of (bio-)geochemical processes was quantitatively tested by reactive transport modeling. In addition, stable iron isotope ($\delta^{56}\text{Fe}$) analyses were performed on dissolved and sequentially extracted iron to disentangle microbially mediated and abiotic drivers of the iron cycling in deep and hot seafloor sediments at Site C0023.

The oldest sediments were deposited on the oceanic basement 15 million years ago (Ma), when Site C0023 was located close to the spreading center of the Shikoku Basin. During the deposition of the deep carbon-starved sediments, sulfate was only partially consumed by organoclastic sulfate reduction. With ongoing tectonic movement towards the Nankai Trough, sedimentation rates and organic carbon contents increased, possibly related to elevated marine productivity. This transition from an organic carbon-starved to elevated carbon burial environment initiated the onset of biogenic methane production and the anaerobic oxidation of methane (AOM) at around 2.5 Ma. The onset of AOM led to the formation of a sulfate-methane transition (SMT) in the shallow sediments. Since sulfate was not completely consumed in the deeper sediments between 15 and 2.5 Ma, a deep inverse SMT could form where downward diffusing methane was oxidized by the preserved sulfate. A continuous increase in carbon burial resulted in elevated biogenic methanogenesis. The resulting increased flux of methane caused an up- and downward migration of the shallow and inverse SMT, respectively, which, in turn, was accompanied by shifts of the sulfidization fronts. Due to the downward shift of the sulfidization front into the deeper carbon-starved sediments, the preserved sedimentary iron (oxyhydr)oxides were diagenetically transformed into pyrite several millions of years after the initial deposition of the sediments.

The sedimentation rate markedly increased when Site C0023 entered the Nankai Trough at around 0.4 Ma. The transition from basin- to trench-style deposition is accompanied by a pronounced increase in temperature of about 50°C across the sediment column. As a result, organic matter that is recalcitrant at seafloor temperatures of 2° to 3°C likely became accessible for microbial processes, which enhanced the biogenic methane production. At present, the sulfate and methane profiles at the deep inverse SMT overlap in a relatively broad zone of ~100 m that corresponds to a temperature of up to 85°C. This temperature coincides with the known temperature limit of AOM-performing microbial communities. Depth-integrated AOM rates derived from the reactive transport model suggest that microbial activity at the deep inverse SMT has already started to cease and the SMT is about to fade away.

To quantify reactive iron phases that could serve as energy substrates for microbially mediated processes in the old and hot sediments at Site C0023, different iron speciation methods were applied. The combination of sequential iron extractions, Mössbauer spectroscopy and rock magnetic end-member unmixing allowed an improved characterization of the iron mineral phases in the sediments at Site C0023. The results indicate that high amounts of reducible iron

that can potentially fuel microbially mediated iron reduction are still preserved as phyllosilicate-bound iron throughout the sediment column.

The stable iron isotopes were analyzed to investigate the (bio-)geochemical iron cycling in sediments at Site C0023. The overall light isotopic composition of dissolved iron ($\delta^{56}\text{Fe} < -1\text{‰}$) does not rule out dissimilatory iron reduction (DIR) as the main pathway releasing dissolved iron. However, some samples have exceptionally low $\delta^{56}\text{Fe}$ values down to almost -5.9‰ , which cannot be attributed solely to DIR. The extremely negative $\delta^{56}\text{Fe}$ values are best explained by a Rayleigh distillation model in which dissolved iron is continuously removed from the pore water by diffusion and adsorption onto iron mineral surfaces. The microbially mediated release of dissolved iron and its diffusional and adsorptive removal initially co-occurred. Due to increased sedimentation rates and the associated pronounced increase in sediment temperature beyond the temperature limit of mesophilic microorganisms, DIR might have ended in the depth range where the dissolved iron was previously released. The abiotic diffusional and adsorptive removal of dissolved iron in contrast continued, which could have led to the uniquely low $\delta^{56}\text{Fe}$ values we observe today. This decoupling of biotic and abiotic processes is ultimately driven by the depositional and thermal history of Site C0023.

The presented doctoral thesis emphasizes that the tectonically induced migration of ocean floor can lead to significant changes in depositional, geochemical and thermal conditions. These changes, in turn, influence the subseafloor habitability and control (bio-)geochemical processes as well as geochemical and isotopic signatures within the entire sediment column. The findings of this study provide important aspects for the interpretation of stable iron isotope data and contribute to an improved understanding of long-term variations in (bio-)geochemical processes in the deep subseafloor biosphere.

ZUSAMMENFASSUNG

Die marinen Sedimente der tiefen Biosphäre stellen das größte Reservoir an organischem Kohlenstoff auf der Erde dar. Der Abbau des organischen Materials ist die treibende Kraft für mikrobielle Aktivität in marinen Sedimenten und verbindet auf diese Weise die (bio-)geochemischen Stoffkreisläufe vor allem von Kohlenstoff, Schwefel und Eisen. (Bio-)geochemische Prozesse in den tiefen Sedimenten können jedoch über geologische Zeiträume durch Schwankungen der Klimabedingungen, der Ozeanzirkulation und der Ablagerungsdynamik stark variieren, was erhebliche Auswirkungen auf die globalen Stoffkreisläufe und die Speicherung von Kohlenstoff in marinen Sedimenten haben kann. Daher ist es von großer Bedeutung die langfristigen Veränderungen in der tiefen Biosphäre besser zu verstehen.

Der Nankai Trog vor der Küste Japans im nordwestlichen Pazifik markiert die Subduktionszone, an der die Philippinische Platte unter die Eurasische Platte abtaucht. Dabei bietet der Nankai Trog optimale Bedingungen, um (bio-)geochemische Prozesse im Sediment zu untersuchen, die unter dem Einfluss sich stark ändernder Umwelt- und Ablagerungsbedingungen stehen. Die Sedimentkerne, die im Rahmen dieser kumulativen Dissertation untersucht wurden, stammen aus einem 1180 m tiefen Bohrloch (Site C0023), das während der International Ocean Discovery Program Expedition 370 im Nankai Trog vor dem Kap Muroto gebohrt wurde. Ziel dieser Expedition war es, die Temperaturgrenze mikrobiellen Lebens in der tiefen marinen Biosphäre zu erforschen. Aktuell steigt die Temperatur in den Sedimenten von 2°C an der Oberfläche des Meeresbodens auf bis zu 120°C an der Grenzfläche zwischen dem Sediment und der Ozeankruste. In den vergangenen 15 Millionen Jahren haben sich die Sedimente an der Site C0023 aufgrund der tektonischen Bewegung der Philippinischen Platte – bezogen auf ihre heutige Position – um mehrere hundert Kilometer vom Shikoku Becken zum Nankai Trog verschoben. Während dieser tektonisch-bedingten Migration haben die Sedimente erhebliche Veränderung in der Ablagerung sowie den geochemischen und thermischen Bedingungen erfahren.

Diese Dissertation befasst sich mit der Entwicklung der (bio-)geochemischen Prozesse entlang der tektonischen Migration des Meeresbodens an der Site C0023, wobei der Fokus auf dem Eisenstoffkreislauf liegt. Durch die Kombination umfassender geochemischer und gesteinsmagnetischer Analysen konnte die mögliche Abfolge (bio-)geochemischer Prozesse und die damit verbundene diagenetische Überprägung der Sedimente in den letzten 15

Millionen Jahren rekonstruiert werden. Die daraus resultierende Entwicklung der (bio-)geochemischen Prozesse wurde in einem weiteren Schritt durch reaktive Transportmodellierung quantitativ überprüft. Darüber hinaus wurde die Isotopenzusammensetzung von gelöstem sowie sequentiell extrahiertem Eisen ($\delta^{56}\text{Fe}$) untersucht, um mikrobielle und abiotische Prozesse im Eisenstoffkreislauf in den tiefen und heißen Sedimenten an der Site C0023 zu unterscheiden.

Die ältesten Sedimente wurden vor 15 Millionen Jahren auf der frisch gebildeten Ozeankruste abgelagert, als sich die Site C0023 in der Nähe des damals noch aktiven Spreizungsrückens des Shikoku Beckens befand. Während der Ablagerung der tiefen kohlenstoffarmen Sedimente wurde Sulfat nur teilweise durch organoklastische Sulfatreduktion verbraucht. Mit fortschreitender tektonisch-bedingter Verschiebung in Richtung des Nankai Troges nahmen die Sedimentationsraten und der Gehalt an organischem Kohlenstoff zu, welches möglicherweise mit einer erhöhten Primärproduktion im Oberflächenwasser zusammenhing. Dieser Übergang von kohlenstoffarmen Bedingungen zu einem Milieu mit erhöhtem Kohlenstoffeintrag führte zum Einsetzen der biogenen Methanproduktion und der anaeroben Oxidation von Methan (AOM) vor etwa 2,5 Millionen Jahren. Das Einsetzen von AOM führte zur Bildung einer Sulfat-Methan-Übergangszone (SMT) in den flachen Sedimenten. Da Sulfat in den tieferen Sedimenten nicht vollständig verbraucht wurde, konnte sich eine weitere, tiefe inverse SMT bilden, an welcher das nach unten diffundierende Methan durch das noch erhaltene Sulfat oxidiert wurde. Die kontinuierliche Ablagerung von erhöhten Gehalten an organischem Kohlenstoff im Sediment führte zu verstärkter biogener Methanogenese. Der daraus resultierende erhöhte Methanfluss führte zu einer Auf- und Abwärtsverschiebung der flachen bzw. der inversen SMT, welches wiederum mit einer Verschiebung der Sulfidisierungsfronten einherging. Aufgrund der abwärts gerichteten Verschiebung der Sulfidisierungsfront in die tiefen kohlenstoffarmen Sedimente wurden die noch erhaltenen Eisen(oxyhydr)oxide mehrere Millionen Jahre nach ihrer ursprünglichen Ablagerung diagenetisch in Pyrit umgewandelt.

Als die Site C0023 vor etwa 0,4 Millionen Jahren den Nankai Trog erreichte, nahm die Sedimentationsrate deutlich zu. Dieser Wechsel in den Ablagerungsbedingungen geht mit einem deutlichen Temperaturanstieg von etwa 50°C über die gesamte Sedimentsäule einher. Dies hatte zur Folge, dass organisches Material, welches bei typischen Meeresbodentemperaturen von 2° bis 3°C refraktär ist, bioverfügbar wurde und so die biogene Methanproduktion gesteigert werden konnte. Derzeit überschneiden sich die Sulfat- und Methanprofile an der tiefen inversen SMT in einer relativ breiten Zone von etwa 100 m. In

diesem Bereich beträgt die Temperatur bis zu 85°C. Diese Temperatur deckt sich mit der bekannten Temperaturgrenze von Methan-oxidierenden Mikroorganismen. Die aus dem reaktiven Transportmodell hergeleiteten tiefen-integrierten AOM-Raten deuten darauf hin, dass die mikrobielle Aktivität an der tiefen inversen SMT bereits nachgelassen hat und die SMT im Begriff ist, zu verschwinden.

Um reaktive Eisenphasen zu quantifizieren, die als mögliche Energiesubstrate für mikrobiell gesteuerte Prozesse in den alten und heißen Sedimenten dienen könnten, wurden verschiedene Methoden zur Eisenspezifizierung angewandt. Die Kombination von sequentiellen Eisenextraktionen, Mössbauer-Spektroskopie und gesteinsmagnetischen Analysen ermöglichte eine verbesserte Charakterisierung von Eisenmineralphasen in den Sedimenten an der Site C0023. Die Ergebnisse zeigen, dass große Mengen an reduzierbarem Eisen, welches die mikrobielle Eisenreduktion ankurbeln könnte, in Schichtsilikaten gebunden und über die gesamte Sedimentsäule vorhanden sind.

Die stabilen Eisenisotope wurden analysiert, um den (bio-)geochemischen Eisenkreislauf in den Sedimenten an der Site C0023 zu untersuchen. Die insgesamt negative Isotopenzusammensetzung des gelösten Eisens ($\delta^{56}\text{Fe} < -1\text{‰}$) schließt die dissimilatorische Eisenreduktion (DIR) als Hauptfreisetzungsweg für Eisen nicht aus. Einige Proben weisen jedoch außergewöhnlich niedrige $\delta^{56}\text{Fe}$ -Werte von bis zu -5.9‰ auf, welche nicht allein auf DIR zurückgeführt werden können. Die extrem negativen $\delta^{56}\text{Fe}$ -Werte lassen sich am besten mithilfe eines Rayleigh-Destillationsmodells erklären, bei dem das gelöste Eisen durch Diffusion und Adsorption an Eisenmineraloberflächen kontinuierlich aus dem Porenwasser entfernt wird. Die mikrobiell gesteuerte Freisetzung sowie die Diffusion und die Adsorption von gelöstem Eisen fanden zunächst gleichzeitig statt. Durch erhöhte Sedimentationsraten und dem damit einhergehenden Anstieg der Sedimenttemperatur über die Temperaturgrenze mesophiler Mikroorganismen vor etwa 0,4 Millionen Jahre könnte die mikrobielle Eisenreduktion jedoch in dem Tiefenbereich, in dem das Eisen zuvor freigesetzt wurde, geendet haben. Die abiotische Diffusion und Adsorption von gelöstem Eisen an Mineraloberflächen dagegen fand weiterhin statt und führte so zu den extrem niedrigen $\delta^{56}\text{Fe}$ -Werten, die wir heute beobachten. Diese Entkopplung von biotischen und abiotischen Prozessen ist letztlich auf die Ablagerungs- und Temperaturdynamik an der Site C0023 zurückzuführen.

Die vorliegende Dissertation verdeutlicht, dass die tektonisch-bedingte Migration des Ozeanbodens und der darüber liegenden Sedimente zu signifikanten Änderungen in der Ablagerung und in den geochemischen und thermischen Bedingungen führen kann. Diese Änderungen beeinflussen wiederum die Bewohnbarkeit der tiefen Biosphäre und kontrollieren die (bio-)geochemischen Prozesse sowie die geochemischen und isotopischen Signaturen innerhalb der gesamten Sedimentsäule. Die Ergebnisse dieser Studie liefern wichtige Erkenntnisse für die Interpretation von stabilen Eisenisotopen in marinen Sedimenten und tragen zu einem besseren Verständnis der langfristigen Variabilität von (bio-)geochemischen Prozessen in der tiefen marinen Biosphäre bei.

LIST OF FIGURES AND TABLES

CHAPTER I: Introduction

Figure 1. Vertical section of the seabed and seafloor structures showing some of the major subseafloor biosphere habitats in the Nankai Trough offshore Japan in the northwestern Pacific Ocean. Modified after Jørgensen and Boetius (2007), Parkes et al. (2014) and Engelen et al. (2014). Schematic definition of the deep biosphere is adapted from Wehrmann and Riedinger (2016).

Figure 2. Schematic overview of organic carbon degradation pathways and associated (bio-)geochemical processes in subseafloor sediments. Modified after Parkes et al. (2014) and Wehrmann and Riedinger (2016). The classification of the geochemical environments is presented on the right according to Canfield and Thamdrup (2012).

Figure 3. (A) Simplified representation of the major pathways of the transformation of Fe (oxyhydr)oxides into Fe sulfides in anoxic marine sediments and the associated alteration of the sedimentary magnetic signal. Modified after Riedinger (2005). Under high H₂S supply, pyrite is precipitated directly from amorphous Fe sulfides and mackinawite. If the H₂S supply or the exposure time to H₂S is limited, the metastable pyrrhotite and/or greigite form, leading to the formation of a secondary magnetic signal. (B) Scanning electron microscope (SEM) photographs of (titano-)magnetite (M; left), euhedral pyrite (P; middle) and framboidal pyrite (P; right) observed in solid-phase samples from IODP Site C0023. The photographs were taken at the Center for Advanced Marine Core Research, Kochi University, Japan (personal photographs).

Figure 4. (A) General tectonic configuration of the Nankai Trough subduction zone. (B) Bathymetric map of IODP Site C0023 (yellow circle) and adjacent ODP Sites 808, 1173 and 1174 (white circles). Modified after Heuer et al. (2017).

CHAPTER II: Evolution of (bio-)geochemical processes and diagenetic alteration of sediments along the tectonic migration of ocean floor in the Shikoku Basin off Japan

Figure 1. Simplified schematic plate tectonic reconstruction for the Shikoku Basin and the relative movement of Site C0023 over the past 15 Ma. Japan is held fixed at its current position. Opened and filled red stars represent the current position of Site C0023 and its position over

the course of 15 Ma, respectively. Modified after Underwood and Guo (2018) (<https://creativecommons.org/licenses/by-nc/4.0/>).

Figure 2. Pore-water profiles of (a) sulfate (SO_4^{2-}), methane (CH_4), (b) dissolved Fe (Fe^{2+}), (c) hydrogen sulfide (HS^-), and (d) dissolved inorganic carbon (DIC) at Site C0023 from Heuer et al. (2017a). Lithological units (Heuer et al., 2017a) are indicated on the right. Corresponding ages on the right-side y-axis are based on the age model by Hagino and the Expedition 370 Scientists (2018).

Figure 3. Down-core solid-phase profiles of (a) reactive Fe ($\text{Fe}_{\text{reactive}} = \text{Fe}_{\text{aca}} + \text{Fe}_{\text{hyam}} + \text{Fe}_{\text{di-ct}} + \text{Fe}_{\text{oxa}}$; see Figure 4), total Fe (Fe_{total}), (b) $\text{Fe}_{\text{total}}/\text{Al}_{\text{total}}$, $\text{S}_{\text{total}}/\text{Al}_{\text{total}}$, (c) total S (S_{total}), and (d) chromium reducible sulfur (pyrite). Dashed vertical lines indicate average shale content (Turekian and Wedepohl, 1961). Color shading and corresponding ages as in Figure 2.

Figure 4. Down-core solid-phase profiles of sequentially extracted (a) Fe_{aca} (Na-acetate-leachable Fe), (b) Fe_{hyam} (Hydroxylamine-HCl-leachable Fe), (c) $\text{Fe}_{\text{di-ct}}$ (Na-dithionite-leachable Fe), and (d) Fe_{oxa} (NH_4 -oxalate/oxalic acid-leachable Fe). Color shading and corresponding ages as in Figure 2. Note that there are only three data points between 200 and 400 mbsf.

Figure 5. Down-core solid-phase profiles of (a) total organic carbon (modified from Heuer et al., 2017a), (b) magnetic susceptibility χ_{lf} , (c) $\text{Fe}_{\text{total}}/\chi_{\text{lf}}$, which indicates the intensity of magnetite dissolution (Funk et al., 2004), and (d) sedimentation rates (from Hagino and the Expedition 370 Scientists, 2018). Color shading and corresponding ages as in Figure 2.

Figure 6. End-member plot showing the relative contributions to the total isothermal remanent magnetization of each end-member (EM) (a) greigite, (b) fine-grained magnetite, (c) hematite, and (d) coarse-grained magnetite in representative samples over depth obtained by using the MAX UnMix web application (Maxbauer et al., 2016). The coercivity distribution could not be modeled in two depth intervals due to low magnetic intensities, referred as to Weak interval I and II. Note that EM 1 is only identified between 200 and 500 mbsf. Color shading and corresponding ages as in Figure 2.

Figure 7. Mössbauer spectra collected for each sample at 295 K (a–c), 77 K (d–f), and 5 K (g–i). All samples measured at room temperature (295 K) show a wide doublet which can be attributed to the presence of a non-magnetically ordered Fe(II) phase (light blue). The narrow doublet can be attributed to the presence of an Fe(III) phase (orange). Low-temperature measurements at 5 K confirm the dominant presence of paramagnetic (non-magnetically ordered) Fe(III) mineral phases to be present in all samples likely to represent (clay-sized) Fe-rich phyllosilicates. The absence (or low abundance) of a sextet feature at 5 K suggests the absence (or only low abundance) of magnetically ordered Fe (oxyhydr)oxide phases (Fe(III)mag; red) such as hematite, goethite or ferrihydrite; or could be a measuring artefact of a paramagnetic relaxation of Fe atoms in phyllosilicates (details given in the text).

Figure 8. Conceptual model showing the evolution of biogeochemical and diagenetic processes at Site C0023 during its tectonic migration over the past 15 Ma. The main driving force for changes in the (bio-)geochemical processes is the significant increase in sedimentation rate which in turn also affects the temperature within the sediment column and the total organic carbon burial. The more intense color shading of each arrow indicates the increase of the respective driving force. These changes in depositional, thermal, and geochemical conditions led to a transition from (a) an organic carbon-starved sedimentary environment with comparably low accumulation rates to (b) an environment with elevated sedimentation and carbon burial rates. Increasing sedimentation and organic carbon burial rates since ~2.5 Ma likely caused the onset of methanogenesis and anaerobic oxidation of methane (AOM) and the formation of a shallow and a lower sulfate-methane transition (SMT) (SMT 1 and SMT 2, respectively). HS⁻ produced by AOM reacted with solid-phase and dissolved Fe to form pyrite. (c) The arrival of Site C0023 at the Nankai Trough at ~0.5 Ma, accompanied by a significant increase in sediment temperature could have resulted in enhanced methanogenesis, likely due to increased bioavailability of organic matter and the up- and downward migration of the SMTs and sulfidization fronts. (d) Present-day situation with the shallow SMT 1 at ~4 mbsf (assumed from ODP Site 1174; Shipboard Science Party, 2001) and the lower SMT 2 at ~730 mbsf. Extremely high sedimentation rates since 0.43 Ma prevented a complete pyritization and the preservation of greigite.

Table 1. Lithological units and associated facies, lithology, depth, age and sedimentation rates of Site C0023 (Heuer et al., 2017b).

CHAPTER III: Influence of early low-temperature and later high-temperature diagenesis on magnetic mineral assemblages in marine sediments from the Nankai Trough

Figure 1. (a) General tectonic configuration of the Japanese islands. The red box is the area indicated in (b), which is a regional bathymetric map around Site C0023, International Ocean Discovery Program Expedition 370, with nearby Ocean Drilling Program Sites 808, 1174, and 1173 (modified after Heuer et al., 2017).

Figure 2. Down-core rock magnetic and coercivity variations at Site C0023. (a) Natural remanent magnetization (NRM), (b) anhysteretic remanent magnetization (ARM), (c) magnetic susceptibility χ_{lf} , (d) frequency-dependent susceptibility χ_{fd} , (e) saturation isothermal remanent magnetization (SIRM), (f) ARM/ χ_{lf} , (g) ARM/SIRM, (h) coercivity ratios, (i) remanent coercivity B_{cr} , and (j) M_{rs}/M_s . Discrete sample measurements are shown in (a–h), whereas (i and j) are dry powder sister sample measurements. Four major magnetic zones (MZs), indicated on the right, are identified from magnetic changes. MZs 1 and 3 correspond to higher magnetic mineral concentrations; MZs 2 and 4 correspond to lower concentrations. On the left, the Lithologic Units (IIA to IV) and décollement (“déc.”) are from Heuer et al. (2017).

Figure 3. First-order reversal curve (FORC)-type diagrams for Sample 370-C0023A-7X-1W, 32–34 cm (depth: 305.32 meters below seafloor) in Magnetic Zone (MZ) 1. (a) Conventional FORC diagram, (b) remanent FORC (remFORC) diagram, (c) transient hysteresis FORC (tFORC) diagram, and (d) induced FORC (iFORC) diagram. This sample has high coercivity ($B_{cr} = 62$ mT). Green contours indicate the 0.05 significance level for the FORC distributions calculated according to Heslop and Roberts (2012). Complementary rock magnetic data discussed in the text for this sample are shown in Figure S3 in Supporting Information S1. See Figures S3 and S4 in Supporting Information S1 for a low coercivity ($B_{cr} = 28$ mT) sample from MZ 1.

Figure 4. First-order reversal curve (FORC)-type diagrams for Sample 370-C0023A-50R-5W, 40–42 cm (depth: 696.53 meters below seafloor) in Magnetic Zone 2. (a) Conventional FORC diagram, (b) remanent FORC (remFORC) diagram, (c) transient hysteresis FORC (tFORC) diagram, and (d) induced FORC (iFORC) diagram. Green contours indicate the 0.05 significance level for the FORC distributions calculated according to Heslop and Roberts (2012). Complementary rock magnetic data discussed in the text for this sample are shown in Figure S5 in Supporting Information S1.

Figure 5. First-order reversal curve (FORC)-type diagrams for Sample 370-C0023A-61R-3W, 70–72 cm (depth: 750.51 meters below seafloor) in Magnetic Zone 3. (a) Conventional FORC diagram, (b) remanent FORC (remFORC) diagram, (c) transient hysteresis FORC (tFORC) diagram, and (d) induced FORC (iFORC) diagram. Green contours indicate the 0.05 significance level for the FORC distributions calculated according to Heslop and Roberts (2012). Complementary rock magnetic data discussed in the text for this sample are shown in Figure S6 in Supporting Information S1.

Figure 6. First-order reversal curve (FORC)-type diagrams for Sample 370-C0023A-93R-6W, 48–50 cm (depth: 962.99 meters below seafloor) in Magnetic Zone 4. (a) Conventional FORC diagram, (b) remanent FORC (remFORC) diagram, (c) transient hysteresis FORC (tFORC) diagram, and (d) induced FORC (iFORC) diagram. Green contours indicate the 0.05 significance level for the FORC distributions calculated according to Heslop and Roberts (2012). Complementary rock magnetic data discussed in the text for this sample are shown in Figure S7 in Supporting Information S1.

Figure 7. Lithological logs for (a) Sites 808 (Shipboard Scientific Party, 1991) and (b) C0023 (Heuer et al., 2017), with (c) illustration of the burial history at C0023 and key events. The color code for lithologic units and décollement is from Heuer et al. (2017). Magnetic zones (MZs) and associated main magnetic minerals (represented by different symbols) at Sites 808 (Lu and Banerjee, 1994) and C0023 (this study) are indicated. See also Figure S11 in Supporting Information S1 for magnetic correlation between sites. T_{\max} is the RockEval parameter and $T_{\max} \sim 435^{\circ}\text{C}$ indicates the onset of catagenesis. The two sulfate-methane transitions (SMTs; Köster et al., 2021a) discussed in the text are reported. Time is indicated on a log scale to illustrate recent events and consequent processes (< 0.5 Ma) that control diagenetic processes. Points used to construct Figure 8 are identified.

Figure 8. Paragenesis proposed from basin analysis (Tsang et al., 2020 and Figure 7) and magnetic mineral assemblage diagenetic histories discussed here and by Köster et al. (2021a). Separate paragenetic sequences are inferred for magnetic zones (MZs) 1 to 4, with a typical history indicated for the mid-point of each zone. Solid black bars indicate the main mineral phases for each MZ (Tsang et al., 2020). The dashed blue lines indicate stability fields for key iron minerals and the onset of other geological processes such as catagenesis. For example, it

can be seen that MZ 2 (containing iron oxides) passes sulfate-methane transition (SMT) 1 (vertical green line) early at ~ 0.6 Ma, but most pyrite formation occurs much later (0.5 Ma). Based on the rate and depth of burial, greigite is inferred to have been stable until ~ 0.5 Ma (blue dashed line). MZ 4 would not have passed through a SMT until more than 5 million years after its deposition, with the formation of iron oxyhydroxides (FeOx) favored prior to this. Time is indicated on a logarithmic scale as for Figure 7.

CHAPTER IV: Uniquely low stable iron isotopic signatures in deep marine sediments caused by Rayleigh distillation

Figure 1. Total and reactive Fe contents and associated isotopic compositions in mud rock and discrete ash layers at Site C0023. (a) Down-core solid-phase profiles of total Fe (Fe_{total}) and reactive Fe ($Fe_{reactive}$: sum of sequentially extracted Fe pools according to Poulton and Canfield, 2005). (b) Na-acetate-leachable Fe (Fe_{aca}) and associated isotopic composition ($\delta^{56}Fe_{aca}$). (c) Hydroxylamine-HCl-leachable Fe (Fe_{hyam}) and the associated isotopic composition ($\delta^{56}Fe_{hyam}$). Error bars indicate the twofold standard deviation (2SD) of duplicate to fourfold measurements. The stars in each panel represent the discrete ash layer samples. Fe_{total} , $Fe_{reactive}$, Fe_{aca} and Fe_{hyam} data of mud rock are taken from Köster et al. (2021).

Figure 2. Dissolved Fe concentrations and associated isotopic compositions at Site C0023. (a) Down-core pore-water profile of dissolved Fe ($Fe(II)_{aq}$) concentrations (red dots) and tephra layer counts (gray bars) (Heuer et al., 2017). Lithological units (IIA-V; see Supplementary Information) and temperature data are from Heuer et al. (2017) and Heuer et al. (2020), respectively. The gray dashed line shows the location of the inverse sulfate-methane transition (SMT) with a methanic zone above and a sulfate-rich zone below the SMT (see Supplementary Fig. 2 for details). (b) Close-up of $Fe(II)_{aq}$ concentrations (red dots) and associated isotopic composition ($\delta^{56}Fe_{aq}$) (black dots) for the ferruginous interval. Error bars indicate the twofold standard deviation (2SD) of the isotope ratio over 20 consecutive measurement cycles. (c) Relationship between $Fe(II)_{aq}$ concentrations (expressed as $\ln[Fe(II)_{aq}]$) and $\delta^{56}Fe_{aq}$ values (data fit following the relation: $\delta^{56}Fe_{aq} = 1.22 * \ln[Fe(II)_{aq}] - 6.09$, Spearman correlation coefficient $r_s=0.77$, $p<0.001$, $n=18$). The shallowest sample (~ 200 mbsf; gray dot) is not included in the linear regression due co-occurrence of $Fe(II)_{aq}$ and HS^- (details given in the text).

Figure 3. Isotopic composition of dissolved and sorbed Fe derived from Rayleigh distillation model. (a)-(f) Isotopic evolution of $\text{Fe(II)}_{\text{aq}}$ (bold line), instantaneous $\text{Fe(II)}_{\text{sorb}}$ (dashed line) and cumulative $\text{Fe(II)}_{\text{sorb}}$ (narrow line) during the adsorption of $\text{Fe(II)}_{\text{aq}}$ onto Fe (oxyhydr)oxide surfaces obtained by using the Rayleigh distillation equations after Wiederhold (2015). The differences between $\text{Fe(II)}_{\text{aq}}$ and instantaneous $\text{Fe(II)}_{\text{sorb}}$ corresponds to the enrichment factors ϵ according to (A) Crosby et al. (2007) and (B) Beard et al. (2010), respectively, at all stages of the reaction. For the initial isotopic composition of $\text{Fe(II)}_{\text{aq}}$ ($\delta^{56}\text{Fe}_0$), different values of -3.0‰ (a, d), -1.5‰ (b, e), and 0.0‰ (c, f) were used. The grayish bar represents the reference $\delta^{56}\text{Fe}_{\text{aq}}$ value of -5.86‰. The model results show that the largest fractionation for $\text{Fe(II)}_{\text{aq}}$ are found at advanced stages of the adsorption process where the remaining fraction f is low ($f < 0.1$).

Figure 4. Schematic overview illustrating the shift of $\delta^{56}\text{Fe}_{\text{aq}}$ towards negative values. (a) A combination of three consecutive processes could have caused extremely negative $\delta^{56}\text{Fe}_{\text{aq}}$ values at Site C0023: (b-c) repetitive DIR, (d) diffusive transport of $\text{Fe(II)}_{\text{aq}}$ along a concentration gradient (DIFF) and (e) adsorption of $\text{Fe(II)}_{\text{aq}}$ onto Fe (oxyhydr)oxide surfaces (ADS). The blue color scheme represents the isotopic composition of $\text{Fe(II)}_{\text{aq}}$, where pale blue colors indicate low and dark blue colors higher $\delta^{56}\text{Fe}_{\text{aq}}$ values. The combination of repetitive DIR and subsequent diffusion and adsorption of $\text{Fe(II)}_{\text{aq}}$ onto mineral surfaces progressively removed $\text{Fe(II)}_{\text{aq}}$ from the pore water, which led to a shift of $\delta^{56}\text{Fe}_{\text{aq}}$ towards extremely negative values. Here, while the zone in which dissimilatory Fe reduction occurs is referred to as “suboxic” zone, where oxygen, nitrate and HS^- are absent, the zone in which $\text{Fe(II)}_{\text{aq}}$ is oxidized is described as “oxic” zone.

CHAPTER V: Fading of a sulfate-methane transition in deep and hot sediments from the Nankai Trough

Figure 1. Overview maps of the Shikoku Basin and the Nankai Trough subduction zone offshore Japan in the northwestern Pacific Ocean. (A) Simplified schematic plate tectonic configuration of the Nankai Trough subduction zone. (B) Bathymetric map around IODP Site C0023 (yellow circle) off Cape Muroto, Shikoku Island, and the adjacent ODP Sites 808, 1173 and 1174 (white circles). Modified after Heuer et al. (2017).

Figure 2. Geochemical profiles of IODP Site C0023. (A) Pore-water profiles of sulfate (SO_4^{2-} ; grey dots) and methane (CH_4 ; black dots). (B) Pore-water profiles of dissolved inorganic carbon (DIC; black dots) and its carbon isotopic composition ($\delta^{13}\text{C-DIC}$; grey dots). (C) Pore-water

profile of dissolved calcium (Ca^{2+}). (D) Solid-phase profile of total organic carbon (C_{org}). All geochemical data except for $\delta^{13}\text{C}$ -DIC (this study) are from Heuer et al. (2017). Corresponding ages on the left-side y-axis are based on the age model by Hagino and the Expedition 370 Scientists (2018). Lithological units and temperature data on the right-side y-axis are from Heuer et al. (2017) and (2020), respectively.

Figure 3. Snapshots of simulated depth-profiles of sulfate (grey line) and methane (black line) derived from the reactive transport model over the past ~ 5.5 Ma. The snapshots from 5.53 to 0.29 Ma correspond to the sedimentation intervals according to the age model for Site C0023 (Hagino and the Expedition 370 Scientists, 2018). *In situ* concentrations of sulfate (dark grey dots) and methane (black dots) from IODP Site C0023 (Heuer et al., 2017) as well as sulfate concentrations from ODP Site 1774 (light grey dots; Shipboard Science Party, 2001) are shown in the present-day situation. Temperature data on the y-axes are based on the steady-state temperature profile from Heuer et al. (2020).

Figure 4. Metabolic reaction rates derived from the reactive transport model. (A) Simulated present-day organoclastic sulfate reduction (SR) rate (black line). Potential sulfate reduction rates (using ^{35}S - SO_4^{2-}) with trace H_2 added (black dots) from Beulig et al. (2022) are shown for comparison. (B) Simulated present-day biogenic methanogenesis (MG) rate (black line). Potential rates of methanogenesis (using ^{14}C -DIC) with trace H_2 added (black dots) are from Beulig et al. (2022). Note that some data points of potential SR and MG rates in (A) and (B), in particular between 190 and 360 mbsf, are off-scale. (C) Simulated present-day rate of anaerobic oxidation of methane (AOM). (D) Simulated present-day calcium sulfate (CaSO_4) precipitation rate. (E) Simulated evolution of the depth-integrated AOM rate since the onset of AOM at ~ 2.5 Ma.

CHAPTER VI: Conclusions and outlook

Figure 1. Left: Simplified schematic overview of the Nankai Trough subduction zone offshore Japan and the relative movement of Site C0023 during its tectonically induced migration over the past 15 Ma. Japan is held fixed at its current position. Light and dark red symbols represent the current position of Site C0023 and its former position during the tectonic migration, respectively. Modified after Lin et al. (2016), Heuer et al. (2017) and Underwood and Guo (2018). Right: Schematic illustration of the evolution of the sulfate (solid grey line) and methane (dotted black line) profiles at Site C0023 during its tectonic migration. The main

driving force for the changes in biogeochemical processes is the significant increase in sedimentation rate, which in turn also affect the sediment temperature and the organic carbon burial.

CHAPTER I: Introduction

1.1 The deep seafloor biosphere

More than two thirds of the Earth's surface is covered by seawater. Marine sediments that accumulated over geological timescales (> millions of years) represent the largest carbon reservoir on Earth (e.g., Hedges and Keil, 1995; Horsfield et al., 2006) and harbor diverse microbial communities. It is suggested that seafloor sediments comprise 0.18 to 3.6% of Earth's total living biomass (Kallmeyer et al., 2012). The sediment thickness considerably varies from a few meters in open-ocean regions that are far from continents and overlain by low-productivity waters (e.g., South Pacific Gyre; Rea et al., 2006) to several thousands of meters at continental margins (e.g., offshore Argentina; Loegering et al., 2013). In contrast to the carbon-starved deep-sea sediments, continental shelf and slope sediments are characterized by high organic carbon burial due to elevated primary productivity, sedimentation rates and riverine input along the continental margins (Fig. 1; e.g., Berner, 1982).

In general, there is no clear scientific definition for the deep biosphere. While Jørgensen and Boetius (2007) defined the deep marine subsurface as the sediment and rock that is deeper than 1 m below the seafloor (mbsf), Wehrmann and Riedinger (2016) refer to sediments deeper than 5 mbsf. In this study, the term "deep seafloor biosphere" is used according to Wehrmann and Riedinger (2016). It continues for several hundreds to thousands of meters down into the seabed (Fig. 1).

Microbial life has been detected down to 2.5 km below the seafloor in coal-bearing sediments offshore Shimokita Peninsula, Japan (Inagaki et al., 2015), as well as in sediments that are more than 100 million years old (Roussel et al., 2008; Morono et al., 2020). Due to the vast extension of the deep seafloor biosphere, microbial activity of the diverse and largely uncharacterized microorganisms within this realm plays an important role in the biogeochemical cycling of different elements including carbon (C), iron (Fe) and sulfur (S) (e.g., D'Hondt et al., 2002, 2004; Inagaki et al., 2006; Hoshino et al., 2020). In order to expand the knowledge and understanding of biogeochemical processes and to explore microbial life within the deep seafloor biosphere, scientific drilling expeditions were extensively conducted since the 1980s within the framework of the Deep Sea Drilling Project (DSDP), the Ocean Drilling Program (ODP), the Integrated Ocean Drilling Program and later the International Ocean Discovery Program (both IODP).

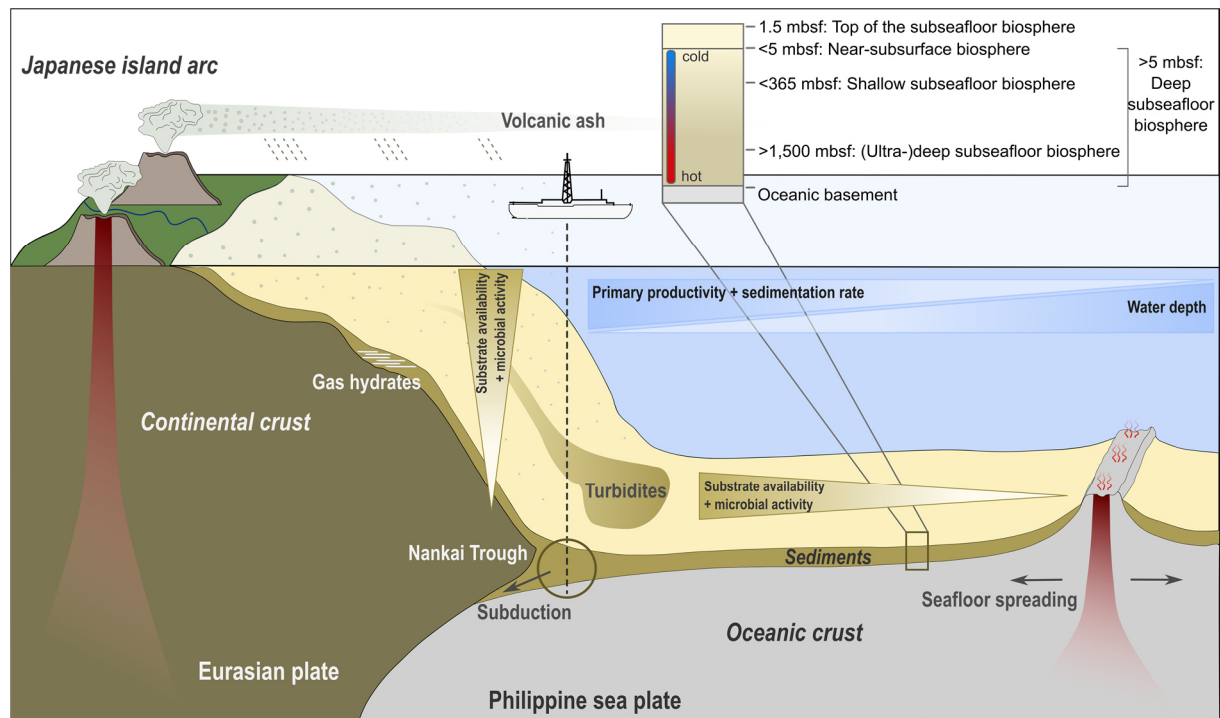


Figure 1. Vertical section of the seabed and seafloor structures showing some of the major subseafloor biosphere habitats in the Nankai Trough offshore Japan in the northwestern Pacific Ocean. Modified after Jørgensen and Boetius (2007), Parkes et al. (2014) and Engelen et al. (2014). Schematic definition of the deep biosphere is adapted from Wehrmann and Riedinger (2016).

1.2 Main drivers of (bio-)geochemical processes in deep subseafloor sediments

The driving force for (bio-)geochemical processes in subseafloor sediments is the degradation of organic matter that originates mainly from primary productivity in ocean surface waters and on land (Fig. 2; e.g., D'Hondt et al., 2002, 2004). On average, 1% of the organic matter produced in the photic zone reaches the seafloor in the deep sea, whereby approximately 97% of this amount is already mineralized during early diagenesis. Thus, in total, only 0.03% of the organic carbon produced in the surface waters will ultimately be buried (Berger et al., 1989). Organic matter entering the seafloor consists of several macromolecular compounds including proteins, lipid complexes and polysaccharides. Bacteria within the subseafloor sediments first need to break down these polymers before they can assimilate the monomeric products such as sugars, amino acids and long chain fatty acids. In a next step, fermenting bacteria take up and convert these monomeric compounds into volatile fatty acids (formate, acetate, propionate and butyrate), as well as H_2 , lactate, some alcohols and CO_2 , which then could serve as substrates for a broad range of prokaryotes within the subseafloor (Fig. 2; Jørgensen, 2006).

The microbial degradation of organic matter proceeds via a successive use of different terminal electron accepting processes (Froelich et al., 1979; Berner, 1981). The general depth sequence of terminal electron acceptors (TEA) utilized in the mineralization process includes dissolved

oxygen (O₂), nitrate (NO₃⁻), solid-phase manganese (Mn[IV]) and iron (Fe[III]) (oxyhydr)oxides as well as dissolved sulfate (SO₄²⁻). The final step during the organic matter degradation is the fermentation, which results in the formation of methane (CH₄) (Fig. 2). This so-called “redox cascade” is determined by the yield of free energy that microbes gain during the respective redox reaction (e.g., Froelich et al., 1979; Jørgensen, 2006).

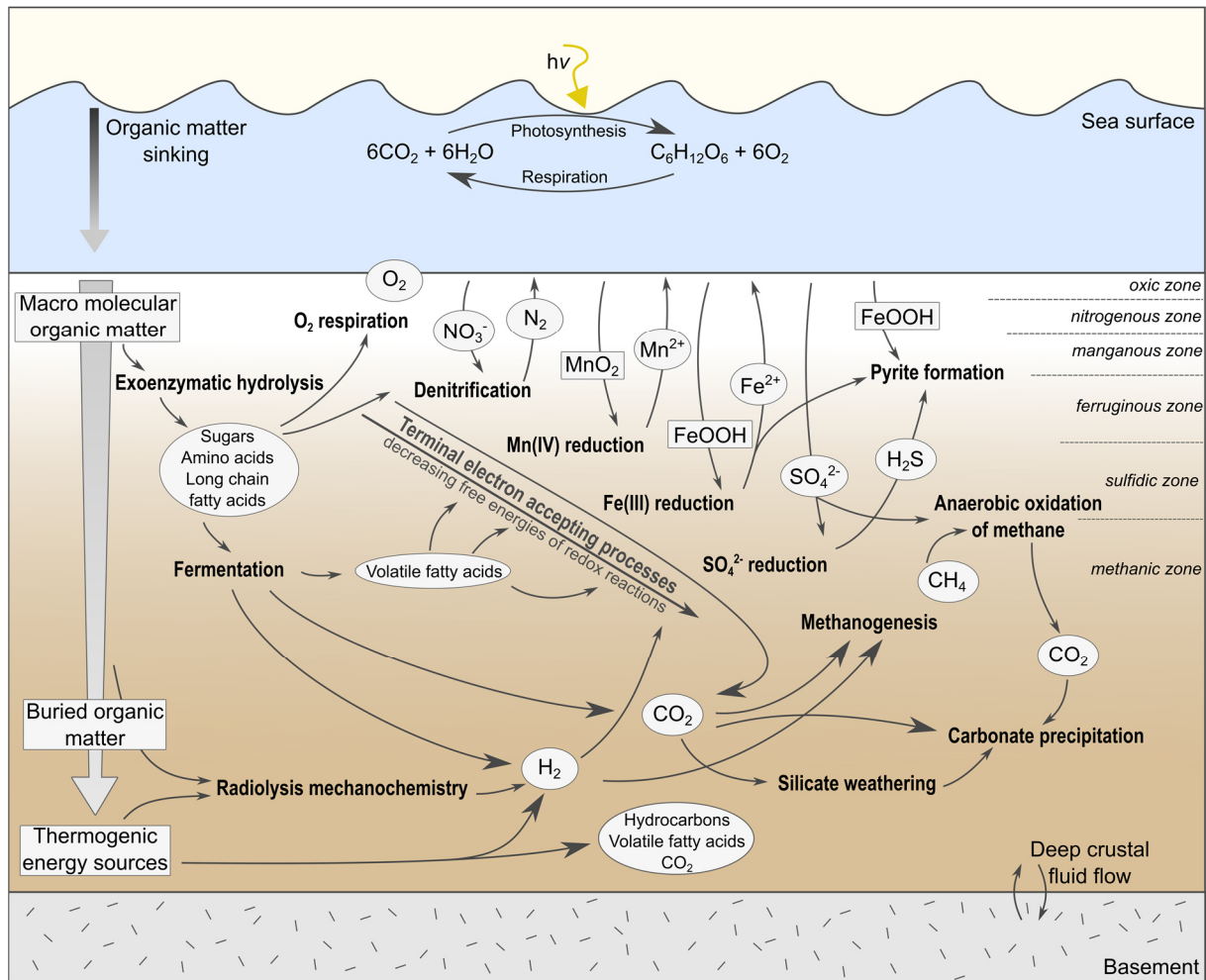


Figure 2. Schematic overview of organic carbon degradation pathways and associated (bio-)geochemical processes in subseafloor sediments. Modified after Parkes et al. (2014) and Wehrmann and Riedinger (2016). The classification of the geochemical environments is presented on the right according to Canfield and Thamdrup (2012).

During the different TEA processes, reduced species including ammonium (NH₄⁺), dissolved Mn(II), Fe(II) and hydrogen sulfide (H₂S) are released into the pore water. Froelich et al. (1979) and Berner (1981) were some of the first who defined distinct redox zones in marine sediments based on the depth distribution of the TEAs and the respective reduced products. For instance, while the suboxic zone refers to the interval where Mn(IV) and Fe(III) reduction occur, the anoxic zone is typically associated with sulfate reduction and methane production (Froelich et

al., 1979). More recently, Canfield and Thamdrup (2009) proposed a new scheme for classifying metabolic zones that accompanies the different respiration processes (Fig. 2). However, it should be noted that some of the respiration processes (e.g., Fe(III) reduction and sulfate reduction) may occur simultaneously and, thus, there could be a considerable overlap between the redox zones (Wersin et al., 1991; Canfield et al., 1993). The vertical extension of the different zones mainly depends on the availability of TEAs, the availability and composition of organic matter, the rate of organic carbon oxidation and the sedimentation rates (e.g., Kasten et al., 2003; Arndt et al., 2013).

As continental shelf and margin sediments are usually characterized by elevated organic carbon contents (> 1 wt%), O₂ and NO₃⁻ are depleted in the upper few centimeters during early diagenetic processes. Consequently, sulfate reduction and methanogenesis are the dominant terminal degradation processes in the underlying sediments (Jørgensen, 1982; D'Hondt et al., 2002, 2004). With increasing distance from continental margins to the open ocean, the water depth is generally increasing while primary productivity as well as sedimentation rates are decreasing, which leads to an overall decrease in organic carbon flux to the seafloor (Fig. 1; e.g., Jahnke, 1996; Engelen et al., 2014). As a consequence of the lower amount and quality of organic matter reaching the deep (abyssal) seafloor, sulfate reduction becomes less important in open-ocean regions, allowing deep penetration of sulfate into the sediments (Jørgensen, 1982; Bowles et al., 2014).

The diagenetic processes that are associated with the microbially mediated organic matter degradation can significantly alter the primary sediment composition as mineral dissolution and the formation of secondary mineral phases typically occurs at the redox boundaries and reaction fronts (e.g., Kasten et al., 2003; Riedinger et al., 2005). For example, dissolved Fe(II) that is released during Fe(III) reduction diffuses up- and downwards until it is re-oxidized at the Fe(II)/Fe(III) redox boundary or consumed by reaction with H₂S, resulting in the precipitation of secondary Fe(III) (oxyhydr)oxides and Fe sulfides, respectively (e.g., Berner et al., 1970). The dissolution and formation of secondary Fe minerals can considerably alter sediment properties such as the magnetic susceptibility (e.g., Riedinger et al., 2005; Roberts, 2015; see subchapter 1.3), which have been intensively used as paleoenvironmental proxy or correlation tool (e.g., Thompson et al., 1980; Dymond et al., 1992).

Another important reaction front within marine sediments is the sulfate-methane transition (SMT) where SO₄²⁻ and CH₄ intersect. At this depth, a consortium of anaerobic methane-oxidizing archaea (ANME) and sulfate-reducing bacteria (SRB) concurrently reduce downward diffusing sulfate and oxidize methane produced deeper in the sediment (Hinrichs et al., 1999;

Boetius et al., 2000). During this anaerobic oxidation of methane (AOM), bicarbonate (HCO_3^-) and H_2S are released into the pore water (e.g., Barnes and Goldberg, 1976; Niewöhner et al. 1998), which in turn favor the precipitation of carbonate and sulfide minerals. By consuming more than 90% of CH_4 produced in marine sediments, the anaerobic oxidation of methane prevents a large amount of CH_4 from escaping into the water column. Therefore, AOM represents an important process in the marine environment (Reeburgh, 1976; Knittel and Boetius, 2009). In addition to sulfate-dependent AOM, recent studies demonstrate that AOM could also be coupled to different electron acceptors including nitrate (Raghoebarsing et al., 2006) as well as Mn(IV) or Fe(III) (oxyhydr)oxides (e.g., Beal et al., 2009; Sivan et al., 2011; Riedinger et al., 2014).

A remarkable biogeochemical feature that has been observed in various deep seafloor environments is an inversion of the typical electron acceptor consumption series close to the basement. The establishment of this reverse redox zonation is due to the diffusional influx of electron acceptors including O_2 , NO_3^- and SO_4^{2-} from the underlying basaltic basement into the sediments (D'Hondt et al., 2004; DeLong, 2004). The diffusional supply of SO_4^{2-} from the underlying basement can also result in the formation of an inverse SMT where downward diffusing methane is oxidized by sulfate diffusing upwards from the underlying basement (e.g., Engelen et al., 2008; Torres et al., 2015).

1.3 Iron cycling and interactions with sulfur in seafloor sediments

Iron is one of the most abundant elements on Earth that mainly occurs as oxidized ferric (III) and reduced ferrous (II) Fe. Microorganisms acquire energy by reducing or oxidizing Fe, whereby Fe is transformed between these two redox states (e.g., Melton et al., 2014). Microbially mediated Fe(III) reduction, also referred to as dissimilatory iron reduction (DIR), is suggested to be among the most ancient metabolic pathways on Earth (Vargas et al., 1998). Furthermore, Fe(III)-reducing microorganisms can grow under high temperature and pressure conditions (Kashefi and Lovley, 2003), suggesting that microbes which use Fe(III) as electron acceptors potentially survive burial into deep and hot seafloor sediments.

The biogeochemical cycle of Fe is closely coupled to the cycles of C and S through the degradation of organic matter (e.g., Canfield, 1989). In addition to the microbially mediated reduction of Fe(III) oxides during organic carbon mineralization (e.g., Froelich et al., 1979), Fe (oxyhydr)oxides can also be reduced by H_2S which is released either during organoclastic sulfate reduction (e.g., Jørgensen, 1982) or during sulfate-dependent AOM (e.g., Barnes and Goldberg, 1976). In marine sediments, solid-phase Fe(III) is mainly present as Fe

(oxyhydr)oxides and incorporated into (phyllo-)silicates (e.g., chlorite, smectite, biotite pyroxene). The Fe (oxyhydr)oxide minerals include the poorly crystalline ferrihydrite ($5\text{Fe}_2\text{O}_3 \cdot 9\text{H}_2\text{O}$), lepidocrocite ($\gamma\text{-FeOOH}$) and goethite ($\alpha\text{-FeOOH}$) as well as the more crystalline hematite ($\alpha\text{-Fe}_2\text{O}_3$) and magnetite ($\text{Fe}^{2+}\text{Fe}^{3+}_2\text{O}_4$) (e.g., Haese, 2006). However, the solid-phase Fe(III) minerals are suggested to display different reactivity times towards H_2S . While the Fe (oxyhydr)oxides have half-lives (i.e., the time it takes for half of the material to react with H_2S) on the order of hours (ferrihydrite and lepidocrocite) to days (goethite, hematite and magnetite), (phyllo-)silicate-bound Fe(III) generally can have half-lives greater than 100 years (Canfield et al., 1992; Poulton et al., 2004).

Dissolved Fe(II) released during DIR and Fe (oxyhydr)oxides react with H_2S to form amorphous iron sulfides or mackinawite (FeS) (e.g., Berner, 1970). This highly unstable Fe sulfide mineral subsequently transforms either directly into pyrite (FeS_2) during the reaction with additional H_2S (Rickard and Luther, 1997), through the addition of elemental sulfur (Berner, 1970; Berner, 1984; Luther, 1991) or via intermediate Fe sulfide minerals such as pyrrhotite (Fe_{x-1}S) or greigite ($\text{Fe}^{2+}\text{Fe}^{3+}_2\text{S}_4$) (Fig. 3; Berner et al., 1970; Pyzik and Sommer, 1981). The formation of Fe sulfides, especially pyrite, represents a long-term sink for Fe and S in deeply buried sediments (Fig. 2; e.g., Berner, 1984).

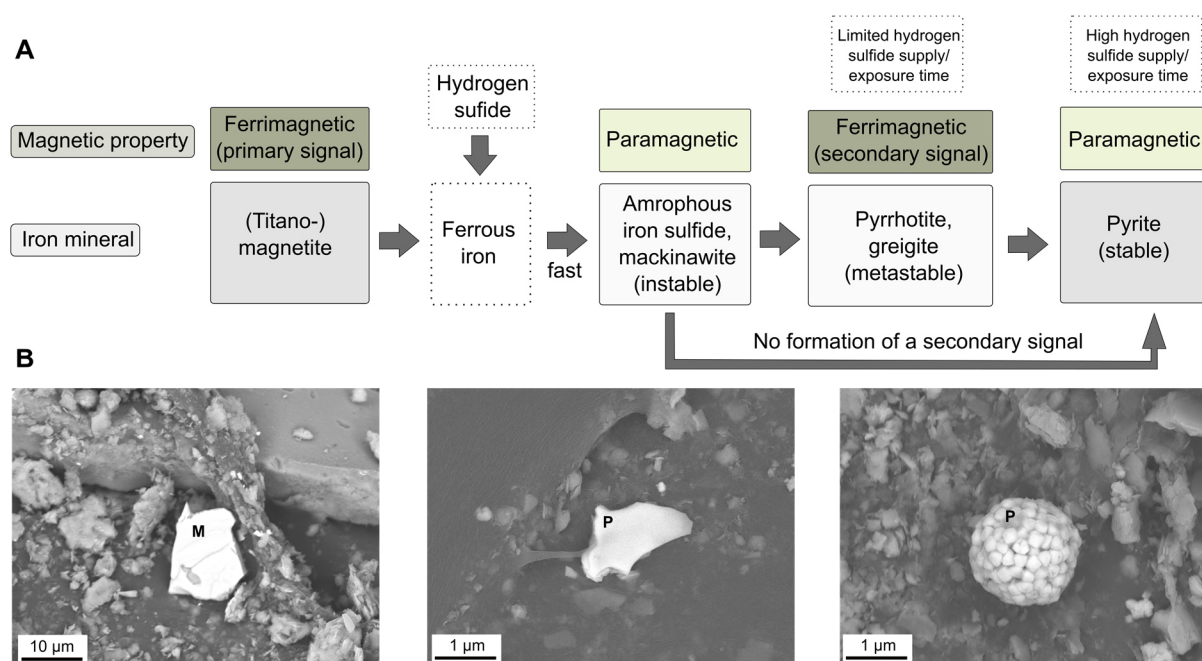


Figure 3. (A) Simplified representation of the major pathways of the transformation of Fe (oxyhydr)oxides into Fe sulfides in anoxic marine sediments and the associated alteration of the sedimentary magnetic signal. Modified after Riedinger (2005). Under high H_2S supply, pyrite is precipitated directly from amorphous Fe sulfides and mackinawite. If the H_2S supply or the exposure time to H_2S is limited, the metastable pyrrhotite and/or greigite form, leading to the formation of a secondary magnetic signal. (B) Scanning electron microscope (SEM)

photographs of (titano-)magnetite (M; left), euhedral pyrite (P; middle) and framboidal pyrite (P; right) observed in solid-phase samples from IODP Site C0023. The photographs were taken at the Center for Advanced Marine Core Research, Kochi University, Japan (personal photographs).

Since Fe minerals, notably (titano-)magnetite, are important carriers of remanent magnetization in sediments, the diagenetic conversion of ferrimagnetic Fe (oxyhydr)oxides into paramagnetic pyrite has important implications for the application and interpretation of rock magnetic properties such as the magnetic susceptibility for paleomagnetic recording (e.g., Karlin and Levi, 1983; Funk et al., 2003). The magnetic susceptibility, defined as the ratio between the induced magnetization of a material to an applied magnetic field, is used as a proxy for the magnetic mineral concentration (e.g., Roberts, 2015). While ferrimagnetic Fe (oxyhydr)oxides produce a high magnetic signal, paramagnetic minerals including pyrite do not contribute to the remanent magnetization of sediments. Consequently, the reductive dissolution of ferrimagnetic Fe (oxyhydr)oxides and the subsequent formation of paramagnetic pyrite is accompanied by a considerable loss of the magnetic signal (Fig. 3; e.g., Berner, 1970; Kasten et al., 1998; Riedinger et al., 2005). The metastable greigite, in contrast, is a ferrimagnetic mineral and, thus, its formation causes a secondary magnetic signal (Fig. 3; Fu et al., 2008). Greigite formation is favored during incomplete conversion of FeS to pyrite due to limited H₂S availability or exposure time to H₂S (e.g., Kasten et al., 1998; Riedinger et al., 2005; Fu et al., 2008).

1.4 Stable iron isotopes as indicator for microbial iron cycling

The use of stable Fe isotopes can provide valuable insights into the (bio-)geochemical cycling of Fe. Originally developed as a tool for tracing the distribution of microorganisms in ancient sedimentary environments (e.g., Beard et al., 1999), stable Fe isotopes are now widely used to decipher sources, transport and reaction pathways of Fe in seawater (e.g., Conway and John, 2014; Homoky et al., 2021) and marine sediments (e.g., Beard et al., 2003; Severmann et al., 2006; Henkel et al., 2016, 2018). Natural Fe consists of four stable isotopes with the following relative abundances: ⁵⁴Fe (5.85%), ⁵⁶Fe (91.75%), ⁵⁷Fe (2.12%) and ⁵⁸Fe (0.28%). Fe isotope variations are typically expressed using the delta notation ($\delta^{56}\text{Fe}$) in per mil (‰) as:

$$\delta^{56}\text{Fe} [\text{‰}] = \left[\left(\frac{{}^{56}\text{Fe}/{}^{54}\text{Fe}_{\text{sample}}}{{}^{56}\text{Fe}/{}^{54}\text{Fe}_{\text{standard}}} \right) - 1 \right] * 1000.$$

where the iron isotopic reference material IRMM-014 (Taylor et al., 1992) or the isotopically identical IRMM-524 (Craddock and Dauphas, 2011; Dauphas et al., 2017) are used as standard. Fe isotopes fractionate during microbially mediated redox processes such as DIR (Beard et al., 1999, 2003; Crosby et al., 2005, 2007) and the anaerobic photosynthetic oxidation of Fe(II) (Croal et al., 2004). The most pronounced fractionation of up to -3‰ compared to the average

isotopic composition of terrestrial igneous rock ($\delta^{56}\text{Fe} = 0.09 \pm 0.05\%$; Beard et al., 2003) is related to DIR (e.g., Beard et al., 1999, Severmann et al., 2006; Crosby et al., 2007). The release of isotopically light dissolved Fe(II) compared to the ferric substrate during DIR is caused by coupled electron and Fe atom exchange between dissolved and sorbed Fe(II) and reactive Fe(III) at the surface of Fe (oxyhydr)oxides (Crosby et al., 2005, 2007). Measurable Fe isotope fractionation up to $\sim 1\%$ is also produced during abiotic processes including the adsorption of dissolved Fe(II) onto minerals surfaces (Icopini et al., 2004; Crosby et al., 2005, 2007) and the precipitation of Fe(III) (oxyhydr)oxides (Bullen et al., 2001; Skulan et al., 2002; Balci et al., 2006), Fe sulfides (Butler et al., 2005; Guilbaud et al., 2011) and Fe carbonates (Wiesli et al., 2004).

Two types of stable isotope fractionation are known to exist in natural environments. Kinetic fractionation is caused by different reaction rates of light and heavy isotopes during incomplete and unidirectional processes. In contrast, equilibrium fractionation is driven by energy differences in bonding environments (i.e., heavier isotopes are enriched in the compound or phase in which they are most stably bound) and occurs when forward and backward reactions between two phases proceed at the same rate (e.g., Wiederhold, 2015).

Kinetic and equilibrium isotope effects may act in opposing directions. For example, kinetically controlled precipitation of Fe sulfides and siderite (FeCO_3) preferentially incorporates isotopically light dissolved Fe (Wiesli et al., 2004; Butler et al., 2005), whereas equilibrium fractionation causes isotopically heavy Fe sulfides (Guilbaud et al., 2011). Kinetic effects, however, generally dominate over equilibrium fractionation in natural, open systems such as marine sediments (Wiederhold, 2015). The preferential incorporation of isotopically light ^{54}Fe into Fe sulfide minerals causes a relative enrichment of ^{56}Fe in the residual dissolved Fe(II) pool and a shift towards higher $\delta^{56}\text{Fe}$ values (e.g., Severmann et al., 2006). Thus, a discrimination between microbially mediated Fe reduction and abiotic Fe-S interactions based on $\delta^{56}\text{Fe}$ signatures is feasible (e.g., Johnson and Beard, 2005). In order to use Fe isotopes as a tool for tracing reaction pathways and to study Fe phase-specific fractionation, the isotopic composition of both the dissolved as well as the different reactive Fe pools is required (Henkel et al., 2016, 2018).

In view of the variety of fractionation processes and the associated imprint on the isotopic composition of dissolved and solid-phase Fe, the application of stable Fe isotopes analyses might also be a useful tool for deciphering the biogeochemical Fe cycling not only in shallow marine but also in deep seafloor sediments.

1.5 Non-steady state diagenesis in the deep subseafloor biosphere

Sediment cores that are retrieved during drilling expeditions usually cover depth ranges of several hundred of meters, thus, representing unique deep-time records to investigate Earth's paleo-climatic and –oceanographic history. The extended sediment sequences further provide important data to study the variability of biogeochemical processes on geological timescales (> millions of years) (e.g., Wehrmann et al., 2013; Wehrmann and Ferdelman, 2014).

(Bio-)geochemical processes in marine sediments are often considered as steady state diagenesis, where fluxes of electron acceptors and donors are balanced and reactions fronts are located at specific depths relative to the sediment surface (Froelich et al., 1979; Berner, 1981). Diagenesis under steady state conditions can only occur if the sediment input, including reactive minerals and organic carbon, remains constant over time (Kasten et al., 2003). However, depositional and oceanographic conditions including the organic carbon flux, sediment composition, sedimentation rates, nutrient supply in surface waters and/or bottom-water oxygen concentrations are highly variable (Pruysers et al., 1993; Kasten et al., 2003; see also Wehrmann and Riedinger, 2016, for review). Therefore, steady state diagenesis is the exception rather than the rule in deep subseafloor sediments, especially on longer timescales from millennia to millions of years.

For example, Wehrmann et al. (2013) demonstrate that an increase in deposition and reactivity of organic matter to the seafloor at Bowers Ridge in the Bearing Sea, possibly linked to elevated surface water primary productivity at around 2.6 Ma, led to higher organoclastic sulfate reduction rates, the onset of methanogenesis and ultimately to AOM coupled to sulfate reduction. Furthermore, variations in the supply and quality of organic carbon in response to glacial-interglacial cycles in sediments drilled on the Peruvian shelf caused a cyclic 100-ka migration of the SMT (Contreras et al., 2013). Variabilities in the quantity and reactivity of organic carbon are not only related to climatic and oceanographic changes, but they can also be controlled by the tectonically induced migration of ocean seafloor. For instance, ODP Leg 202 Site 1237, located off the coast of Peru in the Pacific Ocean, has moved $\sim 20^\circ$ westward relative to South America over the past 42 Ma. This movement is accompanied by a significant increase in organic carbon contents since the last five million years. The increase in organic carbon contents is likely related to a higher primary productivity resulting from enhanced nutrient supply via upwelling of nutrient-rich waters as the site moved towards the coast of Peru (Shipboard Scientific Party, 2003). Ultimately, changes in environmental conditions and tectonic dynamics can have a significant impact on microbial reactions rates, the geochemical zonation and the location of reaction fronts including the SMT.

Since past changes in geochemical conditions are not necessarily reflected in the modern pore-water profiles and the depth distribution of microbial activity, the reconstruction of (bio-)geochemical processes in deep subseafloor sediments relies on diagenetic proxies that are preserved in the solid phase (e.g., Meister, 2015; Meister et al., 2019). For example, vertical shifts of the sulfidization front can cause the dissolution of primary Fe (oxyhydr)oxides and the subsequent formation of Fe sulfides (e.g., Kasten et al., 1998; Riedinger et al., 2005, see subchapter 1.3). In addition, multiple layers of authigenic barite and dolomite can serve as indicators for the migration of the SMT (e.g., Riedinger et al., 2006; Arndt et al., 2009; Contreras et al., 2013) and distinct isotopic signatures in pyrite and dolomite can provide information on changes of biogeochemical activity in the past (Meister et al., 2019).

Another valuable tool to study the temporal evolution of (bio-)geochemical processes in subseafloor sediments as well as to infer past and present reaction rates is the application of reactive transport modeling (e.g., Arndt et al., 2006, 2009; Henkel et al., 2012; Contreras et al., 2013; Wehrmann et al., 2013).

1.6 Temperature limit of microbial life in the deep subseafloor biosphere

(Bio-)geochemical processes are not only controlled by changes in depositional, climatic and oceanographic conditions, but (bio-)geochemical reaction rates are also a function of temperature (e.g., Arndt et al., 2013). The temperature within the subseafloor sediments typically increases with an average thermal gradient of $\sim 30^{\circ}\text{C km}^{-1}$. With ongoing burial, the increasing temperature poses a significant stress factor for microbial communities particularly in deeper sediments as biomolecule-damaging reactions and, consequently, the energy required to repair this thermal damage to cellular components also increase (e.g., Lever et al., 2015).

The lower boundary of the deep biosphere is suggested to be defined by a certain upper temperature limit (e.g., Parkes et al., 2014; LaRowe et al., 2017). While microbial life in energy-rich hydrothermal vent environments is maintained at temperatures up to 122°C (Kashefi and Lovley, 2003; Takai et al., 2008), the upper temperature limit of microbial life in energy-limited subseafloor sediments is unknown to date. However, biological degradation of hydrocarbon ceases at temperatures above $\sim 80^{\circ}\text{C}$, and this temperature threshold has been proposed as thermal barrier for microbial life in the energy-depleted deep subsurface (Wilhelms et al., 2001; Head et al., 2003). Since about one fourth of Earth's marine sediment volume is buried at temperatures above 80°C (LaRowe et al., 2017), there is a great interest in finding the high-temperature limit of microbial life in the deep subseafloor biosphere.

To investigate the influence of temperature on microbial communities and their activities within the deep biosphere, IODP Expedition 370 (Temperature Limit of the Deep Biosphere off Muroto) established Site C0023 down to 1,180 mbsf in the Nankai Trough off Cape Muroto, Japan (Heuer et al., 2017). The Nankai Trough, which marks the subduction boundary between the Philippine Sea plate and the Eurasian plate (Fig. 4; see subchapter 1.7), is characterized by anomalously high heat flows (Yamano et al., 1992). With a steep, geothermal gradient of $110^{\circ}\text{C km}^{-1}$, the temperature at IODP Site C0023 reaches 120°C at the sediment-basement interface (Heuer et al., 2020). Consequently, the recovered sediment sequences span the range of suitable conditions for psychrophilic (optimal growth temperature range $< 20^{\circ}\text{C}$), mesophilic (20° to 43°C), thermophilic (43° to 80°C) and hyperthermophilic ($> 80^{\circ}\text{C}$) microorganisms (Heuer et al., 2017). Due to the high *in situ* temperatures, the Nankai Trough represents an ideal setting to explore the upper temperature limit and prerequisite of microbial life in the deep subseafloor biosphere.

1.7 Geological setting of the Nankai Trough subduction zone

IODP Site C0023 ($32^{\circ}22.00'\text{N}$, $134^{\circ}57.98'\text{E}$; 4,776 m water depth) is located at the seaward end of the Nankai Trough accretionary prism, 125 km southeast of Shikoku Island, Japan, in the northwestern Pacific Ocean (Fig. 4; Heuer et al., 2017). The Nankai Trough accretionary complex is formed due to the subduction of the Philippine Sea plate beneath the Japanese Island arc, which is part of the Eurasian plate. The Philippine Sea plate, including the Shikoku Basin, is subducting along the 700 km-long Nankai Trough at a current rate of $4\text{--}6\text{ cm yr}^{-1}$ (Seno et al., 1993; Miyazaki and Heki, 2001).

Over the last decades, several DSDP, ODP and IODP expeditions targeted the Nankai Trough and the incoming sedimentary sections, mainly to study the role of deformation and fluid flow processes as well as seismogenesis and fault mechanics in the subduction zone (e.g., Pickering et al., 1993; Moore et al., 2001a; Kinoshita et al., 2009). During these expeditions, the drilling sites were established along three transects – namely Ashizuri, Muroto and Kumano transects – that are perpendicular to the Nankai Trough. IODP Site C0023 lies on the Muroto Transect, named after Cape Muroto on Shikoku Island, close to ODP Sites 1173, 1174 and 808 (Fig. 4; Taira et al., 1991; Moore et al., 2001b). Based on the results of the previous expeditions, the geology, depositional structure and lithostratigraphy of the Nankai Trough and the incoming sediments are widely understood by now.

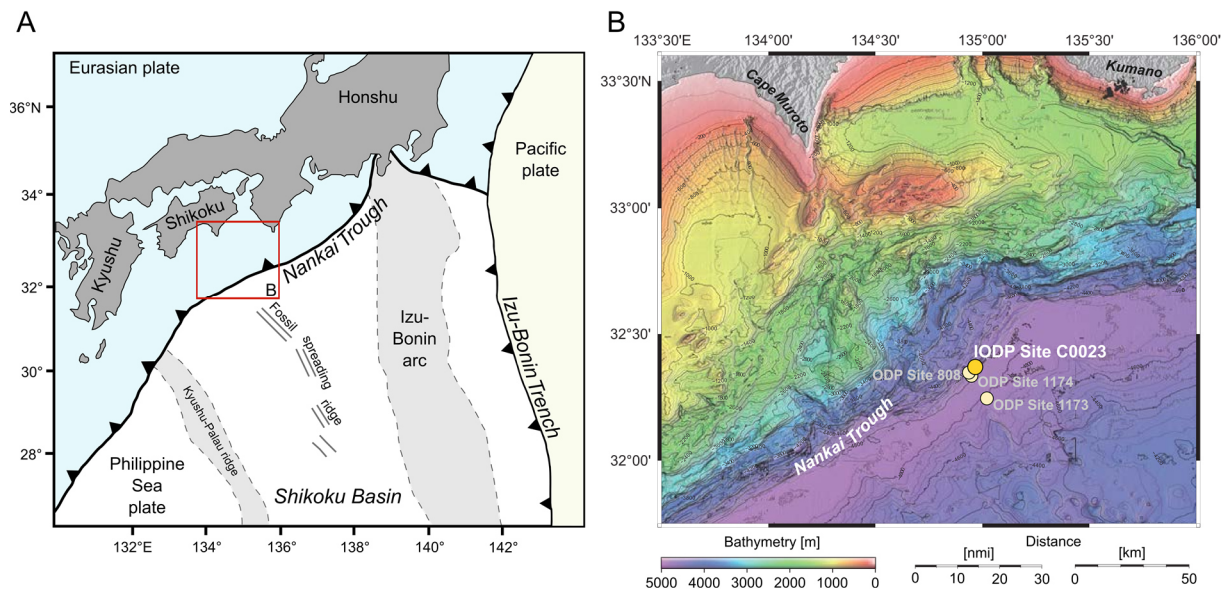


Figure 4. (A) General tectonic configuration of the Nankai Trough subduction zone. (B) Bathymetric map of IODP Site C0023 (yellow circle) and adjacent ODP Sites 808, 1173 and 1174 (white circles). Modified after Heuer et al. (2017).

The Shikoku Basin is a back-arc basin that is located at the northern end of the Philippine Sea plate and bounded by the Kyushu-Palau ridge and the Izu-Bonin arc to the east and west, respectively (Fig. 4; Okino et al., 1994). In the south, the Shikoku Basin merges with the Parece Vela Basin (Mrozowski and Hayes, 1979). The Shikoku Basin formed between 26 and 15 Ma during rifting of the paleo-Izu-Bonin back-arc and seafloor spreading in the eastern part of the Philippine Sea plate (Watts and Wiesel, 1975; Okino et al., 1994, 1999). A bathymetric high, the Kinan Seamount chain, runs along the axis of the Shikoku Basin from north to south and represents the fossil spreading center (Fig. 4; e.g., Sato et al., 2002).

Over the past 15 Ma, IODP Site C0023 has moved relative to its present-day position due to tectonic motion of the Philippine Sea plate (e.g., Mahony et al., 2011; Wu et al., 2016). The subduction of the Philippine Sea plate beneath the proto-Nankai margin began just before the extinction of the Shikoku Basin spreading center at ~15 Ma (Hibbard and Karig, 1990). Between 10 and 6 Ma, sinistral slip along the transcurrent margin of southeast Japan shifted the triple conjunction between the Pacific, Eurasian and Philippine Sea plate to the northeast (Kimura et al., 2014). This sinistral motion also caused the collision of the Izu-Bonin arc with the Honshu Island arc at 8 to 6 Ma. The tectonic movement of the Philippine Sea plate changed at 6 Ma when trench-normal subduction along the proto-Nankai margin was re-initiated and subduction rates increased (e.g., Wu et al., 2016). The subduction of the Philippine Sea plate and the resulting off-scraping of the trench wedge sediment from the descending Philippine Sea

plate led to the formation of the Nankai accretionary prism (e.g., Le Pichon et al., 1987; Taira et al., 1992).

The basaltic basement at IODP Site C0023 was formed at ~16 Ma, when the site was located close the spreading center of the Shikoku Basin. During the tectonically induced migration from the central Shikoku Basin to the Nankai Trough, a volcanoclastics facies (Unit V) and a ~600 m thick sediment sequence of hemipelagic mudstone accumulated on the basement. This sediment section can further be divided into the Lower Shikoku (Unit IV) and the Upper Shikoku Basin facies (Unit III). IODP Site C0023 reached the Nankai Trough at around 0.43 Ma, leading to the deposition of the Trench-to-basin transitional (Subunit IIC) and the Trench-wedge facies (Subunit IIA and IIB) (Heuer et al., 2017). The characteristics of the different lithological units are described in detail in Chapter II.

1.8 Motivation and objectives

The work carried out in this cumulative doctoral thesis contributes to the research questions of IODP Expedition 370 (Temperature Limit of the Deep Biosphere off Muroto), which aimed at exploring the limits and prerequisites of microbial life in the deep biosphere (Heuer et al., 2017). The drilling expedition was designed to study factors that control the microbial abundance, diversity and metabolic activity in deep and hot sediments. This includes the investigation of nutrient and energy substrates that can potentially sustain life at depth. Another aim was to identify geochemical and microbial signatures that differentiate the biotic and abiotic realms and/or the transition (Hinrichs et al., 2016; Heuer et al., 2017).

Within the framework of the overarching questions of IODP Expeditions 370, the objectives of this doctoral thesis were:

- (1) The reconstruction of (bio-)geochemical processes of sediments along the tectonically induced migration of IODP Site C0023 from the central Shikoku Basin to the Nankai Trough and the assessment of the associated diagenetic overprint of the primary Fe pool and its effect on rock magnetic properties

- (2) The quantification and characterization of reactive Fe pools that might serve as energy substrates for microbial respiration in the deep and hot sediments at IODP Site C0023

(3) The investigation of the stable Fe isotopic composition of dissolved and reactive solid-phase Fe pools to disentangle microbially mediated and abiotic drivers of the Fe cycling in deep seafloor sediments at IODP Site C0023

1.9 Declaration of (co)-author contributions

This cumulative doctoral thesis comprises a collection of three first-authorship manuscripts and one co-authorship manuscript. In the following, the individual (co-)author contributions to the scientific articles and the manuscript statuses are reported.

CHAPTER II: Evolution of (bio-)geochemical processes and diagenetic alteration of sediments along the tectonic migration of ocean floor in the Shikoku Basin off Japan

Male Köster, Myriam Kars, Florence Schubotz, Man-Yin Tsang, Markus Maisch, Andreas Kappler, Yuki Morono, Fumio Inagaki, Verena B. Heuer, Sabine Kasten, Susann Henkel

Status: Published in *Geochemistry, Geophysics, Geosystems*; published online June 21, 2021; doi:10.1029/2020GC009585

M. Köster, S. Kasten and S. Henkel designed and planned the study. S. Henkel and F. Schubotz carried out the sampling and analyses onboard *D/V Chikyu* during IODP Expedition 370. M. Köster conducted the analytical work in the laboratories at the Alfred Wegener Institute (AWI) Helmholtz Centre for Polar and Marine Research in Bremerhaven, Germany, with the support of M.-Y. Tsang and a student assistant. M. Köster and M. Kars performed the IRM acquisition end-member unmixing during a research stay of M. Köster at the Center for Advanced Marine Core Research (CMCR), Kochi University, Japan, and evaluated the data. M. Kars conducted magnetic susceptibility measurements at the CMCR. The stable carbon isotopic composition of TOC and biomarker analyses as well as the data evaluation were performed by F. Schubotz at the MARUM – Center for Marine Environmental Sciences, University of Bremen, Germany. M. Maisch and A. Kappler carried out the ^{57}Fe Mössbauer spectroscopy analysis at the Center for Applied Geosciences at the University of Tübingen, Germany, and helped with the data interpretation. V.B. Heuer, F. Inagaki and Y. Morono led the IODP Expedition 370 as co-chief scientist. M. Köster wrote the manuscript with substantial contributions of M. Kars, F. Schubotz, V.B. Heuer, S. Kasten and S. Henkel. All co-authors helped to improve the final manuscript version. The personal contribution is estimated to 80%.

CHAPTER III: Influence of early low-temperature and later high-temperature diagenesis on magnetic mineral assemblages in marine sediments from the Nankai Trough

Myriam Kars, Male Köster, Susann Henkel, Rüdiger Stein, Florence Schubotz, Xiang Zhao, Stephen A. Bowden, Andrew P. Roberts, Kazuto Kodama

Status: Published in *Geochemistry, Geophysics, Geosystems*; published online October 18, 2021; doi:10.1029/2021GC010133

The study was conceived by M. Kars. M. Kars carried out the sampling at Kochi Core Center, Japan, and all rock magnetic measurements at the CMCR. M. Kars, X. Zhao and A.P. Roberts conducted irregular FORC measurements at the Australian National University, Australia. Rock-Eval pyrolysis was performed by R. Stein at the AWI in Bremerhaven. F. Schubotz interpreted and discussed the Rock-Eval data. S.A. Bowden produced the basin modeling. K. Kodama participated to the discussion. M. Kars wrote the manuscript with substantial contributions from M. Köster, S. Henkel, F. Schubotz, S.A. Bowden and A.P. Roberts. The personal contribution is estimated to 10%.

CHAPTER IV: Uniquely low stable iron isotopic signatures in deep marine sediments caused by Rayleigh distillation

Male Köster, Michael Staubwasser, Anette Meixner, Simone A. Kasemann, Hayley R. Manners, Yuki Morono, Fumio Inagaki, Verena B. Heuer, Sabine Kasten, Susann Henkel

Status: Manuscript submitted to *Nature Geoscience* on March 29, 2022

M. Köster, S. Henkel and S. Kasten designed the study. S. Henkel carried out the sampling and analyses onboard *D/V Chikyu* during IODP Expedition 370. M. Köster conducted the analytical work and sample preparation for iron isotope analyses in the laboratories at AWI in Bremerhaven. A. Meixner, M. Staubwasser and S. Henkel performed the iron isotope measurements at the MARUM and the University of Cologne, Germany. M. Köster did the geochemical interpretation with substantial input from M. Staubwasser, S. Henkel and S. Kasten. H.R. Manners provided discrete ash layer samples. V.B. Heuer, F. Inagaki and Y. Morono led the IODP Expedition 370 as co-chief scientist. M. Köster wrote the manuscript

with significant contributions from all co-authors. The personal contribution is estimated to 80%.

CHAPTER V: Fading of a sulfate-methane transition in deep and hot subseafloor sediments from the Nankai Trough

Male Köster, Bo Liu, Akira Ijiri, Arthur J. Spivack, Yuki Morono, Fumio Inagaki, Verena B. Heuer, Sabine Kasten, Susann Henkel

Status: Manuscript in preparation (March 29, 2022), planned submission to *Geology*

The study was devised by M. Köster, S. Kasten and S. Henkel. B. Liu performed the reactive transport modeling and provided model results. S. Henkel and A.J. Spivack carried out the sampling and analyses onboard *D/V Chikyu* during IODP Expedition 370. A.J. Spivack performed the quality control of the sulfate data. A. Ijiri conducted the measurement of the isotopic composition of DIC. The first draft of the manuscript was written by M. Köster with substantial contributions from B. Liu, S. Henkel, and S. Kasten. The personal contribution is estimated to 70%.

References

- Arndt, S., Brumsack, H.-J., and Wirtz, K.W., 2006. Cretaceous black shales as active bioreactors: A biogeochemical model for the deep biosphere encountered during ODP Leg 207 (Demera Rise). *Geochimica et Cosmochimica Acta*, **70**, 408-425. doi:10.1016/j.gca.2005.09.010.
- Arndt, S., Hetzel, A., and Brumsack, H.-J., 2009. Evolution of organic matter degradation in Cretaceous black shales inferred from authigenic barite: A reaction-transport model. *Geochimica et Cosmochimica Acta*, **73**, 2000-2022. doi:10.1016/j.gca.2009.01.018.
- Arndt, S., Jørgensen, B.B., LaRowe, D.E., Middelburg, J.J., Pancost, R.D., and Regnier, P., 2013. Quantifying the degradation of organic matter in marine sediments: A review and synthesis. *Earth-Science Reviews*, **123**, 53-86. doi:10.1016/j.earscirev.2013.02.008.
- Balci, N., Bullen, T.D., Witte-Lien, K., Shanks, W.C., Motelica, M., and Mandernack, K.W., 2006. Iron isotope fractionation during microbially stimulated Fe(II) oxidation and Fe(III) precipitation. *Geochimica et Cosmochimica Acta*, **70**, 622-639. doi:10.1016/j.gca.2005.09.025.
- Barnes, R.O., and Goldberg, D.E., 1976. Methane production and consumption in anoxic marine sediments. *Geology*, **4**, 297-300. doi:10.1130/0091-7613(1976)4%3C297:MPACIA%3E2.0.CO;2.

- Beal, E.J., House, C.H., and Orphan, V.J., 2009. Manganese- and iron-dependent marine methane oxidation. *Science*, **325**, 184-187. doi:10.1126/science.1169984.
- Beard, B.L., Johnson, C.M., Cox, L., Sun, H., Nealson, K.H., and Aguilar, C., 1999. Iron isotope biosignatures. *Science*, **285**, 1889-1892. doi:10.1126/science.285.5435.1889.
- Beard, B.L., Johnson, C.M., Skulan, J.L., Nealson, K.H., Cox, L., and Sun, H., 2003. Application of Fe isotopes to tracing the geochemical and biological cycling of Fe. *Chemical Geology*, **195**, 87-117. doi:10.1016/S0009-2541(02)00390-X.
- Berger, W.H., Smetacek, V.S., and Wefer, G., 1989. Ocean productivity and paleoproductivity – an overview. In: *Productivity of the ocean: present and past* (eds. Berger, W.H., Smetacek, V.S., and Wefer, G.). John Wiley and Sons, Chichester, 1-34.
- Berner, R.A., 1970. Sedimentary pyrite formation. *American Journal of Science*, **268**, 1-23. doi:10.2475/ajs.268.1.1.
- Berner, R.A., 1981. A new geochemical classification of sedimentary environments. *Journal of Sedimentary Research*, **51**, 359-365. doi:10.1306/212F7C7F-2B24-11D7-8648000102C1865D.
- Berner, R.A., 1982. Burial of organic carbon and pyrite sulfur in the modern ocean: its geochemical and environmental significance. *American Journal of Science*, **282**, 451-473. doi:10.2475/ajs.282.4.451.
- Berner, R.A., 1984. Sedimentary pyrite formation: An update. *Geochimica et Cosmochimica Acta*, **48**, 605-615. doi:10.1016/0016-7037(84)90089-9.
- Boetius, A., Ravenschlag, K., Schubert, C.J., Rickert, D., Widdel, F., Gieseke, A., et., 2000. A marine microbial consortium apparently mediating anaerobic oxidation of methane. *Nature*, **407**, 623-626. doi:10.1038/35036572.
- Bowles, M.W., Mogollón, J.M., Kasten, S., Zabel, M., and Hinrichs, K.-U., 2014. Global rates of marine sulfate reduction and implications for sub-seafloor metabolic activities. *Science*, **344**, 889-891. doi:10.1126/science.1249213.
- Bullen, T.D., White, A.F., Childs, C.W., Vivit, D.V., and Schulz, M.S., 2001. Demonstration of significant abiotic iron isotope fractionation in nature. *Geology*, **29**, 699-702. doi:10.1130/0091-7613(2001)029%3C0699:DOSAI%3E2.0.CO;2.
- Butler, I.B., Archer, C., Vance, D., Oldroyd, A., and Rickard, D., 2005. Fe isotope fractionation of FeS formation in ambient aqueous solution. *Earth and Planetary Science Letters*, **236**, 430-442. doi:10.1016/j.epsl.2005.05.022.
- Canfield, D.E., 1989. Reactive iron in marine sediments. *Geochimica et Cosmochimica Acta*, **53**, 619-632. doi:10.1016/0016-7037(89)90005-7.
- Canfield, D.E., Raiswell, R., Bottrell, S.H., 1992. The reactivity of sedimentary iron minerals toward sulfide. *American Journal of Science*, **292**, 659-683. doi:10.2475/ajs.292.9.659.
- Canfield, D.E., Thamdrup, B., and Hansen, J.W., 1993. The anaerobic degradation of organic matter in Danish coastal sediments: Iron reduction, manganese reduction, and sulfate reduction. *Geochimica et Cosmochimica Acta*, **48**, 1223-1235. doi:10.1016/0016-7037(93)90340-3.
- Canfield, D.E., and Thamdrup, B., 2009. Towards a consistent classification scheme for geochemical environments, or, why we wish the term ‘suboxic’ would go away. *Geobiology*, **4**, 385-392. doi:10.1111/j.1472-4669.2009.00214.x.
- Contreras, S., Meister, M., Liu, B., Prieto-Mollar, X., Hinrichs, K.-U, Khalili, A., Ferdelman, T.G., Kuypers, M.M.M., and Jørgensen, B.B., 2013. Cyclic 100-ka (glacial-interglacial)

- migration of subseafloor redox zonation on the Peruvian shelf. *Proceedings of the National Academy of Sciences of the United States of America*, **110**, 18098-18103. doi:10.1073/pnas.1305981110.
- Conway, T.M., and John, S.G., 2014. Quantification of dissolved iron sources to the North Atlantic Ocean. *Nature*, **511**, 212-215. doi:10.1038/nature13482.
- Craddock, P.R., and Dauphas, N., 2011. Iron isotopic compositions of geological reference materials and chondrites. *Geostandards and Geoanalytical Research*, **35**, 101-123. doi:10.1111/j.1751-908X.2010.00085.x.
- Croal, L.R., Johnson, C.M., Beard, B.L., and Newman, D.K., 2004. Iron isotope fractionation by Fe(II)-oxidizing photoautotrophic bacteria. *Geochimica et Cosmochimica Acta*, **68**, 1227-1242. doi:10.1016/j.gca.2003.09.011.
- Crosby, H.A., Johnson, C.M., Roden, E.E., and Beard, B.L., 2005. Coupled Fe(II)-Fe(III) electron and atom exchange as a mechanism for Fe isotope fractionation during dissimilatory iron oxide reduction. *Environmental Science & Technology*, **39**, 6698-6704. doi:10.1021/es0505346.
- Crosby, H.A., Roden, E.E., Johnson, C.M., and Beard, B.L., 2007. The mechanisms of iron isotope fractionation produced during dissimilatory Fe(III) reduction by *Shewanella putrefaciens* and *Geobacter sulfurreducens*. *Geobiology*, **5**, 169-189. doi:10.1111/j.1472-4669.2007.00103.x.
- Dauphas, N., John, S.G., and Rouxel, O., 2017. Iron isotope systematics. *Reviews in Mineralogy and Geochemistry*, **82**, 415-510. doi:10.2138/rmg.2017.82.11.
- DeLong, E.F., 2004. Microbial life breathes deep. *Science*, **306**, 2198-2200. doi:10.1126/science.1107241.
- D'Hondt, S., Rutherford, S., and Spivack, A.J., 2002. Metabolic activity of subsurface life in deep-sea sediments. *Science*, **295**, 2067-2070. doi:10.1126/science.1064878.
- D'Hondt, S., Jørgensen, B.B., Miller, D.J., Batzke, A., Blake, R., Cragg, B.A., et al., 2004. Distributions of microbial activities in deep subseafloor sediments. *Science*, **306**, 2216-2221. doi:10.1126/science.1101155.
- Dymond, J., Suess, E., and Lyle, M., 1992. Barium in deep-sea sediment: A geochemical proxy for paleoproductivity. *Paleoceanography*, **7**, 163-181. doi:10.1029/92PA00181.
- Engelen, B., Ziegelmüller, K., Wolf, L., Köpke, B., Gittel, A., and Cypionka, H., 2008. Fluids from the oceanic crust support microbial activities within the deep biosphere. *Geomicrobiology Journal*, **25**, 56-66. doi:10.1080/01490450701829006.
- Engelen, B., Engelhardt, T., and Cypionka, H., 2014. Phagen in Sedimenten der marinen tiefen Biosphäre. *BIOspektrum*, **20**, 380-382. doi:10.1007/s12268-014-0451-0.
- Froelich, P.N., Klinkhammer, G.P., Bender, M.L., Luedtke, N.A., Heath, G.R., Cullen, D., Dauphin, P., Hammond, D., Hartman, B., and Maynard, V., 1979. Early oxidation of organic matter in pelagic sediments of the eastern equatorial Atlantic: suboxic diagenesis. *Geochimica et Cosmochimica Acta*, **43**, 1075-1090. doi:10.1016/0016-7037(79)90095-4.
- Fu, Y., von Döbeneck, T., Frank, C., Heslop, D., and Kasten, S., 2008. Rock magnetic identification and geochemical process models of greigite formation in Quaternary marine sediments from the Gulf of Mexico (IODP Hole U1319A). *Earth and Planetary Science Letters*, **375**, 233-245. doi:10.1016/j.epsl.2008.07.034.
- Funk, J.A., von Döbeneck, T., and Reitz, A., 2003. Integrated rock magnetic and geochemical quantification of redoxomorphic iron mineral diagenesis in Late Quaternary sediments

- from the equatorial Atlantic. In: *The South Atlantic in the Late Quaternary* (eds. Wefer, G., Mulitza, S., and Ratmeyer, V.). Springer, Berlin Heidelberg, 237-260. doi:10.1007/978-3-642-18917-3_12.
- Guilbaud, R., Butler, I.B., Ellam, R.M., Rickard, D., and Oldroyd, A., 2011. Experimental determination of the equilibrium Fe isotope fractionation between $\text{Fe}^{2+}_{\text{aq}}$ and FeS_m (mackinawite) at 25 and 2 °C. *Chemical Geology*, **75**, 2721-2734. doi:10.1016/j.gca.2011.02.023.
- Haese, R.R., 2006. The reactivity of iron. In: *Marine Geochemistry* (eds. Schulz, H.D., and Zabel, M.). Springer, Berlin Heidelberg, 241-270.
- Head, I.M., Jones, D.M., and Larter, S.R., 2003. Biological activity in the deep subsurface and the origin of heavy oil. *Nature*, **426**, 344-352. doi:10.1038/nature02134.
- Hedges, J.I., and Keil, R.G., 1995. Sedimentary organic matter preservation: an assessment and speculative synthesis. *Marine Chemistry*, **49**, 81-115. doi:10.1016/0304-4203(95)00008-F.
- Henkel, S., Mogollón, J.M., Nöthen, K., Franke, C., Bogus, K., Robin, E., Bahr, A., Blumenberg, M., Pape, T., Seifert, R., März, C., de Lange, G.J., and Kasten, S., 2012. Diagenetic barium cycling in Black Sea sediments – A case study for anoxic marine environments. *Geochimica et Cosmochimica Acta*, **88**, 88-105. doi:10.1016/j.gca.2012.04.021.
- Henkel, S., Kasten, S., Poulton, S.W., and Staubwasser, M., 2016. Determination of the stable iron isotopic composition of sequentially leached iron phases in marine sediments. *Chemical Geology*, **421**, 93-102. doi:10.1016/j.chemgeo.2015.12.003.
- Henkel, S., Kasten, S., Hartmann, J.F., Silva-Busso, A., and Staubwasser, M., 2018. Iron cycling and stable Fe isotope fractionation in Antarctic shelf sediment, King George Island. *Geochimica et Cosmochimica Acta*, **237**, 320-338. doi:10.1016/j.gca.2018.06.042.
- Heuer, V.B., Inagaki, F., Morono, Y., Kubo, Y., Maeda, L., and the Expedition 370 Scientists, 2017. Temperature limit of the deep biosphere off Muroto. *Proceedings of the International Ocean Discovery Program Volume 370*: College Station, TX (International Ocean Discovery Program). doi:10.14379/iodp.proc.370.2017.
- Heuer, V.B., Inagaki, F., Morono, Y., Kubo, Y., Spivack, A., Viehweger, B., et al., 2020. Temperature limits to deep seafloor life in the Nankai Trough subduction zone. *Science*, **370**, 1230-1234. doi:10.1126/science.abd7934.
- Hibbard, J.P., and Karig, D.E., 1990. Alternative plate model for the early Miocene evolution of the southwest Japan margin. *Geology*, **18**, 170-174. doi:10.1130/0091-7613(1990)018%3C0170:APMFTE%3E2.3.CO;2.
- Hinrichs, K.-U., Hayes, J.M., Sylva, S.P., Brewer, P.G., and DeLong, E.F., 1999. Methane-consuming archaeobacteria in marine sediments. *Nature*, **398**, 802-805. doi:10.1038/19751.
- Hinrichs, K.-U., Inagaki, F., Heuer, V.B., Kinoshita, M., Morono, M., and Kubo, Y., 2016. *Expedition 370 Scientific Prospectus: T-Limit of the Deep Biosphere off Muroto (T-Limit)*. International Ocean Discovery Program. doi:10.14379/iodp.sp.370.2016.
- Homoky, W.B., Conway, T.M., John, S.G., König, D., Deng, F., Tagliabue, A., and Mills, R.A., 2021. Iron colloids dominate sedimentary supply to the ocean interior. *Proceedings of the National Academy of Sciences of the United States of America*, **118**, e2016078118. doi:10.1073/pnas.2016078118.

- Horsfield, B., Schenk, H.J., Zink, K., Ondrak, R., Dieckmann, V., Kallmeyer, J., et al., 2006. Living microbial ecosystems within the active zone of catagenesis: Implications for feeding the deep biosphere. *Earth and Planetary Science Letters*, **246**, 55-69. doi:10.1016/j.epsl.2006.03.040.
- Hoshino, T., Doi, H., Uramoto, G.-I., Wörmer, L., Adhikari, R.R., Xiao, N., et al., 2020. Global diversity of microbial communities in marine sediment. *Proceedings of the National Academy of Sciences of the United States of America*, **117**, 27587-27597. doi:10.1073/pnas.1919139117.
- Icopini, G.A., Anbar, A.D., Ruebush, S.S., Tien, M., and Brantley, S.L., 2004. Iron isotope fractionation during microbial reduction of iron: The importance of adsorption. *Geology*, **32**, 205-208. doi:10.1130/G20184.1.
- Inagaki, F., Nunoura, T., Nakagawa, S., Teske, A., Lever, M., Lauer, A., et al., 2006. Biogeographical distribution and diversity of microbes in methane hydrate-bearing deep marine sediments on the Pacific Ocean Margin. *Proceedings of the National Academy of Sciences of the United States of America*, **103**, 2815-2820. https://doi.org/10.1073/pnas.0511033103.
- Inagaki, F., Hinrichs, K.-U., Kubo, Y., Bowles, M.W., Heuer, V.B., Hong, W.L., et al., 2015. Exploring deep microbial life in coal-bearing sediment down to ~2.5 km below the ocean floor. *Science*, **349**, 420-424. doi:10.1126/science.aaa6882.
- Jahnke, R.A., 1996. The global ocean flux of particulate organic carbon: Areal distribution and magnitude. *Global Biogeochemical Cycles*, **10**, 71-88. doi:10.1029/95GB03525.
- Johnson, C.M., and Beard, B.L., 2005. Biogeochemical cycling of iron isotopes. *Science*, **309**, 1025-1027. doi:10.1126/science.1112552.
- Jørgensen, B.B., 1982. Mineralization of organic matter in the sea bed - the role of sulphate reduction. *Nature*, **296**, 643-645. doi:10.1038/296643a0.
- Jørgensen, B.B., 2006. Bacteria and marine biogeochemistry. In: *Marine Geochemistry* (eds. Schulz, H.D., and Zabel, M.). Springer, Berlin Heidelberg, 169-206. doi:10.1007/3-540-32144-6_5.
- Jørgensen, B.B., and Boetius, A., 2007. Feast and famine – microbial life in the deep-sea bed. *Nature Reviews Microbiology*, **5**, 770-781. doi:10.1038/nrmicro1745.
- Kallmeyer, J., Pockalny, R., Adhikari, R.R., Smith, D.C., and D'Hondt, S., 2012. Global distribution of microbial abundance and biomass in subseafloor sediment. *Proceedings of the National Academy of Sciences of the United States of America*, **109**, 16213-16216. doi:10.1073/pnas.1203849109.
- Karlin, R., and Levi, S., 1983. Diagenesis of magnetic minerals in recent hemipelagic sediments. *Nature*, **303**, 327-330. doi:10.1038/303327a0.
- Kashefi, K., and Lovley, D.R., 2003. Extending the upper temperature limit for life. *Science*, **301**, 934-934. doi:10.1126/science.1086823.
- Kasten, S., Freudenthal, T., Gingele, F.X., and Schulz, H.D., 1998. Simultaneous formation of iron-rich layers at different redox boundaries in sediments of the Amazon deep-sea fan. *Geochimica et Cosmochimica Acta*, **62**, 2253-2264. doi:10.1016/S0016-7037(98)00093-3.
- Kasten, S., Zabel, M., Heuer, V., and Hensen, C., 2003. Processes and signals of nonsteady-state diagenesis in deep-sea sediment and their pore waters. In: *The South Atlantic in the*

- Late Quaternary* (eds. Wefer, G., Mulitza, S., and Ratmeyer, V.). Springer, Berlin Heidelberg, 431-459. doi:10.1007/978-3-642-18917-3_20.
- Kimura, G., Hashimoto, Y., Kitamura, Y., Yamaguchi, A., and Koge, H., 2014. Middle Miocene swift migration of the TTT triple junction and rapid crustal growth in southwest Japan: A review. *Tectonics*, **33**, 1219-1238. doi:10.1002/2014TC003531.
- Kinoshita, M., Tobin, H., Ashi, J., Kimura, G., Lallemand, S., Screaton, E.J., Curewitz, D., Masago, H., Moe, K.T., and the Expedition 314/315/316 Scientists. NanTroSeize Stage 1: investigations of seismogenesis, Nankai Trough, Japan. *Proceedings of the International Ocean Discovery Program, 314/315/316*. Washington, DC, (Integrated Ocean Drilling Program Management International, Inc.), 1-50.
- Knittel, K., and Boetius, A., 2007. Anaerobic oxidation of methane: progress with an unknown process. *Annual Review of Microbiology*, **63**, 311-334. doi:10.1146/annurev.micro.61.080706.093130.
- LaRowe, D.E., Burwicz, E., Arndt, S., Dale, A.W., and Amend, J.P., 2017. Temperature and volume of global marine sediment. *Geology*, **45**, 275-278. doi:10.1130/G38601.1
- Le Pichon, X., Iiyama, T., Boulègue, J., Charvet, J., Faure, M., Kano, K., Lallemand, S., Okada, H., Rangin, C., Taira, A., Urabe, T., and Uyeda, S., 1978. Nankai Trough and Zenisu Ridge: a deep-sea submersible survey. *Earth and Planetary Science Letters*, **83**, 285-299. doi:10.1016/0012-821X(87)90072-0.
- Lever, M.A., Rogers, K.L., Lloyd, K.G., Overmann, J., Schink, B., Thauer, R.K., Hoehler, T.M., and Jørgensen, B.B., 2015. Life under extreme energy limitations: a synthesis of laboratory- and field-based investigations. *FEMS Microbiological Reviews*, **39**, 688-728. doi:10.1093/femsre/fuv020.
- Loefering, M.J., Anka, Z., Autin, J., di Primio, R., Marchal, D., Rodriguez, J.F., Franke, D., and Vallejo, E., 2013. Tectonic evolution of the Colorado Basin offshore Argentina, inferred from seismo-stratigraphy and depositional rates analysis. *Tectonophysics*, **604**, 245-263. doi:10.1016/j.tecto.2013.02.008.
- Luther III, G.W., 1991. Pyrite synthesis via polysulfide compounds. *Geochimica et Cosmochimica Acta*, **55**, 2839-2849. doi:10.1016/0016-7037(91)90449-F.
- Mahony, S.H., Wallace, L.M., Miyoshi, M., Villamor, P., Sparks, R.S.J., and Hasenaka, T., 2011. Volcano-tectonic interactions during rapid plate-boundary evolution in the Kyushu region, SW Japan. *GSA Bulletin*, **123**, 2201-2223. doi:10.1130/B30408.1.
- Meister, P., 2015. For the deep biosphere, the present is not always the key to the past: What we can learn from the geological record. *Terra Nova*, **27**, 400-408. doi:10.1111/ter.12174.
- Meister, P., Brunner, B., Picard, A., Böttcher, M.E., and Jørgensen, B.B., 2019. Sulphur and carbon isotopes as tracers of past sub-seafloor microbial activity. *Scientific Reports*, **9**, 1-9. doi:10.1038/s41598-018-36943-7.
- Melton, E.D., Swanner, E.D., Behrens, S., Schmidt, C., and Kappler, A., 2014. The interplay of microbially mediated and abiotic reactions in the biogeochemical Fe cycle. *Nature Reviews Microbiology*, **12**, 797-808. doi:10.1038/nrmicro3347.
- Miyazaki, S., and Heki, K., 2001. Crustal velocity field of southwest Japan: Subduction and arc-arc collision. *Journal of Geophysical Research: Solid Earth*, **106**, 4305-4326. doi:10.1029/2000JB900312.
- Moore, G.F., Taira, A., Klaus, A., Becker, L., Boeckel, B., Cragg, B.A., et al., 2001a. New insights into deformation and fluid flow processes in the Nankai Trough accretionary

- prism: Results of Ocean Drilling Program Leg 190. *Geochimica et Cosmochimica Acta*, **2**, 1525-2027. doi:10.1029/2001GC000166.
- Moore, G.F., Taira, A., Klaus, A., et al., 2001b. *Proceedings of the Ocean Drilling Program, Initial Reports, 190*. College Station, TX (Ocean Drilling Program). doi:10.2973/odp.proc.ir.190.2001.
- Morono, Y., Ito, M., Hoshino, T., Terada, T., Hori, T., Ikehara, M., D'Hondt, S., and Inagaki, F., 2020. Aerobic microbial life persists in oxic marine sediment as old as 101.5 million years. *Nature Communications*, **11**, 3626. doi:10.1038/s41467-020-17330-1.
- Mrozowski, C.L., and Hayes, D.E., 1979. The evolution of the Parece Vela Basin, eastern Philippine Sea. *Earth and Planetary Science Letters*, **46**, 49-67. doi:10.1016/0012-821X(79)90065-7.
- Okino, K., Shimakawa, Y., and Nagaoka, S., 1994. Evolution of the Shikoku Basin. *Journal of Geomagnetism and Geoelectricity*, **46**, 463-479. doi:10.5636/jgg.46.463.
- Okino, K., Ohara, Y., Kasuga, S., and Kato, Y., 1999. The Philippine Sea: new survey results reveal the structure and the history of the marginal basins. *Geophysical Research Letters*, **26**, 2287-2290. doi:10.1029/1999GL900537.
- Parkes, R.J., Cragg, C., Roussel, E., Webster, G., Weightman, A., and Sass, H., 2014. A review of prokaryotic population and processes in sub-seafloor sediments, including biosphere-geosphere interactions. *Marine Geology*, **352**, 409-425. doi:10.1016/j.margeo.2014.02.009.
- Pickering, K.T., Underwood, M.B., and Taira, A., 1993. Stratigraphic synthesis of the DSDP-ODP sites in the Shikoku Basin, Nankai Trough and accretionary prism. In: *Proceedings of the Deep Sea Drilling Program, Scientific Results, 131* (eds. Hill, I.A., Taira, A., Firth, J.V., et al.). College Station, TX (Ocean Drilling Program), 313-330. doi:10.2973/odp.proc.sr.131.135.1993.
- Poulton, S.W., Krom, M.D., and Raiswell, R., 2004. A revised scheme for the reactivity of iron (oxyhydr)oxide minerals towards dissolved sulfide. *Geochimica et Cosmochimica Acta*, **68**, 3703-3715. . doi:10.1016/j.gca.2004.03.012.
- Pruyters, P.A., de Lange, G.J., Middelburg, J.J., and Hydes, D.J., 1993. The diagenetic formation of metal-rich layers in sapropel-containing sediments in the eastern Mediterranean. *Geochimica et Cosmochimica Acta*, **57**, 527-536. doi:10.1016/0016-7037(93)90365-4.
- Pyzik, A.J., and Sommer, S.E., 1981. Sedimentary iron monosulfides: kinetics and mechanism of formation. *Geochimica et Cosmochimica Acta*, **45**, 687-698. doi:10.1016/0016-7037(81)90042-9.
- Raghoebarsing, A.A., Pol, A., van de Pas-Schoonen, K.T., Smolder, A.J.P., Ettwig, K.F., Rijpstra, W.I.C., et al., 2006. A microbial consortium coupled anaerobic methane oxidation to denitrification. *Nature*, **440**, 918-921. doi:10.1038/nature04617.
- Rea, D.K., Lyle, M.W., Liberty, L.M., Hovan, S.A., Bolyn, M.P., Gleason, J.D., et al., 2006. Broad region of no sediment in the southwest Pacific Basin. *Geology*, **34**, 873-876. doi:10.1130/G22864.1.
- Reeburgh, W.S., 1976. Methane consumption in Cariaco Trench waters and sediments. *Earth and Planetary Science Letters*, **28**, 337-344. doi:10.1016/0012-821X(76)90195-3.

- Rickard, D., and Luther III, G.W., 1997. Kinetics of pyrite formation by the H₂S oxidation of iron (II) monosulfide in aqueous solution between 25 and 125°C: The mechanism. *Geochimica et Cosmochimica Acta*, **61**, 135-147. doi:10.1016/S0016-7037(96)00321-3.
- Riedinger, N., 2005. Preservation and diagenetic overprint of geochemical and geophysical signals in ocean margin sediments related to depositional dynamics. *Berichte, Fachbereich Geowissenschaften, Universität Bremen*, **242**, 1-91.
- Riedinger, N., Pfeifer, K., Kasten, S., Garming, J.F.L., Vogt, C., and Hensen, C., 2005. Diagenetic alteration of magnetic signals by anaerobic oxidation of methane related to a change in sedimentation rate. *Geochimica et Cosmochimica Acta*, **69**, 4117-4126. doi:10.1016/j.gca.2005.02.004.
- Riedinger, N., Kasten, S., Gröger, J., Franke, C., and Pfeifer, K., 2006. Active and buried authigenic barite fronts in sediments from the Eastern Cape basin. *Earth and Planetary Science Letters*, **241**, 846-887. doi:10.1016/j.epsl.2005.10.032.
- Riedinger, N., Formolo, M.J., Lyons, T.W., Henkel, S., Beck, A., and Kasten, S., 2014. An inorganic geochemical argument for coupled anaerobic oxidation of methane and iron reduction in marine sediments. *Geobiology*, **12**, 172-181. doi:10.1111/gbi.12077.
- Roberts, A.P., 2015. Magnetic mineral diagenesis. *Earth-Science Reviews*, **151**, 1-47. doi:10.1016/j.earscirev.2015.09.010.
- Roussel, E.G., Cambon Bonavita, M.-A., Querellou, J., Cragg, B.A., Webster, G., Prieur, D., and Parkes, R.J., 2008. Extending the sub-seafloor biosphere. *Science*, **320**, 1046. doi:10.1126/science.1154545.
- Sato, H., Machida, S., Kanayama, S., Taniguchi, H., and Ishii, T., 2002. Geochemical and isotopic characteristics of the Kinan Seamount Chain in the Shikoku Basin. *Geochemical Journal*, **36**, 519-526. doi:10.2343/geochemj.36.519.
- Seno, T., Stein, S., and Gripp, A.E., 1993. A model for the motion of Philippine Sea Plate consistent with NUVEL-1 and geological data. *Journal of Geophysical Research: Solid Earth*, **98**, 17941-17948. doi:10.1029/93JB00782.
- Severmann, S., Johnson, C.M., Beard, B.L., and McManus, J., 2006. The effect of early diagenesis on the Fe isotope compositions of porewaters and authigenic minerals in continental margin sediment. *Geochimica et Cosmochimica Acta*, **70**, 2006-2022. doi:10.1016/j.gca.2006.01.007.
- Shipboard Scientific Party, 2003. Site 1237. In: *Proceedings of the Ocean Drilling Program, Initial Reports, 202* (eds. Mix, A.C., Tiedemann, R., Blum, P., et al.). College Station, TX, (Ocean Drilling Program), 1-145. doi:10.2973/odp.proc.ir.202.108.2003.
- Sivan, O., Adler, M., Pearson, A., Gelman, F., Bar-Or, I., John, S.G., and Eckert, W., 2011. Geochemical evidence for iron-mediated anaerobic oxidation of methane. *Limnology and Oceanography*, **56**, 1536-1544. doi:10.4319/lo.2011.56.4.1536.
- Skulan, J.L., Beard, B.L., and Johnson, C.M., 2002. Kinetic and equilibrium Fe isotope fractionation between aqueous Fe(III) and hematite. *Geochimica et Cosmochimica Acta*, **66**, 2995-3015. doi:10.1016/S0016-7037(02)00902-X.
- Taira, A., Hill, I., and Firth, J.V., et al., 1991. *Proceedings of the Ocean Drilling Program, Initial Reports, 131*. College Station, TX (Ocean Drilling Program). doi:10.2973/odp.proc.ir.131.1991.
- Taira, A., Hill, I., Firth, J., Berner, U., Brückmann, W., Byrne, T., et al., 1992. Sediment deformation and hydrogeology of the Nankai Trough accretionary prism: Synthesis of

- shipboard results of ODP Leg 131. *Earth and Planetary Science Letters*, **109**, 431-450. doi:10.1016/0012-821X(92)90104-4.
- Takai, K., Nakamura, K., Toki, T., Tsunogai, U., Miyazaki, M., Miyazaki, J., et al., 2008. Cell proliferation at 122°C and isotopically heavy CH₄ production by hyperthermophilic methanogen under high-pressure cultivation. *Proceedings of the National Academy of Sciences of the United States of America*, **105**, 10949-10954. doi:10.1073/pnas.0712334105.
- Taylor, P.D.P., Maeck, R., and De Bièvre, P., 1992. Determination of the absolute isotopic composition and atomic weight of a reference sample of natural iron. *International Journal of Mass Spectrometry and Ion Processes*, **121**, 111-125. doi:10.1016/0168-1176(92)80075-C.
- Thompson, R., Stober, J.C., Turner, G.M., Oldfield, F., Bloemendal, J., Dearing, J.A., and Rummery, T.A., 1980. Environmental applications of magnetic measurements. *Science*, **207**, 481-486. doi:10.1126/science.207.4430.481.
- Torres, M.E., Cox, T., Hong, W.-L., McManus, J., Sample, J.C., Destrienneville, C., Gan, H.M., Gan, H.Y., and Moreau, J.W., 2015. Crustal fluid and ash alteration impacts on the biosphere of Shikoku Basin sediments, Nankai Trough, Japan. *Geobiology*, **13**, 562-580. doi:10.1111/gbi.12146.
- Vargas, M., Kashefi, K., Blunt-Harris, E. L., and Lovley, D. R., 1998. Microbiological evidence for Fe (III) reduction on early Earth. *Nature*, **395**, 65-67. doi:10.1038/25720
- Watts, A.B., and Weissel, J.K., 1975. Tectonic history of the Shikoku marginal basin. *Earth and Planetary Science Letters*, **25**, 239-250. doi:10.1016/0012-821X(75)90238-1.
- Wehrmann, L.M., Arndt, S., März, C., Ferdelman, T.G., and Brunner, B., 2013. The evolution of early diagenetic signals in Bering Sea subseafloor sediments in response to varying organic carbon deposition over the last 4.3 Ma. *Geochimica et Cosmochimica Acta*, **109**, 175-196. doi:10.1016/j.gca.2013.01.025.
- Wehrmann, L.M., and Ferdelman, T.G., 2014. Biogeochemical consequences of the sedimentary subseafloor biosphere. In: *Developments in Marine Geology* (eds. Stein, R., Blackman, D.K., Inagaki, F., and Larsen, H.-C.). Elsevier, 217-252. doi:10.1016/B978-0-444-62617-2.00009-8.
- Wehrmann, L.M., and Riedinger, N., 2016. The sedimentary deep subseafloor biosphere. In: *Encyclopedia of Ocean Sciences*, 3rd Edition (eds. Cochran, J.K., Bokuniewicz H.J., and Yager, P.L.). Academic Press, 258-274. doi:10.1016/B978-0-12-409548-9.09741-4.
- Wersin, P., Höhener, P., Giovanoli, R., and Stumm, W., 1991. Early diagenetic influences on iron transformations in a freshwater lake sediment. *Chemical Geology*, **90**, 233-252. doi:10.1016/0009-2541(91)90102-W.
- Whitman, W.B., Coleman, D.C., and Wiebe, W.J., 1998. Prokaryotes: the unseen majority. *Proceedings of the National Academy of Sciences of the United States of America*, **95**, 6578-6583. doi:10.1073/pnas.95.12.6578.
- Wiederhold, J.G., 2015. Metal stable isotope signatures as tracers in environmental geochemistry. *Environmental Science & Technology*, **49**, 2606-2624. doi:10.1021/es504683e.
- Wiesli, R.A., Beard, B.L., and Johnson, C.M., 2004. Experimental determination of Fe isotope fractionation between aqueous Fe(II), siderite and “green rust” in abiotic systems. *Chemical Geology*, **211**, 343-362. doi:10.1016/j.chemgeo.2004.07.002.

- Wilhelms, A., Larter, S.R., Head, I., Farrimond, P., di-Primio, R., and Zwach, C., 2001. Biodegradation of oil in uplifted basins prevented by deep-burial sterilization. *Nature*, **411**, 1034-1037. doi:10.1038/35082535.
- Wu., J., Suppe, J., Lu, R., and Kanda, R., 2016. Philippine Sea and East Asian plate tectonics since 52 Ma constrained by new subducted slab reconstruction methods. *Journal of Geophysical Research: Solid Earth*, **121**, 4670-4741. doi:10.1002/2016JB012923.
- Yamano, M., Kinoshita, M, Goto, S., and Matsubayashi, O., 2003. Extremely high heat flow anomaly in the middle part of the Nankai Trough. *Physics and Chemistry of the Earth, Parts A/B/C*, **28**, 487-497. doi:10.1016/S1474-7065(03)00068-8.

CHAPTER II:
**Evolution of (bio-)geochemical processes and diagenetic alteration of
sediments along the tectonic migration of ocean floor in the Shikoku Basin
off Japan**

Male Köster¹, Myriam Kars², Florence Schubotz³, Man-Yin Tsang^{4,5}, Markus Maisch⁶,
Andreas Kappler^{6,7}, Yuki Morono⁸, Fumio Inagkai^{8,9}, Verena B. Heuer³, Sabine Kasten^{1,3,10},
and Susann Henkel^{1,3}

¹Alfred Wegener Institute Helmholtz Centre for Polar and Marine Research, Bremerhaven, Germany

²Center for Advanced Marine Core Research, Kochi University, Nankoku, Japan

³MARUM – Center for Marine Environmental Sciences, University of Bremen, Bremen, Germany

⁴Department of Applied Earth Sciences, University of Toronto, Toronto, ON, Canada

⁵Now at Department of Planetology, Kobe University, Kobe, Japan

⁶Center for Applied Geosciences, University of Tübingen, Tübingen, Germany

⁷Center for Geomicrobiology, Aarhus University, Aarhus, Denmark

⁸Kochi Institute for Core Sample Research, Japan Agency for Marine-Earth Sciences and Technology (JAMSTEC), Nankoku, Japan

⁹Mantle Drilling Promotion Office (MDP), Institute for Marine-Earth Exploration and Engineering (MarE3), Japan Agency for Marine-Earth Science and Technology (JAMSTEC), Yokohama, Japan

¹⁰University of Bremen, Faculty of Geosciences, Bremen, Germany

Manuscript published in *Geochemistry, Geophysics, Geosystems*, 22, e2020GC009585.

doi:10.1029/2020GC009585

The format has been adapted to the thesis format.

Key Points:

- The tectonic migration of ocean floor led to a transition from an organic carbon-starved to an elevated organic carbon burial environment
- Diagenetic transformation of iron oxides into pyrite within the carbon-lean sediments occurred several millions of years after deposition
- Reducible iron(III), which is mostly present in phyllosilicates, can potentially fuel microbially mediated mineral alteration

Abstract

Biogeochemical processes in subseafloor sediments are closely coupled to global element cycles. To improve the understanding of changes in biogeochemical conditions on geological timescales, we investigate sediment cores from a 1,180 m deep hole in the Nankai Trough offshore Japan (Site C0023) drilled during International Ocean Discovery Program Expedition 370. During its tectonic migration from the Shikoku Basin to the Nankai Trough over the past 15 Ma, Site C0023 has experienced significant changes in depositional, thermal, and geochemical conditions. By combining pore-water, solid-phase, and rock magnetic data, we demonstrate that a transition from organic carbon-starved conditions with predominantly aerobic respiration to an elevated carbon burial environment with increased sedimentation occurred at ~2.5 Ma. Higher rates of organic carbon burial in consequence of increased nutrient supply and productivity likely stimulated the onset of anaerobic electron-accepting processes during organic carbon degradation. A significant temperature increase by ~50°C across the sediment column associated with trench-style sedimentation since ~0.5 Ma could increase the bioavailability of organic matter and enhance biogenic methanogenesis. The resulting shifts in reaction fronts led to diagenetic transformation of iron (oxyhydr)oxides into pyrite in the organic carbon-starved sediments several millions of years after burial. We also show that high amounts of reducible iron(III) which can serve as electron acceptor for microbial iron(III) reduction are preserved and still available as phyllosilicate-bound iron. This is the first study that shows the evolution of long-term variations of (bio-)geochemical processes along tectonic migration of ocean floor, thereby altering the primary sediment composition long after deposition.

Plain Language Summary

During the tectonic migration of ocean floor, deep sediments move over vast distances, thereby passing through different depositional and geochemical environments. We studied subseafloor sediments recovered at Site C0023 in the Nankai Trough offshore Japan during International Ocean Discovery Program Expedition 370, which aimed at exploring the prerequisites and limits of microbial life in marine sediments. Over the past 15 Ma, the sediments at Site C0023 migrated ~750 km from its initial position to the Nankai Trough due to tectonic motion of the Philippine Sea plate. As a result, sedimentation rates and sediment temperature increased significantly. We use different geochemical and rock magnetic analyses to (1) reconstruct the evolution of (bio-)geochemical processes, especially iron cycling, along the migration and to (2) investigate if iron(III) minerals are available to serve as energy substrates for microbial

respiration in the deep sediments. Our results indicate that high amounts of phyllosilicate-bound iron(III), which can be used by microbes to gain energy, are still available throughout the core. The changing depositional history, and consequently the organic carbon availability and temperature, ultimately determine the geochemical patterns we observe today. Such studies are needed to gain a better understanding of changes in (bio-)geochemical cycling on geological timescales.

1. Introduction

The degradation of organic matter is the key driver for microbial activity and global biogeochemical cycles in subseafloor sediments (e.g., Froelich et al., 1979; Berner, 1981; D'Hondt et al., 2002). During burial, marine sediments pass through a sequence of geochemically and microbially determined redox zones (e.g., Froelich et al., 1979; Berner, 1981). In anoxic marine sediments, organic matter is predominantly remineralized by microbial dissimilatory iron (Fe) and sulfate reduction (e.g., Froelich et al., 1979; Canfield et al., 1993; Jørgensen and Kasten, 2006; Bowles et al., 2014), thus, linking the biogeochemical cycles of Fe, sulfur (S), and carbon (C). Hydrogen sulfide released during organoclastic sulfate reduction (e.g., Goldhaber and Kaplan, 1974; Jørgensen, 1982) or anaerobic oxidation of methane (AOM) (e.g., Barnes and Goldberg, 1976; Borowski et al., 1996; Niewöhner et al., 1998; Boetius et al., 2000) reacts with either solid-phase Fe(III) (oxyhydr)oxides or dissolved Fe²⁺ liberated by dissimilatory Fe(III) reduction to form Fe monosulfides (FeS) and/or pyrite (FeS₂) (e.g., Berner, 1970; Jørgensen and Kasten, 2006; Jørgensen et al., 2019). The formation of Fe sulfides represents a long-term sink for Fe and S in deeply buried sediments (e.g., Berner, 1984; Hensen et al., 2003). Fe(III) reduction is considered one of the most ancient forms of microbial respiration (Vargas et al., 1998) and Fe(III)-reducing microorganisms can grow under high temperature and pressure conditions (Kashefi and Lovley, 2003). These findings suggest that microbes which use Fe(III) as electron acceptors are potential candidates to survive burial into deep and hot subseafloor sediments, as long as reducible Fe(III)-containing minerals are available.

Sequential extraction procedures are widely applied to marine sediments to quantify reactive Fe (e.g., Riedinger et al., 2005, 2014; März et al., 2008; Henkel et al., 2018). The extraction protocol after Poulton and Canfield (2005) is one of the most commonly utilized procedures for the selective dissolution of Fe in operationally defined fractions by using specific extracting reagents and reaction times. Despite the operational nature of the sequential extractions, this method has been developed through tests on pure and synthetic Fe-bearing minerals. Recent

studies showed that substantial amounts of Fe from distinct phases can already be dissolved prior to the target extraction step and/or the dissolution can be incomplete (e.g., Henkel et al., 2016; Hepburn et al., 2020; Slotznick et al., 2020). Thus, if the research question requires a specific Fe mineral characterization, the extraction data should be validated by a secondary method (Hepburn et al., 2020; Slotznick et al., 2020). One option to assess the Fe mineralogy is ^{57}Fe -specific Mössbauer spectroscopy, which is, however, relatively time-consuming. Another approach that offers independent information on Fe mineralogy is the application of comparably rapid and non-destructive magnetic techniques such as end-member modeling of isothermal remanent magnetization (IRM) acquisition curves. The basic principle of this method is to “unmix” the coercivity distributions of different magnetic minerals into specific end-members by decomposing the IRM acquisition curves (Kruiver et al., 2001; Heslop et al., 2002).

Early diagenetic processes are often described as steady state diagenesis, where fluxes of oxidants and reductants are balanced, and thus, redox fronts are located at specific depths relative to the sediment surface over long periods (Froelich et al., 1979; Berner, 1981). However, marine sediments are usually subject to non-steady state diagenesis, triggered by changes in fluxes of electron donors and acceptors and/or depositional conditions including sedimentation and carbon burial rates (e.g., Pruyssers et al., 1993; Kasten et al., 2003). Non-steady state conditions typically cause vertical shifts of redox boundaries and geochemical reaction fronts and the dissolution of primary and formation of secondary mineral phases. Typical examples of such diagenetic mineral precipitation are the formation of Fe sulfides (e.g., Passier et al., 1996; Kasten et al., 1998; Riedinger et al., 2005; März et al., 2008) and barite (e.g., Arndt et al., 2006; Riedinger et al., 2006; Henkel et al., 2012). Consequently, there is often a considerable age offset between the time when an authigenic mineral precipitates or other secondary signals form and the age of the surrounding host sediment. Since sedimentary proxies including biogenic barite and magnetic susceptibility have been intensively used for paleoclimatic and oceanographic reconstructions or as a correlation tool (e.g., Thompson et al., 1980; Dymond et al., 1992), the diagenetic alteration of the initially deposited material needs to be considered to avoid misinterpretation of the sedimentary record. Non-steady state diagenesis does not only occur on timescales from centuries to several thousands of years (e.g., Kasten et al., 1998; Riedinger et al., 2005), but can also affect biogeochemical and diagenetic processes on geological timescales (> millions of years) by changes in geochemical and depositional conditions (e.g., Meister, 2015). Deeply buried Cretaceous shales in sediments from the Demerara Rise in the equatorial Atlantic, for example, stimulate biogeochemical

processes in the overlying sediment column even 100 Ma after their deposition (Arndt et al., 2006). Present-day pore-water and solid-phase signatures in sediments at the Bowers Ridge in the Bering Sea (IODP Expedition 323 Site U1341) reflect the impact of changes in the deposition and reactivity of organic matter that occurred ~2.5 Ma ago (Wehrmann et al., 2013). In addition to variations in organic matter quantity and reactivity related to oceanographic and climatic changes, changes in biogeochemical processes can also be induced by tectonic dynamics including fluid flow along faults, hydrothermal circulation and frictional heating (e.g., Fischer et al., 2013; Wehrmann and Riedinger, 2016). For example, recalcitrant organic matter in subseafloor sediments from the Nankai accretionary prism might be reactivated caused by frictional heating associated with earthquakes or advective fluid flow (Riedinger et al., 2015; Ijiri et al., 2018). Marine sediments represent one of the most valuable archives to reconstruct changes in paleoceanographic, depositional and climatic conditions over Earth's history. In order to interpret this record reliably, it is crucial to consider and assess the impact of ocean floor migration on post-depositional overprint of the primary sediment composition. International Ocean Discovery Program (IODP) Expedition 370 (Temperature Limit of the Deep Biosphere off Muroto) established Site C0023 down to 1,180 m below seafloor (mbsf) in the Nankai Trough off Cape Muroto, Japan, to explore the upper temperature limit of microbial life in marine sediments (Heuer et al., 2017a). Site C0023 has experienced a significant increase in sedimentation rates associated with the migration over vast distances from its initial position in the central Shikoku Basin to the Nankai Trough caused by the Philippine Sea plate motion (Mahony et al., 2011; Hagino and the Expedition 370 Scientists, 2018). With ongoing burial, the temperature rapidly rose across the sediment column, leading to a present-day temperature gradient of $110^{\circ}\text{C km}^{-1}$ (Heuer et al., 2020). While the impact of the Philippine Sea plate migration on variations in the sediment composition has been extensively investigated (e.g., Underwood and Steurer, 2003; Saitoh et al., 2015), the effect of a tectonically induced migration of ocean floor through different depositional regimes on the biogeochemical dynamics within the sediments in the Nankai-Shikoku-subduction system has not yet been studied. In order to study long-term variations in biogeochemical and diagenetic processes as well as element fluxes at Site C0023, we combine a unique multi-disciplinary data set that includes shipboard high-resolution pore-water and gas data, organic carbon contents (Heuer et al., 2017a), and sedimentation rates and ages (Hagino and the Expedition 370 Scientists, 2018) with our solid-phase data comprising bulk sediment compositions, Fe speciation, and rock magnetic signals. One objective is to evaluate if reactive Fe is still available to serve as a potential energy substrate for microbially mediated processes in the deep and hot subseafloor sediments at Site C0023. In

order to reliably quantify and characterize the different reactive Fe pools at Site C0023, we combine chemical sequential Fe extractions with IRM acquisition curve end-member unmixing and ^{57}Fe Mössbauer spectroscopy analysis. We further reconstruct past variations in (bio-)geochemical and diagenetic processes driven by changing environmental conditions and assess how these changes affected the sedimentary Fe pool from its initial deposition to progressing burial and diagenetic alteration to the present-day situation. The succession of biogeochemical and diagenetic processes is merged into a conceptual geochemical process model.

2. Study site

2.1 Geological background

Site C0023 ($32^{\circ}22.00'\text{N}$, $134^{\circ}57.98'\text{E}$; 4,776 m water depth) is located in the Nankai Trough, 125 km southeast of Cape Muroto, Japan. The Nankai Trough represents an ideal area to explore the upper temperature limit of seafloor life since it is characterized by high heat flows (Yamano et al., 1992; Heuer et al., 2020). Our study is integrated into a number of microbiological, geochemical, and sedimentological studies. This interdisciplinary approach offers an outstanding opportunity to investigate the prerequisites of deep microbial life. Site C0023 lies on the so-called Muroto Transect (Shipboard Science Party, 2001), which is perpendicular to the Nankai Trough (Heuer et al., 2017a). The Nankai Trough forms the subduction boundary between the southwest Japan arc (Eurasian plate) and the Shikoku Basin (Figure 1).

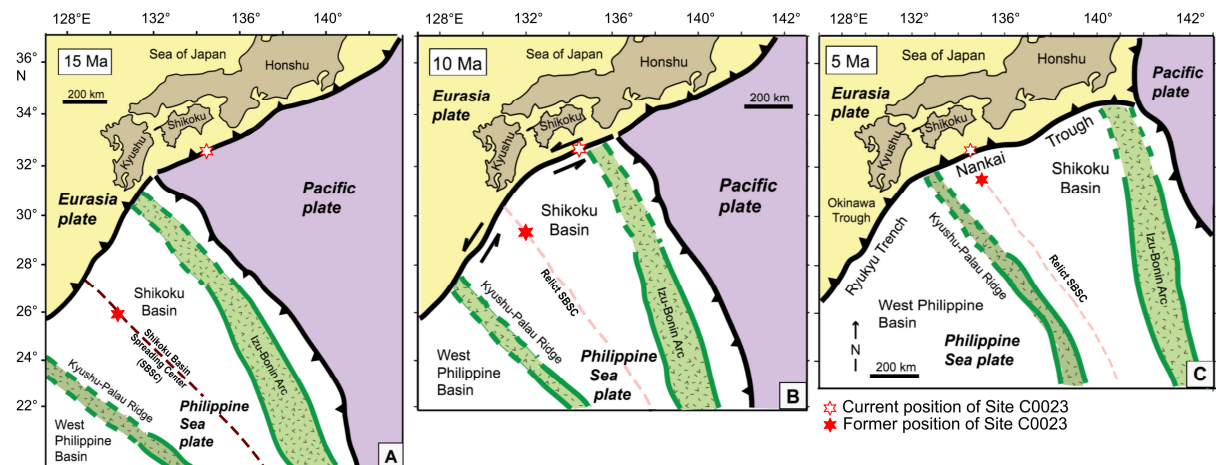


Figure 1. Simplified schematic plate tectonic reconstruction for the Shikoku Basin and the relative movement of Site C0023 over the past 15 Ma. Japan is held fixed at its current position. Opened and filled red stars represent the current position of Site C0023 and its position over the course of 15 Ma, respectively. Modified after Underwood and Guo (2018) (<https://creativecommons.org/licenses/by-nc/4.0/>).

The Shikoku Basin is part of the Philippine Sea plate that is subducting beneath the Eurasian plate at a current rate of 4–6 cm yr⁻¹ in a northwest direction (Seno et al., 1993; DeMets et al., 2010). The trench in general is relatively shallow with water depths < 5,000 m below sea level (Shipboard Science Party, 1991). The subducting oceanic lithosphere of the Shikoku Basin initially formed by rifting of the paleo-Izu-Bonin backarc and seafloor spreading in the eastern part of the Philippine Sea plate between 26 and 15 Ma. The Kyushu-Palau Ridge and the Shichito-Iwojima Ridge are relics of the former arc, which were separated by the spreading, limiting the Shikoku Basin to the east and west, respectively (Watts and Weissel, 1975; Okino et al., 1994, 1999). The Kinan Seamounts Chain runs along the axis of the basin and represents the relic of the extinct spreading center in the Shikoku Basin (e.g., Pickering et al., 2013). Site C0023 has moved relative to its present-day geographic position due to motion of the Philippine Sea plate (e.g., Mahony et al., 2011). Figure 1 shows a schematic plate tectonic reconstruction for the Shikoku Basin and the relative movement of Site C0023 over the past 15 Ma. The oceanic basement of Site C0023 was formed ~16 Ma ago (Shipboard Science Party, 1991, 2001) during a phase when seafloor spreading in the Shikoku Basin ceased to be active (Chamot-Rooke et al., 1987; Okino et al., 1994). Mahony et al. (2011) reconstructed the tectonic evolution of the Philippine Sea plate relative to the Eurasian plate for the past 15 Ma. From 15 to 6 Ma, the triple junction between the Pacific plate, Philippine Sea plate and southwest Japan moved northward, resulting in the subduction of the Philippine Sea plate beneath Kyushu and Shikoku islands. Extensive volcanic activity began at 8 and 6 Ma on Kyushu and in SW Japan, respectively, and is related to the formation of a volcanic front and a deeply penetrating subducting slab (Kamata and Kodama, 1994). The Izu-Bonin arc started colliding with the Honshu arc during the late Miocene, generating the Izu-collision zone. The subduction of the Philippine Sea plate and off-scraping of the trench wedge sediment from the descending Philippine Sea plate led to the formation of the Nankai accretionary prism (Le Pichon et al., 1987; Taira et al., 1992; Costa Pisani et al., 2005). Site C0023 is located at the seaward-end of this accretionary prism (Heuer et al., 2017a).

2.2 Sedimentary setting

The incoming sedimentary sequence of the Nankai subduction zone at Site C0023 is ~1.2 km thick and four lithological units are differentiated (Table 1; Figure S1). In general, a ~500 m thick layer of turbidite-deposited mud, silt, and sand (Unit II) accumulated on a ~620 m thick sequence of basin style-deposited hemipelagic mudstones intercalated with tuffs (Unit III and IV). The décollement zone is located between 760 and 800 mbsf.

Table 1. Lithological units and associated facies, lithology, depth, age and sedimentation rates of Site C0023 (Heuer et al., 2017b).

Unit	Facies	Lithology	Depth [mbsf]	Age [Ma]	Sedimentation rate [cm kyr ⁻¹]
IIA	Axial trench-wedge	Hemipelagic and pelagic sand, muddy sand, turbidite-deposited silt and sandstones	189–318.5		
IIB	Outer trench-wedge	Hemipelagic and pelagic mud, turbidite-deposited mudstones	353–428	0.29	131.9
IIC	Trench-to-basin transition	Turbidite-deposited silt and sand, tuffs and volcanoclastic sediments	428–494	0.29–0.43	61.0
III	Upper Shikoku Basin	Heavily bioturbated volcanoclastic mudstones	494–637.5	0.43–2.53	9.3–6.0
IV	Lower Shikoku Basin	Heavily bioturbated mudstones with green ash-rich laminae	637.5–1112	2.53–13.53	6.0–3.5
V	Acidic volcanoclastics Basaltic basement	Mudstones and felsic ash Hyaloclastites	1112–1125.9 1125.9		

Note. Ages and sedimentation rates are based on biostratigraphic studies on calcareous nannofossil assemblages (Hagino and the Expedition 370 Scientists, 2018).

The Trench-wedge facies (Unit II), Pleistocene in age, is divided into three subunits. The Axial trench-wedge facies (Subunit IIA) mainly consists of thick sand and silt intervals in hemipelagic mud, whereas the Outer trench-wedge facies (Subunit IIB) contains more mud and less sand and silt. The sand- and silt-rich intervals are related to rapid transportation of shelf sand and mud during high-density turbidity flows. The Trench-to-basin transitional facies (Subunit IIC) comprises volcanoclastic beds with high contents of vitric ash (< 75%) and igneous crystals, that are mixed into the overlying mudstones by bioturbation. The Upper Shikoku Basin facies (Unit III) is Pleistocene to Pliocene in age and characterized by bioturbated mudstones with 4–10 cm thick volcanoclastic sand-rich beds and calcareous burrows. The Lower Shikoku Basin facies (Unit IV) was deposited during Miocene times. It is dominated by greenish, heavily bioturbated mudstones and ash-rich laminae with high smectite and detrital chlorite contents. The extent of bioturbation and presence of burrows increase from Unit II to Unit IV, as evidenced by a higher occurrence of calcareous burrows in the Lower Shikoku Basin facies (Taira and Ashi, 1993; Heuer et al., 2017a). The mudstones in Unit IV are intensively altered by low-temperature hydrothermal fluid flow (Figure S1; e.g., Tsang et al., 2020). Pale-yellow to pinkish alteration patches and burrow infills of rhodochrosite (MnCO₃) as well as stratabound and vein-filling crystals of barite (BaSO₄) could be observed in the lower parts of Unit IV. In addition, multiple intervals of green-colored mineralization associated with altered smectite and chlorite are found in the Lower Shikoku Basin facies. Unit V represents the oldest lithological unit at Site C0023. This 14 m thick greenish layer consists of acidic volcanoclastics with a high abundance of chlorite and smectite. Hyaloclastite deposits with glass and basalts as the dominant clasts characterize the lithologic basement (Taira and Ashi, 1993; Heuer et al., 2017a).

The total clay mineral abundance, inferred from shipboard X-ray diffraction (XRD) analyses, moderately increases with depth from 50% in Subunit IIA to 75% in Unit IV. In contrast, quartz and plagioclase contents are enriched (25%) in Subunits IIA and IIB, which is related to the presence of sand- and silt-rich intervals. As a result, porosity values generally decrease from 40% to 50% in Subunit IIA to 32% at the base of Unit IV. Calcium carbonate (CaCO_3) contents are generally low (average of ~ 3.4 wt%), with high scatter from Subunit IIC to Unit IV and contents up to 21.6 wt% due to the occurrence of calcareous horizons (calcite-cemented mudstones) and carbonate-rich hydrothermal alteration patches. A more detailed lithology description of each lithological unit can be found in Heuer et al. (2017a).

The transition from basin style-deposited hemipelagic mudstones to turbidite-deposited mud, silt, and sand led to a significant increase in sedimentation rates from 6.0 to 3.5 cm kyr^{-1} during late Miocene and Pliocene times in Unit IV to 131.9 cm kyr^{-1} in the middle Pleistocene in Subunit IIB (Table 1; Hagino and the Expedition 370 Scientists, 2018).

At present, the temperature at Site C0023 increases from $\sim 1.6^\circ\text{C}$ at the sediment-water interface up to $120 \pm 3^\circ\text{C}$ in the deepest core retrieved from the basement at 1177 mbsf, leading to an *in situ* temperature gradient of $110^\circ\text{C km}^{-1}$ (Heuer et al., 2020). The current heat flow is 140 mW m^{-2} (Heuer et al., 2017a). Based on basin modeling approaches, the temperature and burial history were reconstructed at different sites along the Muroto Transect (Horsfield et al., 2006; Tsang et al., 2020). Consistently, best fits with measured temperature and heat flow data were reached with a basin modeling scenario, in which high heat flows close to the spreading center of the 15 Ma-old oceanic lithosphere are followed by a transition to lower off-axis heat flows and a short increase up to 180 mW m^{-2} around 2 Ma associated with increased volcanic activity in the Japanese Island arc. In addition to heating associated with ongoing burial, evidence for short-term (< 3 days) and localized heating caused by low-temperature hydrothermal fluids ranging from $\sim 120^\circ\text{C}$ to 220°C within fracture zones has been found at Site C0023. As a result, hydrothermal mineralization assemblages including veins and stratabound alteration patches rich in BaSO_4 and MnCO_3 are formed (Tsang et al., 2020).

3. Methods

3.1 Shipboard sampling and pore-water and gas analyses

During IODP Expedition 370, a total of 112 sediment cores were collected from Hole C0023A, covering a depth range from 189 to 1,180 mbsf (Heuer et al., 2017a). All sediment depths used in this study are reported as corrected core depths below seafloor (CSF-B). Whole-round core (WRC) samples for geochemical analyses were selected based on X-ray computed tomography

(CT) image analysis to avoid horizons with fractures and disturbances and taken immediately after dividing the core into sections. The WRC samples varied in length between 10 and 80 cm. Pore-water was extracted from WRC samples using a titanium squeezer modified after the stainless-steel squeezer of Manheim and Sayles (1974). The WRCs dedicated to pore-fluid sampling were transferred into an N₂-flooded glovebag in which they were removed from the liner. To minimize seawater and drilling fluid contamination, the outer sediment layer (3-7 mm) was removed prior to squeezing. The samples were transferred into the titanium vessels and subsequently squeezed at 30,000 lb. Some samples from the deeper core had to be squeezed at 60,000 lb to increase the total pore-water volume yield. Chlorinity titrations were performed on water extracted at both forces to assess whether higher pressures caused sample freshening. The collected pore water was filtered through a Millipore Millex-LH hydrophilic 0.45 µm polytetrafluoroethylene (PTFE) disposable filter (Morono et al., 2017; Heuer et al., 2020). The whole-round squeeze cakes remaining after pore-water extraction were transferred into gas-tight aluminum bags, flushed with N₂, and subsequently vacuum-sealed. Vacuum-sealed bags were stored at -20°C for solid-phase analyses conducted in this study. Further details on the onboard sampling are given in the Method Chapter of the Expedition Report (Morono et al., 2017).

Pore-water and dissolved gas analyses were carried out onboard *D/V Chikyu* as described in Morono et al. (2017). In brief, sulfate concentrations were determined using a Dionex ICS-2100 ion chromatograph with an uncertainty of 0.02 mM. Pore-water samples with seawater contamination > 4% were excluded (Heuer et al., 2017a). Methane concentrations were analyzed with an Agilent 7890B gas chromatograph equipped with a packed column (HP PLOT-Q) and flame ionization detector (FID).

Dissolved Fe and hydrogen sulfide measurements were conducted with a Hach DR 2800 spectrophotometer. Dissolved Fe concentrations were determined using the ferrozine method after Stookey (1970). The detection and quantification limits for diluted samples were 0.3 and 0.8 µM, respectively. Hydrogen sulfide measurements were performed following the methylene blue method after Cline (1969), whereby detection and quantification limits were 0.2 and 0.4 µM, respectively.

Dissolved inorganic carbon (DIC) was measured with a Marianda automated infrared inorganic carbon analyzer (AIRICA) system with an uncertainty of 0.052 mM. The shipboard pore-water and gas data are reported in Tables 14 and 22 of the Expedition Report, respectively (Heuer et al., 2017a).

3.2 Inorganic solid-phase analyses

3.2.1 Bulk sediment composition

Inorganic solid-phase analyses were conducted in the laboratory at the Alfred Wegener Institute (AWI) Helmholtz Centre for Polar and Marine Research in Bremerhaven, Germany. Sub-samples from squeeze cakes were freeze-dried and ground in an agate ball mill for subsequent solid-phase analyses. In this way, the sub-samples were homogenized and integrated over the whole length of the WRC samples. For analyses of the bulk sediment composition, ~50 mg of homogenized sediment was fully dissolved in a mixture of 65% HNO₃ (3 mL), 30% HCl (2 mL) and 40% suprapur® HF (0.5 mL). HNO₃ and HCl were of sub-boiling distilled quality. The total acid digestions were performed in a CEM Mars Xpress microwave system according to the procedure described by Nöthen and Kasten (2011). This method yields data for total Fe (Fe_{total}), S (S_{total}), and Al (Al_{total}) contents. Standard reference material (NIST SRM 2702) and blanks were processed with each set of samples. Elemental concentrations were determined by inductively coupled plasma optical emission spectrometry (ICP-OES) analysis (iCAP 7400, Thermo Fisher Scientific Inc.) under application of an internal yttrium standard. The recoveries for the NIST SRM 2702 were 97.1 ± 4.0% for Al_{total}, 94.7 ± 3.4% for Fe_{total} and 101.0 ± 3.7% for S_{total} (n = 15). Duplicate samples were analyzed to ensure that the elemental contents are representative for the whole WRC interval. The relative differences between duplicate samples were < 5% (Table S1).

3.2.2 Acid volatile sulfide and chromium reducible sulfur

Acid volatile sulfide (AVS) and chromium reducible sulfur (CRS) were determined gravimetrically on ~1 g of homogenized sediment by a two-step extraction. AVS includes Fe monosulfides whereas CRS is considered to represent pyrite. AVS was extracted with boiling 6 M HCl (Cornwell and Morse, 1987) and CRS using a CrCl₂ solution (e.g., Zhabina and Volkov, 1978; Canfield et al., 1986). Sulfide that is released during both extraction steps was trapped as Ag₂S. The amounts of Fe bound to AVS and CRS were calculated from extracted sulfur using the stoichiometry 1:1 (FeS) and 1:2 (FeS₂), respectively. Analytical precision was determined using an in-house sediment standard (HE443-077-cc; anoxic sediment from the North Sea) and a non-reference pyrite standard (> 90% pure; hydrothermal origin). Repetitive analyses resulted in FeS and pyrite contents of 0.02 ± 0.01 wt% (n = 8) and 0.88 ± 0.07 wt% (n = 9), respectively, for the in-house standard and pyrite contents of 86.28 ± 4.35 wt% (n = 9) for the pyrite standard.

3.2.3 Sequential extraction of Fe (oxyhydr)oxides

Sequential extractions following the protocols described by Poulton and Canfield (2005) and Henkel et al. (2016) were applied on ~50 mg of freeze-dried and homogenized sediment (Table S2). It typically targets four Fe pools, namely (a) Fe bound in carbonates (Fe_{carb}), (b) easily reducible Fe oxides (ferrihydrite and lepidocrocite; Fe_{ox1}), (c) reducible Fe oxides (goethite and hematite; Fe_{ox2}) and (d) magnetite (Fe_{mag}). However, in order to emphasize the operational nature of sequential extraction, an extraction stage-based labeling of fractions (Fe_{aca} , Fe_{hyam} , $\text{Fe}_{\text{di-ct}}$, Fe_{oxa} after Henkel et al., 2016) rather than the conventional terminology is used in this study (Table S2). The sum of all sequentially leached Fe pools is defined as “reactive” Fe, which refers to the reactivity towards hydrogen sulfide (Poulton et al., 2004). “Microbial reducible” Fe(III), however, conventionally only comprises Fe bound in carbonates and easily reducible Fe oxides (e.g., Laufer et al., 2020). All extraction steps were carried out under N_2 -atmosphere at room temperature. The sediment samples were first treated with 5 mL of 1 M MgCl_2 (pH 7) for 2 h in order to extract pore-water constituents and adsorbed Fe (Tessier et al., 1979; Heron et al., 1994). The sediment-extraction reagent-suspensions were shaken on a vertical rotating shaker for the respective times and subsequently centrifuged at 4,000 rpm for 5 min. The supernatant was filtered through a 0.2 μm polyethersulfone membrane. Splits of all extracts were analyzed by ICP-OES after dilution in 0.3 M HNO_3 or ultrapure water (in case of Na-dithionite as extractant) for the determination of extracted Fe, Al, and Si. Standards were adapted to the different extraction matrices and all data were corrected for effects of different ionic strengths by use of an internal yttrium standard. Based on triplicate measurement of each sample, the relative standard deviation was $< 2\%$. The in-house house standard HE443-077-cc with overall comparable Fe contents to the C0023 samples resulted in values of $4.43 \pm 0.10 \text{ wt}\%$ for Fe_{aca} , $3.38 \pm 0.08 \text{ wt}\%$ for Fe_{hyam} , $2.78 \pm 0.10 \text{ wt}\%$ for $\text{Fe}_{\text{di-ct}}$ and $1.04 \pm 0.03 \text{ wt}\%$ for Fe_{oxa} ($n = 8$). These values were in the range of respective Fe contents determined over the course of 5 years in the laboratories at the AWI ($\text{Fe}_{\text{aca}} = 4.57 \pm 0.21 \text{ wt}\%$; $\text{Fe}_{\text{hyam}} = 3.15 \pm 0.25 \text{ wt}\%$; $\text{Fe}_{\text{di-ct}} = 2.61 \pm 0.22 \text{ wt}\%$; $\text{Fe}_{\text{oxa}} = 1.07 \pm 0.10 \text{ wt}\%$; $n = 26$). The relative differences between duplicate samples are listed in Table S3.

3.3 Total organic carbon and algal biomarkers

Total organic carbon (TOC) and nitrogen (TN) analyses were conducted onboard *D/V Chikyu* using a Thermo Finnigan Flash EA 1112 CHNS analyzer. TOC contents were determined by subtraction of inorganic carbon (IC; Coulometrics 5012 CO_2 coulometer) from total carbon contents (TC). The TOC/N ratio was determined as a source indicator of the organic matter

(Morono et al., 2017). TOC and TN data are reported in Table 20 of the Expedition Report (Heuer et al., 2017a).

The stable carbon isotopic composition of TOC ($\delta^{13}\text{C}$ -TOC) and biomarker analyses were performed in the laboratory at the MARUM—Center for Environmental Sciences, University of Bremen, Germany. Prior to $\delta^{13}\text{C}$ -TOC analysis, ground and homogenized samples were treated with 12.5% HCl to remove inorganic carbon and oven-dried. Analysis was performed with a Thermo Scientific Flash 2000 elemental analyzer coupled to a Thermo Delta V Plus IRMS. The $\delta^{13}\text{C}$ -TOC values are expressed relative to VPDB (Vienna Pee Dee Belemnite). For biomarker analyses, samples were extracted using a modified Bligh and Dyer extraction technique as described in Sturt et al. (2004). After extracting twice with methanol (MeOH):dichloromethane (DCM):phosphate buffer (2:1:0.8, v/v/v) and twice with MeOH:DCM:TCA buffer (2:1:0.8, v/v/v), a fifth extraction step was added using dichloromethane:methanol (3:1, v/v). An aliquot of the dried lipid extract was measured on a Bruker maXis Plus ultra-high-resolution quadrupole time-of-flight mass spectrometer (Q-TOF) coupled with an APCI II ion source to Dionex Ultimate 3000RS ultra-high-pressure liquid chromatography (UHPLC). Coccolithophore (alkenones) and eustigmatophyte (long-chain diols) biomarkers were separated using two coupled Acquity BEH amide columns (2.1 × 150 mm, 1.7 μm ; Waters, Eschborn, Germany) following protocols described in Becker et al. (2015).

3.4 IRM acquisition curves and end-member unmixing

All magnetic measurements were performed in the paleomagnetic laboratory at the Center for Advanced Marine Core Research, Kochi University, Japan. IRM acquisition curves were measured on 46 samples at room temperature using a Princeton Measurements Corporation Vibrating Sample Magnetometer to characterize the magnetic mineral assemblages. Samples were dry and powdered sediment filled into gelatin capsules and packed with cotton wool (~600 mg). IRM was imparted stepwise (non-linearly) up to a maximum field of 1 T, with an average time of 200 ms. 100 data points describe one IRM acquisition curve. The IRM acquisition curves for a magnetic mineral assemblage can be approximated by cumulative log-Gaussian functions using three parameters: the estimated saturation IRM, the mean coercivity (B_h) of a magnetic phase (i.e., the field at which half of the total IRM is reached on a logarithmic field scale), and the dispersion parameter (DP), which describes the width of the coercivity distribution of a mineral phase (given by one standard deviation in log space;

Robertson and France, 1994; Kruiver et al., 2001; Maxbauer et al., 2016). All IRM acquisition curves were unmixed using the web application MAX UnMix by Maxbauer et al. (2016).

3.5 Magnetic susceptibility

The magnetic susceptibility is defined as the ratio between the induced magnetization of a material to an applied magnetic field. It is used as a relative proxy indicator for changes in the sedimentary composition and as a proxy for magnetic mineral concentration. Low-field and low-frequency (0.465 kHz) magnetic susceptibility (χ_{lf}) was measured on 223 discrete samples (7 cc plastic cubes) using an MS2 Bartington apparatus.

3.6 ^{57}Fe Mössbauer spectroscopy

To improve the interpretation of sequential extraction data, ^{57}Fe Mössbauer spectroscopy analysis was performed on three representative samples (370-C0023A-18R-1, 19.0–41.0 cm; 370-C0023A-81R-7, 0.0–30.0 cm; 370-C0023A-105R-2, 0.0–45.0 cm) from different depths (430, 850, and 1,080 mbsf, respectively) at the Center for Applied Geosciences at the University of Tübingen, Germany. Freeze-dried and mortared sediment samples were loaded into Plexiglas holders (area 1 cm²), forming a thin disc. Samples were then loaded to the instrument and spectra were collected at room temperature (295 K), 77 K, and 5 K using a constant acceleration drive system (WissEL) in transmission mode with a $^{57}\text{Co}/\text{Rh}$ source. All spectra were calibrated against a 7 μm thick α - ^{57}Fe foil that was measured at room temperature. Analysis was carried out using Recoil (University of Ottawa). Based on the prevalent dominance of Fe-rich, clay-sized phyllosilicates (Heuer et al., 2017a), the Lorentzian Site Analysis routine was performed to produce consistent fits and serviceable results that allowed the investigation of Fe(II)/(III) ratios and the comparison with a reference data base (Murad, 1998, 2010).

4. Results

4.1 Pore-water and gas geochemistry

Pore-water sulfate (SO_4^{2-}) concentrations range from 0.3 to 0.9 mM between 206.5 (shallowest sample) and 550 mbsf (Figure 2a). Below 550 mbsf, sulfate concentrations gently increase to 3 mM at 750 mbsf, followed by a strong increase of up to 6.2 mM at 930 mbsf. Sulfate concentrations decrease between 950 and 1,050 mbsf by 1.5 mM and scatter between 5 and 7 mM towards the sediment-basement interface. Some scatter in sulfate concentrations can be attributed to contamination with seawater-derived sulfate, as described in the Expedition Report (Heuer et al., 2017a).

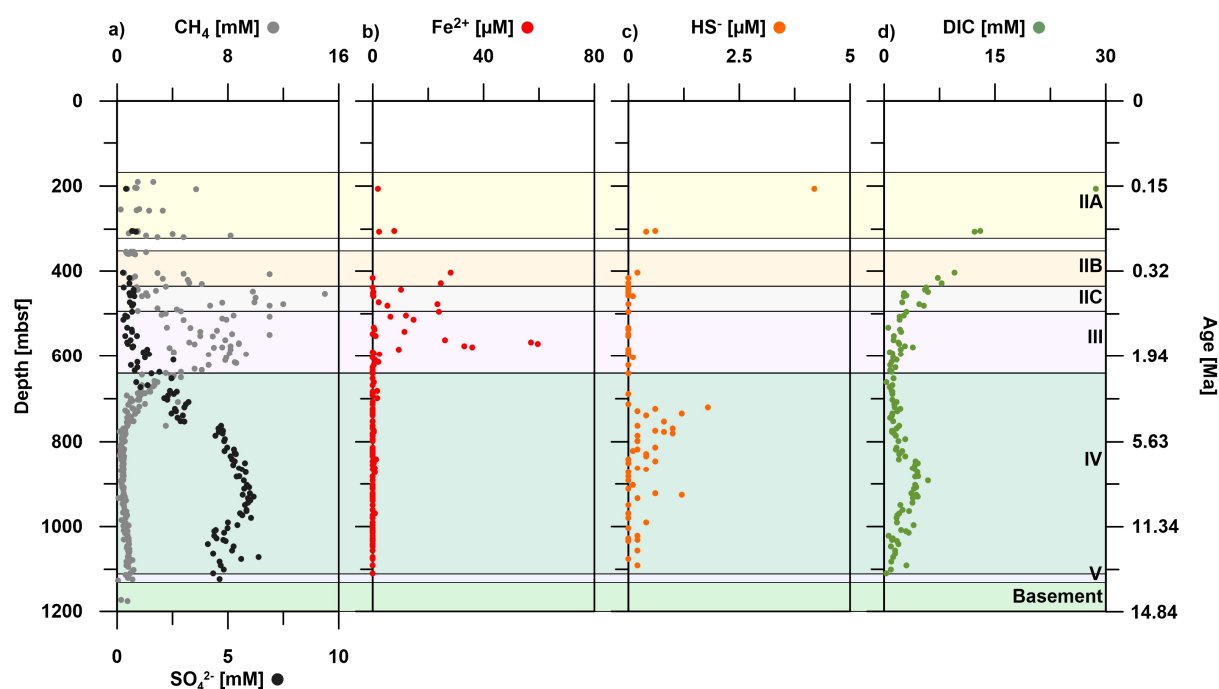


Figure 2. Pore-water profiles of (a) sulfate (SO_4^{2-}), methane (CH_4), (b) dissolved Fe (Fe^{2+}), (c) hydrogen sulfide (HS^-), and (d) dissolved inorganic carbon (DIC) at Site C0023 from Heuer et al. (2017a). Lithological units (Heuer et al., 2017a) are indicated on the right. Corresponding ages on the right-side y-axis are based on the age model by Hagino and the Expedition 370 Scientists (2018).

Methane (CH_4) concentrations strongly fluctuate between 190 and 750 mbsf, varying from 0.3 to ~ 15 mM (Figure 2a). The highest values are detected between 410 and 640 mbsf. Below, CH_4 concentrations decrease to < 0.5 mM at 770 mbsf and remain low down to 900 mbsf, before increasing again to maximum values of 1.2 mM at a depth of 1,100 mbsf. Dissolved Fe (Fe^{2+}) was observed between 200 and 600 mbsf with a maximum concentration of 60 μM at 570 mbsf (Figure 2b). Fe^{2+} concentrations decrease and remain close or below quantification limits of 0.8 μM below 600 mbsf. Dissolved hydrogen sulfide (HS^-) concentrations are generally low at Site C0023. The shallowest sample at ~ 200 mbsf shows the highest values of 4.2 μM (Figure 2c). The hydrogen sulfide concentrations are close to or below detection limit of 0.2 μM between 300 and 720 mbsf, followed by an interval with concentrations of up to 1.8 μM down to the bottom of the core. Dissolved inorganic carbon (DIC) values decrease from ~ 30.0 to 2 mM between 200 and 600 mbsf and remain < 2 mM further downcore (Figure 2d).

4.2 Inorganic sediment geochemistry

Fe_{total} contents range from 3.4 to 5.1 wt% with an average value of 4.2 wt% (Figure 3a). The $\text{Fe}_{\text{total}}/\text{Al}_{\text{total}}$ profile generally mimics the Fe_{total} profile within the range of 0.43–0.61 (Figure 3b), and thus, close to an average shale value of 0.55 (Turekian and Wedepohl, 1961). Both,

Fe_{total} and Fe_{total}/Al_{total} display highest values of 5.1 wt% and 0.61, respectively, at the lower end of Unit IV at $\sim 1,100$ mbsf.

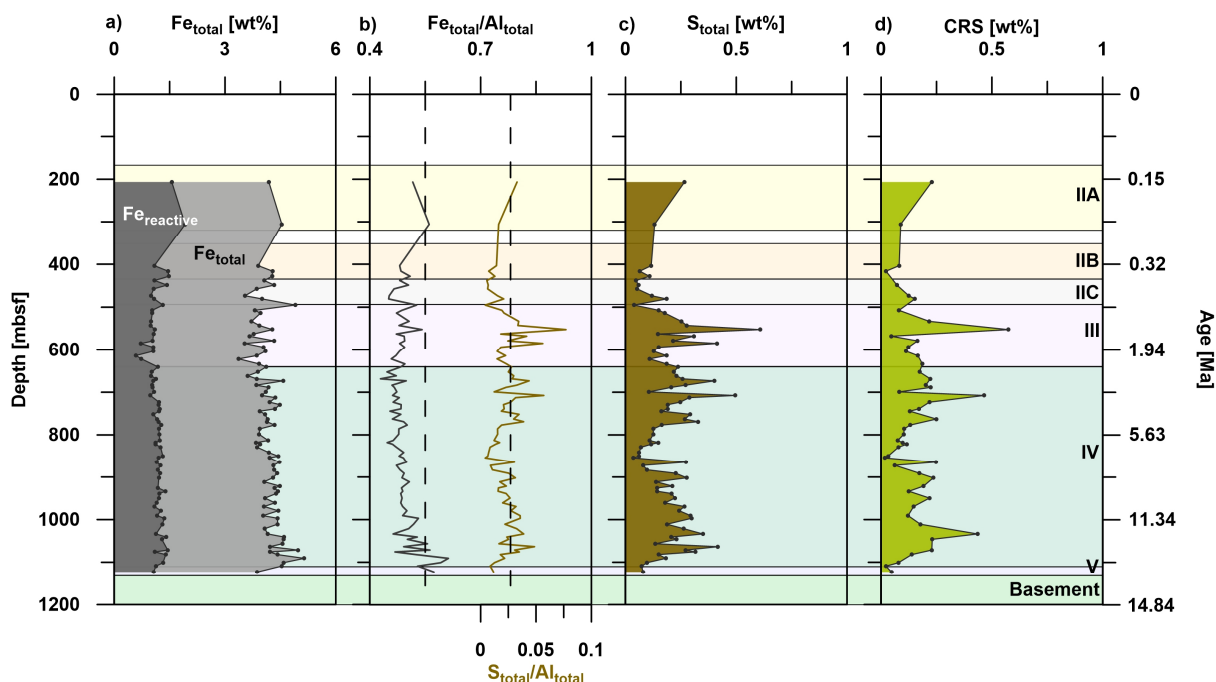


Figure 3. Down-core solid-phase profiles of (a) reactive Fe ($Fe_{reactive} = Fe_{aca} + Fe_{hyam} + Fe_{di-ct} + Fe_{oxa}$; see Figure 4), total Fe (Fe_{total}), (b) Fe_{total}/Al_{total} , S_{total}/Al_{total} , (c) total S (S_{total}), and (d) chromium reducible sulfur (pyrite). Dashed vertical lines indicate average shale content (Turekian and Wedepohl, 1961). Color shading and corresponding ages as in Figure 2.

S_{total} contents show strong variability between 0.04 and 0.61 wt% with an average value of 0.20 wt% (Figure 3c). Intervals with elevated values occur between 500 and 600 mbsf, 640 and 770 mbsf as well as 900 and 1,100 mbsf. The S_{total}/Al_{total} profile resembles the S_{total} profile (Figure 3b). The ratio varies over depth with an average value 0.02, and thus, is close to average shale with 0.03 (Turekian and Wedepohl, 1961). While AVS was absent, CRS contents fluctuate over depth between 0.02 and 0.57 wt% (Figure 3d) and mimic the S_{total} profile, suggesting that bulk S is mainly present as pyrite.

$Fe_{reactive}$, here comprised of the sum of the sequentially extracted Fe, represents $\sim 25\%$ of Fe_{total} (Figure 3a). Fe_{aca} is elevated up to 1 wt% in Subunits IIA and IIB and generally decreases with depth to 0.05 wt% (Figure 4a). Fe_{hyam} is the dominant reactive Fe fraction ($\sim 60\%$ of $Fe_{reactive}$) with contents up to 0.97 wt% and an overall increasing trend with depth (Figure 4b). The average contents of Fe_{di-ct} and Fe_{oxa} are 0.15 and 0.20 wt%, respectively (Figures 4c and 4d). The Fe_{di-ct} and Fe_{oxa} profiles both display an overall decrease in Unit II and III. While Fe_{di-ct} contents are elevated with up to 0.22 wt% between 720 and 890 mbsf and decrease further

below, Fe_{oxa} shows the opposite trend with lower contents in the top of Unit IV and increased values (0.27 wt% on average) between 890 mbsf and the bottom of Unit IV.

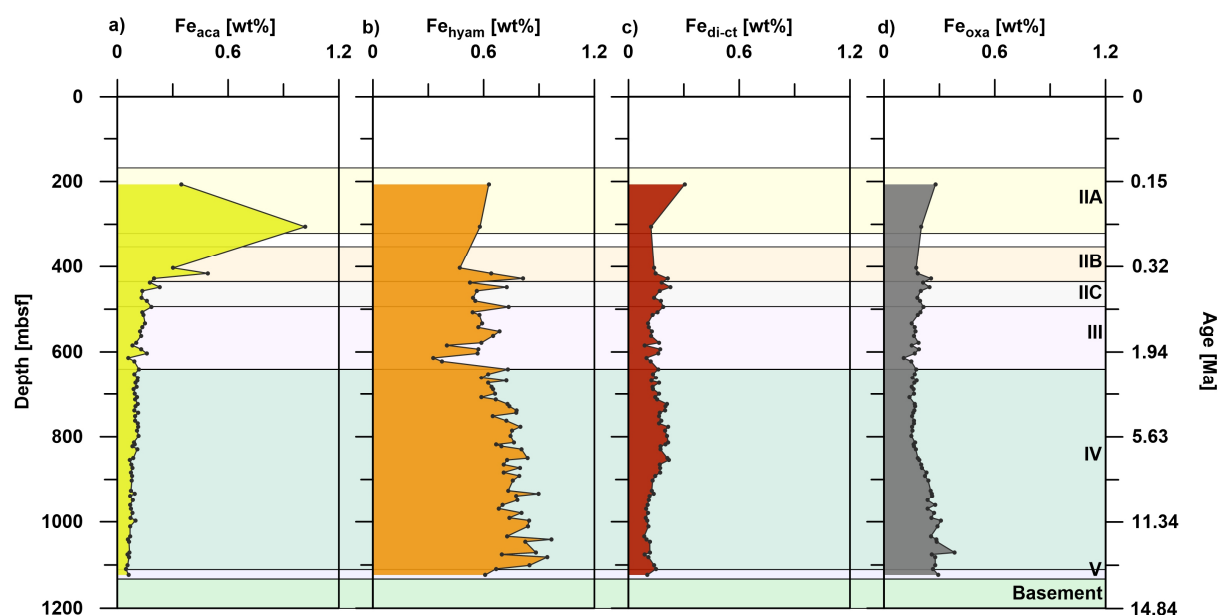


Figure 4. Down-core solid-phase profiles of sequentially extracted (a) Fe_{aca} (Na-acetate-leachable Fe), (b) Fe_{hyam} (Hydroxylamine-HCl-leachable Fe), (c) $Fe_{\text{di-ct}}$ (Na-dithionite-leachable Fe), and (d) Fe_{oxa} (NH_4 -oxalate/oxalic acid-leachable Fe). Color shading and corresponding ages as in Figure 2. Note that there are only three data points between 200 and 400 mbsf.

4.3 Total organic carbon and algal biomarkers

While TOC generally decrease downcore from 0.6 wt% in Unit II to 0.3 wt% in the lower interval of Unit III, the contents are relatively constant at around 0.25 wt% in Unit IV (Figure 5a). TOC/N ratios steadily decrease from 12 in Subunit IIA to < 4 at the bottom of Unit IV and are generally proportional to the TOC contents (Figure S2a; Heuer et al., 2017a). The $\delta^{13}\text{C}$ -TOC values gradually increase from -26‰ in the upper part of Unit II up to -21‰ in Unit III. Below 600 mbsf, $\delta^{13}\text{C}$ -TOC values slightly shift towards lighter values towards the bottom of Unit IV with values ranging between -24‰ and -22‰ (Figure S2b).

Two types of algal lipid biomarkers are detected in the employed analytical window: long-chain diols, which are suggested to be sourced from eustigmatophyte algae (Volkman et al., 1992), and long-chain alkenones and alkyl alkenoates, which are diagnostic biomarkers for coccolithophores (Brassell et al., 1986). Due to the lack of representative standards we are not reporting absolute concentrations but instead report the integrated peak area of the sum of all detected diols normalized to kg extracted sediment (PA/kg) for each depth (Figure S2c and S2d). Long-chain diols are only detected in Unit IIA through Unit III. In this interval C_{26} to C_{34} diols are observed, with $C_{30:0}$ 1,15 diols and $C_{32:0}$ diols being most abundant. Summed long-

chain diol abundance ranges from 221 to 32,000 PA/kg with a maximum observed at 350 mbsf. Diols are not detected below 620 mbsf. Long-chain alkenones are present from the top of the core down to 860 mbsf. C_{37} , C_{38} , and C_{39} long-chain alkenones are most abundant, followed by C_{36} alkyl alkenoates. Similar to the long-chain diols, highest abundances of the summed alkenones and alkyl alkenoates are observed between 350 and 520 mbsf, with concentrations up to 300,000 PA/kg at the top of Unit III.

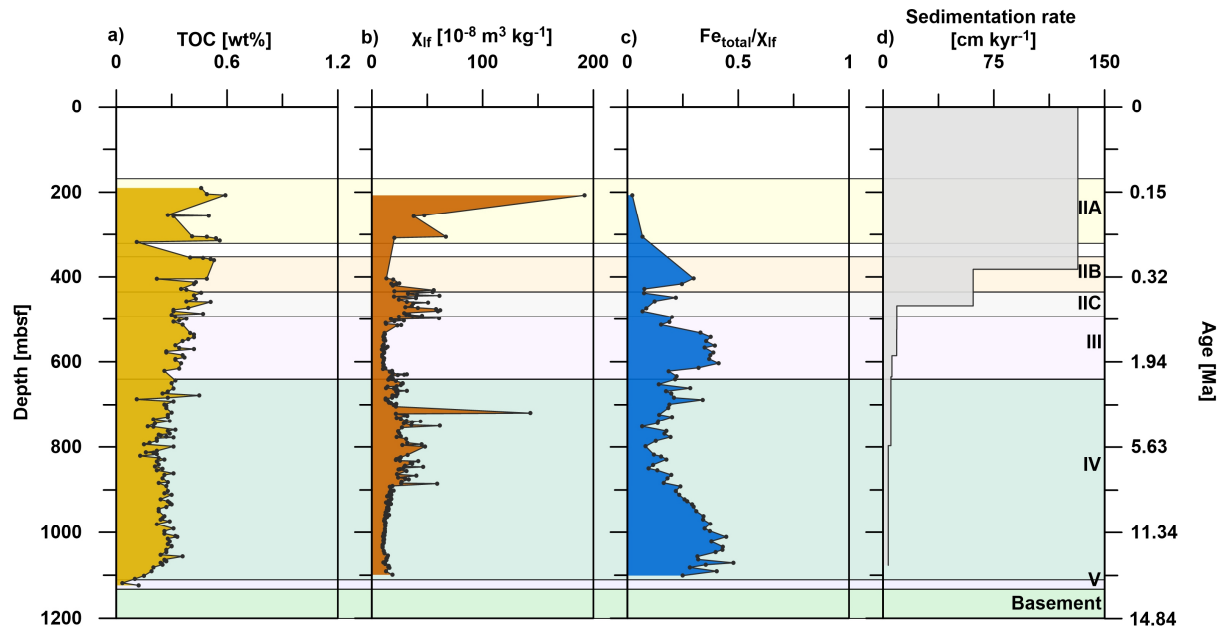


Figure 5. Down-core solid-phase profiles of (a) total organic carbon (modified from Heuer et al., 2017a), (b) magnetic susceptibility χ_{lf} , (c) Fe_{total}/χ_{lf} , which indicates the intensity of magnetite dissolution (Funk et al., 2004), and (d) sedimentation rates (from Hagino and the Expedition 370 Scientists, 2018). Color shading and corresponding ages as in Figure 2.

4.4 IRM end-member unmixing

After unmixing IRM acquisition curves of the studied samples, the magnetic mineral assemblages can be described by one to four coercivity end-members (EM) and by their contribution (extrapolated contribution [EC]) to the total IRM (Maxbauer et al., 2016). The coercivity distributions of three representative samples (370-C0023A-3F-3, 80.0–105.0 cm, 370-C0023A-21R-2, 101.0–103.0 cm, and 370-C0023A-83R-2, 56.0– 58.0 cm) at 206.5, 458.2, and 863.6 mbsf, respectively, are shown in Figure S3. EM 1 (blue) is an intermediate coercivity component with B_h of $1.91 \log_{10}$ (~ 81.3 mT) and a narrow DP of ~ 0.15 , which is interpreted as greigite (e.g., Roberts et al., 2011; Shi et al., 2017). B_h of EM 2 (purple) is $1.61 \log_{10}$ (~ 40.7 mT), which is indicative of fine-grained magnetite (e.g., Abrajvitch et al., 2009). EM 3 (green) represents a higher coercivity component with $B_h > 2 \log_{10}$ (> 100 mT)

and a wide DP (1.03), such as hematite (e.g., Abrajevitch et al., 2009; Abrajevitch and Kodama, 2011). EM 4 (red) is interpreted as coarse-grained magnetite with B_h of $\sim 1.36 \log_{10}$ (~ 22.9 mT) and DP of 0.62.

Down-core variations in the relative proportion of each modeled EM are shown in Figure 6. Due to low magnetic minerals contents and consequently weaker magnetization in samples between 500 and 650 mbsf as well as 950 and 1,100 mbsf, these intervals are indicated as weak intervals I and II. EM 1 (greigite) only occurs between 200 and 500 mbsf, contributing most to the magnetic signal up to 0.76 (Figure 6a). Below 500 mbsf, EM 2 (fine-grained magnetite) is the mineral phase with the highest contribution between 0.66 and 1 (Figure 6b). EM 3 (high coercivity minerals) and EM 4 (coarse-grained magnetite) are present in all samples with minor contributions up to 0.31 (Figures 6c and 6d).

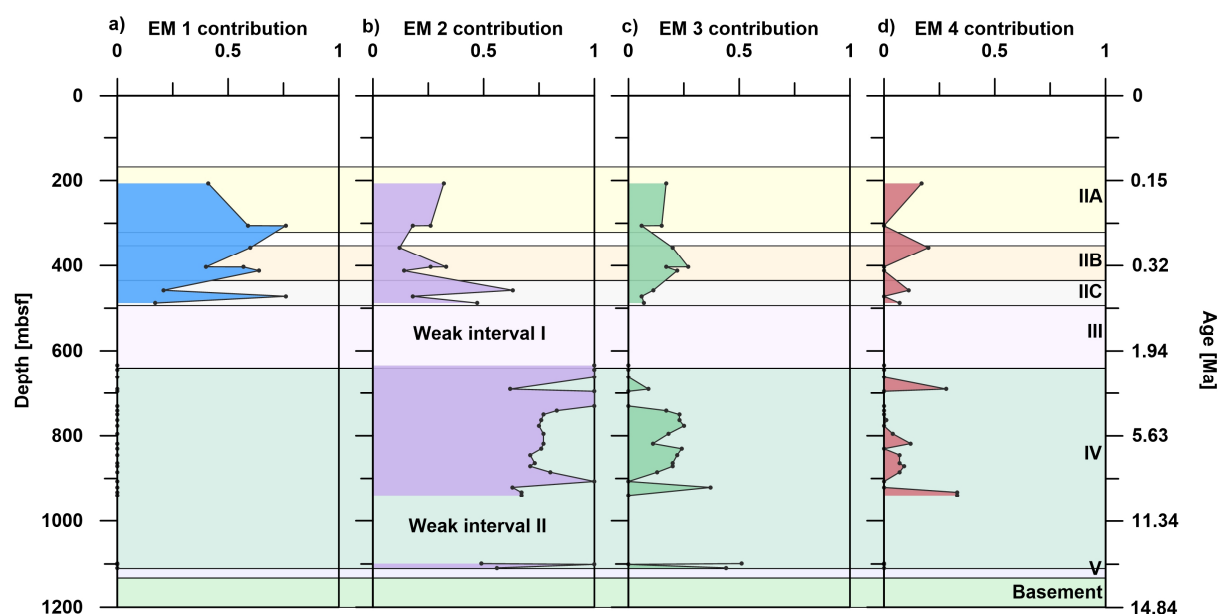


Figure 6. End-member plot showing the relative contributions to the total isothermal remanent magnetization of each end-member (EM) (a) greigite, (b) fine-grained magnetite, (c) hematite, and (d) coarse-grained magnetite in representative samples over depth obtained by using the MAX UnMix web application (Maxbauer et al., 2016). The coercivity distribution could not be modeled in two depth intervals due to low magnetic intensities, referred as to Weak interval I and II. Note that EM 1 is only identified between 200 and 500 mbsf. Color shading and corresponding ages as in Figure 2.

4.5 Magnetic susceptibility

Magnetic susceptibility χ_{if} significantly varies over depth between 10×10^{-8} and $190 \times 10^{-8} \text{ m}^3 \text{ kg}^{-1}$ with an average value of $23 \times 10^{-8} \text{ m}^3 \text{ kg}^{-1}$ (Figure 5b). The highest value is observed in the upper Subunit IIA at 200 mbsf. The χ_{if} profile exhibits two distinct maxima between 400 and 500 mbsf and 600 and 900 mbsf. The Fe_{total} over magnetic susceptibility ratio

is used as a proxy for the intensity of magnetite dissolution, whereby high values indicate a loss of fine magnetite (e.g., Funk et al., 2004). In this study, Fe_{total} is compared to the mass-normalized magnetic susceptibility χ_{lf} (Fe_{total}/χ_{lf} ; Figure 5c). The Fe_{total}/χ_{lf} profile shows the opposite trend compared to χ_{lf} with higher values up to 0.5 between 500 and 600 mbsf in Unit III and between 900 and 1,100 mbsf in the lower half of Unit IV.

4.6 ^{57}Fe Mössbauer spectroscopy

All spectra, collected at room temperature (295 K), generally reveal the dominant presence of a wide doublet (Db1) with a high center shift (CS) ranging from 1.13 to 1.24 mm s⁻¹ and a relatively high quadrupole splitting (ΔE_Q) of 2.64–2.67 mm s⁻¹ (Figures 7a–7c; Table S4). These high hyperfine field values for CS and ΔE_Q are typically indicative of a non-magnetically ordered Fe(II) phase. The relative abundance of this Fe(II) phase is < 60% in all samples (Table S4). The asymmetry in all collected spectra and the bump on the left shoulder indicate the presence of an additional spectral feature, which is designated in the model-fit as Db2 (Figures 7a–7c). The hyperfine field parameters for Db2 show generally lower values for CS ranging from 0.35 to 0.37 mm s⁻¹ and ΔE_Q from 0.57 to 0.64 mm s⁻¹, suggestive for an Fe(III) phase. All samples have a higher relative abundance of Fe(II) over Fe(III) (Table S4).

While the spectra collected at 77 K for samples 370-C0023A-18R-1, 19.0–41.0 cm and 370-C0023A-105R-2, 0.0–45.0 cm only show the dominant doublet features (Figures 7d and 7f), a poorly defined sextet (S1) in the spectrum of sample 370-C0023A-81R-7, 0.0–30.0 cm, points to the presence of a more crystalline, partly magnetically ordering Fe phase with a relative abundance of ~6% (Figure 7e and Table S4). However, the hyperfine field values of S1 do not allow a clear identification of the mineral phase (e.g., goethite or hematite).

Spectra recorded at 5 K still show the very dominant doublet features as being detected at higher temperatures (Figures 7g–7i). The relative abundance for Fe(II) over Fe(III) ranges from 49% (370-C0023A-18R-1, 19.0–41.0 cm) to 61% (370-C0023A-105R-2, 0.0–45.0 cm; Table S4). In the background of all spectra collected at 5 K, a poorly defined sextet feature is visible. This rather collapsed sextet indicates the presence of an Fe phase which was starting to undergo magnetic ordering at 5 K.

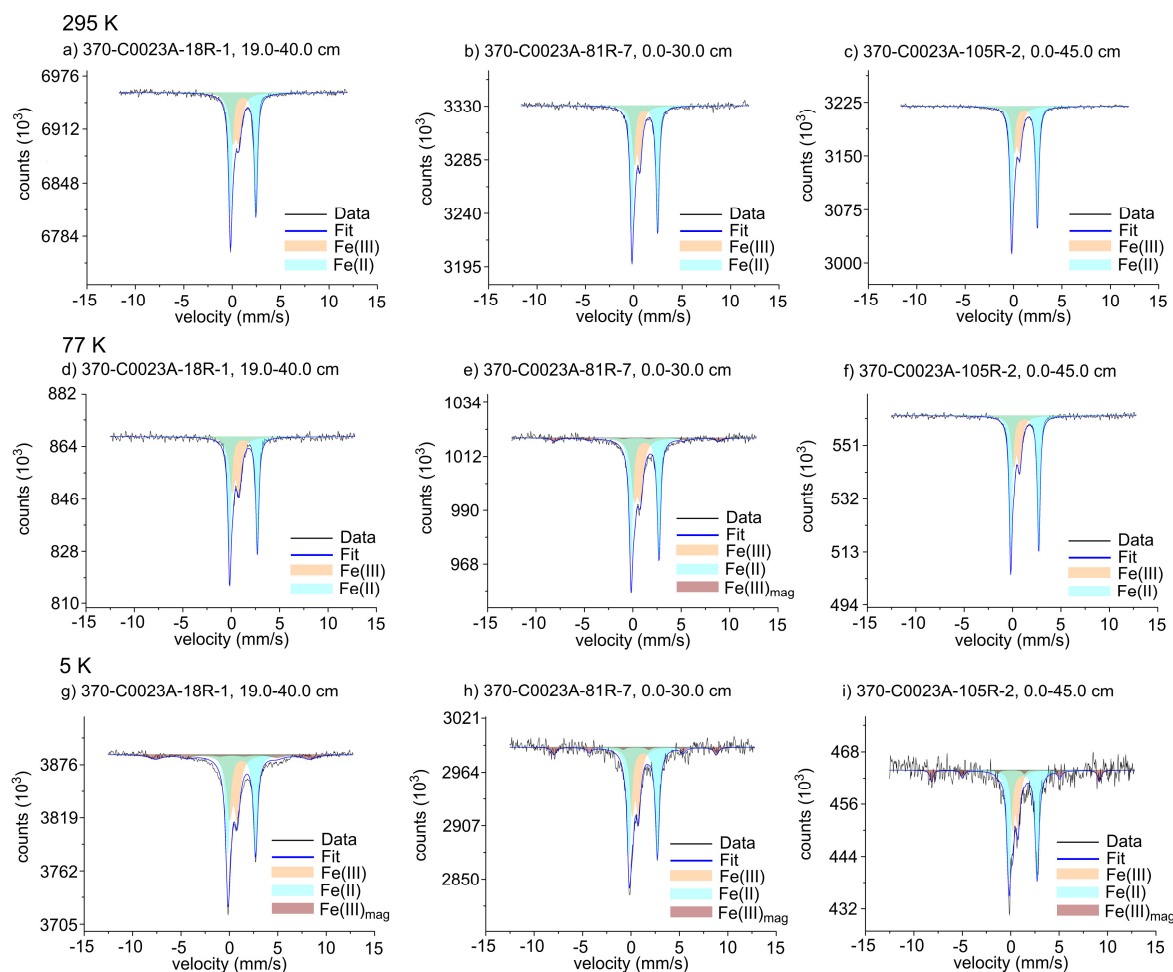


Figure 7. Mössbauer spectra collected for each sample at 295 K (a–c), 77 K (d–f), and 5 K (g–i). All samples measured at room temperature (295 K) show a wide doublet which can be attributed to the presence of a non-magnetically ordered Fe(II) phase (light blue). The narrow doublet can be attributed to the presence of an Fe(III) phase (orange). Low-temperature measurements at 5 K confirm the dominant presence of paramagnetic (non-magnetically ordered) Fe(III) mineral phases to be present in all samples likely to represent (clay-sized) Fe-rich phyllosilicates. The absence (or low abundance) of a sextet feature at 5 K suggests the absence (or only low abundance) of magnetically ordered Fe (oxyhydr)oxide phases (Fe(III)_{mag}; red) such as hematite, goethite or ferrihydrite; or could be a measuring artefact of a paramagnetic relaxation of Fe atoms in phyllosilicates (details given in the text).

5. Discussion

5.1 Quantification and characterization of reactive Fe mineral phases at Site C0023

The average Fe_{total} content at Site C0023 (Figure 3a) is in the range of bulk Fe contents in sediments from the Kumano Transect of the Nankai Trough (IODP Site C0012), located off Kii Peninsula ~200 km northeast of the Muroto Transect (~4 wt%; Torres et al., 2015). The hydroxylamine-HCl-leachable Fe fraction, typically comprised of labile Fe (oxyhydr)oxides (Fe_{hyam}) including ferrihydrite and lepidocrocite (Poulton and Canfield, 2005), dominated the

fractions of extractable Fe at Site C0023 (Figure 4b). According to Canfield et al. (1992) and Poulton et al. (2004), ferrihydrite and lepidocrocite undergo reductive dissolution driven by microbial degradation of organic matter and reactions with hydrogen sulfide on timescales from minutes to days, respectively. Considering the age (up to ~15 Ma) and temperature of the sediments at Site C0023, labile Fe (oxyhydr)oxides are unlikely to be preserved in these ancient sediments. Even though low organic carbon contents during deposition of Unit IV might have been insufficient to drive dissimilatory Fe reduction, which could have led to a preservation of reactive Fe (oxyhydr)oxides (e.g., Riedinger et al., 2005, 2014; see Section 5.2.1), ferrihydrite and lepidocrocite would have been converted to more crystalline Fe oxides such as goethite, especially over timescales of several million years (e.g., Cornell and Schwertmann, 2003). Therefore, the extraction data seemed suspicious in terms of the conventional interpretation of the Fe_{hyam} fraction and was further investigated.

Recent studies by Slotznick et al. (2020) and Hepburn et al. (2020) focused on the efficiency of Fe chemical sequential extractions to dissolve the target phases. Both studies showed that the hydroxylamine-HCl step after Poulton and Canfield (2005) effectively extracts easily reducible Fe (oxyhydr)oxides when present. However, Hepburn et al. (2020) also demonstrated that nontronite, an Fe(III)-rich member of the smectite group, is also dissolved during the hydroxylamine-HCl step. Ryan et al. (2008) further observed a partial dissolution of Fe contained in chlorite and smectite of up to 13.5% of bulk Fe even with a less concentrated hydroxylamine-HCl solution (0.5 M) and a shorter reaction time of only 16 h. The hydroxylamine-HCl treatment leads to the reduction of structural Fe(III) in these phyllosilicates, which creates local instabilities in crystal energies from charge imbalance, thus, promoting mineral dissolution (Stucki et al., 1984). The study by Slotznick et al. (2020) further showed that NH_4 -oxalate appears to solubilize Fe-bearing silicates, specifically berthierine and chamosite.

Phyllosilicates, including the clay minerals chlorite and smectite are abundant at Site C0023, especially in the Lower Shikoku Basin formation (Heuer et al., 2017a). The total clay mineral contents obtained from XRD analyses gradually increase from Subunit IIA towards the sediment-basement interface and is, thus, proportional to the Fe_{hyam} profile (Figure 4b). Aluminum (Al) and silicon (Si) are main components of Fe-rich phyllosilicates including nontronite, chlorite and biotite. In order to examine if Fe bound in phyllosilicates is unintentionally dissolved during the applied Fe sequential extraction, we compared the amounts of Al and Si to Fe released by the different extraction steps for a selection of 16 samples (Figure S4). Our data show very good correlation between Fe_{hyam} and Al_{hyam} ($R^2 = 0.91$) and Fe_{oxa} and

Al_{oxa} ($R^2 = 0.98$) and slightly lower correlation between Fe_{hyam} and Si_{hyam} ($R^2 = 0.70$) and Fe_{oxa} and Si_{oxa} ($R^2 = 0.75$). In addition, the Mössbauer spectroscopy analysis strengthens our hypothesis. The presence of the dominant doublet features in all collected spectra and the prevalent non-magnetic (paramagnetic) behavior at 5 K can be attributed to a high abundance (> 85%) of phyllosilicates in all three samples (Figure 7). The hyperfine parameters of the collapsing sextet feature in all spectra at 5 K could be attributed to a poorly crystalline Fe(III) (oxyhydr)oxide such as ferrihydrite, goethite or even hematite to be present by < 15%. However, this collapsing sextet feature might also reflect an artifact of paramagnetic relaxation of Fe atoms at around 5 K, which can create sextets in the absorbance spectra with similar hyperfine parameters. This effect has been previously shown in phyllosilicates containing low Fe contents (Murad, 1998). From this, we deduce that the most prevalent Fe mineral phase in the analyzed samples are mixed-valent Fe-rich, potentially clay-sized, phyllosilicates and the easily reducible Fe(III) (oxyhydr)oxides ferrihydrite and lepidocrocite are absent or only present in very small quantities. Since clay-sized phyllosilicates are hardly monomineralic, it needs to be considered that multiple Fe-phyllosilicate fractions are abundant in these samples. Current Mössbauer spectroscopy results do not allow a clear distinction between different clay fractions. However, the hyperfine parameters for most of the recorded spectra point towards kaolinite ($Al_4Si_4O_{10}[OH]_8$) to be a relatively abundant candidate which usually occurs with a minor substitution of Fe for Al (Murad, 1998). The appearance of kaolinite was also confirmed by XRD analyses (Kim et al., 2019).

The positive correlation between Al and Fe as well as Si and Fe in the hydroxylamine-HCl and NH_4 -oxalate fractions in combination with the Mössbauer spectroscopy data imply a partial dissolution of phyllosilicates and the remobilization of both the sheet layer matrix components (Al and Si) and substituted Fe atoms in the octahedral (Fe[II] and Fe[III]) and tetrahedral (Fe[III]) sites. Therefore, the high Fe_{hyam} contents at Site C0023 do not indicate the presence of Fe (oxyhydr)oxides such as ferrihydrite and lepidocrocite, but rather represent structural Fe(III) contained in phyllosilicates that survived complete reductive dissolution. Current studies indicate that structural Fe(III) in phyllosilicates can be reduced microbially (e.g., Kim et al., 2004; Vorhies and Gaines, 2009; Jung et al., 2019), although this Fe pool is thought to be reactive only on timescales of 10^2 – 10^5 of years (Canfield et al., 1992). More recently, Kim et al. (2019) showed that microbial reduction of structural Fe(III) in smectite promotes the smectite-to-illite transition at Site C0023 even at relatively low temperature and pressure conditions. Thus, the hydroxylamine-HCl-extracted Fe pool represents the part of phyllosilicate

Fe(III) that has been preserved during burial and can support microbial Fe reduction as suggested by Kim et al. (2019).

Magnetic techniques are great complements to geochemical analyses as they provide independent information on Fe mineralogy, which allows a better Fe speciation interpretation. Here, the combination of the sequential extraction of Fe (oxyhydr)oxides and sulfides with IRM acquisition curves improves the characterization of the Fe mineral assemblages at Site C0023. The coercivity unmixing shows that fine-grained magnetite (EM 2) is the main carrier of the magnetic signal between 600 and 900 mbsf (Figure 6b), coinciding with higher Fe_{di-ct} values (Figure 4c). Furthermore, this zone of elevated Fe_{di-ct} contents is also supported by higher magnetic susceptibility, suggesting that fine-grained magnetite is largely dissolved during the Na-dithionite step. These findings are in agreement with Henkel et al. (2016), Oonk et al. (2017) and Slotznick et al. (2020), who observed a grain-size dependent dissolution of magnetite of up to 75% during the Na-dithionite step after Poulton and Canfield (2005).

To conclude, while Fe_{hyam} and Fe_{oxa} extracted some of the Fe bound in phyllosilicates, Fe_{di-ct} extracted crystalline Fe (oxyhydr)oxides, mainly goethite, hematite and fine-grained magnetite. Our analyses demonstrate that Fe speciation on ancient sediments must be interpreted with caution. As already proposed by Slotznick et al. (2020) and Hepburn et al. (2020), the application of an independent technique such as rock magnetic analyses or Mössbauer spectroscopy on selected samples is very useful to validate chemical Fe extraction data. The Poulton and Canfield (2005) method was tested on modern fluvial and glacial sediments. Thus, if applying this methodology on ancient sediments, the protocol needs to be verified and modified to the specific set of samples prior to the analyses.

5.2 Evolution of biogeochemical and diagenetic processes at Site C0023

During its tectonically induced movement from the Shikoku Basin to the Nankai Trough (e.g., Mahony et al., 2011; Underwood and Guo, 2018; Figure 1), Site C0023 has experienced a transition from hemipelagic basin-style to trench-style deposition, accompanied by significant changes in thermal conditions and resulting (bio-)geochemical processes. Abyssal sediments are generally characterized by low sedimentation rates and organic carbon contents (< 1 wt%) that are insufficient to drive organoclastic Fe and sulfate reduction (e.g., Mewes et al., 2014; D'Hondt et al., 2015; Mogollón et al., 2016; Volz et al., 2018). Nonetheless, diagenetic mineral phases including pyrite (Figure 3d), accompanied by minima in magnetic susceptibility (Figure 5b) and Fe oxide contents (Figure 4c), are observed in the whole sediment column at Site C0023 (Figure 3d) - even in the lowermost carbon-starved unit. This suggests that redox and

sulfidization fronts have changed post-depositionally during the past 15 Ma. High methane concentrations in the Upper Shikoku Basin formation (Unit III) and concurrently low present-day potential methanogenesis rates (Heuer et al., 2020) further suggest that redox dynamics and related microbial activities were markedly different in the past. In the following, the succession of biogeochemical and diagenetic processes as derived from pore-water and solid-phase records that affected the sedimentary Fe pool at Site C0023 from deposition through progressing burial and diagenetic alteration to the present-day situation will be outlined.

5.2.1 Organic carbon-starved, low sedimentation environment

The deposition of the Lower Shikoku Basin formation (Unit IV) began in the middle Miocene (13.53 Ma), ~750 km away from its current location (Figure 1), and lasted until Pliocene times (2.53 Ma), whereby the prevailing sedimentation rates slightly increased from 3.5 to 6.0 cm kyr⁻¹ (Hagino and the Expedition 370 Scientists, 2018). The modern Pacific Ocean circulation established ~14 Ma (Kuhnt et al., 2004). The Shikoku Basin sedimentation is strongly affected by the Kuroshio Current (KC), which represents the western boundary current as part of the North Pacific subtropical gyre (e.g., Qui, 2001). The KC is characterized by nutrient-poor, oligotrophic conditions (e.g., Guo, 1991; Hirota, 1995), and thus, causes low primary productivity and particulate organic carbon (POC) fluxes in surface waters of the Shikoku Basin. Low TOC/N ratios (≤ 10) and $\delta^{13}\text{C}$ -TOC values between -23‰ and -22‰ in Unit IV (Figures S2a and S2b) point to organic matter of marine origin (e.g., Meyers, 1994). Alkenones, which are biomarkers for coccolithophores (haptophyte algae) are only present in low concentrations in the Lower Shikoku Basin formation above 860 mbsf when compared to the Upper Shikoku Basin formation, and long-chain diols, biomarkers for eustigmatophyte algae, are absent (Figures S2c and S2d). The $\delta^{13}\text{C}$ -TOC and TOC/N data in combination with low alkenone and diol concentrations are indicative of an oligotrophic setting. Notably, we cannot exclude that with the onset of catagenetic processes at $\sim 70^\circ\text{C}$ below 600 mbsf (Tsang et al., 2020), thermal degradation of organic matter may also lead to a decline in biomarker concentrations in Unit IV, however, we would expect this decline to be more gradual and not as abrupt as is observed within Unit III.

The combination of relatively low sedimentation rates with low POC fluxes conceivably led to low carbon burial rates and accordingly low TOC contents during the deposition of Unit IV (~ 0.25 wt%, Figure 5a). Therefore, a carbon-starved, low sedimentation depositional environment characterizes the sediments from late Miocene to Pliocene times. In these organic carbon-lean abyssal ocean type sediments, organic matter mineralization is typically dominated

by aerobic respiration and nitrate reduction leading to a high TOC degradation efficiency (e.g., Froelich et al., 1979; Emerson et al., 1980; Mogollón et al., 2016; Volz et al., 2018). The very low preserved TOC contents of ~0.25 wt% were insufficient to drive organoclastic Fe and sulfate reduction (e.g., Riedinger et al., 2014). Hence, between 15 and 2.5 Ma, pore-water sulfate was likely not depleted and could penetrate deep into the sediments of Unit IV at Site C0023 and buried Fe (oxyhydr)oxides were not affected by reductive dissolution (Figure 8a).

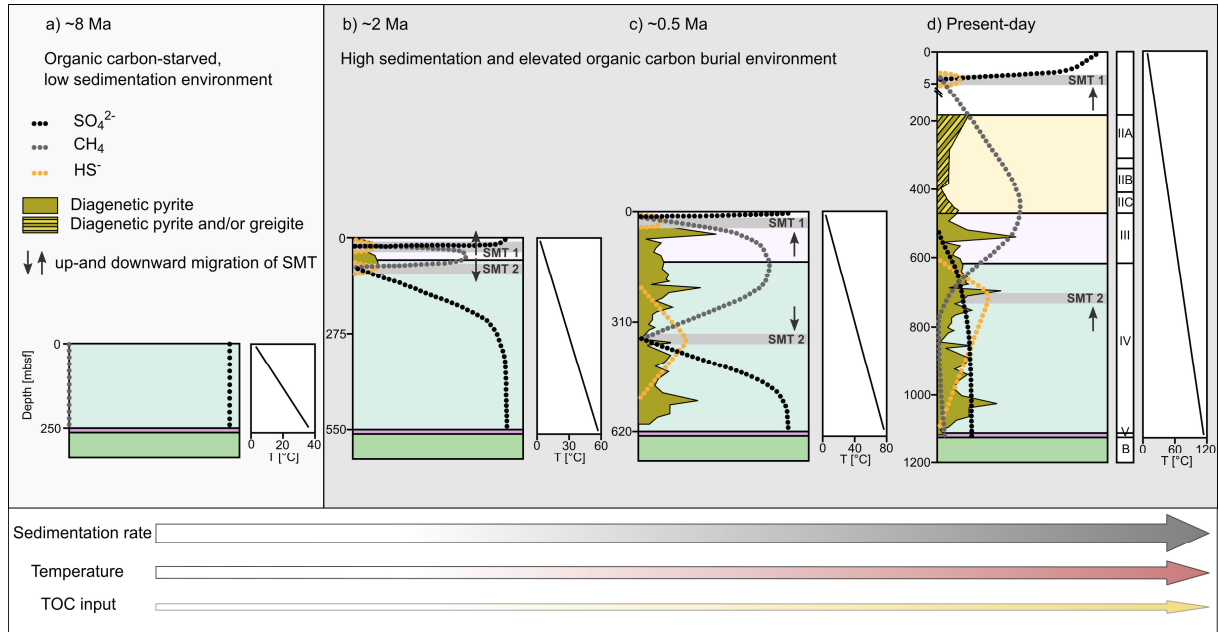


Figure 8. Conceptual model showing the evolution of biogeochemical and diagenetic processes at Site C0023 during its tectonic migration over the past 15 Ma. The main driving force for changes in the (bio-)geochemical processes is the significant increase in sedimentation rate which in turn also affects the temperature within the sediment column and the total organic carbon burial. The more intense color shading of each arrow indicates the increase of the respective driving force. These changes in depositional, thermal, and geochemical conditions led to a transition from (a) an organic carbon-starved sedimentary environment with comparably low accumulation rates to (b) an environment with elevated sedimentation and carbon burial rates. Increasing sedimentation and organic carbon burial rates since ~2.5 Ma likely caused the onset of methanogenesis and anaerobic oxidation of methane (AOM) and the formation of a shallow and a lower sulfate-methane transition (SMT) (SMT 1 and SMT 2, respectively). HS^- produced by AOM reacted with solid-phase and dissolved Fe to form pyrite. (c) The arrival of Site C0023 at the Nankai Trough at ~0.5 Ma, accompanied by a significant increase in sediment temperature could have resulted in enhanced methanogenesis, likely due to increased bioavailability of organic matter and the up- and downward migration of the SMTs and sulfidization fronts. (d) Present-day situation with the shallow SMT 1 at ~4 mbsf (assumed from ODP Site 1174; Shipboard Science Party, 2001) and the lower SMT 2 at ~730 mbsf. Extremely high sedimentation rates since 0.43 Ma prevented a complete pyritization and the preservation of greigite.

Due to high heat flow prevailing in the studied area (Harris et al., 2013), the temperature at the sediment-basement interface was ~40°C during the deposition of the Lower Shikoku Basin

formation. The sediment temperature steadily increased with ongoing burial (Horsfield et al., 2006; Tsang et al., 2020). As Site C0023 continuously moved in northwesterly direction towards the Japanese Island arc, the lithology changed from Lower to Upper Shikoku Basin formation at ~ 2.5 Ma, accompanied by an increase in sedimentation rate to 9.3 cm kyr^{-1} (Hagino and the Expedition 370 Scientists, 2018). TOC contents in the latter unit (Unit III) show an increasing trend compared to Unit IV (Figure 5a), which could be caused by an overall increase in primary productivity during the late Pliocene-early Pleistocene transition or a better preservation due to higher sedimentation rates (e.g., Swann et al., 2006; Zonneveld et al., 2010; Lawrence et al., 2013). Berner and Koch (1993) and Shipboard Science Party (2001) further pointed out that a steady increase in the amount of organic carbon in the transition from the Lower to the Upper Shikoku Basin formation at the adjacent Sites 808 and 1174 of Ocean Drilling Program (ODP) Legs 131 and 190, respectively, may be related to higher nutrient supply caused by the proximity to the coast of Japan. In addition, an intensification of the KC that has occurred in response to the closure of the Central America Seaway at ~ 3 Ma (e.g., Molina-Cruz, 1997; Tsuchi, 1997) could have increased the nutrient supply from the Japanese Island arc (Underwood and Steurer, 2003). The $\delta^{13}\text{C}$ -TOC and algal biomarker data support elevated marine productivity during the deposition of the Upper Shikoku Basin formation. The increase in TOC contents is accompanied by a shift of $\delta^{13}\text{C}$ -TOC towards more positive values in Unit III (Figure S2b). Periods of high primary productivity typically lead to an increased uptake of ^{12}C , whereby the residual inorganic carbon becomes increasingly enriched in ^{13}C , ultimately resulting in more positive $\delta^{13}\text{C}$ values of the preserved sedimentary organic matter (e.g., Mizutani and Wada, 1982; Meyers, 1997). At the same time, alkenone and long-chain diol concentrations significantly increase in Unit III (Figures S2c and S2d), which is consistent with an increased productivity and thus, elevated POC fluxes. We suggest that the concurrent increase in sedimentation and TOC burial rates at ~ 2.5 Ma has caused a transition from an organic carbon-starved sedimentary system with comparable low accumulation rates (3.5 cm kyr^{-1}) to an environment with elevated sedimentation (9.3 cm kyr^{-1}) and carbon burial rates at the Pliocene-Pleistocene boundary.

5.2.2 Elevated organic carbon burial, high sedimentation environment

Higher carbon burial rates since the early Pleistocene could have stimulated the establishment of anoxic sediment conditions, and thus, triggered the onset of organoclastic Fe and sulfate reduction and biogenic methane formation in the deposits of Unit III (Figure 8b). Once produced in Unit III, methane was subsequently oxidized by sulfate present in the pore water

during the anaerobic oxidation of methane (AOM). As methane further diffused up- and downwards, both a shallow and a deep or inverse sulfate-methane transition (SMT) were formed: (1) the shallow SMT must have formed within Unit III where upward diffusing methane reacts with sulfate diffusing downwards from the overlying seawater. (2) The reaction of downward diffusing methane with residual, upward diffusing sulfate in Unit IV resulted in the establishment of the lower inverse SMT. AOM releases hydrogen sulfide and bicarbonate into the pore water (e.g., Barnes and Goldberg, 1976; Borowski et al., 1996; Niewöhner et al., 1998), which also diffuse up- and downwards. At the SMTs, hydrogen sulfide reacted either with preserved Fe (oxyhydr)oxides or with Fe^{2+} in the upper part of Unit III, where TOC contents were high enough to drive organoclastic Fe reduction, to form pyrite (e.g., Berner, 1970).

Site C0023 reached the Nankai Trough ~0.5 Ma ago (Figure 1). The resulting transition from a hemipelagic basin-style to a trench-style deposition led to a pronounced increase in sedimentation rates of one order of magnitude (Figure 5d), accompanied by a temperature increase of about 50°C across the sediment column (Horsfield et al., 2006; Tsang et al., 2020). Several studies on deep seafloor sediments show that organic matter that is highly refractory at seafloor temperature (~2–3°C) becomes accessible for microbial processes with increasing burial and related heating of the sediments (Wellsbury et al., 1997; Parkes et al., 2007; Burdige, 2011). Riedinger et al. (2015) suggested that frictional heating associated with earthquakes might reactivate recalcitrant organic matter in deep sediments from IODP Sites C0006 and C0008 in the Nankai Trough, resulting in the onset of methanogenesis several hundred meters below the seafloor. Although, we cannot provide evidence on the reactivity of the organic material, we hypothesize that the higher temperatures prevailing since ~0.5 Ma increased the bioavailability of organic matter at Site C0023, which caused enhanced rates of biogenic methanogenesis and higher methane fluxes in both, up- and downward directions. The assumption that the increased methane concentrations in Unit III are related to enhanced microbially mediated methanogenesis and not to thermogenic methane production is further supported by the stable carbon isotopic composition of methane ($\delta^{13}\text{C-CH}_4$). The $\delta^{13}\text{C-CH}_4$ values in the methane-rich zone between 200 and 600 mbsf varies between –60‰ and –65‰ (Figure S2f), which is indicative of a biogenic methane source (Heuer et al., 2020). Furthermore, as evidenced by increasing $\delta^{13}\text{C-CH}_4$ values and concurrently decreasing methane/ethane ratios ($\text{C}_1/\text{C}_2 < 10^3$; Figure S2e), thermogenic methane produced by thermal degradation of the organic matter provides an additional source of methane from below (Heuer et al., 2017a, 2020). These increased methane fluxes, in turn, could cause an up- and downward

migration of the shallow and inverse SMT, respectively, and simultaneously slow prograding shifts of the sulfidization fronts (Figure 8c). In this way, the lower sulfidization front could shift into the Lower Shikoku Basin formation, leading to an alteration of the preserved sedimentary Fe pool and the formation of diagenetic pyrite several millions of years after initial deposition. This proposed scenario is confirmed by the magnetic and sequential extraction data: while Fe_{di-ct} contents (Figure 4c) and magnetic susceptibility (Figure 5b) values show minima in the lower parts of Unit IV, CRS contents are enriched (Figure 3d), indicating that ferrimagnetic Fe oxides such as hematite and magnetite are converted into paramagnetic pyrite. Concurrently, high Fe_{total}/χ_{lf} ratios indicate intense reductive magnetite dissolution (Funk et al., 2004; Korff et al., 2016; Figure 5c). Furthermore, all three samples analyzed by Mössbauer spectroscopy show relative abundances for Fe(II) over Fe(III) and thus, relatively high Fe(II)/Fe(III) ratios (Table S4). This suggests that the phyllosilicates at Site C0023 have experienced microbial or abiotic reduction (Stucki et al., 1996) which led to the reduction of Fe(III) and the formation of Fe(II) in the sheet layers as reported for Fe-rich phyllosilicates in marine sediments from the continental shelf off the Antarctic Peninsula (Jung et al., 2019). High Fe(II)/Fe(III) ratios even in the deeper samples from Unit IV are in agreement with the described shift of redox fronts. The results of coercivity unmixing (Figures 6 and S3) indicate the occurrence of greigite down to ~460 mbsf. Greigite ($Fe^{2+}Fe^{3+}_2S_4$) is a meta-stable ferrimagnetic Fe sulfide that forms as a precursor of pyrite (e.g., Sweeney and Kaplan, 1973; Berner, 1984; Wilkin and Barnes, 1996; Kasten et al., 1998; Jørgensen et al., 2004; Fu et al., 2008). The occurrence of greigite correlates with the significant increase in sedimentation rates since 0.29 Ma (Figure 5d; Hagino and the Expedition 370 Scientists, 2018). A complete pyritization might have been prevented by decreasing the time the respective interval was located in the sulfidic zone, and thus, greigite is preserved in Subunits IIA and IIB (e.g., Kasten et al., 1998; Jørgensen et al., 2004; Riedinger et al., 2005; Fu et al., 2008). Authigenic growth of ferrimagnetic greigite has important implications for paleomagnetic recording (e.g., Roberts, 2015) as its formation leads to a secondary increase in the magnetic signal. Therefore, high χ_{lf} values in Subunit IIA (Figure 5b) are probably caused by the preservation of greigite.

In the present-day situation, the interval between 600 and 700 mbsf - located above the lower SMT - is both sulfide- and Fe^{2+} -free, suggesting that upward diffusing hydrogen sulfide currently reacts with downward diffusing Fe^{2+} to form Fe sulfides (Figures 2b and 2c). Downward diffusing sulfide from the lower SMT might still react with residual Fe oxides and/or phyllosilicate-bound Fe(III) in the lower parts of Unit IV to form pyrite (Figure 8d). Shallow sediments (< 189 mbsf) were not recovered during IODP Expedition 370. However, based on

sulfate and methane data from the adjacent ODP Leg 190 Site 1174 (Shipboard Science Party, 2001), the present-day shallow SMT is assumed to be located between 3 and 4.5 mbsf. Cell concentrations at Site C0023 are two to four orders of magnitude lower compared to other continental margin subseafloor sediments, leading to methanogenesis rates below the typical range in marine sediments (Heuer et al., 2020), and hence, generally low DIC concentrations (Figure 2d). Due to the decreased methane flux, the lower inverse SMT migrated upwards to its current position at ~730 mbsf. At the same time, high temperature prevailing at and below the inverse SMT likely exert an important control on the expansion of the AOM zone, and thus, the location of the SMT. The current depth of the lower inverse SMT corresponds to a temperature of ~80–85°C. A sharp increase towards higher $\delta^{13}\text{C}\text{-CH}_4$ values (up to -54‰) at this depth (Figure S2f) indicates a biogenic methane sink and the activity of AOM-performing communities (Heuer et al., 2020). This temperature range overlaps with the known maximum growth temperature of ~70°C for methane-oxidizing communities based on *in vitro* incubation experiments and AOM activity at *in situ* temperatures up to 90°C in hydrothermally influenced sediments from the Guaymas Basin, Gulf of California (Holler et al., 2011; Biddle et al., 2012). Therefore, microbial AOM potentially only barely occurs at present, which results in the observed broad overlap of methane and sulfate and the presence of methane down to the basement (Figure 2a).

5.3 Implications for the interpretation of deep subseafloor pore-water and sedimentary records

The described succession of the biogeochemical and diagenetic processes has been summarized in a conceptual geochemical process model (Figure 8). The main driving forces for the evolution of the (bio-)geochemical processes at Site C0023 are the sedimentation rate, the temperature within the sediment, and the TOC input. During the migration from the Shikoku Basin towards the Nankai Trough, the sediments at Site C0023 have experienced a significant increase in sedimentation rates from 3.5 cm kyr^{-1} in the lower parts of Unit IV to 131.9 cm kyr^{-1} in Unit IIB (Table 1; Hagino and the Expedition 370 Scientists, 2018). The sedimentation rate is strongly interrelated with the sedimentary temperature and the TOC burial. Since the temperature within the sediment column at Site C0023 is a function of heat flow, thermal conductivity, and the sediment depth below seafloor (Heuer et al., 2020), it rose with ongoing burial. Similarly, the TOC contents increased when Site C0023 moved towards Japan. These changes in depositional, thermal, and geochemical conditions resulted in a transition from oxic (Figure 8a) to anoxic conditions within the sediments and the onset of anaerobic

terminal electron-accepting processes (Figure 8b). Higher methane fluxes at ~0.5 Ma caused an up- and downward migration of the SMTs and sulfidization fronts, and thus, promoted the transformation of Fe (oxyhydr)oxides into pyrite in the underlying Lower Shikoku Basin formation several millions of years after the initial sediment deposition (Figure 8c). We do not imply that the up- and downward migration of the lower SMT in Unit IV (Figures 8c and 8d) was due to a migration of the microbial community performing AOM through 150–200 mbsf of consolidated sediment, but we rather assume a long-term survival of microbes (e.g., Inagaki et al., 2015). Comparable observations were made by Arndt et al. (2006), who showed that organic-rich layers in seafloor sediments at Demerara Rise in the equatorial Atlantic (ODP Leg 207, Site 1258) still provide a suitable substrate for ongoing methane formation in the deep biosphere almost 100 Ma after their deposition, thereby controlling the element fluxes and biogeochemical processes within the whole overlying sediment column. Similarly, the primary sediment composition in the Lower Shikoku Basin formation at Site C0023 is significantly overprinted by the onset of methanogenesis and AOM in the overlying Upper Shikoku Basin formation.

Over a long period (15–2.5 Ma), the pore-water sulfate concentrations in the Lower Shikoku Basin formation were comparable with seawater values (~28 mM) due to the absence of organoclastic sulfate reduction during deposition. The lower inverse SMT could have been formed only due to the availability of this sulfate pool preserved at greater depth. The sulfate concentrations continuously decreased since the onset of AOM at ~2.5 Ma. At present, the deep residual sulfate pool is almost exhausted by AOM (< 7 mM; Figure 2a). This finding indicates that the present-day sulfate profile is strongly influenced by (bio-)geochemical processes occurring in the overlying sediments. Thus, in order to avoid a misinterpretation of the origin of the low sulfate in the Lower Shikoku Basin formation, it is crucial to consider the (bio-)geochemical history of Site C0023. A similar consideration applies for methane. Highest methane concentrations are observed in an interval, where cells were not detectable (Heuer et al., 2020). At the same time, present-day methanogenesis rates are low, suggesting that microbial activities and (bio-)geochemical processes were significantly different in the past. Therefore, our study demonstrates that the pore-water patterns we observe today are strongly correlated with the succession and past evolution of the (bio-)geochemical processes at Site C0023. Elevated sulfate concentrations at greater depth and a lower inverse SMT were also observed at IODP Site C0012 (Torres et al., 2015), which is located on the Kashinosaki Knoll - an isolated seamount of volcanic origin on the subducting Philippine Sea plate - in the Kumano Transect (Ike et al., 2008). However, due to its location on a basement high and a significant

reduced sediment thickness, the depositional and geochemical conditions are different compared to Site C0023. Chloride concentrations at Site C0012 significantly increase above a typical seawater value of 558 mM below 300 mbsf until the sediment-basement interface. Thus, the observed increase in sulfate concentrations with depth at Site C0012 is likely not related to a relict sulfate pool but attributed to a diffusional sulfate supply from the basement aquifer (Underwood et al., 2010; Torres et al., 2015). This comparison demonstrates that the sedimentary packages in the Nankai-Shikoku-subduction system are exposed to different geochemical controls even on comparably small-scale spatial distances. Nonetheless, following our conceptual model (Figure 8), a relict sulfate pool should be considered when interpreting sulfate concentrations in subseafloor sediments from the Nankai Trough and the incoming Shikoku Basin.

6. Conclusions

We studied deep subseafloor sediments from Site C0023 offshore Japan in the Nankai Trough, northwest Pacific Ocean drilled during IODP Expedition 370. During its tectonic migration from the Shikoku Basin to the Nankai Trough, Site C0023 has experienced significant changes in depositional and thermal conditions as well as resulting biogeochemical processes over the past 15 Ma. By combining a large set of complementary pore-water, solid-phase, and rock magnetic data with sedimentation rates and sediment ages, we derived a conceptual geochemical process model that shows the potential succession of biogeochemical processes, element fluxes, and the associated diagenetic overprint of the primary sediment composition. In summary, the changes in depositional and thermal conditions led to a transition from an organic carbon-starved environment characterized by aerobic respiration and a deep sulfate penetration to elevated carbon burial and the onset of organoclastic Fe and sulfate reduction, biogenic methanogenesis, and AOM at ~2.5 Ma. Increased biogenic methane production presumably caused by a pronounced temperature increase at ~0.5 Ma likely resulted in higher methane fluxes and an up-and downward migration of the SMTs and the sulfidization fronts. Due to the downward migration of the sulfidization front into the lower organic carbon-starved sediments, the preserved Fe (oxyhydr)oxides were diagenetically transformed into pyrite several millions of years after initial deposition of these sediments.

While the combination of chemical and rock magnetic Fe speciation methods with ^{57}Fe Mössbauer spectroscopy analysis generally allows a better quantification and characterization of the reactive Fe pool at Site C0023, our analyses also demonstrate that Fe speciation data need to be interpreted with caution if applying chemical sequential Fe extraction on ancient

sediments such as in this study. Thus, we recommend a crosscheck with Al and Si or, even better, the application of a secondary independent Fe speciation technique on a selection of samples. Our results indicate that high amounts of reducible Fe(III) are present in phyllosilicates and can potentially serve as electron acceptor for microbial Fe reduction in the deep seafloor sediments at Site C0023.

Our study emphasizes that depositional and thermal changes ultimately driven by the tectonically induced migration have the potential to strongly influence (bio-)geochemical processes and element fluxes within the whole sediment column. Thus, to ensure a proper use and interpretation of sedimentary records it is crucial to consider the geological background and the (bio-)geochemical history of deep seafloor sediments. Such studies are indispensable to gain a fundamental understanding of the coupling between depositional history, biogeochemical processes and the resulting diagenetic overprint on geological timescale, thereby linking the sedimentary Fe, S, and C cycles.

Conflict of interest

The authors declare no conflicts of interest relevant to this study.

Data availability statement

Additional data and figures relevant for this study are provided in the Supporting Information or archived in the World Data Center PANGAEA via <https://doi.org/10.1594/PANGAEA.930858> (solid-phase geochemistry; Köster et al., 2021a), <https://doi.org/10.1594/PANGAEA.929317> (rock magnetic end-member unmixing; Köster et al., 2021b) and <https://doi.pangaea.de/10.1594/PANGAEA.929380> (magnetic susceptibility; Kars and Köster, 2021).

Acknowledgments

This research used samples and data provided by the International Ocean Discovery Program (IODP). The authors would like to thank all personnel involved in the operations aboard the *D/V Chikyu* during Expedition 370, especially Arthur Spivack, Justine Sauvage, Kira Homola, and Yusuke Kubo, as well as the support team at Kochi Core Center. For analytical support in the home laboratory, the authors thank Johann Hollop, Ingrid Stimac, Ingrid Dohrmann, Jenny Wendt, Lea Schabernack, and Oliver Helten. The authors are grateful to Kyoko Hagino for providing sediment ages and sedimentation rates, which were highly beneficial for this study. This work benefited from discussions with Arthur Spivack (University of Rhode Island) and

Wolfgang Bach (MARUM, University of Bremen). Finally, the authors thank Nicolas Tribouvillard and one anonymous reviewer for their helpful and constructive comments which have significantly improved this manuscript. This study is funded by the German Research Foundation (DFG) in the framework of the priority program 527 (Bereich Infrastruktur—International Ocean Discovery Program; project 388260220). The authors are grateful to the Japan Society for the Promotion of Science (JSPS) and the European Consortium for Ocean Research Drilling (ECORD) for funding Male Köster's research stay at Kochi Core Center in the framework of the JSPS Summer Program 2019 as well as Man-Yin Tsang's research stay at the Alfred Wegener Institute in September 2017, respectively. The authors acknowledge further financial support from the Helmholtz Association (Alfred Wegener Institute Helmholtz Centre for Polar and Marine Research). Myriam Kars's study was supported by the JSPS Grant-in-Aid for Scientific Research (grant 17K05681). Florence Schubotz acknowledges funding by the DFG (project 408178672). Verena B. Heuer further acknowledges support through the DFG (project 387745511) and the Cluster of Excellence “The Ocean Floor—Earth's Uncharted Interface” (project 390741603). Yuki Morono acknowledges funding by the JSPS (19H00730). Additional support enabling this project was provided by the Deep Carbon Observatory. Open access funding enabled and organized by Projekt DEAL.

References

- Abrajevitch, A., Van der Voo, R., and Rea, D.K., 2009. Variations in relative abundances of goethite and hematite in Bengal Fan sediments: Climatic vs. diagenetic signals. *Marine Geology*, **267**, 191-206. doi:10.1016/j.margeo.2009.10.010.
- Abrajevitch, A., and Kodama, K., 2011. Diagenetic sensitivity of paleoenvironmental proxies: A rock magnetic study of Australian continental margin sediments. *Geochemistry, Geophysics, Geosystems*, **12**. doi:10.1029/2010GC003481.
- Arndt, S., Brumsack, H.-J., and Wirtz, K.W., 2006. Cretaceous black shales as active bioreactors: A biogeochemical model for the deep biosphere encountered during ODP Leg 2007 (Demerara Rise). *Geochimica et Cosmochimica Acta*, **70**, 408-425. doi:10.1016/j.gca.2005.09.010.
- Barnes, R.O., and Goldberg, D.E., 1976. Methane production and consumption in anoxic marine sediments. *Geology*, **4**, 297-300. doi:10.1130/0091-7613(1976)4%3C297:MPACIA%3E2.0.CO;2.
- Becker, K.W., Lipp, J.S., Versteegh, G.M., Wörmer, L., and Hinrichs, K.-U., 2015. Rapid and simultaneous analysis of three molecular sea surface temperature proxies and application to sediments from the Sea of Marmara. *Organic Geochemistry*, **85**, 42-53. doi:10.1016/j.orggeochem.2015.04.008.
- Berner, R.A., 1970. Sedimentary pyrite formation. *American Journal of Science*, **268**, 1-23. doi:10.2475/ajs.268.1.1.

- Berner, R.A., 1981. A new geochemical classification of sedimentary environments. *Journal of Sedimentary Research*, **51**, 359-365. doi:10.1306/212F7C7F-2B24-11D7-8648000102C1865D.
- Berner, R.A., 1984. Sedimentary pyrite formation: An update. *Geochimica et Cosmochimica Acta*, **48**, 605-615. doi:10.1016/0016-7037(84)90089-9.
- Berner, U., and Koch, J., 1993. Organic matter in sediments of Site 808, Nankai accretionary prism, Japan. In: *Proceedings of the Ocean Drilling Program, Initial Reports, 131* (eds. Hill, I.A., Taira, A., Firth, J.V., et al.). College Station, TX (Ocean Drilling Program), 379-385. doi:10.2973/odp.proc.sr.131.132.1993.
- Biddle, F.F., Cardman, Z., Mendlovitz, H., Albert, D.B., Lloydm K.G., Boetius, A., and Teske, A., 2012. Anaerobic oxidation of methane at different temperature regimes in Guaymas Basin hydrothermal sediments. *The ISME Journal*, **6**, 1018-1031. doi:10.1038/ismej.2011.164.
- Boetius, A., Ravensschlag, K., Schubert, C.J., Rickert, D., Widdel, F., Gieseke, A., et al., 2000. A marine microbial consortium apparently mediating anaerobic oxidation of methane. *Nature*, **407**, 623-626. doi:10.1038/35036572.
- Borowski, W.S., Paull, C.K., and Ussler III, W., 1996. Marine pore-water sulfate profiles indicate in situ methane flux from underlying gas hydrate. *Geology*, **24**, 655-658. doi:10.1130/0091-7613(1996)024%3C0655:MPWSPI%3E2.3.CO;2.
- Bowles, M.W., Mogollón, J.M., Kasten, S., Zabel, M., and Hinrichs, K.-U., 2014. Global rates of marine sulfate reduction and implications for sub-seafloor metabolic activities. *Science*, **344**, 889-891. doi:10.1126/science.1249213.
- Brassell, S., Eglinton, G., Marlowe, I.T., Pflaumann, U., and Sarnthein, M., 1986. Molecular stratigraphy: a new tool for climatic assessment. *Nature*, **320**, 129-133. doi:10.1038/320129a0.
- Burdige, D.J., 2011. Temperature dependence of organic matter remineralization in deeply-buried marine sediments. *Earth and Planetary Science Letters*, **311**, 396-410. doi:10.1016/j.epsl.2011.09.043.
- Canfield, D.E., Raiswell, R., Westrich, J.T., Reaves, C.M., and Berner, R.A., 1986. The use of chromium reduction in the analysis of reduced inorganic sulfur in sediments and shales. *Chemical Geology*, **54**, 149-155. doi:10.1016/0009-2541(86)90078-1.
- Canfield, D.E., Raiswell, R., and Bottrell, S.H., 1992. The reactivity of sedimentary iron minerals toward sulfide. *American Journal of Science*, **292**, 659-683. doi:10.2475/ajs.292.9.659.
- Canfield, D.E., Thamdrup, B., and Hansen, J.W., 1993. The anaerobic degradation of organic matter in Danish coastal sediments: Iron reduction, manganese reduction and sulfate reduction. *Geochimica et Cosmochimica Acta*, **57**, 3867-3883. doi:10.1016/0016-7037(93)90340-3.
- Chamot-Rooke, N., Renard, V., and Le Pichon, X., 1987. Magnetic anomalies in the Shikoku Basin: a new interpretation. *Earth and Planetary Science Letters*, **83**, 214-228. doi:10.1016/0012-821X(87)90067-7.
- Cline, J.D., 1969. Spectrophotometric determination of hydrogen sulfide in natural waters. *Limnology and Oceanography*, **14**, 454-458.
- Cornell, R.M., and Schwertmann, U., 2003. Transformations. In: *The iron oxides: Structure, properties, reactions, occurrences and uses* (eds. Cornell, R.M., and Schwertmann, U.).

- Weinheim: Wiley-VCH Verlag GmbH & Co. KGaA, 365-407. doi:10.1002/3527602097.ch14.
- Cornwell, J.C., and Morse, J.W., 1987. The characterization of iron sulfide minerals in anoxic marine sediments. *Marine Chemistry*, **22**, 193-206. doi:10.1016/0304-4203(87)90008-9.
- Costa Pisani, P., Reshef, M., and Moore, G., 2005. Targeted 3-D prestack depth imaging at Legs 190-196 ODP drill sites (Nankai Trough, Japan). *Geophysical Research Letters*, **32**, L20309. doi:10.1029/2005GL024191.
- DeMets, C., Gordon, R.G., and Argus, D.F., 2010. Geologically current plate motions. *Geophysical Journal International*, **181**, 1-80. doi:10.1111/j.1365-246X.2009.04491.x.
- D'Hondt, S., Rutherford, S., and Spivack, A.J., 2002. Metabolic activity of subsurface life in deep-sea sediments. *Science*, **295**, 2067-2070. doi:10.1126/science.1064878.
- D'Hondt, S., Inagaki, F., Zarikian, C.A., Abrams, L.J., Dubois, N., Engelhardt, T., et al., 2015. Presence of oxygen and anaerobic communities from sea floor to basement in deep-sea sediments. *Nature Geoscience*, **8**, 299-304. doi:10.1038/ngeo2387.
- Dymond, J., Suess, E., and Lyle, M., 1992. Barium in deep-sea sediment: A geochemical proxy for paleoproductivity. *Paleoceanography*, **7**, 163-181. doi:10.1029/92PA00181.
- Emerson, S., Jahnke, R., Bender, M., Froelich, P., Klinkhammer, G., Bowser, C., and Setlock, G., 1980. Early diagenesis in sediments from the eastern equatorial Pacific, I. Pore water nutrient and carbonate results. *Earth and Planetary Science Letters*, **49**, 57-80. doi:10.1016/0012-821X(80)90150-8.
- Fischer, D., Mogollón, J.M., Strasser, M., Pape, T., Bohrmann, G., Fekete, N., et al., 2013. Subduction zone earthquake as potential trigger of submarine hydrocarbon seepage. *Nature Geoscience*, **6**, 647-651. doi:10.1038/ngeo1886.
- Froelich, P.N., Klinkhammer, G.P., Bender, M.L., Luedtke, N.A., Heath, G.R., Cullen, D., et al., 1979. Early oxidation of organic matter in pelagic sediments of the eastern equatorial Atlantic: suboxic diagenesis. *Geochimica et Cosmochimica Acta*, **43**, 1075-1090. doi:10.1016/0016-7037(79)90095-4.
- Fu, Y., von Döbenek, T., Franke, C., Heslop, D., and Kasten, S., 2008. Rock magnetic identification and geochemical process models of greigite formation in Quaternary marine sediments from the Gulf of Mexico (IODP Hole U1319A). *Earth and Planetary Science Letters*, **275**, 233-245. doi:10.1016/j.epsl.2008.07.034.
- Funk, J.A., von Döbenek, T., and Reitz, A., 2004. Integrated rock magnetic and geochemical quantification of redoxomorphic iron mineral diagenesis in Late Quaternary sediments from the Equatorial Atlantic. In: *The South Atlantic in the Late Quaternary* (eds. Wefer, G., Mulitza, S., and Ratmeyer, V.). Berlin, Heidelberg: Springer, 61-101. doi:10.1007/978-3-642-18917-3_12.
- Goldhaber, M.B., and Kaplan, I.R., 1974. The sulfur cycle. In: *The Sea (Volume 5)* (ed. Goldberg, E.D.). New York: Wiley-Interscience, 569-655.
- Guo, Y.J., 1991. The Kuroshio, Part II. Primary production and phytoplankton. *Oceanography and Marine Biology*, **29**, 155-189.
- Hagino, K., and the Expedition 370 Scientists, 2018. Data report: calcareous nannofossils from the middle Miocene to Pleistocene, IODP Expedition 370 Site C0023. In: *Proceedings of the International Ocean Discovery Program Volume 370* (eds. Heuer, V.B., Inagaki, F., Morono, Y., Kubo, Y., Maeda, L., and the Expedition 370 Scientists). College Station, TX (International Ocean Discovery Program). doi:10.14379/iodp.proc.370.201.2018.

- Harris, R., Yamano, M., Kinoshita, M., Spinelli, G., Hamamoto, H., and Ashi, J., 2013. A synthesis of heat flow determinations and thermal modeling along the Nankai Trough, Japan. *Journal of Geophysical Research: Solid Earth*, **118**, 2687-2702. doi:10.1002/jgrb.50230.
- Henkel, S., Mogollón, J.M., Nöthen, K., Franke, C., Bogus, K., Robin, E., et al., 2012. Diagenetic barium cycling in Black Sea sediments – A case study for anoxic marine environments. *Geochimica et Cosmochimica Acta*, **88**, 88-105. doi:10.1016/j.gca.2012.04.021.
- Henkel, S., Kasten, S., Poulton, S.W., and Staubwasser, M., 2016. Determination of the stable iron isotopic composition of sequentially leached iron phases in marine sediments. *Chemical Geology*, **421**, 93-102. doi:10.1016/j.chemgeo.2015.12.003.
- Henkel, S., Kasten, S., Hartmann, J.F., Silva-Busso, A., and Staubwasser, M., 2018. Iron cycling and stable Fe isotope fractionation in Antarctic shelf sediments, King George Island. *Geochimica et Cosmochimica Acta*, **237**, 320-338. doi:10.1016/j.gca.2018.06.042.
- Hensen, C., Zabel, M., Pfeifer, K., Schwenk, T., Kasten, S., Riedinger, N., Schulz, H.D., and Boetius, A., 2003. Control of sulfate pore-water profiles by sedimentary events and the significance of anaerobic oxidation of methane for the burial of sulfur in marine sediments. *Geochimica et Cosmochimica Acta*, **67**, 2631-2647. doi:10.1016/S0016-7037(03)00199-6.
- Hepburn, L.E., Butler, I.B., Boyce, A., and Schröder, C., 2020. The use of operationally-defined sequential Fe extraction methods for mineralogical applications: A cautionary tale from Mössbauer spectroscopy. *Chemical Geology*, **543**, 119584. doi:10.1016/j.chemgeo.2020.119584.
- Heron, G., Crouzet, C., Bourg, A.C., and Christensen, T.H., 1994. Speciation of Fe (II) and Fe (III) in contaminated aquifer sediments using chemical extraction techniques. *Environmental Science & Technology*, **28**, 1698-1705.
- Heslop, D., Dekkers, M.J., Kruiver, P.P., and van Oorschot, I.H.M., 2002. Analysis of isothermal remanent magnetization acquisition curves using expectation-maximization algorithm. *Geophysical Journal International*, **148**, 58-64. doi:10.1046/j.0956-540x.2001.01558.x.
- Heuer, V.B., Inagaki, F., Morono, Y., Kubo, Y., Maeda, L., and the Expedition 370 Scientists, 2017a. Temperature limit of the deep biosphere off Muroto. *Proceedings of the International Ocean Discovery Program Volume 370*: College Station, TX (International Ocean Discovery Program). doi:10.14379/iodp.proc.370.2017.
- Heuer, V.B., Inagaki, F., Morono, Y., Kubo, Y., Maeda, L., and the Expedition 370 Scientists, 2017b. Site C0023. In: *Proceedings of the International Ocean Discovery Program Volume 370* (eds. Heuer, V.B., Inagaki, F., Morono, Y., Kubo, Y., Maeda, L., and the Expedition 370 Scientists). College Station, TX (International Ocean Discovery Program). doi:10.14379/iodp.proc.370.103.2017.
- Heuer, V.B., Inagaki, F., Morono, Y., Kubo, Y., Spivack, A., Viehweger, B., et al., 2020. Temperature limits to deep seafloor life in the Nankai Trough subduction zone. *Science*, **370**, 1230-1234. doi:10.1126/science.abd7934.
- Hirota, Y., 1995. The Kuroshio, Part III. Zooplankton. *Oceanography and Marine Biology*, **33**, 151-220.

- Holler, T., Widdel, F., Knittel, K., Amann, R., Kellermann, M.Y., Hinrichs, K.-U., et al., 2011. Thermophilic anaerobic oxidation of methane by marine microbial consortia. *The ISME Journal*, **5**, 1946-1956. doi:10.1038/ismej.2011.77.
- Horsfield, B., Schenk, H.J., Zink, K., Ondrak, R., Dieckmann, V., Kallmeyer, J., et al., 2006. Living microbial ecosystems within the active zone of catagenesis: implications for feeding the deep biosphere. *Earth and Planetary Science Letters*, **246**, 55-69. doi:10.1016/j.epsl.2006.03.040.
- Ijiri, A., Inagaki, F., Kubo, Y., Adhikari, R.R., Hattori, S., Hoshino, T., et al., 2018. Deep-biosphere methane production stimulated by geofluids in the Nankai accretionary complex. *Science Advances*, **4**, eaao4631. doi:10.1126/sciadv.aao4631.
- Ike, T., Moore, G.F., Kuramoto, S., Park, J.-O., Kaneda, Y., and Taira, A., 2008. Tectonics and sedimentation around Kashinosaki Knoll: A subducting basement high in the eastern Nankai Trough. *Island Arc*, **17**, 358-375. doi:10.1111/j.1440-1738.2008.00625.x.
- Inagaki, F., Hinrichs, K.-U., Kubo, Y., Bowles, M.W., Heuer, V.B., Hong, W.-L., et al., 2015. Exploring deep microbial life in coal-bearing sediment down to ~2.5 km below the ocean floor. *Science*, **349**, 420-424. doi:10.1126/science.aaa6882.
- Jørgensen, B.B., 1982. Mineralization of organic matter in the sea bed – the role of sulphate reduction. *Nature*, **296**, 643-645. doi:10.1038/296643a0.
- Jørgensen, B.B., Böttcher, M.E., Lüschen, H., Neretin, L.N., and Volkov, I.I., 2004. Anaerobic methane oxidation and a deep H₂S sink generate isotopically heavy sulfides in Black Sea sediments. *Geochimica et Cosmochimica Acta*, **68**, 2095-2118. doi:10.1016/j.gca.2003.07.017.
- Jørgensen, B.B., and Kasten, S., 2006. Sulfur cycling and methane oxidation. In: *Marine Geochemistry* (eds. Schulz, H.D., and Zabel, M.). Berlin, Heidelberg: Springer, 271-309. doi:10.1007/3-540-32144-6_8.
- Jørgensen, B.B., Findlay, A.J., and Pellerin, A., 2019. The biogeochemical sulfur cycle of marine sediment. *Frontiers in Microbiology*, **10**, 849. doi:10.3389/fmicb.2019.00849.
- Jung, J., Yoo, K.-C., Rosenheim, B.E., Conway, T.M., Lee, J.I., Yoon, H.I., et al., 2019. Microbial Fe(III) reduction as a potential iron source from Holocene sediments beneath Larsen Ice Shelf. *Nature Communications*, **10**, 1-10. doi:10.1038/s41467-019-13741-x.
- Kars, M., and Köster, M., 2021. Rock magnetic data of IODP Hole 370-C0023. *PANGAEA*. doi:10.1594/PANGAEA.929380.
- Kamata, H., and Kodama, K., 1994. Tectonics of an arc-arc junction: an example from Kyushu Island at the junction of the Southwest Japan Arc and the Ryukyu Arc. *Tectonophysics*, **233**, 69-81. doi:10.1016/0040-1951(94)90220-8.
- Kashefi, K., and Lovley, D.R., 2003. Extending the upper temperature limit for life. *Science*, **301**, 934-934. doi:10.1126/science.1086823.
- Kasten, S., Freudenthal, T., Gingele, F. X., and Schulz, H.D., 1998. Simultaneous formation of iron-rich layers at different redox boundaries in sediments of the Amazon deep-sea fan. *Geochimica et Cosmochimica Acta*, **62**, 2253-2264. doi:10.1016/S0016-7037(98)00093-3.
- Kasten, S., Zabel, M., Heuer, V., and Hensen, C., 2003. Processes and signals of nonsteady-state diagenesis in deep-sea sediments and their pore waters. In: *The South Atlantic in the Late Quaternary* (eds. Wefer, G., Mulitza, S., and Ratmeyer, V.). Berlin, Heidelberg: Springer, 431-459. doi:10.1007/978-3-642-18917-3_20.

- Kim, J., Dong, H., Seabaugh, J., Newell, S.W., and Eberl, D.D., 2004. Role of microbes in the smectite-to-illite reaction. *Science*, **303**, 830-832. doi:10.1126/science.1093245.
- Kim, J., Dong, H., Yang, K., Park, H., Elliott, W.C., Spivack, A., et al., 2019. Naturally occurring, microbially induced smectite-to-illite reaction. *Geology*, **47**, 535-539. doi:10.1130/G46122.1.
- Korff, L., von Dobeneck, T., Frederichs, T., Kasten, S., Kuhn, G., Gersonde, R., and Diekmann, B., 2016. Cyclic magnetite dissolution in Pleistocene sediments of the abyssal northwest Pacific Ocean: Evidence for glacial oxygen depletion and carbon trapping. *Paleoceanography*, **31**, 600-624. doi:10.1002/2015PA002882.
- Köster, M., Kars, M., Schubotz, F., Tsang, M.-Y., Maisch, M., Kappler, A., et al., 2021a. Solid-phase geochemistry of sediment cores from IODP Hole 370-C0023A. *PANGAEA*. doi:10.1594/PANGAEA.930858.
- Köster, M., Kars, M., Schubotz, F., Tsang, M.-Y., Maisch, M., Kappler, A., et al., 2021b. Rock magnetic end-member unmixing of sediment cores from IODP Hole 370-C0023A. *PANGAEA*. doi:10.1594/PANGAEA.929317.
- Kruiver, P.P., Dekkers, M.J., and Heslop, D., 2001. Quantification of magnetic coercivity components by the analysis of acquisition curves of isothermal remanent magnetisation. *Earth and Planetary Science Letters*, **189**, 269-276. doi:10.1016/S0012-821X(01)00367-3.
- Kuhnt, W., Holbourn, A., Hall, R., Zuvela, M., and Käse, R., 2004. Neogene history of the Indoneasian throughflow. In: *Continent-ocean interactions within East Asian marginal seas. Geophysical monograph series 149* (eds. Clift, P., Kuhnt, W., Wang, P., and Hayes, D.). Washington, DC: American Geophysical Union, 299-320.
- Laufer, K., Michaud, A.B., Røy, H., and Jørgensen, B.B., 2020. Reactivity of iron minerals in the seabed toward microbial reduction – A comparison of different extraction techniques. *Geomicrobiology Journal*, **37**, 170-189. doi:10.1080/01490451.2019.1679291.
- Lawrence, K.T., Sigman, D.M., Herbert, T.D., Riihimaki, C.A., Bolton, C.T., Martinez-Garcia, A., et al., 2013. Time-transgressive North Atlantic productivity changes upon Northern Hemisphere glaciation. *Paleoceanography*, **28**, 740-751. doi:10.1002/2013PA002546.
- Le Pichon, X., Iiyama, T., Boulègue, J., Charvet, J., Faure, M., Kano, K., et al., 1987. Nankai Trough and Zenisu Ridge: A deep-sea submersible survey. *Earth and Planetary Science Letters*, **83**, 285-299. doi:10.1016/0012-821X(87)90072-0.
- Mahony, S.H., Wallace, L.M., Miyoshi, M., Villamor, P., Sparks, R.S.J., and Hasenaka, T., 2011. Volcano-tectonic interactions during rapid plate-boundary evolution in the Kyushu region, SW Japan. *Bulletin*, **123**, 2201-2223. doi:10.1130/B30408.1.
- Manheim, F.T., and Sayles, F.L., 1974. Composition and origin of interstitial waters of marine sediments, based on deep sea drill cores. In: *The Sea (Volume 5): Marine Chemistry: The Sedimentary Cycle* (ed. Goldberg, E.D.). New York: Wiley-Interscience, 527-568.
- März, C., Hoffmann, J., Bleil, U., de Lange, G.J., and Kasten, S., 2008. Diagenetic changes of magnetic and geochemical signals by anaerobic methane oxidation in sediments of the Zambezi deep-sea fan (SW Indian Ocean). *Marine Geology*, **255**, 118-130. doi:10.1016/j.margeo.2008.05.013.
- Maxbauer, D.P., Feinberg, J.M., and Fox, D.L., 2016. MAX UnMix: A web application for unmixing magnetic coercivity distributions. *Computers & Geosciences*, **95**, 140-145. doi:10.1016/j.cageo.2016.07.009.

- Meister, P., 2015. For the deep biosphere, the present is not always the key to the past: what we can learn from the geological record. *Terra Nova*, **27**, 400-408. doi:10.1111/ter.12174.
- Mewes, K., Mogollón, J.M., Picard, A., Rühlemann, C., Kuhn, T., Nöthen, K., and Kasten, S., 2014. Impact of depositional and biogeochemical processes on small scale variations in nodule abundance in the Clarion-Clipperton Fracture Zone. *Deep Sea Research Part I: Oceanographic Research Papers*, **91**, 125-141. doi:10.1016/j.dsr.2014.06.001.
- Meyers, P.A., 1994. Preservation of elemental and isotopic source identification of sedimentary organic matter. *Chemical Geology*, **114**, 289-302. doi:10.1016/0009-2541(94)90059-0.
- Meyers, P.A., 1997. Organic geochemical proxies of paleoceanographic, paleolimnologic, and paleoclimatic processes. *Organic Geochemistry*, **27**, 213-250. doi:10.1016/S0146-6380(97)00049-1.
- Mizutani, H., and Wada, E., 1982. Effect of high atmospheric CO₂ concentration on δ¹³ of algae. *Origin of Life*, **12**, 377-390. doi:10.1007/BF00927070.
- Mogollón, J.M., Mewes, K., and Kasten, S., 2016. Quantifying manganese and nitrogen cycle coupling in manganese-rich, organic carbon-starved marine sediments: Examples from the Clarion-Clipperton fracture zone. *Geophysical Research Letters*, **43**, 7114-7123. doi:10.1002/2016GL069117.
- Molina-Cruz, A., 1997. Closing of the Central American Gateway and its effect on the distribution of late Pliocene radiolarians in the eastern tropical Pacific. *Tectonophysics*, **281**, 105-111. doi: 10.1016/S0040-1951(97)00162-5.
- Morono, Y., Inagaki, F., Heuer, V.B., Kubo, Y., Maeda, L., and the Expedition 370 Scientists, 2017. Expedition 370 methods. In: *Proceedings of the International Ocean Discovery Program Volume 370* (eds. Heuer, F. Inagaki, Y. Morono, Y. Kubo, L. Maeda, and the Expedition 370 Scientists). College Station, TX (International Ocean Discovery Program). doi:10.14379/iodp.proc.370.102.2017.
- Murad, E., 1998. Clays and clay minerals: What can Mössbauer spectroscopy do to help understand them? *Hyperfine Interactions*, **117**, 39-70. doi:10.1023/A:1012635124874.
- Murad, E., 2010. Mössbauer spectroscopy of clays, soils and their mineral constituents. *Clay Minerals*, **45**, 413-430. doi:10.1180/claymin.2010.045.4.413.
- Niewöhner, C., Hensen, C., Kasten, S., Zabel, M., and Schulz, H.D., 1998. Deep sulfate reduction completely mediated by anaerobic methane oxidation in sediments of the upwelling area off Namibia. *Geochimica et Cosmochimica Acta*, **62**, 455-464. doi:10.1016/S0016-7037(98)00055-6.
- Nöthen, K., and Kasten, S., 2011. Reconstructing changes in seep activity by means of pore water and solid phase Sr/Ca and Mg/Ca ratios in pockmark sediments of the Northern Congo Fan. *Marine Geology*, **287**, 1-13. doi:10.1016/j.margeo.2011.06.008.
- Okino, K., Shimakawa, Y., and Nagaoka, S., 1994. Evolution of the Shikoku basin. *Journal of Geomagnetism and Geoelectricity*, **46**, 463-479. doi:10.5636/jgg.46.463.
- Okino, K., Ohara, Y., Kasuga, S., and Kato, Y., 1999. The Philippine Sea: New survey results reveal the structure and the history of the marginal basins. *Geophysical Research Letters*, **26**, 2287-2290. doi:10.1029/1999GL900537.
- Oonk, P.B., Tsikos, H., Mason, P.R., Henkel, S., Staubwasser, M., Fryer, L., et al., 2017. Fraction-specific controls on the trace element distribution in iron formations: Implications for trace metal stable isotope proxies. *Chemical Geology*, **474**, 17-32. doi:10.1016/j.chemgeo.2017.10.018.

- Parkes, R.J., Wellsbury, P., Mather, I.D., Cobb, S.J., Cragg, B.A., Hornibrook, E.R.C., and Horsfield, B., 2007. Temperature activation of organic matter and minerals during burial has the potential to sustain the deep biosphere over geological timescales. *Organic Geochemistry*, **38**, 845-852. doi:10.1016/j.orggeochem.2006.12.011.
- Passier, H.F., Middelburg, J.J., van Os, B.J.H., and de Lange, G.J., 1996. Diagenetic pyritisation under eastern Mediterranean sapropels caused by downward sulphide diffusion. *Geochimica et Cosmochimica Acta*, **60**, 751-763. doi:10.1016/0016-7037(95)00419-X.
- Pickering, K.T., Underwood, M.B., Saito, S., Naruse, H., Kutterolf, S., Scudder, R., et al., 2013. Depositional architecture, provenance, and tectonic/eustatic modulation of Miocene submarine fans in the Shikoku Basin: Results from Nankai Trough Seismogenic Zone Experiment. *Geochemistry, Geophysics, Geosystems*, **14**, 1722-1739. doi:10.1002/ggge.20107.
- Poulton, S.W., Krom, M.D., and Raiswell, R., 2004. A revised scheme for the reactivity of iron (oxyhydr) oxide minerals towards dissolved sulfide. *Geochimica et Cosmochimica Acta*, **68**, 3703-3715. doi:10.1016/j.gca.2004.03.012.
- Poulton, S.W., and Canfield, D.E., 2005. Development of a sequential extraction procedure for iron: implications for iron partitioning in continentally derived particulates. *Chemical Geology*, **214**, 209-221. doi:10.1016/j.chemgeo.2004.09.003.
- Pruyters, P.A., de Lange, G.J., Middelburg, J.J., and Hydes, D.J., 1993. The diagenetic formation of metal-rich layers in sapropel-containing sediments in the eastern Mediterranean. *Geochimica et Cosmochimica Acta*, **57**, 527-536. doi:10.1016/0016-7037(93)90365-4.
- Qui, B., 2001. Kuroshio and Oyashio currents. In: *Encyclopedia of Ocean Sciences* (eds. Turekian, K.K., Steele, J.H., and Thorpe, S.A.). Cambridge, MA: Academic Press, 1413-1425. doi:10.1006/rwos.2001.0350.
- Riedinger, N., Pfeifer, K., Kasten, S., Garming, J.F.L., Vogt, C., and Hensen, C., 2005. Diagenetic alteration of magnetic signals by anaerobic oxidation of methane related to a change in sedimentation rate. *Geochimica et Cosmochimica Acta*, **69**, 4117-4126. doi:10.1016/j.gca.2005.02.004.
- Riedinger, N., Kasten, S., Gröger, J., Franke, C., and Pfeifer, K., 2006. Active and buried authigenic barite fronts in sediments from the Eastern Cape Basin. *Earth and Planetary Science Letters*, **241**, 876-887. doi:10.1016/j.epsl.2005.10.032.
- Riedinger, N., Formolo, M.J., Lyons, T.W., Henkel, S., Beck, A., and Kasten, S., 2014. An inorganic geochemical argument for coupled anaerobic oxidation of methane and iron reduction in marine sediments. *Geobiology*, **12**, 172-181. doi:10.1111/gbi.12077.
- Riedinger, N., Strasser, M., Harris, R.N., Klockgether, G., Lyons, T.W., and Scretton, E.J., 2015. Deep subsurface carbon cycling in the Nankai Trough (Japan) – Evidence of tectonically induced stimulation of a deep microbial biosphere. *Geochemistry, Geophysics, Geosystem*, **16**, 3257-3270. doi:10.1002/2015GC006050.
- Roberts, A.P., Chang, L., Rowan, C.J., Horng, C.S., and Florindo, F., 2011. Magnetic properties of sedimentary greigite (Fe₃S₄): An update. *Reviews of Geophysics*, **49**, RG1002. doi:10.1029/2010RG000336.
- Roberts, A.P., 2015. Magnetic mineral diagenesis. *Earth-Science Reviews*, **151**, 1-47. doi:10.1016/j.earscirev.2015.09.010.

- Robertson, D.J., and France, D.E., 1994. Discrimination of remanence-carrying minerals in mixtures, using isothermal remanent magnetization acquisition curves. *Physics of the Earth and Planetary Interiors*, **82**, 223-234. doi:10.1016/0031-9201(94)90074-4.
- Ryan, P.C., Hillier, S., and Wall, J., 2008. Stepwise effects of the BCR sequential chemical extraction procedure on dissolution and metal release from common ferromagnesian clay minerals: A combined solution chemistry and X-ray powder diffraction study. *Science of the Total Environment*, **407**, 603-614. doi:10.1016/j.scitotenv.2008.09.019.
- Saitoh, Y., Ishikawa, T., Tanimizu, M., Murayama, M., Ujiie, Y., Yamamoto, Y., et al., 2015. Sr, Nd, and Pb isotope compositions of hemipelagic sediment in the Shikoku Basin: Implications for sediment transport by the Kuroshio and Philippine Sea plate motion in the late Cenozoic. *Earth and Planetary Science Letters*, **421**, 47-57. doi:10.1016/j.epsl.2015.04.001.
- Seno, T., Stein, S., and Gripp, A.E., 1993. A model for the motion of the Philippine Sea Plate consistent with NUVEL-1 and geological data. *Journal of Geophysical Research: Solid Earth*, **98**, 17941-17948. doi:10.1029/93JB00782.
- Shi, M., Wu, H., Roberts, A.P., Zhang, S., Zhao, X., Li, H., et al., 2017. Tectonic, climatic, and diagenetic control of magnetic properties of sediments from Kumano Basin, Nankai margin, southwestern Japan. *Marine Geology*, **391**, 1-12. doi:10.1016/j.margeo.2017.07.006.
- Shipboard Science Party, 1991. Site 808. In: *Proceedings of the Ocean Drilling Program, Initial Reports, 131* (eds. Taira, A., Hill, I., Firth, J.V., et al.). College Station, TX (Ocean Drilling Program), 71-269. doi:10.2973/odp.proc.ir.131.106.1991.
- Shipboard Science Party, 2001. Site 1174. In: *Proceedings of the Ocean Drilling Program, Initial Reports, 190* (eds. Moore, G.F., Taira, A., Klaus, A., et al.). College Station, TX (Ocean Drilling Program), 1-149. doi:10.2973/odp.proc.ir.190.105.2001.
- Slotznick, S.P., Sperling, E.A., Tosca, N.J., Miller, A.J., Clayton, K.E., van Helmond, N.A.G.M., et al., 2020. Unraveling the mineralogy complexity of sediment iron speciation using sequential extractions. *Geochemistry, Geophysics, Geosystems*, **21**. E2019GC008666. doi:10.1029/2019GC008666.
- Stookey, L.L., 1970. Ferrozine – A new spectrophotometric reagent for iron. *Analytical Chemistry*, **42**, 779-781.
- Stucki, J.W., Golden, D.C., and Roth, C.B., 1984. Effects of reduction and reoxidation of structural iron on the surface charge and dissolution of dioctahedral smectites. *Clays and Clay Minerals*, **32**, 350-356. doi:10.1346/CCMN.1984.0320502.
- Stucki, J.W., Bailey, G.W., and Gan, H.M., 1996. Oxidation-reduction mechanisms in iron-bearing phyllosilicates. *Applied Clay Science*, **10**, 417-430. doi:10.1016/0169-1317(96)00002-6.
- Sturt, H.F., Summons, R.E., Smith, K., Elvert, M. and Hinrichs, K.-U., 2004. Intact polar membrane lipids in prokaryotes and sediments deciphered by high-performance liquid chromatography/electrospray ionization multistage mass spectrometry – new biomarkers for biogeochemistry and microbial ecology. *Rapid Communications in Mass Spectrometry*, **18**, 617-628. doi:10.1002/rcm.1378.
- Swann, G.E., Maslin, M.A., Leng, M.J., Sloane, H.J., and Haug, G.H., 2006. Diatom $\delta^{18}\text{O}$ evidence for the development of the modern halocline system in the subarctic northwest

- Pacific at the onset of major Northern Hemisphere glaciation. *Paleoceanography*, **21**, PA1009. doi:10.1029/2005PA001147.
- Sweeney, R.E., and Kaplan, I.R., 1973. Pyrite framboid formation: Laboratory synthesis and marine sediments. *Economic Geology*, **68**, 618-634. doi:10.2113/gsecongeo.68.5.618.
- Taira, A., Hill, I., Firth, J., Berner, U., Brückmann, W., Byrne, T., et al., 1992. Sediment deformation and hydrogeology of the Nankai Trough accretionary prism: synthesis of shipboard results of ODP Leg 131, *Earth and Planetary Science Letters*, **109**, 431-450. doi:10.1016/0012-821X(92)90104-4.
- Taira, A., and Ashi, J., 1993. Sedimentary facies evolution of the Nankai forearc and its implications for the growth of the Shimanto accretionary prism. In: *Proceedings of the Ocean Drilling Program, Initial Reports, 131* (eds. Hill, I.A., Taira, A., Firth, J.V., et al.). College Station, TX (Ocean Drilling Program), 331-341. doi:10.2973/odp.proc.sr.131.136.1993.
- Tessier, A., Campbell, P.G., and Bisson, M., 1979. Sequential extraction procedure for the speciation of particulate trace metals. *Analytical Chemistry*, **51**, 844-851.
- Thompson, R., Stober, J.C., Turner, G.M., Oldfield, F., Bloemendal, J., Dearing, J.A., and Rummery, T.A., 1980. Environmental applications of magnetic measurements. *Science*, **207**, 481-486. doi:10.1126/science.207.4430.481.
- Torres, M.E., Cox, T., Hong, W.-L., McManus, J., Sample, J.C., Destriqneville, C., et al., 2015. Crustal fluid and ash alteration impacts on the biosphere of Shikoku Basin sediments, Nankai Trough, Japan. *Geobiology*, **13**, 562-580. doi:10.1111/gbi.12146.
- Tsang, M. Y., Bowden, S. A., Wang, Z., Mohammed, A., Tonai, S., Muirhead, D., et al., 2020. Hot fluids, burial metamorphism and thermal histories in the underthrust sediments at IODP 370 site C0023, Nankai Accretionary Complex. *Marine and Petroleum Geology*, **112**, 104080. doi:10.1016/j.marpetgeo.2019.104080.
- Tsuchi, R. (1977). Marine climatic responses to Neogene tectonics to the Pacific Ocean seaways. *Tectonophysics*, **281**(1-2), 113-124. doi:10.1016/S0040-1951(97)00163-7.
- Turekian, K.K., and Wedepohl, K.H., 1961. Distribution of the elements in some major units of the Earth's crust. *Geological Society of America Bulletin*, **72**, 175-192. doi:10.1130/0016-7606(1961)72[175:DOTSIS]2.0.CO;2.
- Underwood, M.B., and Steurer, J.F., 2003. Composition and sources of clay from the trench slope and shallow accretionary prism of Nankai Trough. In: *Proceedings of the Ocean Drilling Program, Scientific Results, 190/196* (eds. Mikada, H., Moore, G.F., Taira, A., Becker, J.C., Moore, J.C., and Klaus, A.). College Station, TX (Ocean Drilling Program), 1-28. doi:10.2973/odp.proc.sr.190196.206.2003.
- Underwood, M.B., Saito, S., and Kubo, Y., 2010. IODP Expedition 322 drills two sites to document inputs to the Nankai Trough subduction zone. *Scientific Drilling*, **10**, 14-25. doi:10.2204/iodp.sd.10.02.210.
- Underwood, M.B., and Guo, J., 2018. Clay-mineral assemblages across the Nankai-Shikoku subduction system, offshore Japan: A synthesis of results from the NanTroSEIZE project. *Geosphere*, **14**, 2009-2043. doi:10.1130/GES01626.1.
- Vargas, M., Kashefi, K., Blunt-Harris, E.L., and Lovley, D.R., 1998. Microbiological evidence for Fe (III) reduction on early Earth. *Nature*, **395**, 65-67. doi:10.1038/25720.

- Volkman, J.K., Barrett, S.M., Dunstan, G.A., and Jeffrey, S.W., 1992. C₃₀-C₃₂ alkyl diols and unsaturated alcohols in microalgae of the class Eustigmatophyceae. *Organic Geochemistry*, **18**, 131-138. doi:10.1016/0146-6380(92)90150-V.
- Volz, J.B., Mogollón, J.M., Geibert, W., Martínez Arbizu, P., Koschinsky, A., and Kasten, S., 2018. Natural spatial variability of depositional conditions, biogeochemical processes and element fluxes in sediments of the eastern Clarion-Clipperton Zone, Pacific Ocean. *Deep Sea Research Part I: Oceanographic research Papers*, **140**, 159-172. doi:10.1016/j.dsr.2018.08.006.
- Vorhies, J.S., and Gaines, R.R., 2009. Microbial dissolution of clay minerals as a source of iron and silica in marine sediments. *Nature Geoscience*, **2**, 221-225. doi:10.1038/ngeo441.
- Watts, A.B., and Weissel, J.K., 1975. Tectonic history of the Shikoku marginal basin. *Earth and Planetary Science Letters*, **25**, 239-250. doi:10.1016/0012-821X(75)90238-1.
- Wehrmann, L.M., Arndt, S., März, C., Ferdelman, T.G., and Brunner, B., 2013. The evolution of early diagenetic signals in Bering Sea subseafloor sediments in response to varying organic carbon deposition over the last 4.3 Ma. *Geochimica et Cosmochimica Acta*, **109**, 175-196. doi:10.1016/j.gca.2013.01.025.
- Wehrmann, L.M., and Riedinger, N., 2016. The sedimentary deep subseafloor biosphere. In: *Encyclopedia of Ocean Sciences*, 3rd Edition (eds. Cochran, J.K., Bokuniewicz H.J., and Yager, P.L.). Academic Press, 258-274. doi:10.1016/B978-0-12-409548-9.09741-4.
- Wellsbury, P., Goodman, K., Barth, T., Cragg, B.A., Barnes, S.P., and Parkes, R.J., 1997. Deep marine biosphere fueled by increasing organic matter availability during burial and heating. *Nature*, **388**, 573-576. doi:10.1038/41544.
- Wilkin, R.T., and Barnes, H.L., 1996. Pyrite formation by reactions of iron monosulfides with dissolved inorganic and organic sulfur species. *Geochimica et Cosmochimica Acta*, **60**, 4167-4179. doi:10.1016/S0016-7037(97)81466-4.
- Yamano, M., Kinoshita, M, Goto, S., and Matsubayashi, O., 1992. Extremely high heat flow anomaly in the middle part of the Nankai Trough. *Physics and Chemistry of the Earth, Parts A/B/C*, **28**, 487-497. doi:10.1016/S1474-7065(03)00068-8.
- Zhabina, N.N., and Volkov, I.I., 1978. A method of determination of various sulfur compounds in sea sediments and rocks. In: *Environmental Biogeochemistry and Geomicrobiology; Methods, Metals and Assessment, Vol 3* (eds. Krumbein, W.E.). Michigan: Ann Arbor Scientific Publications, 735-745.
- Zonneveld, K.A.F., Versteegh, G.J.M., Kasten, S., Eglinton, T.I., Emeis, K.-C., Huguet, C., et al., 2010. Selective preservation of organic matter in marine environments; processes and impact on the sedimentary record. *Biogeosciences*, **7**, 483-511. doi:10.5194/bg-7-483-2010.

CHAPTER III:
**Influence of early low-temperature and later high-temperature diagenesis
on magnetic mineral assemblages in marine sediments from the Nankai
Trough**

Myriam Kars¹, Male Köster², Susann Henkel^{2,3}, Rüdiger Stein^{2,3}, Florence Schubotz³, Xiang Zhao⁴, Stephen A. Bowden⁵, Andrew P. Roberts⁴, and Kazuto Kodama⁶

¹Center for Advanced Marine Core Research, Kochi University, Nankoku, Japan

²Alfred Wegener Institute Helmholtz Centre for Polar and Marine Research, Bremerhaven, Germany

³MARUM – Center for Marine Environmental Sciences, University of Bremen, Bremen, Germany

⁴Research School of Earth Sciences, Australian National University, Canberra, ACT, Australia

⁵School of Geosciences, University of Aberdeen, Aberdeen, UK

⁶Research Center for Knowledge Science in Cultural Heritage, Doshisha University, Kyoto, Japan

Manuscript published in *Geochemistry, Geophysics, Geosystems*, 22, e2021GC010133.

doi:10.1029/2021GC010133

The format has been adapted to the thesis format.

Key Points:

- Four down-core diagenetic zones are identified with magnetic mineral assemblages reflecting sediment provenance and diagenetic processes
- Limited exposure of sediments to dissolved sulfide due to rapid burial leads to greigite preservation in the upper ~460 m
- High-temperature diagenetic processes are responsible for later iron oxide formation and reduction in deeper sediments

Abstract

Diagenesis can have a major impact on sedimentary mineralogy. Primary magnetic mineral assemblages can be modified significantly by dissolution or by formation of new magnetic minerals during early or late diagenesis. At International Ocean Discovery Program Site C0023, which was drilled in the prot thrust zone of the Nankai Trough during Expedition 370, offshore of Shikoku Island, Japan, non-steady state conditions have produced a complex sequence of magnetic overprints. Detailed rock magnetic measurements, which characterize magnetic mineral assemblages in terms of abundance, grain size, and composition, were conducted to assess magnetic mineral alteration and diagenetic overprinting. Four magnetic zones (MZs) are identified down-core from ~200 to 1,100 m below sea floor based on rock magnetic variations. MZ 1 is a high magnetic intensity zone that contains ferrimagnetic greigite, which formed at shallow depths and is preserved because of rapid sedimentation. MZs 2 and 4 are low magnetic intensity zones with fewer magnetic minerals, mainly coarse-grained (titano-)magnetite and hematite. This magnetic mineral assemblage is a remnant of a more complex assemblage that was altered diagenetically a few million years after deposition when the site entered the Nankai Trough. MZ 3 is a high magnetic intensity zone between MZs 2 and 4. It contains authigenic single-domain magnetic particles that probably formed from fluids that circulated through faults in the accretionary prism. Varying sediment supply and organic matter input through time, burial temperature, and tectonic fluid circulation are the primary drivers of magnetic mineral assemblage variations.

1. Introduction

Dissimilatory iron reduction plays an important role in iron cycling in reducing environments (e.g., Lovley, 1991). Detrital and authigenic iron oxides are used by microbes as electron acceptors to oxidize organic matter, releasing dissolved iron (Fe^{2+}) into porewater. In marine environments, early formation of authigenic iron oxides results from Fe^{2+} diffusion into the overlying oxic and nitrogenous zones. In underlying sulfidic environments, dissolved iron and iron-bearing solid phases react with dissolved sulfide ($\text{HS}^-/\text{H}_2\text{S}$) to form iron sulfides. $\text{HS}^-/\text{H}_2\text{S}$ results from organoclastic sulfate reduction associated with organic matter decomposition (e.g., Berner, 1981; Jørgensen et al., 2019) and microbial anaerobic oxidation of methane (AOM) above and at the sulfate-methane transition (SMT) zone (e.g., Treude et al., 2005; Knittel and Boetius, 2009). These processes strongly affect iron-bearing magnetic minerals, which affects the magnetic properties of sediments and sedimentary rocks (Roberts, 2015). Iron reduction and the subsequent incorporation of released Fe^{2+} into iron sulfides, is an important mechanism

responsible for magnetic mineral alteration. Destruction of detrital and biogenic ferrimagnetic minerals during diagenesis can destroy primary magnetic records. Limited exposure of sediments to dissolved sulfide can prevent pyritization (e.g., Berner, 1984; Canfield and Berner, 1987) and favor preservation of metastable iron sulfide precursors such as greigite (Kao et al., 2004). Greigite is ferrimagnetic and can carry a secondary magnetization that can potentially obscure the original paleomagnetic record (Roberts and Weaver, 2005; Rowan and Roberts, 2005; Rowan et al., 2009). Generally, the presence of greigite indicates environments with limited availability of dissolved sulfide, such as in gas hydrate-bearing zones (e.g., Housen and Musgrave, 1996; Larrasoña et al., 2007; Kars and Kodama, 2015a, 2015b), which lie below the sulfidic zone (Roberts, 2015).

The Nankai Trough and its accretionary complex are located southwest of Japan (Figure 1a) and have been intensively studied to understand earthquake mechanisms and tsunami generation (NanTroSEIZE project). It is also ideal for studying the deep biosphere and the temperature limit of life due to exceptionally high prevailing heat flow. After Ocean Drilling Program (ODP) Leg 131 (Taira et al., 1991) and ODP Leg 190 (Moore et al., 2001), International Ocean Discovery Program (IODP) Expedition 370 drilled Site C0023 offshore of Cape Muroto, Shikoku Island, Japan (Heuer et al., 2017). This expedition mainly aimed to investigate the temperature limit of life in marine sediments. Site C0023 (Hole C0023A) is a 1.2-km borehole that was drilled using *D/V Chikyu* close to Site 1174 of ODP Leg 190 (Figure 1b). Parkes et al. (2007) showed that methanogen activity at Site 1174 is enhanced by adding iron oxides (magnetite and ferrihydrite) into the medium, which led to increased methane release. The process by which iron and methane are coupled is not fully understood. Aromokeye et al. (2021) suggested that during methanogenic benzoate degradation, crystalline Fe oxides serve as conduits for microbes and are reduced to contributing to the Fe²⁺ pool in methanogenic marine sediments. Reduction of Fe³⁺-bearing magnetic minerals by microbial activity affects magnetic mineral assemblages to extents that remain unassessed (e.g., Riedinger et al., 2005, 2010). Here, we present a detailed rock magnetic study of diagenetic events at Site C0023. The sensitivity of magnetic minerals to biogeochemical processes makes them useful for investigating magnetic mineral assemblage variations to obtain new insights into environmental conditions. Microbial activity, high burial temperature, and fluid circulation through faults are the main investigated processes to understand magnetic mineralogy variations at Site C0023.

2. Material and methods

2.1 Geologic setting and materials

The Nankai Trough formed by subduction of the Philippine Sea Plate beneath the Eurasian Plate. The Nankai Accretionary Complex formed by scraping of sediment from the descending plate, which has a current subduction rate of $\sim 2\text{--}4\text{ cm yr}^{-1}$ (Seno et al., 1993; Figure 1a). Three major scientific ocean drilling transects have been sampled: the Ashizuri and Muroto transects offshore of Shikoku Island (e.g., Taira et al., 1991; Moore et al., 2001) and the Kumano transect (NanTroSEIZE) off Kii peninsula (e.g., Kinoshita et al., 2009). IODP Expedition 370 drilled Site C0023 ($32^{\circ}22.00'\text{N}$, $134^{\circ}57.98'\text{E}$, water depth: 4,776 m) in the prothrust zone of the prism, near ODP Leg 131 Site 808 and ODP Leg 190 Site 1174 in the Muroto transect (Figure 1b).

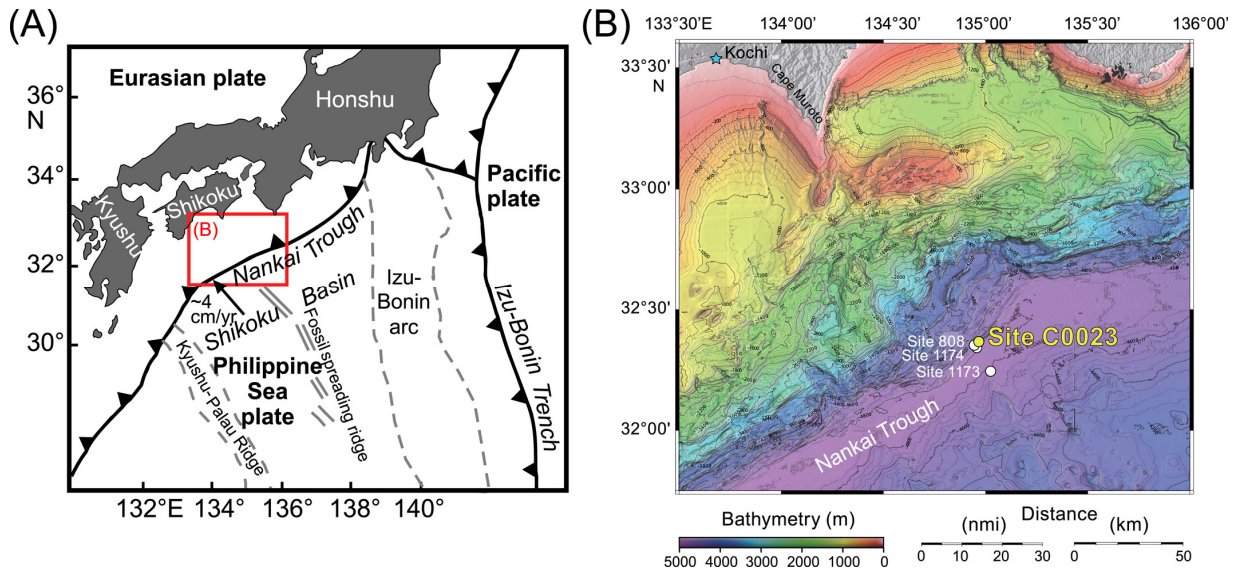


Figure 1. (a) General tectonic configuration of the Japanese islands. The red box is the area indicated in (b), which is a regional bathymetric map around Site C0023, International Ocean Discovery Program Expedition 370, with nearby Ocean Drilling Program Sites 808, 1174, and 1173 (modified after Heuer et al., 2017).

Site C0023 is at the seaward end of the Nankai accretionary prism. At this site, ~ 16 Ma basaltic basement is overlain from bottom to top by a volcanoclastic facies (Lithologic Unit V, 1,125.9–1,112 meters below seafloor [mbsf]), the Lower Shikoku Basin facies (hemipelagic mudstone, Unit IV, 1,112–637.25 mbsf) that includes the décollement zone of the accretionary prism with reverse faults that pass through the core ($\sim 758\text{--}796$ mbsf), the Upper Shikoku Basin facies (hemipelagic bioturbated mudstones with numerous ash layers, Unit III, 637.25–494 mbsf), a trench-to-basin transitional facies (Subunit IIC, 494–428 mbsf), an outer trench-wedge facies (Subunit IIB, 428–353 mbsf), and an axial trench-wedge facies (Subunit IIA, 318.5–189 mbsf) that consists mainly of sand and turbidites, with hemipelagic mud and volcanoclastic sediment (Subunit IIC) (Figures 2 and S1 in Supporting Information S1; Heuer et al., 2017). Shallower

sediments (< 189 mbsf) were not recovered during IODP Expedition 370. Paleomagnetic samples (225 samples) were taken from hemipelagic fine-grained mudstones in 7-cm³ plastic boxes from cores 3F to 86R (~206–892 mbsf). In more lithified lithologies, 10-cm³ mini-cores were drilled from cores 87R to 107R (~900–1,099 mbsf).

2.2 Methods

2.2.1 Rock magnetic measurements

All rock magnetic measurements were made at the Center for Advanced Marine Core Research (Kochi University, Japan) unless stated otherwise. Low-field, low-frequency (0.465 kHz) and low-field, high-frequency (4.65 kHz) magnetic susceptibility (χ_{lf} and χ_{hf} , respectively) measurements were made with a MS2B Bartington Instruments magnetic susceptibility meter (field = 250 μ T). The frequency-dependent susceptibility χ_{fd} (%) ($= (\chi_{lf} - \chi_{hf}) / \chi_{lf} \times 100$) is used as a proxy for small (superparamagnetic, SP) particles. The natural remanent magnetization (NRM) and an anhysteretic remanent magnetization (ARM) were measured with a 2-G Enterprises 760R cryogenic magnetometer in a shielded paleomagnetic laboratory. ARM was imparted in a direct current (DC) bias field of 50 μ T in the presence of an 80 mT peak alternating field (AF). A saturation isothermal remanent magnetization (SIRM) was subsequently imparted to samples along the +z direction at 1.2 T using a MMPM10 impulse magnetizer before being analyzed with a Natsuhara Giken spinner magnetometer. The samples were then remagnetized along the -z direction with DC fields of 0.1 and 0.3 T and were measured again to calculate $S_{-0.1T}$ and $S_{-0.3T}$ ($= [(-IRM_{-0.3T}) / SIRM] + 1] / 2$; Bloemendal et al., 1992), which indicate the relative proportion of high coercivity minerals (e.g., hematite, goethite, some ferrimagnetic iron sulfides) in mixtures with soft ferrimagnetic minerals (e.g., magnetite, maghemite).

Hysteresis loops were measured to 1-T maximum applied fields on dry sediment powdered sister samples at room temperature with a Princeton Measurements Corporation (PMC) vibrating sample magnetometer (VSM). The saturation magnetization (M_s), saturation remanent magnetization (M_{rs}), and coercivity (B_c) were derived from the loops. Saturation was assumed above 70% of the maximum applied field, which might underestimate M_{rs} / M_s (Roberts et al., 2018 and references therein). The coercivity of remanence (B_{cr}) was determined from backfield demagnetization curves of M_{rs} . Conventional first-order reversal curves (FORCs; Pike et al., 1999) were measured for 91 samples selected at ~5–10-m stratigraphic intervals, with a 1-T saturating field (100 ms averaging time; 4 mT field increment; 91 FORCs). Regular FORC diagrams with evenly spaced field steps were processed using the FORCinel software

(Harrison and Feinberg, 2008) with constant smoothing factor, SF. Twenty-one samples were selected for irregular FORCs measurements. Irregularly spaced field steps enable use of different resolutions for different parts of a FORC diagram (Zhao et al., 2015). Irregular FORCs were measured at the Australian National University with a PMC VSM. Remanent FORC (remFORC), transient FORC (tFORC), and induced FORC (iFORC) diagrams were processed following the approach of Zhao et al. (2017). FORC diagrams measured with regularly spaced field steps for samples shown in Figures 3–6 are in Supporting Information S1.

Low-temperature magnetic measurements (from 300 to 10 K) were made with a Quantum Design Magnetic Properties Measurement System (MPMS) for 18 selected samples. The samples each have ~100–120 mg mass and were dried, ground lightly to a fine powder, and sealed in a gelatin capsule before being measured. A room temperature SIRM (RT-SIRM) was acquired at 2.5 T. A 300-10-300 K cooling-warming cycle of the RT-SIRM was then carried out in zero magnetic field ($< 20 \mu\text{T}$) trapped within the MPMS. A low-temperature SIRM (LT-SIRM) was imparted at 10 K at 2.5 T and samples were then warmed to room temperature in zero magnetic field and measured (termed ZFC for zero-field-cooled). Samples were subsequently cooled to 10 K in a 2.5 T magnetic field and the LT-SIRM was analyzed during warming to 300 K (termed FC for field-cooled). Thermomagnetic experiments in vacuum were made on 40 selected specimens with a Natsuhara Giken NMB-89 magnetic balance from room temperature to 700°C (at a heating rate of $10^\circ\text{C min}^{-1}$ in a 0.3 T field).

2.2.2 Rock-Eval pyrolysis

Rock-Eval pyrolysis allows determination of the quantity, type, and thermal maturity of organic matter (e.g., Espitalié et al., 1977; Tissot and Welte, 1984; Peters, 1986; Stein et al., 1986). Our measurements were made with a Rock-Eval 6 analyzer (cf. Behar et al., 2001) at the Alfred Wegener Institute, Germany (Stein, 2021). Pyrolysis was conducted on ground bulk sediment samples (100 mg/sample) to determine (a) the hydrocarbon (HC) content (S1 peak in mgHC/g of sediment), (b) the amount of HC generated by pyrolytic degradation of kerogen during heating to 550°C (S2 peak in mgHC/g of sediment), (c) the amount of carbon dioxide (CO_2) generated during heating to 390°C (S3 peak in mg CO_2 /g of sediment), and (d) the temperature of maximum pyrolysis yield (T_{max} value in °C). T_{max} values $< 435^\circ\text{C}$ are indicative of immature organic matter. Total organic carbon values of the analyzed sediments are known from shipboard measurements (Heuer et al., 2017).

2.2.3 Basin modeling

Basin modeling at Site C0023 was performed with the Petromod 2017 package (Tsang et al., 2020). A 1D model was constructed using lithological and biostratigraphic information from Heuer et al. (2017) and Hagino and the Expedition 370 Scientists (2018). Inbuilt libraries of formation properties were used to match thermal conductivity and porosity measurements, which yields a better match to physical aspects than previous modeling (Horsfield et al., 2006) and basin modeling studies in general (where thermal conductivity is not measured at high resolution or not measured at all). The model was calibrated and conditioned to reproduce present-day temperatures and measured thermal maturities (biomarker parameters for pre-oil window thermal maturities and unpublished vitrinite reflectance). Present-day heat flow at Site C0023 is 140 mW m^{-2} (shipboard results in Heuer et al., 2017). Model boundary conditions and other time-variant aspects are detailed by Tsang et al. (2020); in brief, paleo-seafloor temperature was fixed to the present-day value of 2°C (the site has been continuously in deep water since basement formation) and past heat flows are taken from analog environments and modern observations in the region (Tsang et al., 2020 and references therein).

3. Results

NRM, ARM, magnetic susceptibility χ_{lf} , and SIRM are widely used as magnetic mineral concentration proxies. In ODP Leg 131 (Shipboard Scientific Party, 1991) and Leg 190 sites (Shipboard Scientific Party, 2001), which were drilled next to Site C0023, these parameters were used to define sediment magnetic zones (MZs). Site C0023 has similar down-core variations with four main MZs (Figure 2, Table S1 in Supporting Information S2). MZ 1 (from ~ 207 to ~ 498 mbsf) has the highest NRM, χ_{lf} , ARM, and SIRM values (core gap between 318.5 and 353 mbsf) and corresponds roughly to Lithologic Subunits IIA, IIB, and IIC (Figure 2; Heuer et al., 2017). MZ 2 (from ~ 500 to ~ 704 mbsf) has lower values of these magnetic parameters. MZ 2' (from ~ 621 to ~ 684 mbsf), within MZ 2, has slightly higher values compared to adjacent samples. MZ 3 (from ~ 719.4 to ~ 885 mbsf) has higher magnetic mineral concentrations. MZ 4 (from ~ 890.5 to $\sim 1,099$ mbsf) has the lowest values. Below MZ 1, down-core rock magnetic variations do not appear to correlate with lithological units. This is evident in Lithologic Unit IV, which includes MZs 3 and 4, which have higher and lower magnetic mineral concentrations, respectively (Figure 2). The MZs are described further below.

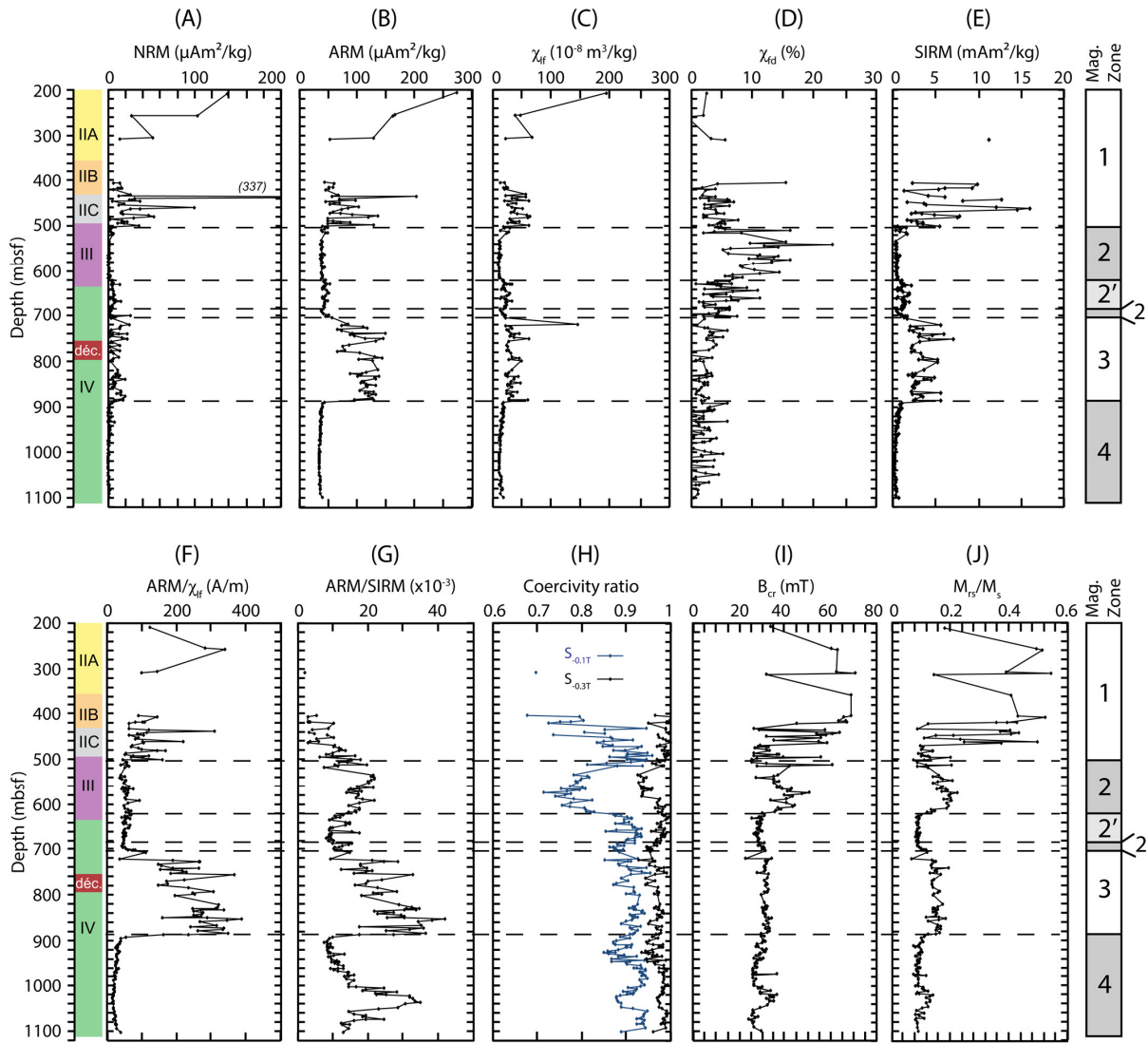


Figure 2. Down-core rock magnetic and coercivity variations at Site C0023. (a) Natural remanent magnetization (NRM), (b) anhysteretic remanent magnetization (ARM), (c) magnetic susceptibility χ_{f1} , (d) frequency-dependent susceptibility χ_{fd} , (e) saturation isothermal remanent magnetization (SIRM), (f) ARM/ χ_{f1} , (g) ARM/SIRM, (h) coercivity ratios, (i) remanent coercivity B_{cr} , and (j) M_{rs}/M_s . Discrete sample measurements are shown in (a–h), whereas (i and j) are dry powder sister sample measurements. Four major magnetic zones (MZs), indicated on the right, are identified from magnetic changes. MZs 1 and 3 correspond to higher magnetic mineral concentrations; MZs 2 and 4 correspond to lower concentrations. On the left, the Lithologic Units (IIA to IV) and décollement (“déc.”) are from Heuer et al. (2017).

Lower concentration-dependent magnetic parameters could partially reflect dilution by increased carbonate (CaCO_3) contents. At Site C0023, CaCO_3 contents are generally scattered with an average of ~ 3.4 wt% and vary between 0.07 and 21.6 wt% (Figure S2 in Supporting Information S1; Heuer et al., 2017). Higher CaCO_3 values coincide with calcite veins and cements (Heuer et al., 2017). In the studied interval, ferrimagnetic mineral concentrations can only be diluted by a factor of 1.2 at maximum (dilution factor = $(100 - \text{CaCO}_{3\text{min}})/(100 - \text{CaCO}_{3\text{max}})$) where $\text{CaCO}_{3\text{min}} = 0.1$ and $\text{CaCO}_{3\text{max}} = 16.5$ are the minimum and maximum CaCO_3

contents (wt%), respectively; Heuer et al., 2017). Therefore, carbonate dilution alone cannot explain the order of magnitude NRM, ARM, and SIRM decrease between MZs 1 and 2, and between MZs 3 and 4. Grain size parameters, ARM/χ_{lf} and $ARM/SIRM$, behave differently down-core (Figure 2). ARM/χ_{lf} mirrors ARM variations and suggests the presence of finer magnetic grains in MZs 1 and 3. Lu and Banerjee (1994) suggested use of $ARM/SIRM$ at nearby Site 808 because it is less sensitive to paramagnetism. Higher $ARM/SIRM$ values suggest the presence of finer magnetic grains at the top of MZ 2, in MZ 3, and in a small interval within MZ 4. As discussed below, a mixture of magnetic minerals with different compositions, and in low concentrations in some intervals, challenge interpretation of these two ratios as magnetic grain size proxies.

3.1 Magnetic zone 1 (~207 to ~498 mbsf)

MZ 1 corresponds to Lithologic Subunits IIA, IIB, IIC, and the top of Unit III. NRM, χ_{lf} , ARM, and SIRM are higher in MZ 1 compared to underlying sediments. These parameters are highest in Subunit IIA and indicate a higher magnetic mineral concentration, with high SIRM values in Subunit IIA due to the presence of high coercivity ferrimagnetic iron sulfides as shown below. $S_{-0.1T}$ is as low as 0.7 and B_{cr} is ~60 mT in Subunit IIA with lower values (< 40 mT) likely corresponding to iron oxides (Figure 2).

Thermomagnetic curves indicate a mixture of magnetic minerals. Slope breaks at ~300–350°C, ~560°C, and ~650°C correspond, respectively, to thermal alteration of ferrimagnetic iron sulfides (greigite and/or pyrrhotite) and to Curie/Néel temperatures of (titano-)magnetite and hematite (Dunlop and Özdemir, 1997) (Figures S3a and S3e in Supporting Information S1). Hematite could be either detrital or a result of magnetite alteration during heating (van Velzen and Zijdeveld, 1992). Ferrimagnetic iron sulfides are only present in higher coercivity samples (i.e., with $B_{cr} > 40$ mT).

Low-temperature magnetic measurements cannot discriminate the presence of greigite because it does not have a low-temperature magnetic transition (Chang et al., 2009; Roberts et al., 2011). A transition is evident in RT-SIRM, ZFC, and FC curves at ~115 K, which is close to the Verwey transition temperature in magnetite ($T_V = 120$ K) (e.g., Muxworthy and McClelland, 2000; Özdemir et al., 2002) (Figures S3c, S3d, S3g and S3h in Supporting Information S1). The RT-SIRM curve is not reversible through T_V , which suggests the presence of single vortex (SV) to multidomain (MD) (titano-)magnetite (Özdemir et al., 2002). Selected samples have a clear Besnus transition due to monoclinic (4C) pyrrhotite at ~35 K (Besnus and Meyer, 1964; Dekkers et al., 1989; Rochette et al., 1990).

Conventional FORC diagrams either have closed contours with a 50–70 mT peak coercivity (Figure S3b in Supporting Information S1), which is typical of interacting single-domain (SD) greigite (e.g., Roberts et al., 2006, 2011), or triangular contours with peak coercivity at ~10–20 mT (Figure S3f in Supporting Information S1), which suggest the occurrence of vortex state iron oxides (e.g., Roberts et al., 2000, 2017; Muxworthy and Dunlop, 2002; Lascu et al., 2018). A few FORC diagrams have kidney-shaped contours typical of SD 4C (Wehland et al., 2005) or 3C pyrrhotite (Horng, 2018). To better characterize the domain states of magnetic minerals, additional FORC-type diagrams were measured for a subset of samples from MZ 1. Conventional FORC diagrams confirm the presence of SD greigite (Figure 3a). The positive region along the negative B_i axis in remFORC diagrams suggests the presence of viscous SP/SD particles (Zhao et al., 2017; Figure 3b). Two “wings” along the B_u axis with low coercivity peaks are present in tFORC diagrams (Figure 3c), which are typical of SV grains (Roberts et al., 2017; Zhao et al., 2017) or interacting SD particles (Harrison et al., 2018). Such grains are not evident in conventional FORC diagrams for sister samples (e.g., Figure S3b in Supporting Information S1), possibly because their contribution is lower than that of SD greigite. The negative-positive-negative pattern in the iFORC diagram (Figure 3d) indicates the presence of SD particles. A few samples from the bottom of MZ 1 have triangular FORC diagrams with low coercivity peaks (10–20 mT) and no evidence of ferrimagnetic iron sulfides (Figure S4 in Supporting Information S1). The iFORC diagram has two adjacent patterns: a negative-positive-negative response due to SD particles and a negative-positive-negative-positive response due to SV particles (Figure S4 in Supporting Information S1). Other rock magnetic results suggest that these grains are iron oxides (Figure S3 in Supporting Information S1).

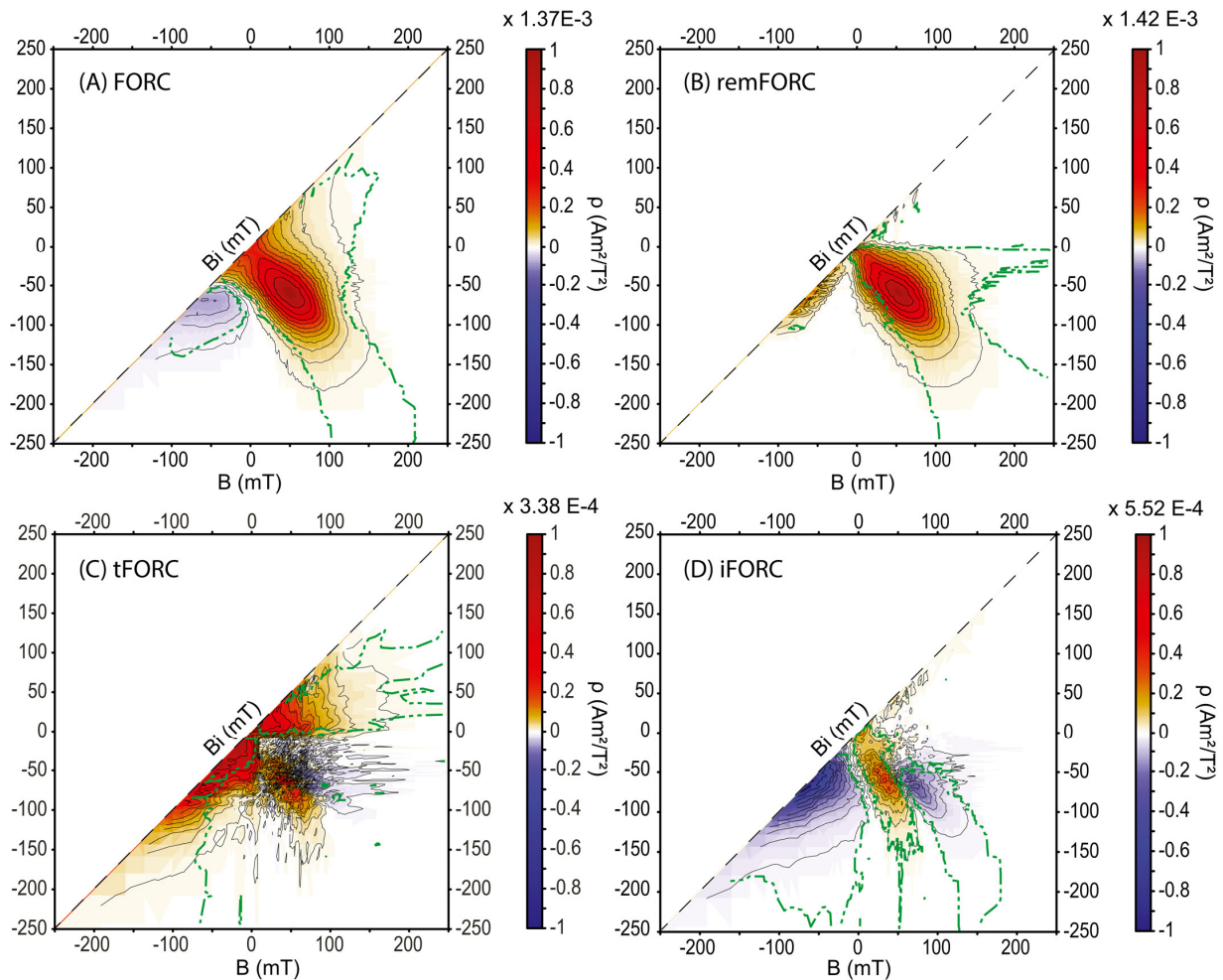


Figure 3. First-order reversal curve (FORC)-type diagrams for Sample 370-C0023A-7X-1W, 32–34 cm (depth: 305.32 meters below seafloor) in Magnetic Zone (MZ) 1. (a) Conventional FORC diagram, (b) remanent FORC (remFORC) diagram, (c) transient hysteresis FORC (tFORC) diagram, and (d) induced FORC (iFORC) diagram. This sample has high coercivity ($B_{cr} = 62$ mT). Green contours indicate the 0.05 significance level for the FORC distributions calculated according to Heslop and Roberts (2012). Complementary rock magnetic data discussed in the text for this sample are shown in Figure S3 in Supporting Information S1. See Figures S3 and S4 in Supporting Information S1 for a low coercivity ($B_{cr} = 28$ mT) sample from MZ 1.

3.2 Magnetic zone 2 (~500 to ~704 mbsf)

NRM, χ_{lf} , ARM, and SIRM are lower in MZ 2 by about an order of magnitude compared to MZ 1 (Table S1 in Supporting Information S2), which suggests a lower magnetic mineral concentration. In this zone, $\chi_{fd}\%$ is higher compared to adjacent zones by a factor of 5–10 (Figure 2). This indicates that smaller SP/SD particles are more abundant, especially in upper MZ 2 (~500 to ~620 mbsf), which corresponds roughly to Lithologic Unit III. Ash layers are abundant in this interval (Heuer et al., 2017), and the SP/SD grains likely come from disseminated volcanic ashes, even though discrete ash layers were avoided during sampling. Magnetic measurements indicate a simpler magnetic mineral assemblage compared to that of MZ 1, which is composed mainly of low coercivity minerals. Thermomagnetic results (Figure

S5a in Supporting Information S1) have a slope break at $\sim 570\text{--}575^\circ\text{C}$, which is indicative of magnetite, and at $\sim 650^\circ\text{C}$, which is indicative of hematite. By contrast to MZ 1, no slope break is observed at $300\text{--}350^\circ\text{C}$. Low-temperature magnetic measurements (Figures S5c and S5d in Supporting Information S1) have a marked irreversible Verwey transition, which supports the presence of magnetite. All measured conventional FORC diagrams have triangular contours with peak coercivity $< 20\text{--}30$ mT (Figure S5b in Supporting Information S1), which is characteristic of vortex state magnetic grains (e.g., Roberts et al., 2017; Lascu et al., 2018). FORC and tFORC diagrams have low coercivity SV magnetic minerals with typical wing-shaped contours (Figures 4a and 4c) and a noisy negative-positive-negative-positive iFORC pattern (Figure 4d). Non-interacting SD particles with higher coercivities may be present, as indicated by a tail along the B_c axis. A remFORC diagram has a positive region on the negative B_i axis that indicates thermal activation of particles near the SP/SD threshold size (Figure 4b), which is consistent with higher $\chi_{fd}\%$ values (Figure 2).

Within MZ 2, a thin interval (~ 621 to ~ 684 mbsf) has slightly higher NRM, ARM, χ_{lf} , and SIRM values (Figure 2), which suggest higher magnetic mineral concentrations. This zone was defined as MZ 2' in nearby sites (Shipboard Scientific Party, 1991, 2001). In this zone, $\chi_{fd}\%$ decreases, which indicates less abundant SP particles (Figure 2). The magnetic mineralogy in MZ 2' is not different from that of MZ 2 with vortex state magnetite and hematite present. However, the average coercivity is slightly different between MZs 2 and 2'. The former has a larger higher coercivity mineral contribution. $S_{-0.1T}$ and $S_{-0.3T}$ are lower and the average B_{cr} value is ~ 36 mT in MZ 2 (compared to ~ 29 mT in MZ 2') (Table S2 in Supporting Information S2).

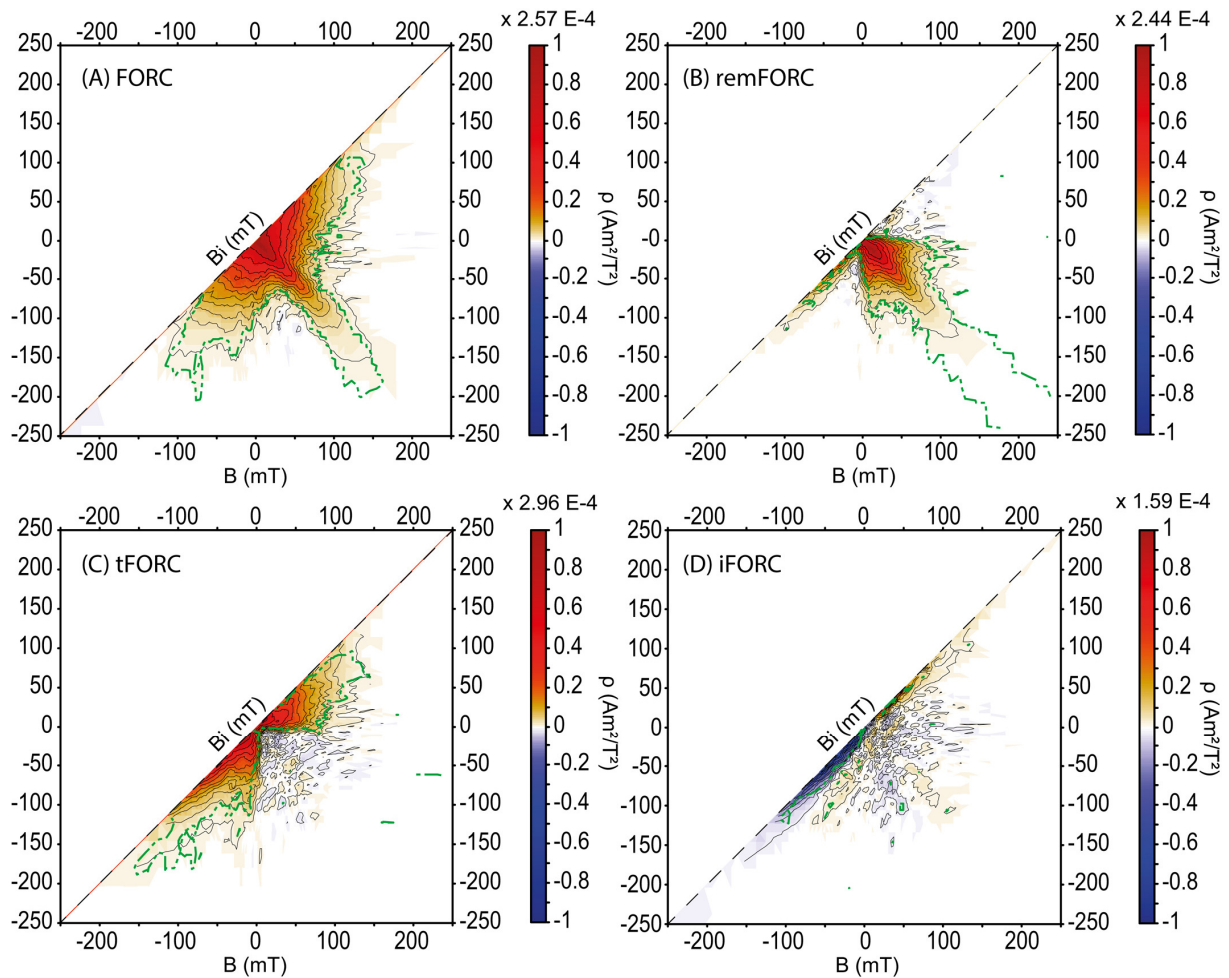


Figure 4. First-order reversal curve (FORC)-type diagrams for Sample 370-C0023A-50R-5W, 40–42 cm (depth: 696.53 meters below seafloor) in Magnetic Zone 2. (a) Conventional FORC diagram, (b) remanent FORC (remFORC) diagram, (c) transient hysteresis FORC (tFORC) diagram, and (d) induced FORC (iFORC) diagram. Green contours indicate the 0.05 significance level for the FORC distributions calculated according to Heslop and Roberts (2012). Complementary rock magnetic data discussed in the text for this sample are shown in Figure S5 in Supporting Information S1.

3.3 Magnetic zone 3 (~719.4 to ~885 mbsf)

MZ 3 lies within Lithologic Unit IV and has higher NRM, ARM, χ_{lf} , and SIRM compared to MZs 2 and 4 (Figure 2). These parameters have lower average values (Table S1 in Supporting Information S2) than in MZ 1, except for ARM, which is higher in MZ 3 compared to MZ 1 and is nearly one order of magnitude higher than NRM, which suggests the occurrence of SD grains. These parameters have slightly lower values in the décollement zone (Figure 2) where the mean B_{cr} is ~32 mT, which is higher than in MZs 2' and 4 (Table S2 in Supporting Information S2).

Thermomagnetic measurements (Figure S6a in Supporting Information S1) indicate a mixture of titanomagnetite ($T_C \sim 465\text{--}470^\circ\text{C}$), magnetite ($T_C \sim 560^\circ\text{C}$), and hematite ($T_N \sim 620\text{--}650^\circ\text{C}$) in MZ 3. The Curie/Néel temperatures of magnetite and hematite are slightly lower than

expected, which suggests that they are non-stoichiometric. Titanomagnetite and hematite are not always indicated in high temperature measurements. Low-temperature magnetization curves contain, similar to the intervals above, a well-marked Verwey transition (Figures S6c and S6d in Supporting Information S1), with two shoulders at ~ 100 and ~ 120 K, as seen in first derivatives of ZFC and FC curves (Figure S6d in Supporting Information S1). This suggests the presence of two (titano)-magnetite populations with different stoichiometry or grain size rather than a mixture of biogenic or detrital magnetite (Chang et al., 2016). Conventional FORC diagrams (Figure S6b in Supporting Information S1) are similar to those for MZ 2, with triangular-shaped contours and mean coercivity < 20 - 30 mT. However, interactions among magnetic particles are slightly stronger in samples from MZ 3, which likely indicates a higher SD particle contribution. FORC and tFORC diagrams are typical of low coercivity vortex state minerals (Figures 5a and 5c), which is supported by a negative-positive-negative-positive iFORC pattern (Figure 5d). Non-interacting SD particles with higher coercivities are present, as indicated by a marked tail along the B_c axis, compared to MZ 2 (Figure 4a). A remFORC diagram contains a strong signal due to thermal activation in viscous SP/SD particles (Figure 5b), as characterized by the positive region along the negative B_i axis, compared to MZ 2 (Figure 4b).

MZ 3 includes the décollement zone (758.15–796.4 mbsf) with alternating meter-thick intact intervals and thinner fault zones (Heuer et al., 2017). In the décollement zone, ARM, χ_{IF} , and SIRM are lower than in adjacent areas (Figure 2). However, the coercivity (Figure 2) and magnetic mineral assemblage identified from low and high temperature measurements and FORC diagrams are not different from the rest of MZ 3.

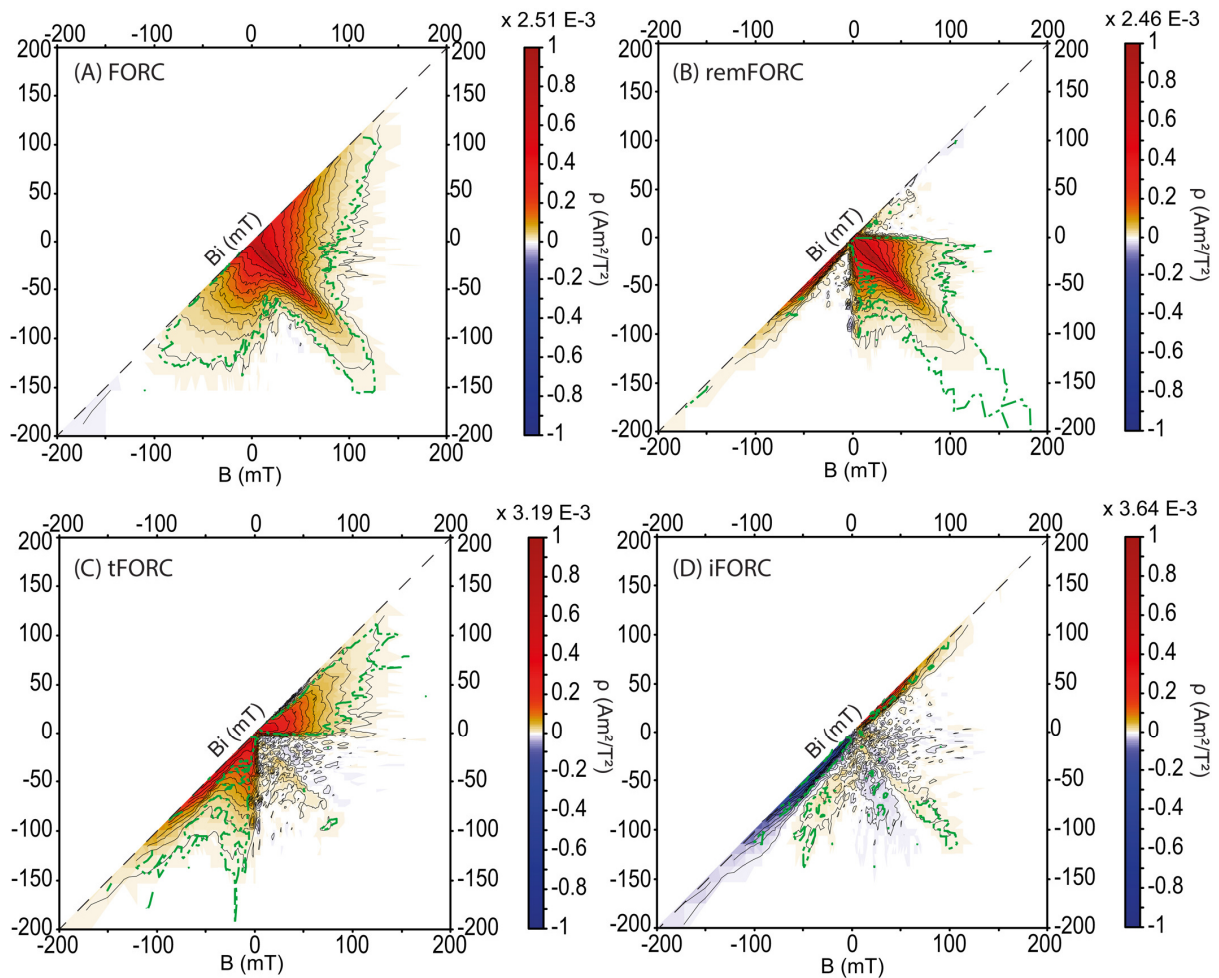


Figure 5. First-order reversal curve (FORC)-type diagrams for Sample 370-C0023A-61R-3W, 70–72 cm (depth: 750.51 meters below seafloor) in Magnetic Zone 3. (a) Conventional FORC diagram, (b) remanent FORC (remFORC) diagram, (c) transient hysteresis FORC (tFORC) diagram, and (d) induced FORC (iFORC) diagram. Green contours indicate the 0.05 significance level for the FORC distributions calculated according to Heslop and Roberts (2012). Complementary rock magnetic data discussed in the text for this sample are shown in Figure S6 in Supporting Information S1.

3.4 Magnetic zone 4 (~890.5 to ~1,099 mbsf)

MZ 4 occurs in the lower half of Lithologic Unit IV. NRM, χ_{lf} , ARM, and SIRM are the lowest on average compared to overlying MZs (Table S1 in Supporting Information S2), which indicate lower magnetic mineral contents. Magnetic parameters do not vary much in this interval, except for a 50-m thick interval (~1,000–1,050 mbsf) where ARM/SIRM, M_{rs}/M_s , and B_{cr} are higher and coercivity ratios lower (Figure 2). Magnetic results for samples from MZ 4 are similar to those from MZ 2. Thermomagnetic, low-temperature, and conventional FORC results are comparable (Figure S7 in Supporting Information S1) and the main identified magnetic phases are coarse vortex state magnetite and hematite. FORC diagrams are identical and indicate the presence of low coercivity vortex state particles, probable viscous particles

near the SP/SD threshold size, and a higher coercivity magnetic phase (Figure 6). Overall, MZ 4 is similar to MZ 2 and differs only by having a lower magnetic mineral concentration.

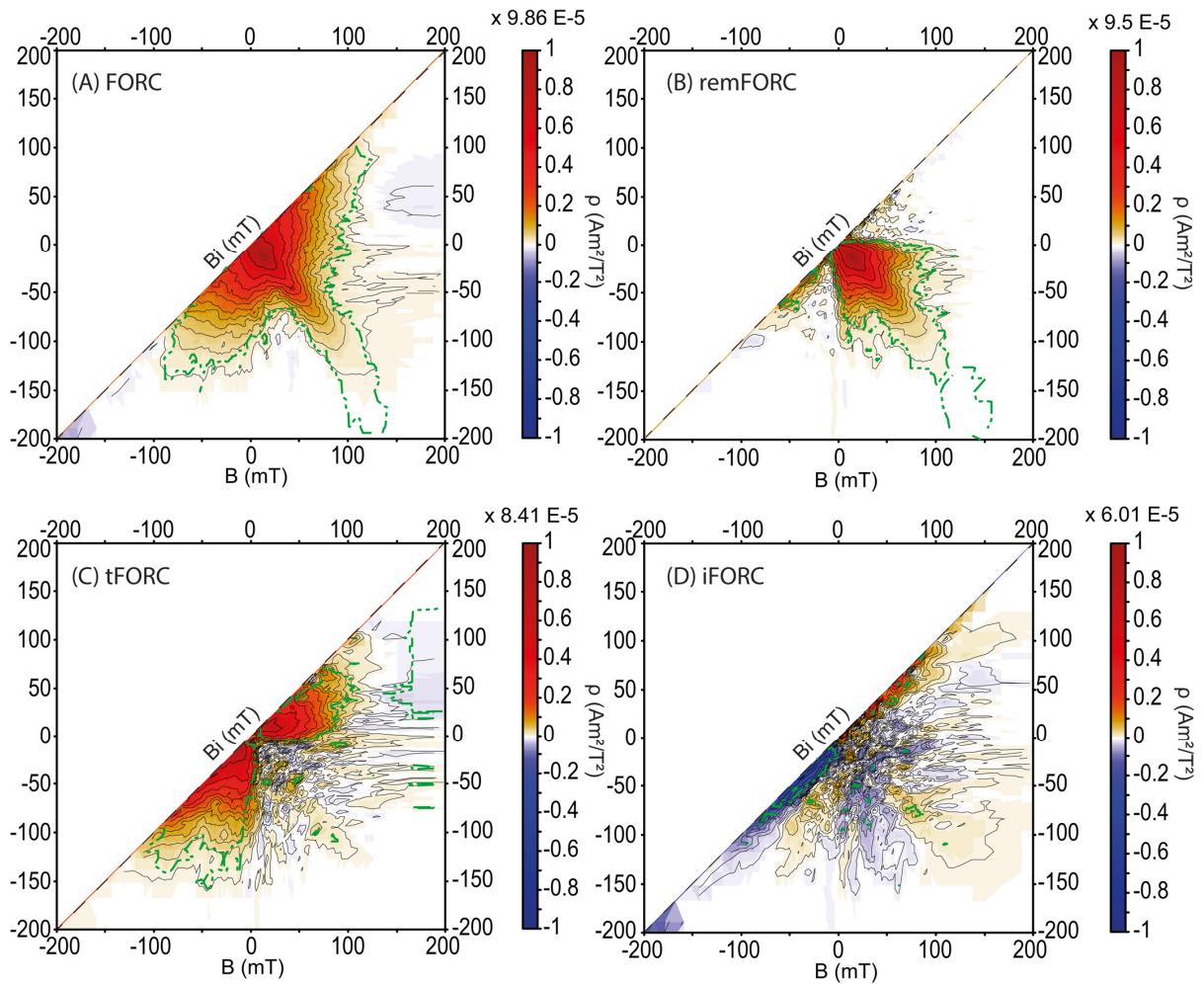


Figure 6. First-order reversal curve (FORC)-type diagrams for Sample 370-C0023A-93R-6W, 48–50 cm (depth: 962.99 meters below seafloor) in Magnetic Zone 4. (a) Conventional FORC diagram, (b) remanent FORC (remFORC) diagram, (c) transient hysteresis FORC (tFORC) diagram, and (d) induced FORC (iFORC) diagram. Green contours indicate the 0.05 significance level for the FORC distributions calculated according to Heslop and Roberts (2012). Complementary rock magnetic data discussed in the text for this sample are shown in Figure S7 in Supporting Information S1.

3.5 Magnetic mineral assemblage at Site C0023: summary

To summarize, the magnetic mineral assemblage at Site C0023 is dominated by vortex state (titano-)magnetite, which is found in all MZs (Figure S8 in Supporting Information S1). Weakly interacting higher coercivity grains are also present in all zones, which could be detrital SD hematite (identified by its Néel/Curie temperature in thermomagnetic curves). Iron oxides at Site C0023 are mainly detrital and are present in the four MZs with varying grain sizes and concentrations (Figure S9 in Supporting Information S1). MZ 1 is the only zone that contains

authigenic ferrimagnetic iron sulfides. MZs 2 and 4 have similar magnetic mineral assemblages, with low vortex state (titano-)magnetite concentrations as indicated by down-core concentration-dependent parameter variations (Figure 2). Dia- and para-magnetic contributions are high (> 60%) in MZs 2 and 4 (Figure S8 in Supporting Information S1), while ferrimagnetic contributions are higher in MZs 1 and 3.

4. Discussion

Magnetic mineral assemblages at Site C0023 vary with depth to define four main MZs. This zonation cannot only be explained by depositional processes because the lithologic units, which represent specific depositional episodes and/or sediment provenance changes (Heuer et al., 2017), do not always correspond to the MZs. The overall sediment composition (sediment type, grain size, CaCO₃ content) does not vary significantly among the four MZs (Figure S10 in Supporting Information S1). However, sedimentation rates (Hagino and the Expedition 370 Scientists, 2018) and organic matter contents (Figure S2 in Supporting Information S1; Heuer et al., 2017) vary at Site C0023 and control mainly the extent of diagenetic alteration of magnetic mineral assemblages. Diagenetic processes at Site C0023 have been reconstructed by Köster et al. (2021a) based on sedimentary Fe pool analysis. In the following, we discuss the rock magnetism of Site C0023 along with the findings of Köster et al. (2021a) and propose a burial diagenetic magnetic model for this site (Figures 7 and 8). Figure 8 gathers key information on the timing of key diagenetic events for the different formations, and stability fields for key iron minerals.

4.1 Depositional environment and SMT zones

Site C0023 experienced depositional environment changes during its tectonic displacement from the Shikoku Basin to the Nankai Trough. This was accompanied by burial temperature and resulting (bio-)geochemical process changes (Horsfield et al., 2006; Tsang et al., 2020; Köster et al., 2021a). The Lower Shikoku Basin facies (Lithologic Unit IV ~637–1,112 mbsf; 13.53–2.53 Ma) was deposited in an organic carbon-starved, low sedimentation abyssal environment (Köster et al., 2021a). Aerobic conditions prevented reductive dissolution and favored detrital magnetic mineral preservation, mainly iron (oxyhydr)oxides (Figures 7 and 8). As Site C0023 moved toward the Japanese island arc, sedimentation rates and organic carbon supply increased, leading to organoclastic iron and sulfate reduction as well as biogenic methanogenesis, and, thus, to anoxic depositional conditions for the Upper Shikoku Basin facies (Unit III at ~494–637 mbsf; 2.43–0.43 Ma, Köster et al., 2021a) (Figures 7 and 8).

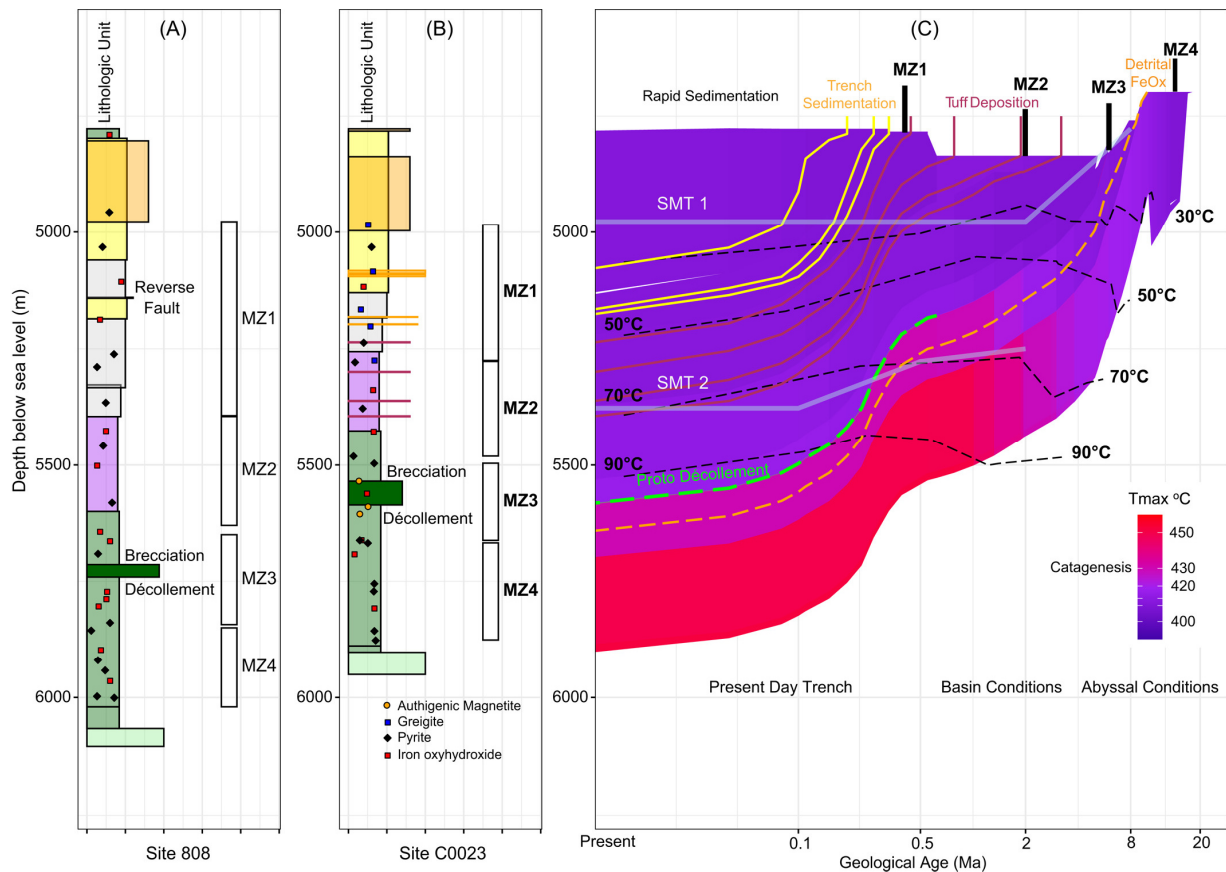


Figure 7. Lithological logs for (a) Sites 808 (Shipboard Scientific Party, 1991) and (b) C0023 (Heuer et al., 2017), with (c) illustration of the burial history at C0023 and key events. The color code for lithologic units and décollement is from Heuer et al. (2017). Magnetic zones (MZs) and associated main magnetic minerals (represented by different symbols) at Sites 808 (Lu and Banerjee, 1994) and C0023 (this study) are indicated. See also Figure S11 in Supporting Information S1 for magnetic correlation between sites. T_{max} is the RockEval parameter and $T_{max} \sim 435^{\circ}\text{C}$ indicates the onset of catagenesis. The two sulfate-methane transitions (SMTs; Köster et al., 2021a) discussed in the text are reported. Time is indicated on a log scale to illustrate recent events and consequent processes (< 0.5 Ma) that control diagenetic processes. Points used to construct Figure 8 are identified.

Following the onset of methanogenesis, sulfate diffusing down from the overlying seawater reacted with biogenic methane during AOM and a shallow SMT formed (Köster et al., 2021a). Therefore, most of the Upper Shikoku Basin facies was buried beneath a SMT by ~ 2 Ma (SMT 1 in Figures 7 and 8). Downward diffusing methane (from shallow SMT 1) reacted with residual upward diffusing sulfate in Unit IV to form a second, reverse SMT (SMT 2 in Figures 7 and 8; Köster et al., 2021a). Iron (oxyhydr)oxides were reduced by hydrogen sulfide produced during AOM to form iron sulfides (pyrite). The onset of SMT 2 coincided with the onset of catagenesis at 2 Ma in MZ 3 (Figures 7 and 8). Methane in SMT 2 is, thus, partly produced during catagenesis because Unit IV has generated thermogenic methane since 2 Ma (Figure 7). At SMT 2, methane and sulfate were consumed, and dissolved sulfide was released into porewater.

This led to deep reductive iron dissolution in Unit IV with alteration of original magnetic mineral assemblages and pyrite formation occurring several million years after deposition (Köster et al., 2021a). At ~0.5 Ma, Site C0023 reached the Nankai Trough and the sedimentary and depositional environment changed to trench-deposited formations (Units IIA-IIC) that favored rapid burial below the shallow SMT with authigenic greigite preservation (Figure 7). About half of the sediment cover was deposited in < 10% of the site history (Figure 7).

The presence of two SMTs can explain the nature of the magnetic mineral assemblages in MZs 2 and 4, that is, few preserved detrital ferrimagnetic minerals with authigenic pyrite formed from post-depositional reductive dissolution (Figure 8). However, it does not satisfactorily explain MZ 3. The present-day deep reverse SMT (between 640 and 764 mbsf) occurs in lowermost MZ 2 (including MZ 2') and upper MZ 3. Despite MZs 2 and 3 both being similarly situated with respect to SMT 2, they have contrasting magnetization and magnetic mineral assemblages.

Between ~400 and 600 mbsf, Fe²⁺ release coincides with abundant ash layers (Figures 7 and S2 in Supporting Information S1) where dissolved silica (Si[OH]₄) averages about 500 μM (Heuer et al., 2017). Magnetite is unstable under elevated porewater silica concentrations, such as those around abundant silicic volcanic ashes, and will dissolve rapidly to produce Fe-bearing smectite (Florindo et al., 2003). The dissolved silica concentration at Site C0023 is lower than in silica-rich sediments in which magnetite dissolution has been reported (Florindo et al., 2003). Although (abiotic) silicate weathering could partly explain Fe²⁺ release (e.g., Luo et al., 2020), this is not the main mechanism that explains low magnetic susceptibility values in MZ 2. Therefore, it is reasonable to consider potential biogeochemical processes in MZs 2 and 3. DNA-based community analyses for samples below ~320 mbsf are not informative because of low vegetative cell concentrations, and no cells or endospores are detectable between 840 and 1,100 mbsf, that is, in MZ 4 (Heuer et al., 2020). The current depth of the lower reverse SMT has a temperature of ~85°C (Heuer et al., 2020), which is the “cut-off” temperature for microbial life in the surface of deep petroleum reservoirs (Head et al., 2003) and in the hot Guaymas Basin (McKay et al., 2016). However, microorganisms can still be active at this temperature (Kallmeyer and Boetius, 2004; Holler et al., 2011), so microbial processes need not be ruled out based on this temperature threshold alone. If present-day AOM reactions are active in the deep reverse SMT, they probably have extremely low rates (Köster et al., 2021a), and are unlikely to explain magnetic mineral assemblage differences between MZs 2 and 3. Subsurface temperatures at C0023 were also higher in the near past (Horsfield et al., 2006;

Tsang et al., 2020), so both MZs have been heated to temperatures near the “cut-off” for life in petroleum reservoirs (Figure 7).

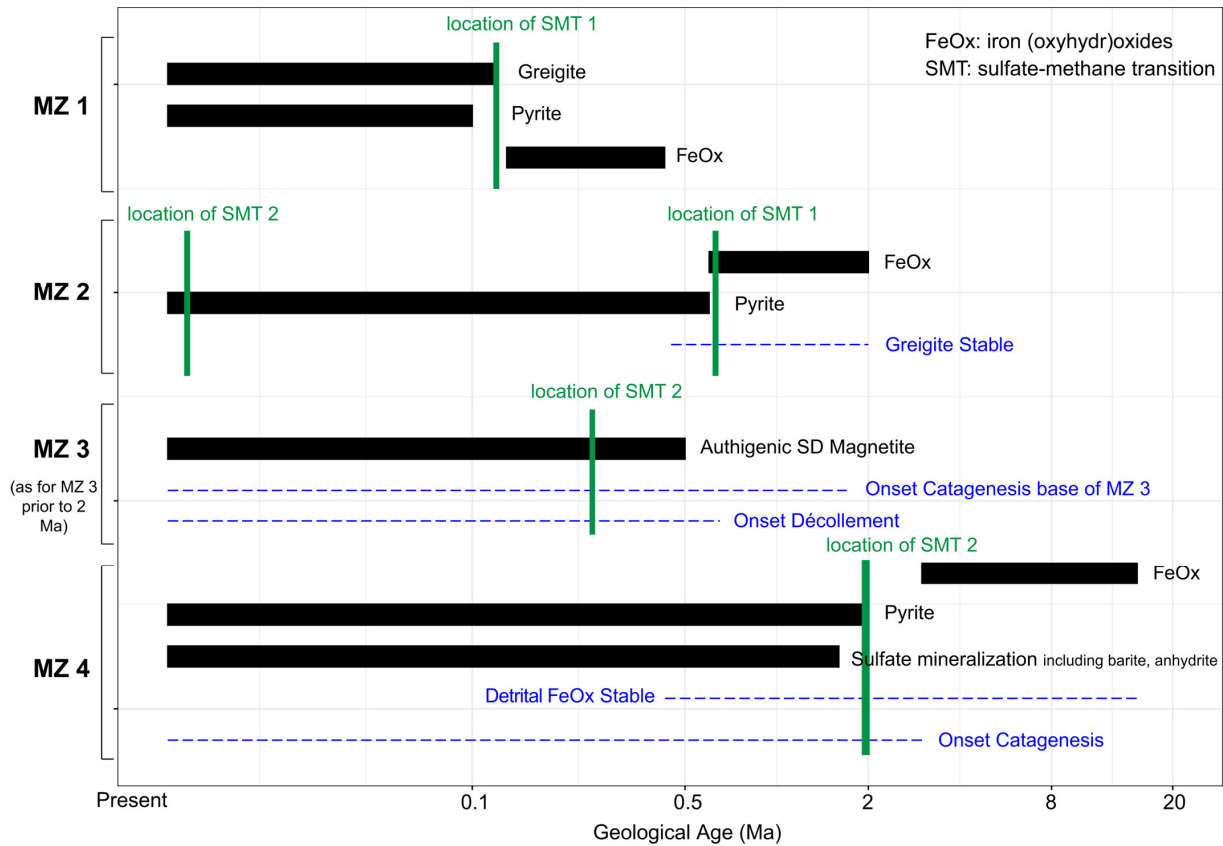


Figure 8. Paragenesis proposed from basin analysis (Tsang et al., 2020 and Figure 7) and magnetic mineral assemblage diagenetic histories discussed here and by Köster et al. (2021a). Separate paragenetic sequences are inferred for magnetic zones (MZs) 1 to 4, with a typical history indicated for the mid-point of each zone. Solid black bars indicate the main mineral phases for each MZ (Tsang et al., 2020). The dashed blue lines indicate stability fields for key iron minerals and the onset of other geological processes such as catagenesis. For example, it can be seen that MZ 2 (containing iron oxides) passes sulfate-methane transition (SMT) 1 (vertical green line) early at ~0.6 Ma, but most pyrite formation occurs much later (0.5 Ma). Based on the rate and depth of burial, greigite is inferred to have been stable until ~0.5 Ma (blue dashed line). MZ 4 would not have passed through a SMT until more than 5 million years after its deposition, with the formation of iron oxyhydroxides (FeOx) favored prior to this. Time is indicated on a logarithmic scale as for Figure 7.

4.2 Greigite formation and preservation

MZ 1 differs from the three other MZs because it contains ferrimagnetic iron sulfides. Greigite can form authigenically by different pathways either biotically or abiotically (Roberts, 2015; and references therein). Under steady state conditions, greigite eventually transforms into pyrite. The presence of greigite down to ~460 mbsf at Site C0023 suggests that *in situ* conditions favored its preservation and inhibition of pyritization, that is, by low availability of

dissolved sulfide $\text{H}_2\text{S}/\text{HS}^-$. Sulfate (SO_4^{2-}) and $\text{H}_2\text{S}/\text{HS}^-$ concentrations are low or below detection limits down to at least ~550 mbsf (Figure S2 in Supporting Information S1; Heuer et al., 2017), which favors greigite preservation (Kao et al., 2004). Shallow sediment was not drilled during IODP Expedition 370, so no information on a shallow SMT is available at Site C0023. Nevertheless, at nearby ODP Site 1174, a shallow SMT is identified below 5 mbsf (Shipboard Scientific Party, 2001), so we assume that it also occurs at Site C0023. Authigenic greigite was preserved as a microbial by-product during burial under anoxic conditions. *Atribacteria* occur above 254 mbsf at Site C0023 (Heuer et al., 2017), which provides a further indication of organic-rich anoxic (Reed et al., 2002). Greigite preservation can occur because of high sedimentation rates ($> 600 \text{ m Myr}^{-1}$ for $< 473 \text{ mbsf}$; Hagino and the Expedition 370 Scientists, 2018). Rapid burial of Units IIC-IIA through the shallow SMT gives insufficient time for full pyritization of greigite that formed ~0.5 Ma ago (Köster et al., 2021a; contrast between MZs 1 and 2 in Figure 8).

4.3 Role of burial temperature and fluids

Whereas (titano-)magnetite is ubiquitous at Site C0023 and is present in all MZs, MZ 3 (~720–885 mbsf) has an additional fine-grained magnetic phase. Larger ARMs (Figure 2) and two shoulders on derivatives of ZFC and FC curves (Figure S6 in Supporting Information S1) suggest the presence of SD magnetite, which is also supported by the IRM unmixing results of Köster et al. (2021a, 2021b). Three main hypotheses are suggested to explain the presence of authigenic fine-grained magnetite in MZ 3: (a) a burial temperature increase that may or may not be associated with hydrocarbon generation, (b) fluid circulation, (c) microbial iron reduction, or a combination of these hypotheses, as discussed further here.

(a) Present-day heat flow at Site C0023 is 140 mW m^{-2} , with an average geothermal gradient of $111^\circ\text{C km}^{-1}$ (Heuer et al., 2017; Heuer et al., 2020). This converts to down-hole temperatures of ~32–62°C, ~62–82°C, ~82–97°C, and ~97–114°C for MZs 1, 2, 3, and 4, respectively. Laboratory heating of sediments indicates that new magnetic minerals, such as magnetite, can form under the sole effect of increased temperature (e.g., Aubourg et al., 2008; Aubourg and Pozzi, 2010; Kars et al., 2012). Temperatures as low as 50°C are sufficient to form new magnetic minerals (Kars et al., 2012). Hydrocarbon generation deeper in the sediment (e.g., Elmore et al., 1987; McCabe et al., 1987; Abubakar et al., 2015; Badejo et al., 2021) and tectonic fluid circulation (e.g., McCabe et al., 1989; Elmore et al., 2001) can lead to abiotic magnetic mineral formation and/or to alteration of pre-existing magnetic minerals. Rock-Eval pyrolysis measurements were carried out to further investigate potential effects of progressive

increases in temperature, magnetic mineral content, and catagenesis (high temperature organic matter decomposition). T_{\max} varies between 349 and 450°C in the ~190–1,177 mbsf interval (average: $430 \pm 12^\circ\text{C}$; Figure S10 in Supporting Information S1) (Stein, 2021). T_{\max} is above 435°C below 800 mbsf (i.e., below the décollement), which represents the boundary between immature and mature organic matter (Tissot et al., 1987). Basin modeling also suggests that the lower part of Lithologic Unit IV below the décollement has been heated sufficiently by burial diagenesis to generate hydrocarbons since 2 Ma for the lower part of the Lower Shikoku Basin facies (Tsang et al., 2020; Figures 7 and 8). Heuer et al. (2020) reported that methane occurs with other hydrocarbons (ethane, propane, butane) at Site C0023, which were likely generated by catagenesis (Heuer et al., 2017; Heuer et al., 2020). Below ~800 mbsf, MZs 3 and 4 have distinct magnetic mineral assemblages and contrasting magnetic properties (Figure 2). MZ 4 and parts of MZ 3 have undergone catagenesis for comparable lengths of time (Figures 7 and 8), so it is unlikely that magnetite in MZ 3 is solely related to hydrocarbon generation or MZ 4 would have similar magnetite contents.

(b) Sediments underthrust below the décollement and above basement (at 775–1,121 mbsf) host hydrothermal barite (BaSO_4) and rhodochrosite (MnCO_3) that precipitated in stratabound patches and veins (Tsang et al., 2020; Figure 8). Time-limited and repeated hydrothermal fluid ingressions (~140–220°C) occurred in the underthrust sediments where short-term, localized heating may have occurred within the fracture zone (~200°C for less than a year) (Tsang et al., 2020). It is, thus, reasonable to propose that thrust faults above and faulting below the décollement (Heuer et al., 2017) facilitated fluid circulation to promote fine-grained magnetite formation in MZ 3. Authigenic magnetite could have formed from smectite-derived iron during diagenetic illitization triggered by potassium-rich brines (e.g., McCabe et al., 1989). By contrast to Lithologic Unit III (494–673.25 mbsf), which includes MZ 2 and where major tuff layers are observed, Unit IV, which includes MZ 3, consists of 97% mudstone (Heuer et al., 2017). MZ 3 (720–890 mbsf) is characterized by downward decreasing smectite contents from 80 (at ~600 mbsf) to 20 wt% (at ~850 mbsf) in association with progressive illitization (Kim et al., 2019). However, porewater K^+ is low (< 1 mM) in this interval (Heuer et al., 2017; Kim et al., 2019), although this is the present-day situation, and might not have been the case during episodic short-term pulses of hydrothermal fluids. Kim et al. (2019) suggested that thermogenic oxidative conditions exist below 700 mbsf and above 80°C to initiate abiotic illitization. Therefore, authigenic magnetite formation via hydrothermal fluid ingressions is a plausible mechanism. Sediments in MZ 4 are more compacted, porosities are lower (Heuer et al., 2017), and faulting is generally associated with closed or mineralized faults. Thus, the two MZs, that

is, MZs 3 and 4, today have contrasting hydrodynamic regimes, despite ultimately resulting from the same processes that formed the accretionary prism.

(c) Microbial iron reduction in methanogenic environments is a further mechanism to explain SD authigenic magnetite in MZ 3. It has been proposed that under variable methane seepage intensities, secondary iron (oxyhydr)oxides formed from iron sulfide oxidation associated with downward percolating oxidizing fluids and then rapidly buried below a SMT, can act as electron acceptors to form microbially driven magnetite, although the magnetite formation mechanism is yet to be determined (Lin et al., 2021). It is possible that after ~0.5 Ma, with increased methanogenesis and sediment temperature (Köster et al., 2021a), iron (oxyhydr)oxide reduction in the sediment could have occurred concurrently with fault-related fluid circulation.

4.4 Comparison with ODP Sites 808 and 1174

The MZs at Site C0023 are defined based on NRM intensity as was the case for nearby ODP Sites 808 (Shipboard Scientific Party, 1991) and 1174 (Shipboard Scientific Party, 2001). The depth and thickness of MZs differ from each other at the three sites (Table S3 in Supporting Information S2, Figure S12 in Supporting Information S1). Common features are: MZ 1 corresponds to all sedimentary facies in Unit II; MZ 2 (including MZ 2') corresponds to the lower Upper Shikoku Basin and upper Lower Shikoku Basin facies; MZ 3 includes the décollement zone at all three sites, and MZ 4 is within the Lower Shikoku Basin (Figure 8). The proximity of the three sites indicates that similar diagenetic processes are responsible for the observed magnetic mineral variations.

At Site 808, episodically enhanced non-steady state magnetite dissolution has been invoked to explain lower NRM intensities in some intervals (Lu and Banerjee, 1994). Variable sediment provenance and calcite dilution were ruled out as responsible for lower NRM intensities. Instead, catagenesis was proposed to be responsible for magnetite dissolution at Site 808 (Lu and Banerjee, 1994): CO₂ produced by catagenesis results in Fe³⁺ reduction, which causes magnetite dissolution. CaCO₃ contents and total sulfur (TS) are also higher in low intensity intervals (Lu and Banerjee, 1994). At Site C0023, CaCO₃ is not clearly higher in MZs 2 and 4 (Figure S2 in Supporting Information S1; Heuer et al., 2017). However, TS coincides with elevated chromium reducible sulfur (CRS), which suggests that Fe oxides were diagenetically converted into pyrite in the Lower Shikoku Basin facies (Köster et al., 2021a). The lower magnetic intensity in MZs 2 and 4 could be partly due to magnetite dissolution from catagenesis.

Higher hydrocarbon gas (e.g., butane and pentane) contents were detected at Site 808 (Taira et al., 1991) in low magnetic intensity intervals (Lu and Banerjee, 1994). Similar gas anomalies within the Upper and Lower Shikoku Basin facies occur at Site 1174 (Shipboard Scientific Party, 2001). At Site C0023, notable propane and i-butane increases are observed between 470 and 640 mbsf (corresponding roughly to MZ 2) and below the décollement (> 900 mbsf) (Heuer et al., 2017). These anomalies were explained at Site 808 as due to combined upward thermogenic gas migration along faults and gas production from immature kerogen (Berner and Faber, 1993). Tsang et al. (2020) showed that organic matter in underthrust sediments reaches pre-oil window to early oil window thermal maturity with temperatures < 120°C under the sole effect of burial diagenesis, which is consistent with Rock-Eval data (Figure S10 in Supporting Information S1; Stein, 2021). Higher burial paleotemperature are not expected in the low magnetic intensity zones based on basin modeling and thermal maturity proxies (Tsang et al., 2020), which rules out a higher degree of maturity in MZs 2 and 4. The onset of catagenesis with associated thermal maturity ($T_{\max} \sim 435^{\circ}\text{C}$) is insufficient to catalyze reactions that produce SD magnetic minerals in petroleum rocks. From laboratory heating experiments, Aubourg et al. (2012) and Abubakar et al. (2015), amongst others, suggested that the peak temperature of magnetic minerals is $\sim 200\text{--}250^{\circ}\text{C}$ in source rocks. It remains challenging to extrapolate laboratory results to natural processes. These two studies focused only on abiotic processes and did not consider microbial activity, which also plays a role in magnetic mineral formation during oil biodegradation (Emmerton et al., 2013). Catagenesis, as proposed by Lu and Banerjee (1994) for Site 808, is likely not the main explanation for low magnetic intensities at Site C0023. At Site 808, the higher magnetic intensity zone (i.e., MZ 3 at Site C0023) between low intensity MZs 2 and 4 was explained either as an interval with better magnetite preservation because of less corrosive porewaters or as an interval where cold water circulates and prevents catagenesis, or as a combination of both (Lu and Banerjee, 1994). SD magnetite authigenesis in MZ 3 may be a better explanation for producing higher magnetizations between the two low magnetic intensity zones. No detailed magnetic study has been published for Site 1174, but similar diagenetic processes are expected to have acted because of the close geographical proximity and similar magnetic assemblages at Sites C0023 and 808 (Shipboard Scientific Party, 2001; Figures 8 and S12 in Supporting Information S1).

5. Conclusions

At Site C0023, four major MZs are identified based on down-core magnetic properties. MZs 2 and 4 contain few magnetic minerals, which are mainly coarse relict vortex state

(titano-)magnetite that survived diagenetic dissolution. MZ 1 is a high magnetic intensity zone that contains greigite that formed as a by-product of microbial activity at a shallow SMT. Greigite is preserved because of high sedimentation rates. MZ 3 is another high magnetic intensity zone that contains authigenic fine-grained magnetite, although the process responsible for its presence is yet to be determined. Catagenesis, fluid circulation, ash alteration, and microbial iron reduction all affect magnetic mineral assemblages at Site C0023 to varying degrees. Processes such as catagenesis and elevated interstitial silica due to ash alteration would lead to magnetic mineral dissolution, whereas fluid circulation could be responsible for mineral authigenesis. Microbial iron reduction is versatile and can contribute to both magnetic mineral formation and reduction. Diagenetic processes (early/late, biotic/abiotic) are important in active tectonic settings such as the Nankai accretionary prism. They can modify paleomagnetic records substantially by changing the primary magnetic mineral assemblage and by adding later formed authigenic magnetic minerals. Therefore, to correctly interpret the paleomagnetic record, it is essential to investigate possible overprinting due to diagenetic transformations. We demonstrate the importance of combining different magnetic techniques, that is, rapid bulk measurements and more time-consuming high-resolution magnetic measurements (irregular FORCs), to characterize complex magnetic mineral assemblages. Use of irregular FORCs brings key insights into the complex magnetic mineral assemblages at Site C0023. Our study was conducted more than 25+ years after that of Lu and Banerjee (1994) at Site 808 and indicates that diagenetic processes responsible for magnetic mineralogy variations are much more complex than only catagenesis, as initially proposed, with several mechanisms possibly acting at the same time. Assessing the types and extent of non-steady state diagenetic alteration and its impact on magnetic mineralogy is important in marine sediments to assess the reliability of paleomagnetic records, including possible remagnetizations, and for redox paleo-reconstructions to determine the relative sequence of biogeochemical conditions in the geologic record. Integrated multidisciplinary magnetic, geochemical, and microbial analyses are essential to better understand diagenetic processes.

Conflict of interest

The authors declare no conflicts of interest relevant to this study.

Data availability statement

Shipboard data from IODP Expedition 370 are accessible at <https://sio7.jamstec.go.jp>. Expedition 370 Proceedings are available from

<https://publications.iodp.org/proceedings/370/370title.html>. Additional relevant data and figures are provided in Supporting Information S1 or are archived in the World Data Center PANGAEA. Rock magnetic data are available at <https://doi.pangaea.de/10.1594/PANGAEA.929380> (Kars and Köster, 2021) and thermal maturity data at <https://doi.pangaea.de/10.1594/PANGAEA.936510> (Stein, 2021).

Acknowledgements

This research used samples and data provided by the International Ocean Discovery Program (IODP). The authors thank the Marine Works Japan staff at the Kochi Core Center for support during sampling. This work was supported by the Japan Society for the Promotion of Science Grant-in-Aid for Science Research (grant 17K05681 to Myriam Kars), the German Research Foundation (DFG grants 388260220 to Male Köster and Susann Henkel, and 408178672 to Florence Schubotz), and the Australian Research Council (grant DP200100765 to Andrew P. Roberts). The authors also thank two anonymous reviewers for their constructive comments and Editor Joshua Feinberg for handling the manuscript.

References

- Abubakar, R., Muxworthy, A.R., Sephton, M.A., Southern, P., Watson, J.S., Fraser, J.S., and Almeida, T.P., 2015. Formation of magnetic minerals at hydrocarbon-generation conditions. *Marine and Petroleum Geology*, **68**, 509–519. doi:10.1016/j.marpetgeo.2015.10.003.
- Aromokeye, D.A., Oni, O.E., Tebben, J., Yin, X., Richter-Heitmann, T., Wendt, J., et al., 2021. Crystalline iron oxides stimulate methanogenic benzoate degradation in marine sediment-derived enrichment cultures. *The ISME Journal*, **15**, 965–980. doi:10.1038/s41396-020-00824-7.
- Aubourg, C., Pozzi, J.-P., Janots, D., and Sahraoui, L., 2008. Imprinting chemical remanent magnetization in claystones at 95°C. *Earth and Planetary Science Letters*, **272**, 172–180. doi:10.1016/j.epsl.2008.04.038.
- Aubourg, C., and Pozzi, J.-P., 2010. Toward a new <250 °C pyrrhotite–magnetite geothermometer for claystones. *Earth and Planetary Science Letters*, **294**, 47–57. doi:10.1016/j.epsl.2010.02.045.
- Aubourg, C., Pozzi, J.-P., and Kars, M., 2012. Burial, claystones remagnetization and some consequences to magnetostratigraphy. *Geological Society, London, Special Publication*, **371**, 181–188. doi: 10.1144/SP371.4.
- Badejo, S.A., Muxworthy, A.R., Fraser, A., Neumaier, M., Perkins, J.R., Stevenson, G.R., and Davey, R., 2021. Using magnetic techniques to calibrate hydrocarbon migration in petroleum systems modelling: A case study from the Lower Tertiary, UK Central North Sea. *Geophysical Journal International*, **227**, 617–631. doi:10.1093/gji/ggab236.

- Behar, F., Beaumont, V., and Penteadó, H.L.D.B., 2001. Rock-Eval 6 technology: Performances and developments. *Oil & Gas Science and Technology IFP*, **56**, 111–134. doi:10.2516/ogst:2001013.
- Berner, R.A., 1981. A new geochemical classification of sedimentary environments. *Journal of Sedimentary Petrology*, **51**, 359–365. doi:10.1306/212F7C7F-2B24-11D7-8648000102C1865D.
- Berner, R.A., 1984. Sedimentary pyrite formation: An update. *Geochimica et Cosmochimica Acta*, **48**, 605–615. doi:10.1016/0016-7037(84)90089-9.
- Berner, U., and Faber, E., 1993. Light hydrocarbons in sediments of the Nankai accretionary prism (Leg 131, Site 808). In: *Proceedings of the Ocean Drilling Program, Scientific Results, 131* (eds. Hill, I.A., Taira, A., Firth, J.V., et al.). College Station, TX (Ocean Drilling Program), 185–195. doi:10.2973/odp.proc.sr.131.120.1993.
- Besnus, M.J., and Meyer, A.J.P., 1964. Nouvelles données expérimentales sur le magnétisme de la pyrrhotine naturelle. In: *Proceedings of the International Conference on Magnetism* (Vol. 20). Nottingham, London: Institute of Physics, 507-511.
- Bloemendal, J., King, J.W., Hall, F.R., and Doh, S.-J., 1992. Rock magnetism of Late Neogene and Pleistocene deep-sea sediments: Relationship to sediment sources, diagenetic processes and sediment lithology. *Journal of Geophysical Research*, **97**, 4361–4375. doi:10.1029/91JB03068.
- Canfield, D.E., and Berner, R.A., 1987. Dissolution and pyritization of magnetite in anoxic marine sediments. *Geochimica et Cosmochimica Acta*, **51**, 645–659. doi:10.1016/0016-7037(87)90076-7.
- Chang, L., Roberts, A.P., Rowan, C.J., Tang, Y., Pruner, P., Chen, Q., and Horng, C.-S., 2009. Low-temperature magnetic properties of greigite (Fe₃S₄). *Geochemistry, Geophysics, Geosystems*, **10**, Q01Y04. doi:10.1029/2008GC002276.
- Chang, L., Heslop, D., Roberts, A.P., Rey, D., and Mohamed, K.J., 2016. Discrimination of biogenic and detrital magnetite through a double Verwey transition temperature. *Journal of Geophysical Research: Solid Earth*, **121**, 3–14. doi:10.1002/2015JB012485.
- Dekkers, M.J., Mattéi, J.L., Fillion, G., and Rochette, P., 1989. Grain-size dependence of magnetic behavior of pyrrhotite during its low temperature transition at 34 K. *Geophysical Research Letters*, **16**, 855–858. doi:10.1029/GL016i008p00855.
- Dunlop, D.J., and Özdemir, Ö., 1997. *Rock magnetism: Fundamentals and frontiers* (p. 573). Cambridge University Press, New York. doi:10.1017/CBO9780511612794.
- Elmore, R.D., Engel, M.H., Crawford, L., Nick, K., Imbus, S., and Sofer, Z., 1987. Evidence for a relationship between hydrocarbons and authigenic magnetite. *Nature*, **325**, 428–430. doi:10.1038/325428a0.
- Elmore, R., Kelley, J., Evans, M., and Lewchuk, M., 2001. Remagnetization and orogenic fluids: Testing the hypothesis in the Central Appalachians. *Geophysical Journal International*, **144**, 568–576. doi:10.1046/j.0956-540X.2000.01349.x.
- Emmertson, S., Muxworthy, A.R., Sephton, M.A., Aldana, M., Costanzo-Alvarez, V., Bayona, G., and Williams, W., 2013. Correlating biodegradation to magnetization in oil bearing sedimentary rocks. *Geochimica et Cosmochimica Acta*, **112**, 146–165. doi:10.1016/j.gca.2013.03.008.
- Espitalié, J., Laporte, J.L., Madec, M., Marquis, F., Leplat, P., Paulet, J., and Boutefeu, A., 1977. Méthode rapide de caractérisation des roches mères, de leur potentiel pétrolier et

- de leur degré d'évolution. *Revue de l'Institut Français du Pétrole*, **32**, 23–42. doi:10.2516/ogst:1977002.
- Florindo, F., Roberts, A.P., and Palmer, M.R., 2003. Magnetite dissolution in siliceous sediments. *Geochemistry, Geophysics, Geosystems*, **4**, 1053. doi:10.1029/2003GC000516.
- Hagino, K., and the Expedition 370 Scientists, 2018. Data report: calcareous nannofossils from the middle Miocene to Pleistocene, IODP Expedition 370 Site C0023. In: *Proceedings of the International Ocean Discovery Program Volume 370* (eds. Heuer, V.B., Inagaki, F., Morono, Y., Kubo, Y., Maeda, L., and the Expedition 370 Scientists). College Station, TX (International Ocean Discovery Program). doi:10.14379/iodp.proc.370.201.2018.
- Harrison, R.J., and Feinberg, J.M., 2008. FORCInel: An improved algorithm for calculating first order reversal curve distributions using locally weighted regression smoothing. *Geochemistry, Geophysics, Geosystems*, **9**, Q05016. doi:10.1029/2008GC001987.
- Harrison, R.J., Muraszko, J., Heslop, D., Lascu, I., Muxworthy, A.R., and Roberts, A.P., 2018. An improved algorithm for unmixing first-order reversal curve diagrams using principal component analysis. *Geochemistry, Geophysics, Geosystems*, **19**, 1595–1610. doi:10.1029/2018GC007511.
- Head, I.M., Jones, D.M., and Larter, S.R., 2003. Biological activity in the deep subsurface and the origin of heavy oil. *Nature*, **426**, 344–352. doi:10.1038/nature02134.
- Heslop, D., and Roberts, A.P., 2012. Estimation of significance levels and confidence intervals for first-order reversal curve distributions. *Geochemistry Geophysics Geosystems*, **13**, Q12Z40. doi:10.1029/2012GC004115.
- Heuer, V.B., Inagaki, F., Morono, Y., Kubo, Y., Maeda, L., and the Expedition 370 Scientists, 2017. Temperature limit of the deep biosphere off Muroto. *Proceedings of the International Ocean Discovery Program Volume 370*: College Station, TX (International Ocean Discovery Program). doi:10.14379/iodp.proc.370.2017.
- Heuer, V.B., Inagaki, F., Morono, Y., Kubo, Y., Spivack, A., Viehweger, B., et al., 2020. Temperature limits to deep seafloor life in the Nankai Trough subduction zone. *Science*, **370**, 1230-1234. doi:10.1126/science.abd7934.
- Holler, T., Widdel, F., Knittel, K., Amann, R., Kellermann, M.Y., Hinrichs, K.-U., et al., 2011. Thermophilic anaerobic oxidation of methane by marine microbial consortia. *The ISME Journal*, **5**, 1946-1956. doi:10.1038/ismej.2011.77.
- Hornig, C.-S., 2018. Unusual magnetic properties of sedimentary pyrrhotite in methane seepage sediments: Comparison with metamorphic pyrrhotite and sedimentary greigite. *Journal of Geophysical Research: Solid Earth*, **123**, 4601-4617. doi:10.1002/2017JB015262.
- Horsfield, B., Schenk, H.J., Zink, K., Ondrak, R., Dieckmann, V., Kallmeyer, J., et al., 2006. Living microbial ecosystems within the active zone of catagenesis: implications for feeding the deep biosphere. *Earth and Planetary Science Letters*, **246**, 55-69. doi:10.1016/j.epsl.2006.03.040.
- Housen, B.A., and Musgrave, R.J., 1996. Rock-magnetic signature of gas hydrates in accretionary prism sediments. *Earth and Planetary Science Letters*, **139**, 509–519. doi:10.1016/0012-821X(95)00245-8.
- Jørgensen, B.B., Beulig, F., Egger, M., Petro, C., Scholze, C., and Røy, H., 2019. Organoclastic sulfate reduction in the sulfate-methane transition of marine sediments. *Geochimica et Cosmochimica Acta*, **254**, 231–245. doi:10.1016/j.gca.2019.03.016.

- Kallmeyer, J., and Boetius, A., 2004. Effects of temperature and pressure on sulfate reduction and anaerobic oxidation of methane in hydrothermal sediments of Guaymas Basin. *Applied and Environmental Microbiology*, **70**, 1231–1233. doi:10.1128/AEM.70.2.1231–1233.2004.
- Kao, S.-J., Horng, C.-S., Roberts, A.P., and Liu, K.-K., 2004. Carbon-sulfur-iron relationships in sedimentary rocks from southwestern Taiwan: Influence of geochemical environment on greigite and pyrrhotite formation. *Chemical Geology*, **203**, 153–168. doi:10.1016/j.chemgeo.2003.09.007.
- Kars, M., Aubourg, C., Pozzi, J.-P., and Janots, D., 2012. Continuous production of nanosized magnetite through low grade burial. *Geochemistry, Geophysics, Geosystems*, **13**, Q08Z48. doi:10.1029/2012GC004104.
- Kars, M., and Kodama, K., 2015a. Authigenesis of magnetic minerals in gas hydrate-bearing sediments in the Nankai Trough, offshore Japan. *Geochemistry, Geophysics, Geosystems*, **16**, 947–961. doi:10.1002/2014GC005614.
- Kars, M., and Kodama, K., 2015b. Rock magnetic characterization of ferrimagnetic iron sulfides in gas hydrate-bearing marine sediments at Site C0008, Nankai Trough, Pacific Ocean, off-coast Japan. *Earth, Planets and Space*, **67**, 18. doi:10.1186/s40623-015-0287-y.
- Kars, M., and Köster, M., 2021. Rock magnetic data of IODP Hole 370-C0023A. *PANGAEA*. doi:10.1594/PANGAEA.929380.
- Kim, J., Dong, H., Yang, K., Park, H., Elliott, W.C., Spivack, A., et al., (2019). Naturally occurring, microbially induced smectite-to-illite reaction. *Geology*, **47**, 535–539. doi:10.1130/G46122.1
- Kinoshita, M., Tobin, H., Ashi, J., Kimura, G., Lallement, S., Sreaton, E. J., Curewitz, D., Masago, H., Moe, K. T., and the Expedition 314/315/316 Scientists, 2009. *Proceedings of the Integrated Ocean Drilling Program, 314/315/316*. Washington, DC, (Integrated Ocean Drilling Program Management International, Inc.). doi:10.2204/iodp.proc.314315316.2009.
- Köster, M., Kars, M., Schubotz, F., Tsang, M.-Y., Maisch, M., Kappler, A., et al., 2021a. Evolution of (bio-)geochemical processes and diagenetic alteration of sediments along the tectonic migration of ocean floor in the Shikoku Basin off Japan. *Geochemistry, Geophysics, Geosystems*, e2020GC009585. doi:10.1029/2020GC009585.
- Köster, M., Kars, M., Schubotz, F., Tsang, M.-Y., Maisch, M., Kappler, A., et al., 2021b. Rock magnetic end-member unmixing of sediment cores from IODP Hole 370-C0023A. *PANGAEA*. doi:10.1594/PANGAEA.929317.
- Knittel, K., and Boetius, A., 2009. Anaerobic oxidation of methane: Progress with an unknown process. *Annual Review of Microbiology*, **63**, 311–334. doi:10.1146/annurev.micro.61.080706.093130.
- Larrasoana, J.C., Roberts, A.P., Musgrave, R.J., Gràcia, E., Piñero, E., Vega, M., and Martínez-Ruiz, F., 2007. Diagenetic formation of greigite and pyrrhotite in marine sedimentary systems containing gas hydrates. *Earth and Planetary Science Letters*, **261**, 350–366. doi:10.1016/j.epsl.2007.06.032.
- Lascu, I., Einsle, J.F., Ball, M.R., and Harrison, R.J., 2018. The vortex state in geologic materials: A micromagnetic perspective. *Journal of Geophysical Research: Solid Earth*, **123**, 7285–7304. doi:10.1029/2018JB015909.

- Lin, Z., Sun, X., Roberts, A.P., Strauss, H., Lu, Y., Yang, X., et al., 2021. A novel authigenic magnetite source for sedimentary magnetization. *Geology*, **49**, 360-365. <https://doi.org/10.1130/G48069.1>.
- Lovley, D.R., 1991. Dissimilatory Fe(III) and Mn(IV) reduction. *Microbiological Reviews*, **55**, 259–287. doi:10.1128/mr.55.2.259-287.1991.
- Lu, R., and Banerjee, S.K., 1994. Magnetite dissolution in deep sediments and its hydrologic implication: A detailed study of sediments from Site 808, Leg 131. *Journal of Geophysical Research*, **99**, 9051–9059. doi:10.1029/93JB03204.
- Luo, M., Torres, M. E., Hong, W.-L., Pape, T., Fronzek, J., Kutterolf, S., et al., 2020. Impact of iron release by volcanic ash alteration on carbon cycling in sediments of the northern Hikurangi margin. *Earth and Planetary Science Letters*, **541**, 116288. doi:10.1016/j.epsl.2020.116288.
- McCabe, C., Sassen, R., and Saffer, B., 1987. Occurrence of secondary magnetite within biodegraded oil. *Geology*, **15**, 7–10. doi:10.1130/0091-7613(1987)15%3C7:OOSMWB%3E2.0.CO;2.
- McCabe, C., Jackson, M., and Saffer, B., 1989. Regional patterns of magnetite authigenesis in the Appalachian basin: Implications for the mechanism of Late Paleozoic remagnetization. *Journal of Geophysical Research*, **94**, 10429–10443. doi:10.1029/JB094iB08p10429.
- McKay, L., Klokman, V.W., Mendlovitz, H.P., LaRowe, D.E., Hoer, D.R., Albert, D., Amend, J.P., and Teske, A., 2016. Thermal and geochemical influences on microbial biogeography in the hydrothermal sediments of Guaymas Basin, Gulf of California. *Environmental Microbiology Reports*, **8**, 150–161. doi:10.1111/1758-2229.12365.
- Moore, G. F., Taira, A., Klaus, A., et al., 2001. *Proceedings of the Ocean Drilling Program, Initial Reports, 190*, College Station, TX (Ocean Drilling Program).
- Moskowitz, B., Frankel, R.B., and Bazylinski, D.A., 1993. Rock magnetic criteria for the detection of biogenic magnetite. *Earth and Planetary Science Letters*, **120**, 283–300. doi:10.1016/0012-821X(93)90245-5.
- Muxworthy, A.R., and McClelland, E., 2000. Review of the low-temperature magnetic properties of magnetite from a rock magnetic perspective. *Geophysical Journal International*, **140**, 101–114. doi:10.1046/j.1365-246x.2000.00999.x.
- Muxworthy, A.R., and Dunlop, D.J., 2002. First-order reversal curve (FORC) diagrams for pseudosingle-domain magnetites at high temperature. *Earth and Planetary Science Letters*, **203**, 369–382. doi:10.1016/S0012-821X(02)00880-4.
- Özdemir, Ö., Dunlop, D.J., and Moskowitz, B.M., 2002. Changes in remanence, coercivity and domain state at low temperature in magnetite. *Earth and Planetary Science Letters*, **194**, 343–358. doi:10.1016/S0012-821X(01)00562-3.
- Parkes, R.J., Wellsbury, P., Mather, I. D., Cobb, S.J., Cragg, B.A., Hornibrook, E.R.C., and Horsfield, B., 2007. Temperature activation of organic matter and minerals during burial has the potential to sustain the deep biosphere over geological timescales. *Organic Geochemistry*, **38**, 845–852. doi:10.1016/j.orggeochem.2006.12.011.
- Peters, K.E., 1986. Guidelines for evaluating petroleum source rocks using programmed pyrolysis. *American Association of Petroleum Geologists Bulletin*, **70**, 318–329.

- Pike, C.R., Roberts, A.P., and Verosub, K.L., 1999. Characterizing interactions in fine magnetic particle systems using first order reversal curves. *Journal of Applied Physics*, **85**, 6660–6667. doi:10.1063/1.370176.
- Reed, D.W., Fujita, Y., Delwiche, M.E., Blackwelder, D.B., Sheridan, P.P., Uchida, T., and Colwell, F.S., 2002. Microbial communities from methane hydrate-bearing deep-marine sediments in a forearc basin. *Applied and Environmental Microbiology*, **68**, 3759–3770. doi:10.1128/AEM.68.8.3759-3770.2002.
- Riedinger, N., Pfeifer, K., Kasten, S., Garming, J.F.L., Vogt, C., and Hensen, C., 2005. Diagenetic alteration of magnetic signals by anaerobic oxidation of methane related to a change in sedimentation rate. *Geochimica et Cosmochimica Acta*, **69**, 4117–4126. doi:10.1016/j.gca.2005.02.004.
- Riedinger, N., Brunner, B., Formolo, M.J., Solomon, E., Kasten, S., Strasser, M., and Ferdelman, T.G., 2010. Oxidative sulfur cycling in the deep biosphere of the Nankai Trough, Japan. *Geology*, **38**, 851–854. doi:10.1130/G31085.1.
- Roberts, A.P., Pike, C.R., and Verosub, K.L., 2000. First-order reversal curve diagrams: A new tool for characterizing the magnetic properties of natural samples. *Journal of Geophysical Research*, **105**, 28461–28475. doi:10.1029/2000JB900326.
- Roberts, A.P., and Weaver, R., 2005. Multiple mechanisms of remagnetization involving sedimentary greigite (Fe₃S₄). *Earth and Planetary Science Letters*, **231**, 263–277. doi:10.1016/j.epsl.2004.11.024.
- Roberts, A.P., Liu, Q., Rowan, C.J., Chang, L., Carvallo, C., Torrent, J., and Horng, C.S., 2006. Characterization of hematite (α -Fe₂O₃), goethite (α -FeOOH), greigite (Fe₃S₄), and pyrrhotite (Fe₇S₈) using first-order reversal curve diagrams. *Journal of Geophysical Research*, **111**, B12S35. doi:10.1029/2006JB004715.
- Roberts, A.P., Chang, L., Rowan, C.J., Horng, C.-S., and Florindo, F., 2011. Magnetic properties of sedimentary greigite (Fe₃S₄): An update. *Reviews of Geophysics*, **49**, RG1002. doi:10.1029/2010rg000336.1.
- Roberts, A.P., 2015. Magnetic mineral diagenesis. *Earth-Science Reviews*, **151**, 1–47. doi:10.1016/j.earscirev.2015.09.010.
- Roberts, A.P., Almeida, T.P., Church, N.S., Harrison, R.J., Heslop, D., Li, Y., et al., 2017. Resolving the origin of pseudo-single domain magnetic behavior. *Journal of Geophysical Research: Solid Earth*, **122**, 9534–9558. doi:10.1002/2017JB014860.
- Roberts, A.P., Tauxe, L., Heslop, D., Zhao, X., and Jiang, Z., 2018. A critical appraisal of the “Day” diagram. *Journal of Geophysical Research: Solid Earth*, **123**, 2618–2644. doi:10.1002/2017JB015247.
- Rochette, P., Fillion, G., Mattéi, J.-L., and Dekkers, M.J., 1990. Magnetic transition at 30–34 Kelvin in pyrrhotite: Insight into a widespread occurrence of this mineral in rocks. *Earth and Planetary Science Letters*, **98**, 319–328. doi:10.1016/0012-821X(90)90034-U.
- Rowan, C.J., and Roberts, A.P., 2005. Tectonic and geochronological implications of variably timed magnetizations carried by authigenic greigite in marine sediments from New Zealand. *Geology*, **33**, 553–556. doi:10.1130/G21382.1.
- Rowan, C.J., Roberts, A.P., and Broadbent, T., 2009. Reductive diagenesis, magnetite dissolution, greigite growth and paleomagnetic smoothing in marine sediments: A new view. *Earth and Planetary Science Letters*, **277**, 223–235. doi:10.1016/j.epsl.2008.10.016.

- Seno, T., Stein, S., and Gripp, A.E., 1993. A model for the motion of the Philippine Sea plate consistent with NUVEL-1 and geological data. *Journal of Geophysical Research: Solid Earth*, **98**, 17941–17948. doi:10.1029/93JB00782.
- Shipboard Science Party, 1991. Site 808. In: *Proceedings of the Ocean Drilling Program, Initial Reports, 131* (eds. Taira, A., Hill, I., Firth, J.V., et al.). College Station, TX (Ocean Drilling Program), 71-269. doi:10.2973/odp.proc.ir.131.106.1991.
- Shipboard Science Party, 2001. Site 1174. In: *Proceedings of the Ocean Drilling Program, Initial Reports, 190* (eds. Moore, G.F., Taira, A., Klaus, A., et al.). College Station, TX (Ocean Drilling Program), 1-149. doi:10.2973/odp.proc.ir.190.105.2001.
- Stein, R., Rullkötter, J., and Welte, D.H., 1986. Accumulation of organic-carbon-rich sediments in the Late Jurassic and Cretaceous Atlantic Ocean - A synthesis. *Chemical Geology*, **56**, 1–32. doi:10.1016/0009-2541(86)90107-5.
- Stein, R., 2021. Rock-Eval data of IODP Hole 370-C0023A. *PANGAEA*. doi:10.1594/PANGAEA.936510.
- Taira, A., Hill, I., Firth, J.V., et al., 1991. *Proceedings of the Ocean Drilling Program, Initial Reports, 131*, College Station, TX (Ocean Drilling Program).
- Tissot, B.P., and Welte, D.H., 1984. *Petroleum formation and occurrence*. Springer-Verlag, Heidelberg, 699 pp.
- Tissot, B., Pelet, R., and Ungerer, P., 1987. Thermal history of sedimentary basins, maturation indexes, and kinetics of oil and gas generation. *AAPG Bulletin*, **71**, 1445–1466. doi:10.1306/703C80E7-1707-11D7-8645000102C1865D.
- Treude, T., Niggemann, J., Kallmeyer, J., Wintersteller, P., Schubert, C.J., Boetius, A., and Jørgensen, B.B., 2005. Anaerobic oxidation of methane in the sulfate-methane transition along the Chilean continental margin. *Geochimica et Cosmochimica Acta*, **69**, 2767–2779. doi:10.1016/j.gca.2005.01.002.
- Tsang, M. Y., Bowden, S. A., Wang, Z., Mohammed, A., Tonai, S., Muirhead, D., et al., 2020. Hot fluids, burial metamorphism and thermal histories in the underthrust sediments at IODP 370 site C0023, Nankai Accretionary Complex. *Marine and Petroleum Geology*, **112**, 104080. doi:10.1016/j.marpetgeo.2019.104080.
- Van Velzen, A.J., and Zijdeveld, J.D.A., 1992. A method to study alterations of magnetic minerals during thermal demagnetization applied to a fine-grained marine marl (Trubi formation, Sicily). *Geophysical Journal International*, **110**, 79–90. doi:10.1111/j.1365-246X.1992.tb00715.x.
- Wehland, F., Stancu, A., Rochette, P., Dekkers, M.J., and Appel, E., 2005. Experimental evaluation of magnetic interaction in pyrrhotite bearing samples. *Physics of the Earth and Planetary Interiors*, **153**, 181–190. doi:10.1016/j.pepi.2005.05.006.
- Zhao, X., Heslop, D., and Roberts, A.P., 2015. A protocol for variable resolution first-order reversal curve measurements. *Geochemistry, Geophysics, Geosystems*, **16**, 1364–1377, doi:10.1002/2014GC005680.
- Zhao, X., Roberts, A.P., Heslop, D., Paterson, G.A., Li, Y., and Li, J., 2017. Magnetic domain state diagnosis using hysteresis reversal curves. *Journal of Geophysical Research: Solid Earth*, **122**, 4767–4789. doi:10.1002/2016JB013683.

CHAPTER IV:
**Uniquely low stable iron isotopic signatures in deep marine sediments
caused by Rayleigh distillation**

Male Köster¹, Michael Staubwasser², Anette Meixner^{3,4}, Simone A. Kasemann^{3,4}, Hayley R. Manners⁵, Yuki Morono⁶, Fumio Inagaki^{7,8}, Verena B. Heuer³, Sabine Kasten^{1,3,4}, and Susann Henkel^{1,3}

¹Alfred Wegener Institute Helmholtz Centre for Polar and Marine Research, Bremerhaven, Germany

²University of Cologne, Cologne, Germany

³MARUM – Center for Marine Environmental Sciences, University of Bremen, Bremen, Germany

⁴University of Bremen, Faculty of Geosciences, Bremen, Germany

⁵School of Geography, Earth and Environmental Sciences, University of Plymouth, Plymouth, United Kingdom

⁶Kochi Institute for Core Sample Research, Japan Agency for Marine-Earth Sciences and Technology (JAMSTEC), Nankoku, Japan

⁷Mantle Drilling Promotion Office, Institute for Marine-Earth Exploration and Engineering (MarE3), JAMSTEC, Yokohama, Japan

⁸Department of Earth Sciences, Graduate School of Science, Tohoku University, Sendai, Japan

Manuscript submitted for publication in *Nature Geoscience*

The format has been adapted to the thesis format.

Abstract

Dissimilatory iron reduction (DIR) is suggested to be one of the earliest forms of microbial respiration. It plays an important role in the biogeochemical cycling of iron in modern and ancient sediments. Since microbial iron cycling is typically accompanied by iron isotope fractionation, stable iron isotopes are used as tracer for biological activity. Here we present iron isotope data for dissolved and sequentially extracted sedimentary iron pools from deep and hot seafloor sediments retrieved in the Nankai Trough off Japan. Dissolved iron is isotopically light throughout the ferruginous sediment interval but some samples have exceptionally light isotope values. Such light values have never been reported in natural marine environments and cannot be solely attributed to DIR. We show that the light isotope values are best explained by a Rayleigh distillation model in which dissolved iron is continuously removed from the pore water by diffusion and adsorption onto iron (oxyhydr)oxide surfaces. While the microbially mediated $\text{Fe(II)}_{\text{aq}}$ release has ceased due to an increase in temperature beyond the threshold of mesophilic microorganisms, the abiotic diffusional and adsorptive removal of $\text{Fe(II)}_{\text{aq}}$ continued, leading to uniquely light isotope values. These findings have significant implications for the interpretation of iron isotope records especially in deep seafloor sediments.

1. Introduction

Iron (Fe), one of the most abundant elements on Earth, is a redox-sensitive element that mainly occurs as ferrous (II) and ferric (III) Fe. Microorganisms acquire energy by reducing or oxidizing Fe between Fe(II) and Fe(III) redox/oxidation states (e.g., Melton et al., 2014). These reactions are strongly linked to the element cycles of carbon and sulfur, thus, imposing an important driver of global biogeochemical cycles. Dissimilatory Fe(III) reduction (DIR) is among the earliest microbial metabolic pathways on Earth, and Fe(III)-reducing microorganisms might be key inhabitants of the deep and hot biosphere (Vargas et al., 1998; Kashefi and Lovley, 2003).

Stable iron isotope analyses are widely applied to trace and decipher Fe sources, transport and reaction pathways in marine environments (Johnson and Beard, 2005; Severmann et al., 2006; Conway and John, 2014; Henkel et al., 2018; Homoky et al., 2021). The ratio of the two most abundant Fe isotopes (^{54}Fe and ^{56}Fe), commonly expressed as $\delta^{56}\text{Fe}$ (‰), can provide valuable insight into biogeochemical Fe cycling, and may be used as a proxy for microbially mediated processes in modern and ancient marine sediments (Beard et al., 1999; Anbar and Rouxel, 2007; Johnson et al., 2008). Notable Fe isotope fractionation occurs during redox processes (Welch et al., 2003; Crosby et al., 2005, 2007). The most pronounced fractionation of up to -3‰

compared to the average isotopic composition of igneous rocks ($\delta^{56}\text{Fe} = 0.09 \pm 0.05\%$, 1SD; Beard et al., 2003) is caused by coupled electron and Fe atom exchange between Fe(II) and Fe(III) at Fe oxide surfaces during DIR (Crosby et al., 2005, 2007). Since microbes preferentially consume ^{54}Fe over ^{56}Fe , the respective dissolved Fe is isotopically light while the residual Fe(III) becomes progressively enriched in isotopically heavy ^{56}Fe (Johnson and Beard, 2005; Crosby et al., 2007; Henkel et al., 2016). Iron isotopes also fractionate during abiotic processes, including adsorption of dissolved ($\text{Fe(II)}_{\text{aq}}$) on mineral surfaces (Icopini et al., 2004; Crosby et al., 2005, 2007) or the precipitation of Fe minerals (Bullen et al., 2001; Welch et al., 2003; Wiesli et al., 2004; Butler et al., 2005). While several studies have focused on Fe isotope fractionation during early diagenesis in shallow sediments (Severmann et al., 2006; Staubwasser et al., 2006; Henkel et al., 2016), no isotopic records exist for dissolved Fe in deep seafloor sediments so far.

Here, we investigate pore-water and solid-phase samples that were recovered during International Ocean Discovery Program (IODP) Expedition 370 from a 1,180 m deep hole (Site C0023) drilled in the Nankai Trough off Cape Muroto, Japan. Temperatures of up to 120°C at the sediment-basement interface and high heat flow characterize Site C0023 (Heuer et al., 2020). The aim of the expedition was to explore the temperature limit of microbial life and to identify geochemical and microbial signatures that differentiate the biotic and abiotic realms (Heuer et al., 2017). Shipboard data show a release of dissolved Fe in an interval characterized by elevated amounts of volcanic ash (Fig. 2a; Heuer et al., 2017). To assess the role of ash layers and the availability of Fe phases for biogeochemical processes in the deep and hot biosphere, we performed sequential extractions of reactive Fe phases on discrete volcanic ash and surrounding mud rock samples (Poulton and Canfield, 2005; Henkel et al., 2016). By combining $\delta^{56}\text{Fe}$ analyses of pore-water and extracted Fe, another aim was to decipher if the isotopic composition of dissolved and reactive solid-phase Fe is indicative of microbial Fe reduction. We initially hypothesized that negative $\delta^{56}\text{Fe}$ values in the pore water would be a strong argument for microbially driven processes. Indeed, we find extremely low $\delta^{56}\text{Fe}$ pore-water values that are unlikely to be caused by microbial Fe reduction alone. As the most likely explanation for this finding, we present a Rayleigh distillation model that includes the adsorption of $\text{Fe(II)}_{\text{aq}}$ onto Fe (oxyhydr)oxide surfaces.

2. Methods

2.1 Pore-water and sediment sampling

Pore-water and solid-phase samples were obtained from whole-round core (WRC) samples onboard *D/V Chikyu* as described in the Method Chapter of the Expedition Report (Morono et al., 2017) and by Heuer et al. (2020). Pore water was extracted by squeezing WRC samples in titanium squeezers modified after the stainless steel squeezer of Manheim and Sayles (1974), whereby contact of WRCs and pore water with oxygen was avoided until redox-sensitive parameters have been measured.

For shore-based $\delta^{56}\text{Fe}$ analyses, pore-water aliquots were acidified (100 μl /1 ml sample volume) with concentrated ultrapure HCl (TAMAPURE AA-100 grade, Tama Chemicals Co. Ltd., Japan) directly after sampling and stored in pre-cleaned vials at +4°C. The remaining solid-phase samples (i.e., whole-round squeeze cakes) were transferred into gas-tight aluminum bags, flushed with nitrogen, vacuum-sealed, and stored at -20°C for further solid-phase analyses. In addition to whole-round squeeze cakes, solid-phase samples taken from discrete ash layers were analyzed in the framework of this study. The discrete ash layers were visually identified and samples were obtained from the working halves (Supplementary Fig. 4). All sediment depths in this study are given as corrected core composite depths below seafloor (CCSF-B) in meters below seafloor (mbsf).

2.2 Pore-water analyses

Pore-water constituents were analyzed onboard *D/V Chikyu* and are described in detail in the Method Chapter of the Expedition Report (Morono et al., 2020) and in Köster et al. (2021). Briefly, dissolved Fe ($\text{Fe(II)}_{\text{aq}}$) was determined using the ferrozine method after Stookey (1970).

Pore-water samples for $\delta^{56}\text{Fe}$ analyses (n=19) were processed in the laboratory at the Alfred Wegener Institute (AWI) Helmholtz Centre for Polar and Marine Research in Bremerhaven, Germany. After evaporation and re-dissolution in 5 M HCl + 0.001% v/v suprapur[®] H₂O₂, pore-water Fe was purified from sample matrices by column chromatography using the AG-MP1 anion exchange resin according to Homoky et al. (2013). The Fe eluate was dried and re-dissolved in 1 ml of 0.3 M HNO₃. HCl and HNO₃ were of sub-boiling distilled quality. In order to exclude Fe loss during column separation, sample loading and matrix elements eluting fractions were collected in separate vials and aliquots of each sample were analyzed by inductively coupled plasma-mass spectrometer (ICP-MS; Element 2, Thermo Fisher Scientific Inc.). The loss of Fe was < 2% of the total Fe concentration in all samples. Column calibrations

with artificial pore-water samples confirmed the effective extraction of Fe from the salt matrix (e.g., Na, Ca, Mg, S) and trace metals such as Ni and Cr (Supplementary Fig. 5).

The Fe isotope measurement was performed using a Multicollector-inductively coupled plasma-mass spectrometer (MC-ICP-MS) (ThermoFinnigan Neptune) at the University of Cologne, Germany. The purified samples were measured by ICP-MS (Element 2, Thermo Fisher Scientific Inc.) and sub-samples of 0.2 ppm ($\pm 10\%$) were prepared for MC-ICP-MS analysis (Fe matching). The Neptune was equipped with an ESI Apex-Q desolvating system and standard (H) nickel cones. We used the sample-standard-bracketing (SSB) approach with the isotopic reference material (RM) IRMM-524 to correct instrumental mass bias (Schoenberg and von Blanckenburg, 2005). Data are reported as:

$$\delta^{56}\text{Fe} [\text{‰}] = \left[\left(\frac{{}^{56}\text{Fe}/{}^{54}\text{Fe}_{\text{sample}}}{{}^{56}\text{Fe}/{}^{54}\text{Fe}_{\text{IRMM-014}}} \right) - 1 \right] * 1000.$$

The instrumental reproducibility was monitored using the internal laboratory RM JM (Johnson&Matthey, Fe Puratronic wire). The measured $\delta^{56}\text{Fe}$ values for the JM samples ($0.42 \pm 0.06\text{‰}$, 2SD, $n=19$; Supplementary Fig. 6) were similar to the target value of $0.42 \pm 0.05\text{‰}$ (2SD; Schoenberg and von Blanckenburg, 2005). Uncertainty for the individual samples is expressed as twofold standard deviation (2SD) of the isotope ratio over 20 consecutive measurement cycles (Fig. 2b). Duplicate sample measurements ($n=5$) were within the uncertainty of the respective individual samples (2SD).

Two RMs of known isotopic composition (a granite rock (AC-E; Ailsa Craig Island, Scotland; Service d'Analyse des Roches et des Minéraux (SARM) and the internal laboratory standard JM; 2 and 4 ppm Fe each) underwent the same chemical processing to verify analytical accuracy and preclude Fe isotope fractionation during column chromatography. The measured $\delta^{56}\text{Fe}$ values were: 1) $0.31 \pm 0.06\text{‰}$ (2SD, $n=8$) for the RM AC-E and 2) $0.45 \pm 0.09\text{‰}$ (2SD, $n=4$) for the internal laboratory RM JM and, thus, within analytical uncertainty of the target values (AC-E: $0.320 \pm 0.010\text{‰}$, 2SD_{mean} (Craddock and Dauphas, 2010); JM: $0.42 \pm 0.05\text{‰}$, 2SD (Schoenberg and von Blanckenburg, 2005); Supplementary Fig. 7).

2.3 Solid-phase analyses

Solid-phase analyses include total acid digestions, sequential extraction of different reactive Fe pools and $\delta^{56}\text{Fe}$ analyses of extracted Fe. While bulk Fe, Al and Ti and reactive Fe contents of whole-round squeeze cake samples were taken from Köster et al. (2021), all solid-phase data of ash layer samples and $\delta^{56}\text{Fe}$ analyses were conducted in this study. Total acid digestions and

sequential extractions of ash layer samples were performed similarly as described in Köster et al. (2021). All solid-phase analyses were conducted in the laboratory at the AWI.

Total acid digestions were performed using a CEM Mars Xpress microwave system. Bulk element contents of Fe, Mn, Al and Ti were determined by inductively coupled plasma optical emission spectrometry (ICP-OES; iCAP 7400, Thermo Fisher Scientific Inc.) analysis under application of an internal yttrium standard. The RM NIST SRM 2702 and the RM MESS-4 were processed with each set of samples to monitor analytical accuracy. Recoveries were $93.4 \pm 2.8\%$ (2SD) for Fe, $93.9 \pm 4.0\%$ (2SD) for Mn, $91.3 \pm 2.4\%$ (2SD) for Al and $94.7 \pm 3.5\%$ (2SD) for Ti for NIST SRM 2702 (n=4) and $100.7 \pm 3.6\%$ (2SD) for Fe, $93.8 \pm 5.5\%$ (2SD) for Mn, $90.5 \pm 4.6\%$ (2SD) for Al and $95.1 \pm 4.2\%$ (2SD) for Ti for MESS-4 (n=4).

Sequential extractions were performed following the protocols described by Poulton and Canfield (2005) and Henkel et al. (2016) (Supplementary Tab. 2). An internal laboratory RM (HE443-077-cc; anoxic sediment from the Helgoland mud area, North Sea) was processed in each batch of samples to determine the analytical precision. Repetitive analyses of the internal laboratory RM resulted in values similar to the respective Fe and Mn contents determined over the previous years in the laboratories at the AWI (Supplementary Tab. 3).

For $\delta^{56}\text{Fe}$ analyses, the Na-acetate- and hydroxylamine-HCl-leached extracts (Fe_{aca} and Fe_{hyam}) were further processed following the protocol by Henkel et al. (2016). After repeated oxidation in a mixture of distilled HNO_3 , HCl and suprapur[®] H_2O_2 , Fe precipitation and anion exchange chromatography after Schoenberg and von Blanckenburg (2005), the purified samples were matched to 0.5 ppm ($\pm 10\%$) following ICP-OES analysis.

Iron isotope measurements of extracted Fe pools were performed on a MC-ICP-MS Neptune plus (ThermoScientific) at MARUM - Center for Marine Environmental Sciences, University of Bremen. The instrument was equipped with a normal interface and the stable introduction system (SIS) including a low flow PFA nebulizer (50 μl) and a cyclonic/Scott quartz spray chamber that was combined with a high efficiency X-cone. Similar to the pore-water $\delta^{56}\text{Fe}$ measurement, we applied SSB with the isotopic RM IRMM-014 and the internal laboratory RM JM was measured to check analytical reproducibility of the analyses. The average $\delta^{56}\text{Fe}$ value of the JM samples was $0.43 \pm 0.08\text{‰}$ (2SD, n=65; Supplementary Fig. 6). Sub-samples of the Fe standard solution Certipur[®] to which the extracting reagents Na-acetate and hydroxylamine-HCl were added and the Fe_{aca} and Fe_{hyam} extracts of the internal laboratory RM HE443-077-cc underwent the same purification processing as the samples. Values for the Certipur[®] standards were $0.12 \pm 0.09\text{‰}$ (2SD) for Na-acetate (n=2) and $0.17 \pm 0.04\text{‰}$ (2SD) for hydroxylamine-HCl (n=2) and are, thus, within standard deviation of the unprocessed

solution ($\delta^{56}\text{Fe} = 0.15 \pm 0.06\%$, 2SD) as given in Henkel et al. (2016). The $\delta^{56}\text{Fe}$ values for the Fe_{aca} and Fe_{hyam} extracts of the internal laboratory RM HE443-077-cc in this study are within the analytical uncertainty of $\delta^{56}\text{Fe}$ values determined over the past five years (Supplementary Tab. 3). Uncertainty for $\delta^{56}\text{Fe}$ indicate the twofold standard deviation (2SD) of duplicate to fourfold measurements.

3. Results and discussion

3.1 Differences in Fe contents between ash-bearing layers and surrounding mud rock

In contrast to previous studies in depositional environments that are characterized by abundant ash layers (Inagaki et al., 2003; Homoky et al., 2011; Torres et al., 2015; Luo et al., 2020), the contents of reactive Fe ($\text{Fe}_{\text{reactive}}$; sum of all sequentially extracted Fe pools; Poulton and Canfield, 2005) in ash samples at Site C0023 are on average more than 50% lower compared to the surrounding mud rock (Fig. 1a). The Na-acetate step of the leaching sequence predominantly dissolves adsorbed Fe(II) ($\text{Fe}(\text{II})_{\text{sorb}}$), carbonate-bound Fe and Fe monosulfides (Fe_{aca}) (Poulton and Canfield, 2005; Henkel et al., 2016). The average Fe_{aca} contents in ash layer and mud rock samples are ~ 0.1 wt% (Fig. 1b). Since Fe monosulfides were not detected in the sediments of Site C0023 (Köster et al., 2021), Fe_{aca} represents abundantly present siderite and Fe-rich calcite (Heuer et al., 2017), whose formation can most likely be attributed to the alteration of volcanic ash (Sample et al., 2017; Torres et al., 2020), and some adsorbed Fe(II). Hydroxylamine-HCl typically extracts ferrihydrite and lepidocrocite (Fe_{hyam}) (Poulton and Canfield, 2005; Henkel et al., 2016). These Fe minerals represents the dominant Fe fraction with contents of up to 1.0 wt% in mud rock (Köster et al., 2021) and 0.6 wt% in discrete ash samples (Fig. 1c). However, Fe_{hyam} in sediments at Site C0023 was shown to mainly consist of reactive phyllosilicate-bound Fe (Köster et al., 2021). The significantly lower $\text{Fe}_{\text{reactive}}$ and Fe_{hyam} contents in ash-bearing layers indicate that either 1) part of the Fe(III) deposited synsedimentary with the tephra has already been used by microbes and is thus not preserved or 2) Fe(III) in tephra was originally lower due to the specific chemistry of the volcanic source material. The Ti/Al ratios in the discrete ash samples vary between 0.01 and 0.06 (Supplementary Fig. 3) indicating a dacitic to rhyolitic composition. This is in line with felsic ash derived from the Japanese Islands (Masuda et al., 1993). Rhyolitic ash is generally characterized by low Fe contents (~ 2 wt%) (Le Maitre, 1976). Higher Fe contents in mud rock samples are likely due to a high amount of mafic minerals such as pyroxene and amphibole (Heuer et al., 2017), suggesting that the reactive Fe contents in the discrete ash layers were already lower during the deposition. Although we cannot completely exclude a combination of

both possibilities, there is no clear indication that the depth distribution of $\text{Fe(II)}_{\text{aq}}$ is related to the occurrence of discrete ash layers.

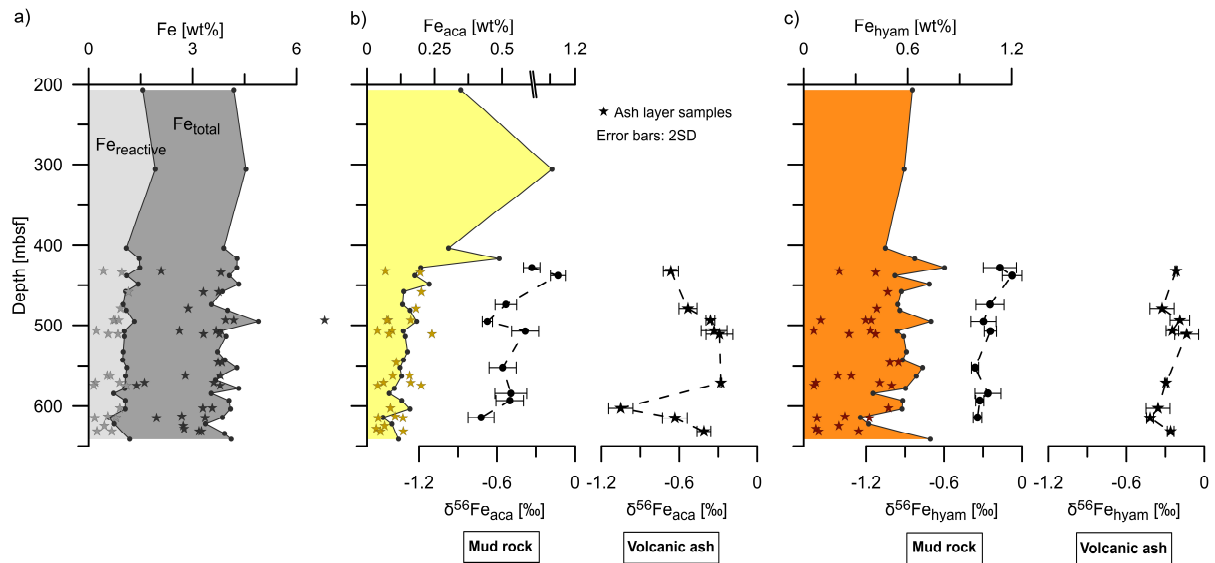


Figure 1. Total and reactive Fe contents and associated isotopic compositions in mud rock and discrete ash layers at Site C0023. (a) Down-core solid-phase profiles of total Fe (Fe_{total}) and reactive Fe ($\text{Fe}_{\text{reactive}}$: sum of sequentially extracted Fe pools according to Poulton and Canfield, 2005). (b) Na-acetate-leachable Fe (Fe_{aca}) and associated isotopic composition ($\delta^{56}\text{Fe}_{\text{aca}}$). (c) Hydroxylamine-HCl-leachable Fe (Fe_{hyam}) and the associated isotopic composition ($\delta^{56}\text{Fe}_{\text{hyam}}$). Error bars indicate the twofold standard deviation (2SD) of duplicate to fourfold measurements. The stars in each panel represent the discrete ash layer samples. Fe_{total} , $\text{Fe}_{\text{reactive}}$, Fe_{aca} and Fe_{hyam} data of mud rock are taken from Köster et al. (2021).

3.2 Indications of microbial Fe cycling

The isotopic composition of dissolved Fe ($\delta^{56}\text{Fe}_{\text{aq}}$) is $< -1.0\text{‰}$ over the whole ferruginous ($\text{Fe(II)}_{\text{aq}}$ -enriched) interval between 200 and 600 mbsf (Fig. 2b), thus, lower than the average isotopic composition of igneous rocks ($\delta^{56}\text{Fe} = 0.09 \pm 0.05\text{‰}$, 1SD; Beard et al., 2003). The $\text{Fe(II)}_{\text{aq}}$ concentrations (expressed as $\ln[\text{Fe(II)}_{\text{aq}}]$) correlate with $\delta^{56}\text{Fe}_{\text{aq}}$ values ($r_s=0.77$, $p < 0.001$, $n=18$; Fig. 2c) except for the shallowest samples at ~ 200 mbsf. The maximum $\text{Fe(II)}_{\text{aq}}$ concentration of $\sim 60 \mu\text{M}$ at 570 mbsf corresponds to $\delta^{56}\text{Fe}_{\text{aq}} = -1.5\text{‰}$, whereas an extremely low $\delta^{56}\text{Fe}_{\text{aq}}$ value of -5.86‰ at 473 mbsf coincides with a low $\text{Fe(II)}_{\text{aq}}$ concentration of $2 \mu\text{M}$ (Fig. 2b). The highest value of -1.09‰ at ~ 200 mbsf can likely be attributed to reactions between $\text{Fe(II)}_{\text{aq}}$ and hydrogen sulfide (HS^-), since local minima of both compounds were detected at the same depth ($< 2 \mu\text{M}$ and $< 4 \mu\text{M}$, respectively; Supplementary Fig. 2b,c; Heuer et al., 2017). Fe sulfide precipitation kinetically favors ^{54}Fe over ^{56}Fe , leading to higher residual $\delta^{56}\text{Fe}_{\text{aq}}$ values (Butler et al., 2005; Severmann et al., 2006).

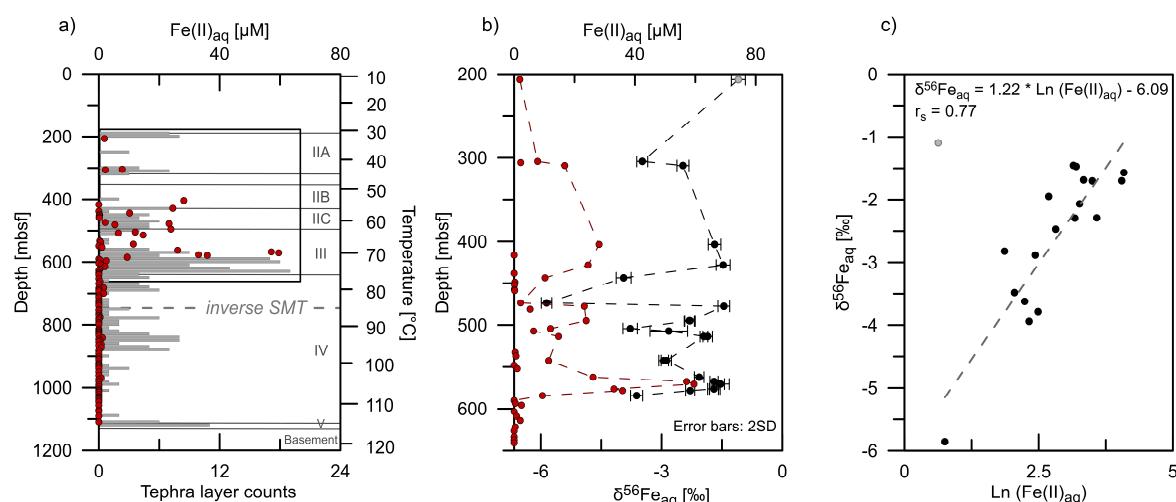


Figure 2. Dissolved Fe concentrations and associated isotopic compositions at Site C0023. (a) Down-core pore-water profile of dissolved Fe ($\text{Fe(II)}_{\text{aq}}$) concentrations (red dots) and tephra layer counts (gray bars) (Heuer et al., 2017). Lithological units (IIA-V; see Supplementary Information) and temperature data are from Heuer et al. (2017) and Heuer et al. (2020), respectively. The gray dashed line shows the location of the inverse sulfate-methane transition (SMT) with a methanic zone above and a sulfate-rich zone below the SMT (see Supplementary Fig. 2 for details). (b) Close-up of $\text{Fe(II)}_{\text{aq}}$ concentrations (red dots) and associated isotopic composition ($\delta^{56}\text{Fe}_{\text{aq}}$) (black dots) for the ferruginous interval. Error bars indicate the twofold standard deviation (2SD) of the isotope ratio over 20 consecutive measurement cycles. (c) Relationship between $\text{Fe(II)}_{\text{aq}}$ concentrations (expressed as $\text{Ln}[\text{Fe(II)}_{\text{aq}}]$) and $\delta^{56}\text{Fe}_{\text{aq}}$ values (data fit following the relation: $\delta^{56}\text{Fe}_{\text{aq}} = 1.22 * \text{Ln}[\text{Fe(II)}_{\text{aq}}] - 6.09$, Spearman correlation coefficient $r_s = 0.77$, $p < 0.001$, $n = 18$). The shallowest sample (~200 mbsf; gray dot) is not included in the linear regression due co-occurrence of $\text{Fe(II)}_{\text{aq}}$ and HS^- (details given in the text).

To our knowledge, the $\delta^{56}\text{Fe}_{\text{aq}}$ value of -5.86‰ is the lowest ever measured in marine pore waters. To use Fe isotopes as a proxy for biogeochemical processes, the isotopic composition of the co-occurring solid reactive Fe phases is also required (Staubwasser et al., 2006; Henkel et al., 2016, 2018). Stable Fe isotope analyses were performed on the Fe_{aca} ($\delta^{56}\text{Fe}_{\text{aca}}$) and Fe_{hyam} ($\delta^{56}\text{Fe}_{\text{hyam}}$) extracts, as variations in the $\delta^{56}\text{Fe}$ values are most likely to occur in these reducible Fe pools (Henkel et al., 2016, 2018). The $\delta^{56}\text{Fe}_{\text{aca}}$ values of mud rock samples decrease downcore from -0.33 to -0.72‰ , whereas the $\delta^{56}\text{Fe}_{\text{aca}}$ values of ash layers are more variable, ranging between -0.28 and -1.05‰ (Fig. 1b). Average $\delta^{56}\text{Fe}_{\text{hyam}}$ values are similar for both set of samples with $-0.26 \pm 0.09\text{‰}$ (1SD, $n = 9$) for mud rock and $-0.27 \pm 0.09\text{‰}$ (1SD, $n = 9$) for ash samples (Fig. 1c). Given that low $^{56}\text{Fe}/^{54}\text{Fe}$ ratios of $\text{Fe(II)}_{\text{aq}}$ relative to ferric substrates are often related to DIR with an isotopic fractionation of up to -3‰ (Beard et al., 1999; Severmann et al., 2006; Johnson et al., 2008), the more negative $\delta^{56}\text{Fe}_{\text{aq}}$ values compared to $\delta^{56}\text{Fe}_{\text{aca}}$ and $\delta^{56}\text{Fe}_{\text{hyam}}$ values first pointed towards DIR. However, the extremely negative $\delta^{56}\text{Fe}_{\text{aq}}$ values down to -5.86‰ cannot be explained by DIR alone. Considering the elevated temperatures of up to $\sim 70^\circ\text{C}$ in the ferruginous zone (Fig. 2a), the DIR related isotopic fractionation would be

even less than -3‰ (Welch et al., 2003). In the following, we highlight possible reaction pathways that typically cause Fe isotope fractionation in marine sediments and discuss them in terms of their applicability to Site C0023.

The formation of Fe carbonates such as siderite (FeCO_3) and Ca-substituted siderite, for instance, is associated with a fractionation of up to $\sim 1\%$ between $\text{Fe(II)}_{\text{aq}}$ and Fe bound in carbonates whereby the light ^{54}Fe is preferentially incorporated into the Fe carbonate precipitate (Johnson et al., 2005). However, we observe a much greater difference of more than 4‰ between $\delta^{56}\text{Fe}_{\text{aq}}$ and $\delta^{56}\text{Fe}_{\text{aca}}$ and a relative enrichment of ^{54}Fe in the residual $\text{Fe(II)}_{\text{aq}}$ pool. Similarly, the kinetically controlled Fe sulfide precipitation, which dominates over equilibrium fractionation in natural systems, would also result in higher $\delta^{56}\text{Fe}_{\text{aq}}$ values (Butler et al., 2005; Severmann et al., 2006). Thus, we can rule out the precipitation of Fe sulfide and carbonate minerals as possible reaction pathways explaining the observed extremely low $\delta^{56}\text{Fe}_{\text{aq}}$ values. The zone with elevated $\text{Fe(II)}_{\text{aq}}$ concentrations corresponds to an age of ~ 0.3 to 2.5 Ma (Fig. 2b; Hagino and the Expedition 270 Scientists, 2018). One conceivable scenario leading to extremely negative $\delta^{56}\text{Fe}_{\text{aq}}$ values is the repetitive redox cycling of Fe at the Fe(II)/Fe(III) redox boundary. The onset of DIR and, thus, the establishment of the Fe(II)/Fe(III) redox boundary was at ~ 2.5 Ma, when the organic carbon burial increased due to higher sedimentation rates and elevated primary productivity (Köster et al., 2021). DIR leads to a preferential release of isotopically light ^{54}Fe into the pore water, and consequently negative $\delta^{56}\text{Fe}_{\text{aq}}$ values (Johnson and Beard, 2005; Crosby et al., 2005, 2007). As $\text{Fe(II)}_{\text{aq}}$ diffused up towards the Fe(II)/Fe(III) redox boundary, $\text{Fe(II)}_{\text{aq}}$ could have been oxidized to $\text{Fe(III)}_{\text{aq}}$ and precipitated as secondary Fe(III) (oxyhydr)oxides. The oxidation of $\text{Fe(II)}_{\text{aq}}$ and the subsequent precipitation as solid-phase Fe(III) also results in isotope fractionation (Bullen et al., 2001; Welch et al., 2003; Staubwasser et al., 2013), whereby secondary Fe(III) (oxyhydr)oxides are isotopically heavier than $\text{Fe(II)}_{\text{aq}}$, but lighter compared to the primary ferric substrate. With ongoing deposition and changes in geochemical conditions, the Fe(II)/Fe(III) redox boundary at Site C0023 presumably migrated upwards (Köster et al., 2021) so that secondary Fe(III) (oxyhydr)oxides could have been successively buried and used as energy substrates. The repetitive Fe-reduction-oxidation cycling could have led to a continuous shift of pore-water $\delta^{56}\text{Fe}$ towards more negative values over time. However, considering the sediment age of 0.3 to 2.5 Ma (Hagino and the Expedition 370 Scientists, 2018), it is unlikely that the present-day isotopic composition of $\text{Fe(II)}_{\text{aq}}$ still records the repetitive Fe redox cycling that occurred several hundreds of thousands of years ago.

The microbial reduction of Fe(III)-containing clays can be considered as an alternative explanation for the release of Fe(II)_{aq} and its extremely negative isotopic composition (Shi et al., 2016, 2021). Structural Fe(III) in clay minerals can serve as electron acceptor for the degradation of organic matter (Kostka et al., 2002; Jung et al., 2019). Recently, Kim et al. (2019) postulated that microbial reduction of structural Fe(III) in smectite promotes the transformation of smectite to illite at Site C0023 between 500 and 700 mbsf, leading to the observed Fe(II)_{aq} release (Fig. 2a). The fractionation between Fe(II)_{aq} and structural Fe(III) in nontronite, an Fe-rich member of the smectite group, ranges between -1.2 to +0.8‰ (Shi et al., 2016). If microbial reduction of Fe(III)-containing clays is the only process leading to isotope fractionation, $\delta^{56}\text{Fe}_{\text{hyam}}$ would need to be at least -2.0‰ for samples with $\delta^{56}\text{Fe}_{\text{aq}} < -3.5\text{‰}$. Since we observe much greater differences between $\delta^{56}\text{Fe}_{\text{aq}}$ and $\delta^{56}\text{Fe}_{\text{hyam}}$ values in all samples, we infer that additional processes are responsible for the uniquely low $\delta^{56}\text{Fe}_{\text{aq}}$ values at Site C0023.

3.3 Adsorption of Fe(II)_{aq} onto mineral surfaces

The co-variation between Fe(II)_{aq} concentrations and $\delta^{56}\text{Fe}_{\text{aq}}$ (Fig. 2c) could suggest progressive removal of Fe(II)_{aq} in a Rayleigh distillation process (Rayleigh, 1896). A conceivable scenario in which Fe(II)_{aq} is continuously removed from the pore water is a combined process of diffusive transport of Fe(II)_{aq} along a concentration gradient and subsequent adsorption onto Fe (oxyhydr)oxide surfaces. Kinetic enrichment of ^{54}Fe during diffusion (Dauphas et al., 2017) and a preference of ^{56}Fe during Fe(II)_{aq} adsorption (Icopini et al., 2004; Crosby et al., 2005, 2007) over a long diffusion distance could lead to very low residual $\delta^{56}\text{Fe}_{\text{aq}}$, as observed in this study. Fractionation factors between Fe(II)_{sorb} on goethite and Fe(II)_{aq} ($\Delta^{56}\text{Fe}_{\text{Fe(II)sorb-Fe(II)aq}}$) are between +0.87‰ and +1.24‰ (Crosby et al., 2005, 2007; Beard et al., 2010). Since we cannot differentiate between carbonate-bound Fe and Fe(II)_{sorb} within the Fe_{aca} pool, an assessment of the isotopic composition of Fe(II)_{sorb} is not feasible in the framework of this study.

To assess the plausibility of the proposed scenario, we calculated the evolution of the isotopic composition of Fe(II)_{aq} and Fe(II)_{sorb} using the Rayleigh distillation equations after Wiederhold (2015). The isotopic composition of Fe(II)_{aq} is described in good approximation by:

$$\delta^{56}\text{Fe}_{\text{aq}} = \delta^{56}\text{Fe}_0 + \epsilon \ln f, \quad (1)$$

where $\delta^{56}\text{Fe}_0$ is the initial isotopic composition of $\text{Fe(II)}_{\text{aq}}$, ε is the isotopic enrichment factor in permil and f is the remaining fraction of $\text{Fe(II)}_{\text{aq}}$. The isotopic composition of the instantaneous product $\text{Fe(II)}_{\text{sorb}}$ ($\delta^{56}\text{Fe}_{\text{sorb-instant}}$) is calculated as:

$$\delta^{56}\text{Fe}_{\text{sorb-instant}} = \delta^{56}\text{Fe}_0 + \varepsilon \ln f + \varepsilon, \quad (2)$$

and the cumulative product $\text{Fe(II)}_{\text{sorb}}$ ($\delta^{56}\text{Fe}_{\text{sorb-cumulative}}$) as:

$$\delta^{56}\text{Fe}_{\text{sorb-cumulative}} = \delta^{56}\text{Fe}_0 + \varepsilon \ln f - \frac{\varepsilon \ln f}{1-f}. \quad (3)$$

We tested different values for the initial isotopic composition of $\text{Fe(II)}_{\text{aq}}$ (Fig. 3). We argue that an initial $\delta^{56}\text{Fe}_0$ value between -1.5 and -3.0‰ is reasonable due to the onset of DIR at ~2.5 Ma. For the enrichment factor ε , we have used 0.87‰ (Crosby et al., 2007) and 1.24‰ (Beard et al., 2010). It should be noted that the enrichment factors are estimated based on laboratory studies that were performed at room temperature. Fractionation factors in natural systems could be different due to lower or higher *in situ* temperatures such as at Site C0023 and the availability of competing adsorbents including dissolved silica (Wu et al., 2009).

The Rayleigh distillation model results show that extremely low $\delta^{56}\text{Fe}_{\text{aq}}$ values of almost -5.9‰ are reached in all scenarios at advanced stages of the adsorption process when the remaining fraction is low ($f < 0.1$; Fig. 3). Except for the scenarios with the lowest ($f = 0.001$; Fig. 3c) and highest ($f = 0.1$; Fig. 3d) values for f , this corresponds to an initial $\text{Fe(II)}_{\text{aq}}$ concentration between 55 and 320 μM if considering the actual $\text{Fe(II)}_{\text{aq}}$ concentration of ~2 μM in the sample with the uniquely low $\delta^{56}\text{Fe}_{\text{aq}}$ value (Fig. 2b). This calculated range of initial $\text{Fe(II)}_{\text{aq}}$ concentrations is in line with concentrations typically associated with DIR in shallow sediments (Severmann et al., 2006; Oni et al., 2015; Henkel et al., 2016). Assuming that $\text{Fe(II)}_{\text{aq}}$ with the extremely low $\delta^{56}\text{Fe}_{\text{aq}}$ value at 470 mbsf was released during DIR in the interval with the present-day maximum $\text{Fe(II)}_{\text{aq}}$ concentrations, it diffused over a distance of ~100 m. The mean diffusion time of a dissolved compound relates to the square of the diffusion length (Jørgensen, 2006; Wehrmann and Ferdelman, 2014) and the diffusion coefficients of dissolved species generally depends on temperature and porosity (Supplementary Tab. 1; Boudreau, 1997). While diffusion accelerates with increasing temperature, the compaction of sediments due to ongoing burial leads to longer diffusion times. Considering the present-day porosity of ~40% and a temperature between 30° and 75°C, the average diffusion time of $\text{Fe(II)}_{\text{aq}}$ through the compacted, 100 m thick sediment package at Site C0023 ranges between one and two millions

of years and is thus consistent with the reconstructed onset of DIR at ~ 2.5 Ma (Köster et al., 2021).

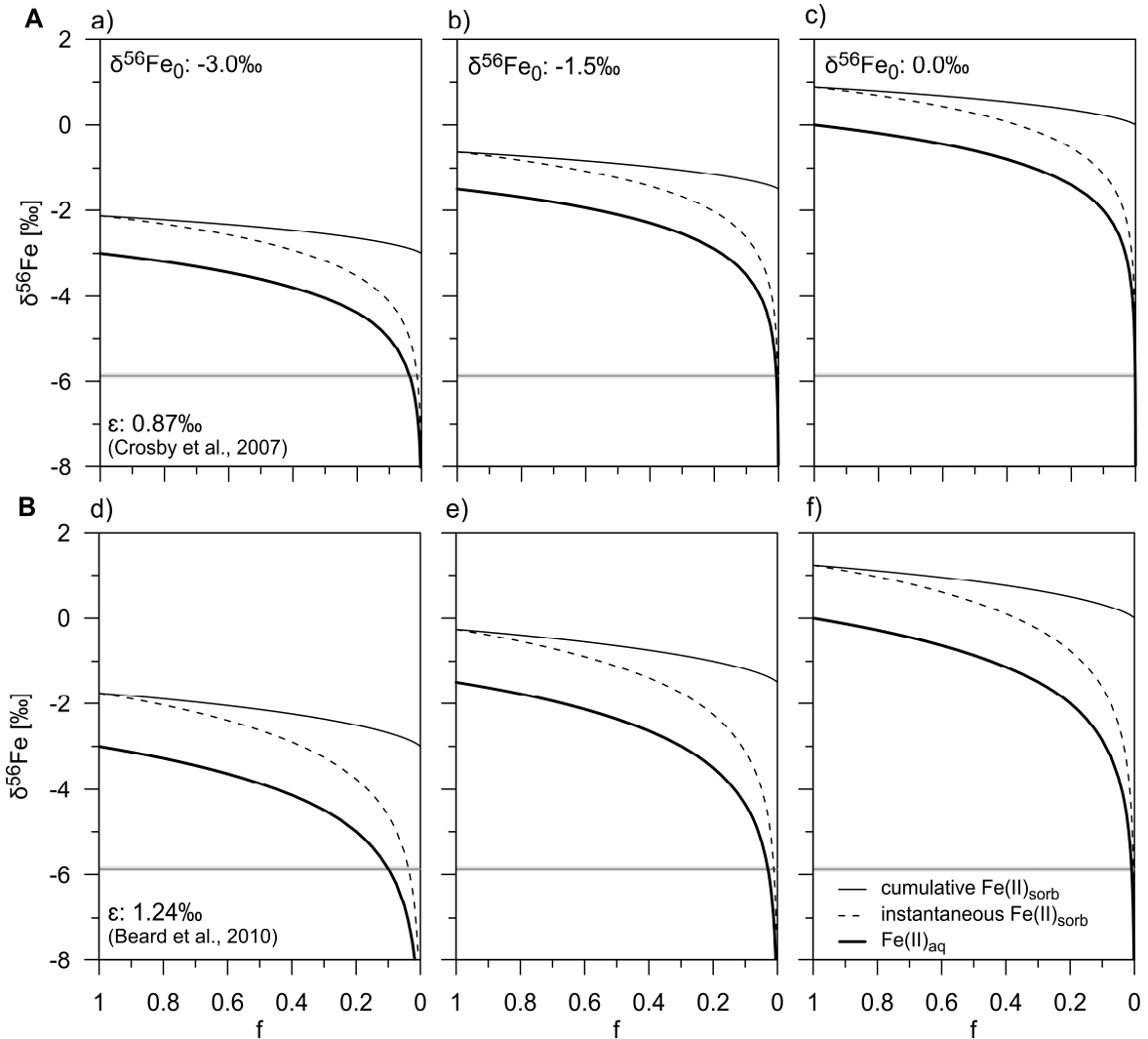


Figure 3. Isotopic composition of dissolved and sorbed Fe derived from Rayleigh distillation model. (a)-(f) Isotopic evolution of $\text{Fe(II)}_{\text{aq}}$ (bold line), instantaneous $\text{Fe(II)}_{\text{sorb}}$ (dashed line) and cumulative $\text{Fe(II)}_{\text{sorb}}$ (narrow line) during the adsorption of $\text{Fe(II)}_{\text{aq}}$ onto Fe (oxyhydr)oxide surfaces obtained by using the Rayleigh distillation equations after Wiederhold (2015). The differences between $\text{Fe(II)}_{\text{aq}}$ and instantaneous $\text{Fe(II)}_{\text{sorb}}$ corresponds to the enrichment factors ϵ according to (A) Crosby et al. (2007) and (B) Beard et al. (2010), respectively, at all stages of the reaction. For the initial isotopic composition of $\text{Fe(II)}_{\text{aq}}$ ($\delta^{56}\text{Fe}_0$), different values of -3.0‰ (a, d), -1.5‰ (b, e), and 0.0‰ (c, f) were used. The grayish bar represents the reference $\delta^{56}\text{Fe}_{\text{aq}}$ value of -5.86‰ . The model results show that the largest fractionation for $\text{Fe(II)}_{\text{aq}}$ are found at advanced stages of the adsorption process where the remaining fraction f is low ($f < 0.1$).

The described scenario including DIR-mediated release of $\text{Fe(II)}_{\text{aq}}$ followed by its diffusional and adsorptive removal only holds true if DIR once occurred but has ceased at that specific depth during progressive burial and heating. If DIR had continued, the successively released

$\text{Fe(II)}_{\text{aq}}$ would have continuously overprinted the isotopic composition of $\text{Fe(II)}_{\text{aq}}$ by shifting $\delta^{56}\text{Fe}_{\text{aq}}$ values towards 0‰. A recent study has shown that the population of vegetative cells at Site C0023 sharply drops by two orders of magnitude at 300 to 400 mbsf, which corresponds to the temperature limit for growth of mesophilic microorganisms of $\sim 45^\circ\text{C}$, and remains close to the minimum quantification limit further below. The collapse likely occurred when the temperature significantly increased since the onset of trench-style deposition at ~ 0.4 Ma (Heuer et al., 2020). Based on the present-day extremely low vegetative cell population including Fe-reducing bacteria, we suggest that DIR is currently not occurring or only at very low rates since ~ 0.4 Ma. At the same time, potential reactants such as HS^- are not present in the specific depth interval (Supplementary Fig. 2c). Consequently, Rayleigh distillation – in this case diffusive transport and adsorption of $\text{Fe(II)}_{\text{aq}}$ onto Fe oxide surfaces - could proceed unimpeded over several thousands of years. To conclude, the applied Rayleigh distillation model successfully explains the observed exceptionally low stable Fe isotope signatures. Based on the processes outlined, we developed a schematic conceptual model (Fig. 4).

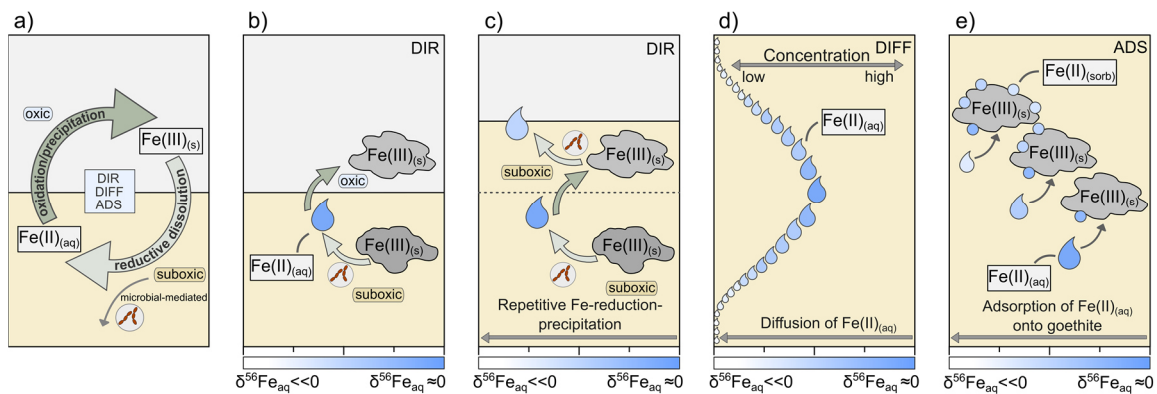


Figure 4. Schematic overview illustrating the shift of $\delta^{56}\text{Fe}_{\text{aq}}$ towards negative values. (a) A combination of three consecutive processes could have caused extremely negative $\delta^{56}\text{Fe}_{\text{aq}}$ values at Site C0023: (b-c) repetitive DIR, (d) diffusive transport of $\text{Fe(II)}_{\text{aq}}$ along a concentration gradient (DIFF) and (e) adsorption of $\text{Fe(II)}_{\text{aq}}$ onto Fe (oxyhydr)oxide surfaces (ADS). The blue color scheme represents the isotopic composition of $\text{Fe(II)}_{\text{aq}}$, where pale blue colors indicate low and dark blue colors higher $\delta^{56}\text{Fe}_{\text{aq}}$ values. The combination of repetitive DIR and subsequent diffusion and adsorption of $\text{Fe(II)}_{\text{aq}}$ onto mineral surfaces progressively removed $\text{Fe(II)}_{\text{aq}}$ from the pore water, which led to a shift of $\delta^{56}\text{Fe}_{\text{aq}}$ towards extremely negative values. Here, while the zone in which dissimilatory Fe reduction occurs is referred to as “suboxic” zone, where oxygen, nitrate and HS^- are absent, the zone in which $\text{Fe(II)}_{\text{aq}}$ is oxidized is described as “oxic” zone.

3.4 Implications for the interpretation of stable Fe isotope data

This is the first study that reports stable isotopic records of $\text{Fe(II)}_{\text{aq}}$ in deep subseafloor sediments. $\text{Fe(II)}_{\text{aq}}$ at Site C0023 most likely derives from microbial Fe reduction of either Fe

(oxyhydr)oxides or structural Fe(III) bound in phyllosilicates as postulated by Kim et al. (2019) since the onset of DIR at ~2.5 Ma. Repetitive Fe-reduction-oxidation cycles could have led to increasing negative $\delta^{56}\text{Fe}_{\text{aq}}$ values (Fig. 4b,c). We argue that $\text{Fe(II)}_{\text{aq}}$ release by DIR and adsorptive removal of $\text{Fe(II)}_{\text{aq}}$ likely co-occurred during this stage. The increase in temperature beyond the temperature limit of mesophilic microorganisms and the associated collapse of the vegetative cell population since the onset of trench-style deposition at ~0.4 Ma might have stopped the microbially mediated $\text{Fe(II)}_{\text{aq}}$ release while diffusional and adsorptive $\text{Fe(II)}_{\text{aq}}$ removal continued (Fig. 4d,e). Due to the elevated temperatures, diffusion could proceed at even accelerated rates. Our findings demonstrate that the overall low isotopic composition of $\text{Fe(II)}_{\text{aq}}$ throughout the ferruginous sediment interval does not rule out microbial reduction as the main pathway releasing $\text{Fe(II)}_{\text{aq}}$. However, the uniquely low $\delta^{56}\text{Fe}_{\text{aq}}$ values are caused by the decoupling of biotic and abiotic processes, which is ultimately driven by the depositional and thermal history of Site C0023. In contrast to deep and consolidated sediments, Rayleigh fractionation probably only plays a minor role in soft near-surface sediments where generally higher reaction rates and shorter diffusion times and distances prevail. This study advances our knowledge about Fe cycling pathways in deep seafloor sediments and provides crucial aspects for the interpretation of Fe isotope records especially in deep seafloor sediments. We conclude that the described decoupling of biotic and abiotic processes is important to consider in seafloor environments where DIR cannot be maintained either due to the absence of reactive Fe phases as energy substrates as they have been already consumed or as a consequence of changing environmental and depositional conditions – in particular temperature increase beyond the threshold of mesophilic Fe-reducing microorganisms – such as shown for Site C0023.

Acknowledgements

This research used samples and data provided by the International Ocean Discovery Program (IODP). We would like to thank all personnel involved in the operations on *D/V Chikyu* and in the Kochi Core Center (KCC) during IODP Expedition 370. For analytical support in the home laboratory, we thank D. Bethke, I. Stimac and I. Dohrmann. This study is funded by the German Research Foundation (DFG) in the framework of the Priority Program 527 (Bereich Infrastruktur – International Ocean Discovery Program; project 388260220). We acknowledge additional financial support from the Helmholtz Association (Alfred Wegener Institute, Helmholtz Centre for Polar and Marine Research). All data generated in this study will be available in the data library PANGAEA.

References

- Anbar, A.D., and Rouxel, O., 2007. Metal stable isotopes in paleoceanography. *Annual Review of Earth and Planetary Science*, **35**, 717-746. doi:10.1146/annurev.earth.34.031405.125029.
- Beard, B.L., Johnson, C.M., Cox, L., Sun, H., Neelson, K.H., and Aguilar, C., 1999. Iron isotope biosignatures. *Science*, **285**, 1889-1892. doi:10.1126/science.285.5435.1889.
- Beard, B.L., Johnson, C.M., Skulan, J.L., Neelson, K.H., Cox, L., and Sun, H., 2003. Application of Fe isotopes to tracing the geochemical and biological cycling of Fe. *Chemical Geology*, **195**, 87-117. doi:10.1016/S0009-2541(02)00390-X.
- Beard, B.L., Handler, R.M., Scherer, M.M., Wu, L., Czaja, A.D., Heimann, A., and Johnson, C.M., 2010. Iron isotope fractionation between aqueous ferrous iron and goethite. *Earth and Planetary Science Letters*, **295**, 241-250. doi:10.1016/j.epsl.2010.04.006.
- Boudreau, B.P., 1997. *Diagenetic Models and Their Implementation: Modelling Transport and Reactions in Aquatic Sediments*. Springer, Berlin, Heidelberg, New York, 428 p.
- Bullen, T.D., White, A.F., Childs, C.W., Vivit, D.V., and Schulz, M.S., 2001. Demonstration of significant abiotic iron isotope fractionation in nature. *Geology*, **29**, 699-702. doi:10.1130/0091-7613(2001)029%3C0699:DOSAII%3E2.0.CO;2.
- Butler, I.B., Archer, C., Vance, D., Oldroyd, A., and Rickard, D., 2005. Fe isotope fractionation of FeS formation in ambient aqueous solution. *Earth and Planetary Science Letters*, **236**, 430-442. doi:10.1016/j.epsl.2005.05.022.
- Conway, T.M., and John S.G., 2014. Quantification of dissolved iron sources to the North Atlantic Ocean. *Nature*, **511**, 212-215. doi:10.1038/nature13482.
- Craddock, P.R., and Dauphas, N., 2010. Iron isotopic compositions of geological reference materials and chondrites. *Geostandards and Geoanalytical Research*, **35**, 101-123. doi:10.1111/j.1751-908X.2010.00085.x.
- Crosby, H.A., Johnson, C.M., Roden, E.E., and Beard, B.L., 2005. Coupled Fe(II)-Fe(III) electron and atom exchange as a mechanism for Fe isotope fractionation during dissimilatory iron oxide reduction. *Environmental Science & Technology*, **39**, 6698-6704. doi:10.1021/es0505346.
- Crosby, H.A., Roden, E.E., Johnson, C.M., and Beard, B.L., 2007. The mechanisms of iron isotope fractionation produced during dissimilatory Fe(III) reduction by *Shewanella putrefaciens* and *Geobacter sulfurreducens*. *Geobiology*, **5**, 169-189. doi:10.1111/j.1472-4669.2007.00103.x.
- Dauphas, N., John, S.G., and Rouxel, O., 2017. Iron isotope systematics. *Reviews in Mineralogy and Geochemistry*, **82**, 415-510. doi:10.2138/rmg.2017.82.11.
- Hagino, K., and the Expedition 370 Scientists, 2018. Data report: calcareous nannofossils from the middle Miocene to Pleistocene, IODP Expedition 370 Site C0023. In: *Proceedings of the International Ocean Discovery Program Volume 370* (eds. Heuer, V.B., Inagaki, F., Morono, Y., Kubo, Y., Maeda, L., and the Expedition 370 Scientists). College Station, TX (International Ocean Discovery Program). doi:10.14379/iodp.proc.370.201.2018.
- Henkel, S., Kasten, S., Poulton, S.W., and Staubwasser, M., 2016. Determination of the stable iron isotopic composition of sequentially leached iron phases in marine sediments. *Chemical Geology*, **421**, 93-102. doi:10.1016/j.chemgeo.2015.12.003.

- Henkel, S., Kasten, S., Hartmann, J.F., Silva-Busso, A., and Staubwasser, M., 2018. Iron cycling and stable Fe isotope fractionation in Antarctic shelf sediments, King George Island. *Geochimica et Cosmochimica Acta*, **237**, 320-338. doi:10.1016/j.gca.2018.06.042.
- Heuer, V.B., Inagaki, F., Morono, Y., Kubo, Y., Maeda, L., and the Expedition 370 Scientists, 2017. Temperature limit of the deep biosphere off Muroto. *Proceedings of the International Ocean Discovery Program Volume 370*: College Station, TX (International Ocean Discovery Program). doi:10.14379/iodp.proc.370.2017.
- Heuer, V.B., Inagaki, F., Morono, Y., Kubo, Y., Spivack, A., Viehweger, B., et al., 2020. Temperature limits to deep seafloor life in the Nankai Trough subduction zone. *Science*, **370**, 1230-1234. doi:10.1126/science.abd7934.
- Homoky, W.B., Hembury, D.J., Hepburn, L.E., Mills, R.A., Statham, P.J., Fones, G.R., Palmer, M.R., 2011. Iron and manganese diagenesis in deep sea volcanogenic sediments and the origins of pore water colloids. *Geochimica et Cosmochimica Acta*, **75**, 5032-5048. doi:10.1016/j.gca.2011.06.019.
- Homoky, W.B., John, S.G., Conway, T.M., and Mills, R.A., 2013. Distinct iron isotopic signatures and supply from marine dissolution. *Nature Communications*, **4**, 2143. doi:10.1038/ncomms3143.
- Homoky, W.B., Conway, T.M., John, S.G., König, D., Deng, F., Tagliabue, A., and Mills, R.A., 2021. Iron colloids dominate sedimentary supply to the ocean interior. *Proceedings of the National Academy of Sciences of the United States of America*, **118**, e2016078118. doi:10.1073/pnas.2016078118.
- Icopini, G.A., Anbar, A.D., Ruebush, S.S., Tien, M., and Brantley, S.L., 2004. Iron isotope fractionation during microbial reduction of iron: The importance of adsorption. *Geology*, **32**, 205-208. doi:10.1130/G20184.1.
- Inagaki, F., Suzuki, M., Takai, K., Oida, H., Sakamoto, T., Aoki, K., Nealson, K.H., Horikoshi, K., 2003. Microbial communities associated with geological horizons in coastal seafloor sediments from the Sea of Okhotsk. *Applied Environmental Microbiology*, **69**, 7224-7235. doi:10.1128/AEM.69.12.7224-7235.2003.
- Johnson, C.M., and Beard, B.L., 2005. Biogeochemical cycling of iron isotopes. *Science*, **309**, 1025-1027. doi:10.1126/science.1112552.
- Johnson, C.M., Roden, E.E., Welch, S.A., and Beard, B.L., 2005. Experimental constraints on Fe isotope fractionation during magnetite and Fe carbonate formation coupled to dissimilatory hydrous ferric oxide reduction. *Geochimica et Cosmochimica Acta*, **69**, 963-993. doi:10.1016/j.gca.2004.06.043.
- Johnson, C.M., Beard, B.L., and Roden E.E., 2008. The iron isotope fingerprints of redox and biogeochemical cycling in modern and ancient Earth. *Annual Review of Earth and Planetary Science*, **36**, 457-493. doi:10.1146/annurev.earth.36.031207.124139.
- Jørgensen, B.B., 2006. Bacteria and marine biogeochemistry. In: *Marine Geochemistry* (eds. Schulz, H.D., and Zabel, M.). Springer, Berlin, Heidelberg, New York, 169-206.
- Jung, J., Yoo, K.-C., Rosenheim, B.E., Conway, T.M., Lee, J.I., Yoon, H.I., et al., 2019. Microbial Fe(III) reduction as a potential iron source from Holocene sediments beneath Larsen Ice Shelf. *Nature Communications*, **10**, 1-10. doi:10.1038/s41467-019-13741-x.
- Kashefi, K., and Lovley, D.R., 2003. Extending the upper temperature limit for life. *Science*, **301**, 934-934. doi:10.1126/science.1086823.

- Kim, J., Dong, H., Yang, K., Park, H., Elliott, W.C., Spivack, A., et al., 2019. Naturally occurring, microbially induced smectite-to-illite reaction. *Geology*, **47**, 535-539. doi:10.1130/G46122.1.
- Kostka, J.E., Dalton, D.D., Skelton, H., Dollhopf, S., and Stucki, J.W., 2002. Growth of iron(III)-reducing bacteria on clay minerals as the sole electron acceptor and comparison of growth yields on a variety of oxidized iron forms. *Applied Environmental Microbiology*, **68**, 6256-6262. doi:10.1128/AEM.68.12.6256-6262.2002.
- Köster, M., Kars, M., Schubotz, F., Tsang, M.-Y., Maisch, M., Kappler, A., et al., 2021. Evolution of (bio-)geochemical processes and diagenetic alteration of sediments along the tectonic migration of ocean floor in the Shikoku Basin off Japan. *Geochemistry, Geophysics, Geosystems*, e2020GC009585. doi:10.1029/2020GC009585.
- Le Maitre, R.W., 1976. The chemical variability of some common igneous rocks. *Journal of Petrology*, **17**, 589-298. doi:10.1093/petrology/17.4.589.
- Luo, M., Torres, M. E., Hong, W.-L., Pape, T., Fronzek, J., Kutterolf, S., et al., 2020. Impact of iron release by volcanic ash alteration on carbon cycling in sediments of the northern Hikurangi margin. *Earth and Planetary Science Letters*, **541**, 116288. doi:10.1016/j.epsl.2020.116288.
- Manheim, F.T., and Sayles, F.L., 1974. Composition and origin of interstitial waters of marine sediments, based on deep sea drill cores. In: *The Sea (Volume 5): Marine Chemistry: The Sedimentary Cycle* (ed. Goldberg, E.D.). New York: Wiley-Interscience, 527-568.
- Masuda, H., Tanaka, H., Gamo, T., Soh, W. and Taira, A., 1993. 14. Major-element chemistry and alteration mineralogy of volcanic ash, Site 808 in the Nankai Trough. In: *Proceedings of the Ocean Drilling Program, Scientific Reports, 131* (eds. Hill, I.A., Taira, A., Firth, J.V., et al.). College Station, TX (Ocean Drilling Program).
- Melton, E.D., Swanner, E.D., Behrens, S., Schmidt, C., and Kappler, A., 2014. The interplay of microbially mediated and abiotic reactions in the biogeochemical Fe cycle. *Nature Reviews Microbiology*, **12**, 797-808. doi:10.1038/nrmicro3347.
- Morono, Y., Inagaki, F., Heuer, V.B., Kubo, Y., Maeda, L., and the Expedition 370 Scientists, 2017. Expedition 370 methods. In: *Proceedings of the International Ocean Discovery Program Volume 370* (eds. Heuer, F. Inagaki, Y. Morono, Y. Kubo, L. Maeda, and the Expedition 370 Scientists). College Station, TX (International Ocean Discovery Program). doi:10.14379/iodp.proc.370.102.2017.
- Oni, O.E., Miyatake, T., Kasten, S., Heitmann-Richter, T., Fischer, D., Wagenknecht, L., et al., 2015. Distinct microbial population are tightly linked to the profile of dissolved iron in the methanic sediments of the Helgoland mud area, North Sea. *Frontiers in Microbiology*, **6**, 365. doi:10.3389/fmicb.2015.00365.
- Poulton, S.W., and Canfield, D.E., 2005. Development of a sequential extraction procedure for iron: implications for iron partitioning in continentally derived particulates. *Chemical Geology*, **214**, 209-221. doi:10.1016/j.chemgeo.2004.09.003.
- Rayleigh, J.W.S., 1986. Theoretical considerations respecting the separation of gases by diffusion and similar processes. *Philosophical Magazine and Journal of Science*, **42**, 493-593. doi:10.1080/14786449608620944.
- Sample, J.C., Torres, M.E., Fisher, A., Hong, Wei-Li, Destrigneville, C., Defliese, W.F., and Tripathi, A.E., 2017. Geochemical constraints on the temperature and timing of carbonate

- formation and lithification in the Nankai Trough, NanTroSEIZE transect. *Geochimica et Cosmochimica Acta*, **198**, 92-114. doi:10.1016/j.gca.2016.10.013.
- Schoenberg, R., and von Blanckenburg, F., 2005. An assessment of the accuracy of stable Fe isotope ratio measurements on samples with organic and inorganic matrices by high-resolution multicollector ICP-MS. *International Journal of Mass Spectrometry*, **242**, 257-272 doi:10.1016/j.ijms.2004.11.025.
- Severmann, S., Johnson, C.M., Beard, B.L. and McManus, J., 2006. The effect of early diagenesis on the Fe isotope compositions of porewaters and authigenic minerals in continental margin sediment. *Geochimica et Cosmochimica Acta*, **70**, 2006-2022. doi:10.1016/j.gca.2006.01.007.
- Shi, B., Liu, K., Wu, L., Li, W., Smeaton, C.M., Beard, B.L., et al., 2016. Iron isotope fractionations reveal a finite bioavailable Fe pool for structural Fe(III) reduction in nontronite. *Environmental Science & Technology*, **50**, 8661-8669. doi:10.1021/acs.est.6b02019.
- Shi, B., Smeaton, C.M., Roden, E.E., Lee, S., Liu, K., Xu, H., et al., 2021. Consecutive Fe redox cycles decrease bioreducible Fe(III) and Fe isotope fractionations by eliminating small clay particles. *Geochimica et Cosmochimica Acta*, **308**, 118-135. doi:10.1016/j.gca.2021.05.040.
- Staubwasser, M., von Blanckenburg, F., and Schoenberg, R., 2006. Iron isotopes in the early marine diagenetic cycle. *Geology*, **34**, 629-632. doi:10.1130/G22647.1.
- Staubwasser, M., Schoenberg, R., von Blanckenburg, F., Krüger, S., and Pohl, C., 2013. Isotope fractionation between dissolved and suspended particulate Fe in the oxic and anoxic water column of the Baltic Sea. *Biogeosciences*, **10**, 233-245. doi:10.5194/bg-10-233-2013.
- Stookey, L.L., 1970. Ferrozine – A new spectrophotometric reagent for iron. *Analytical Chemistry*, **42**, 779-781.
- Torres, M.E., Cox, T., Hong, W.-L., McManus, J., Sample, J.C., Destgrigneville, C., et al., 2015. Crustal fluid and ash alteration impacts on the biosphere of Shikoku Basin sediments, Nankai Trough, Japan. *Geobiology*, **13**, 562-580. doi:10.1111/gbi.12146.
- Torres, M.E., Hong, W.-L., Solomon, E.A., Milliken, K., Kim, J.-H., Sample, J.C., Teichert, B.M.A., Wallmann, K., 2020. Silicate weathering in anoxic marine sediment as a requirement for authigenic carbonate burial. *Earth-Science Reviews*, **200**, 102960. doi:10.1016/j.earscirev.2019.102960.
- Vargas, M., Kashefi, K., Blunt-Harris, E.L., and Lovley, D.R., 1998. Microbiological evidence for Fe (III) reduction on early Earth. *Nature*, **395**, 65-67. doi:10.1038/25720.
- Wehrmann, L.M., and Ferdelman, T.G., 2014. Biogeochemical consequences of the sedimentary subseafloor biosphere. In: *Developments in Marine Geology* (eds. Stein, R., Blackman, D.K., Inagaki, F., and Larsen, H.-C.). Elsevier, 217-252. doi:10.1016/B978-0-444-62617-2.00009-8.
- Welch, S.A., Beard, B.L., Johnson, C.M., and Braterman, P.S., 2003. Kinetic and equilibrium Fe isotope fractionation between aqueous Fe(II) and Fe(III). *Geochimica et Cosmochimica Acta*, **67**, 4231-4250. doi:10.1016/S0016-7037(03)00266-7.
- Wiederhold, J.G., 2015. Metal stable isotope signatures as tracers in environmental geochemistry. *Environmental Science & Technology*, **49**, 2606-2624. doi:10.1021/es504683e.

- Wiesli, R.A., Beard, B.L., and Johnson, C.M., 2004. Experimental determination of Fe isotope fractionation between aqueous Fe(II), siderite and “green rust” in abiotic systems. *Chemical Geology*, **211**, 343-362. doi:10.1016/j.chemgeo.2004.07.002.
- Wu, L., Beard, B.L., Roden, E.E., and Johnson, C.M., 2009. Influence of pH and dissolved Si on Fe isotope fractionation during dissimilatory microbial reduction of hematite. *Geochimica et Cosmochimica Acta*, **73**, 5584-5599. doi:10.1016/j.gca.2009.06.026.

**CHAPTER V:
Fading of a sulfate-methane transition in deep and hot sediments from the
Nankai Trough**

Male Köster¹, Bo Liu¹, Akira Ijiri^{2,3}, Arthur J. Spivack⁴, Yuki Morono², Fumio Inagaki^{5,6},
Verena B. Heuer⁷, Sabine Kasten^{1,7,8}, and Susann Henkel^{1,7}

¹Alfred Wegener Institute Helmholtz Centre for Polar and Marine Research, Bremerhaven, Germany

²Kochi Institute for Core Sample Research, Japan Agency for Marine-Earth Sciences and Technology (JAMSTEC), Nankoku, Japan

³Now at Kobe University, Graduate School of Maritime Sciences, Kobe, Japan

⁴University of Rhode Island, Graduate School of Oceanography, Rhode Island, USA

⁵Mantle Drilling Promotion Office, Institute for Marine-Earth Exploration and Engineering (MarE3), Japan Agency for Marine-Earth Sciences and Technology (JAMSTEC), Yokohama, Japan

⁶Department of Earth Sciences, Graduate School of Science, Tohoku University, Sendai, Japan

⁷MARUM - Center for Marine Environmental Sciences, University of Bremen, Bremen, Germany

⁸Faculty of Geosciences, University of Bremen, Bremen, Germany

Manuscript in preparation for submission to *Geology*

The format has been adapted to the thesis format.

Abstract

Biogeochemical processes within deep subseafloor sediments can significantly change over geological timescales due to variations in oceanographic, climatic or depositional conditions. By using reactive transport modeling, we reconstructed the evolution of biogeochemical processes in ~1.2-km deep and up to 120°C hot subseafloor sediments from International Ocean Discovery Program (IODP) Site C0023 in the Nankai Trough over the past 5.5 Ma. Due to its complex depositional and thermal history, Site C0023 offers a great opportunity to study biogeochemical processes under strongly changing environmental and depositional conditions. A distinctive biogeochemical feature at Site C0023 is an inverse sulfate-methane transition (SMT) with a relatively broad overlap zone between sulfate and methane of ~100 m, which is located in 80° to 85°C hot sediments. This temperature range coincides with the known temperature limit of anaerobic methane-oxidizing communities. Based on the reactive transport model, we demonstrate that the deep inverse SMT was formed after the onset of biogenic methanogenesis and anaerobic oxidation of methane (AOM) at ~2.5 Ma as a consequence of enhanced organic carbon burial. Depth-integrated AOM rates derived from the model have markedly decreased since the beginning of trench-style deposition and the associated rapid heating of ~50°C across the sediment column at ~0.4 Ma. We argue that the microbial activity of anaerobic methane-oxidizing communities at the deep inverse SMT has already started to cease and the SMT is about to further disappear. This is the first study that documents the successive fading of an SMT and the decrease in the efficiency of this microbial methane sink as a consequence of sediment temperatures increasing beyond the threshold of being suitable for anaerobic methane-oxidizing microbial communities.

1. Introduction

The deep subseafloor biosphere is generally referred to sediments deeper than 5 m below seafloor (mbsf) and represents the largest reservoir of organic carbon on Earth (e.g., Horsfield et al., 2006). The driving force for microbial activity in subseafloor sediments is the degradation of organic matter (e.g., D'Hondt et al., 2002). Due to the vast extension of deep subseafloor sediments, the diverse and mostly uncharacterized microorganisms inhabiting the deep biosphere might play an important role in global biogeochemical cycles (D'Hondt et al., 2002, 2004; Inagaki et al., 2006; Hoshino et al., 2020). However, microbial communities within subseafloor sediments are not only exposed to extreme energy-limited and nutrient-poor conditions, but they are also facing increasing temperature with ongoing burial with a typical geothermal gradient of 30°C km⁻¹ (Inagaki et al., 2015; Lever et al., 2015). The upper

temperature limit for microbial life in subseafloor sediments and, thus, the lower boundary of the deep biosphere is unknown as yet. While microbial activity in deep and energy-starved sediments is assumed to cease at $\sim 80^{\circ}\text{C}$ (Head et al., 2003, Parkes et al., 2007), the currently known temperature limit for microbial life determined in laboratory experiments with microbial communities from hydrothermal vent environments is around 120°C or even higher (Blöchl et al., 1997; Kashefi and Lovley, 2003; Takai et al., 2008).

To explore the prerequisite of microbial life under such extreme conditions and/or nutrient limitation, Site C0023 was drilled during International Ocean Discovery Program (IODP) Expedition 370 down to 1,180 mbsf in the Nankai Trough off Cape Muroto, Japan (Fig. 1; Heuer et al., 2017). Even though the sediment temperature reaches $120^{\circ} \pm 3^{\circ}\text{C}$ at the sediment-basement interface (Heuer et al., 2020), vegetative cells as well as microbial activity were observed throughout the entire sediment column, indicating that microbial life in the energy-limited marine sedimentary biosphere can persist well above 80°C (Heuer et al., 2020; Beulig et al., 2022). However, cell concentrations and potential metabolic rates determined in radiotracer incubation experiments significantly dropped by two to three orders of magnitude above 45°C , which likely marks the temperature limit for the growth of mesophilic microorganisms (Heuer et al., 2020; Beulig et al., 2022). Site C0023 does not only represent an unique environment with regard to the thermal conditions and the existence of microbial activity in up to 120°C hot sediments, but the present-day profiles of sulfate and methane also display an unusual situation. Besides a conventional sulfate-methane transition (SMT) located in the upper 5 m of the sediment column (Shipboard Scientific Party, 2001), there is an inverse SMT with elevated methane concentrations in the upper core part above 700 mbsf and increasing sulfate concentrations further downcore (Fig. 2A; Heuer et al., 2017).

Biogeochemical processes can significantly change over geological timescales due to changing oceanographic, climatic and/or depositional conditions (e.g., Meister et al., 2019). However, while several studies have focused on the present-day microbial distribution, diversity and metabolic activity in different subseafloor regions (e.g., D'Hondt et al., 2004; Kallmeyer et al., 2012), the evolution of microbial activity that may be accompanied by changes in geochemical, depositional and thermal changes on longer timescales is less understood. In a previous study, we reconstructed the evolution of (bio-)geochemical processes at Site C0023 over the past 15 Ma along the tectonically induced migration from the Shikoku Basin to the Nankai Trough and presented a conceptual geochemical process model (Köster et al., 2021). We demonstrated that significant changes in sedimentation rates, organic matter contents and thermal conditions led to a transition from an organic carbon-starved environment with predominantly aerobic

respiration processes and deep sulfate penetration to elevated carbon burial and the onset of anaerobic electron-accepting processes including the biogenic methane production and the anaerobic oxidation of methane (AOM).

Here, we assess the plausibility of the conceptual model we proposed in our previous study (Köster et al., 2021) by using reactive transport modeling. We simulate the profiles of sulfate and methane including the depth of the SMT as a function of sedimentation rates, carbon contents and sediment temperature. We further derive metabolic reaction rates from the model and investigate how microbial activity within the deep SMT changed with ongoing burial and heating of the sediments.

2. Geological, sedimentary and geochemical setting

IODP Site C0023 (32°22.00'N, 134°57.98'E; 4,776 m water depth) is situated southwest of Shikoku Island, Japan, in the Nankai Trough subduction zone, where the Philippine Sea plate is subducting beneath the Eurasian plate (Fig. 1; Heuer et al., 2017). The Nankai Trough off Cape Muroto is characterized by anomalously high heat flows (Yamano et al., 1992). With a geothermal gradient of 110°C km⁻¹, the temperature at Site C0023 increases from ~2°C at the sediment-water interface up to 120°C ± 3°C in the deepest core retrieved from the basement at 1177 mbsf (Heuer et al., 2020).

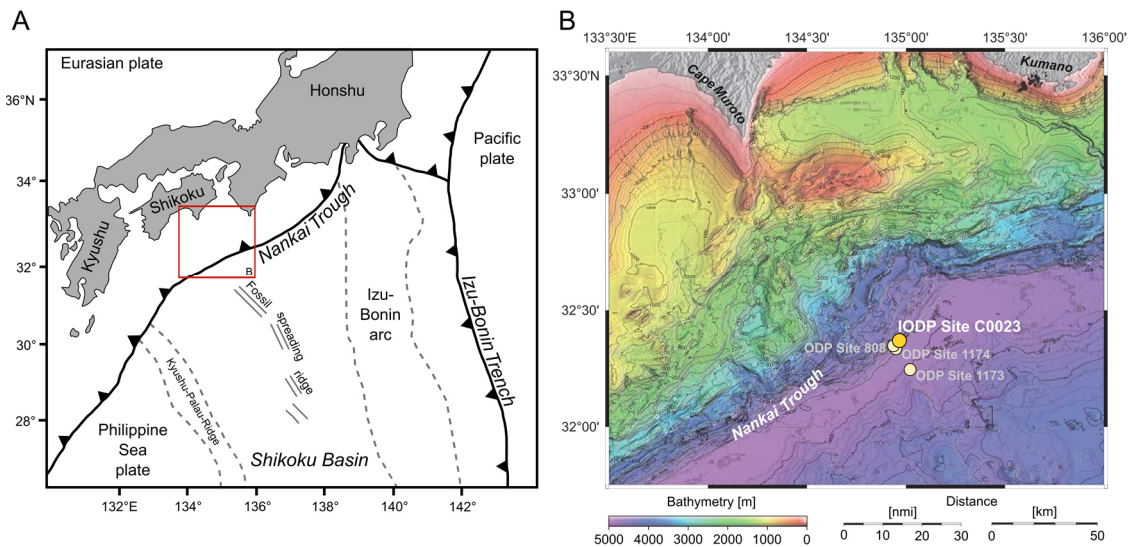


Figure 1. Overview maps of the Shikoku Basin and the Nankai Trough subduction zone offshore Japan in the northwestern Pacific Ocean. (A) Simplified schematic plate tectonic configuration of the Nankai Trough subduction zone. (B) Bathymetric map around IODP Site C0023 (yellow circle) off Cape Muroto, Shikoku Island, and the adjacent ODP Sites 808, 1173 and 1174 (white circles). Modified after Heuer et al. (2017).

The ~1.2 km-thick sediment sequence at Site C0023 can be grouped into five lithological units (Fig. 2). The volcanoclastic facies is the oldest unit that accumulated on the ~16-million-year-old basaltic basement when Site C0023 was located close to the spreading center of the Shikoku Basin. Unit V is overlain by the Lower and the Upper Shikoku Basin facies, both characterized by hemipelagic bioturbated mudstones (Taira et al., 1992). Site C0023 has moved ~750 km relative to its present-day geographic position from the central Shikoku Basin to the Nankai Trough due to tectonic motion of the Philippine Sea plate (Mahony et al., 2011) and the Trench-to-basin transitional and the Trench-wedge facies accumulated on the ~600 m thick sequence of basin-style deposited hemipelagic mudstones. The trench facies are characterized by turbidite-deposited mud, silt and sand (Taira et al., 1992). The transition from hemipelagic basin-style to trench-style deposition is accompanied by a significant increase in sedimentation rates by two orders of magnitude from 3.5-6.0 cm kyr⁻¹ during deposition of the Lower Shikoku Basin facies up to ~130 cm kyr⁻¹ during deposition of the Trench-wedge facies (Tab. S1; Hagino and the Expedition 370 Scientists, 2018). This increase in sedimentation rates led to a rapid temperature increase of about 50°C across the sediment column (Horsfield et al., 2006; Tsang et al., 2020). At present, Site C0023 is characterized by overall low (< 0.6 wt%) total organic carbon contents (C_{org}) (Fig. 2D; Heuer et al., 2017). The deep inverse SMT where downward diffusing methane intersects with upward diffusing sulfate, which is preserved in the Lower Shikoku Basin facies, is located at ~730 mbsf (Fig. 2A; Heuer et al., 2020; Köster et al., 2021).

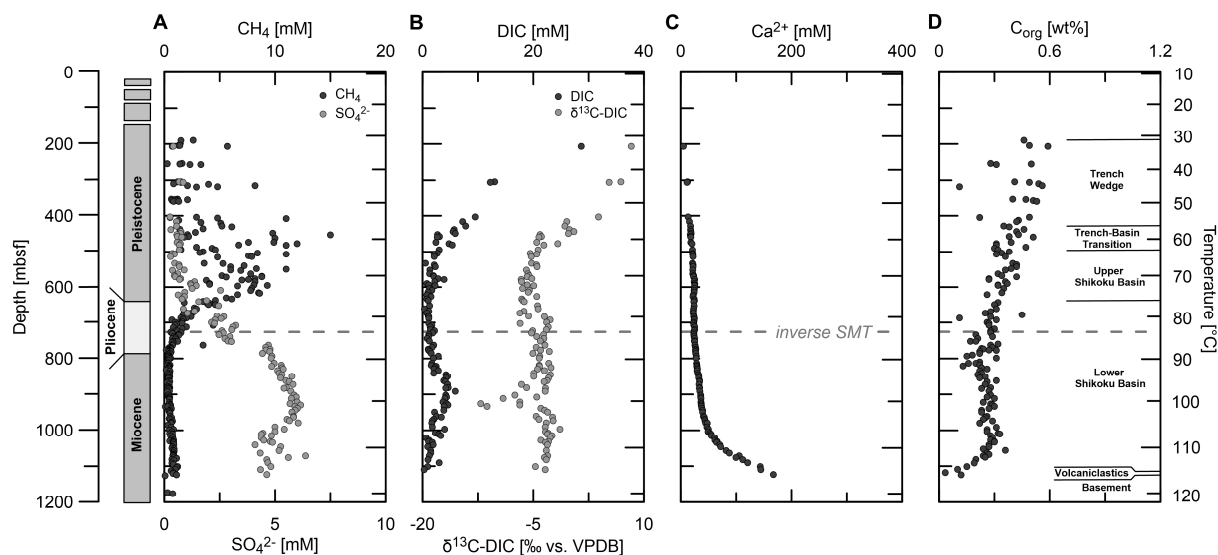


Figure 2. Geochemical profiles of IODP Site C0023. (A) Pore-water profiles of sulfate (SO_4^{2-} ; grey dots) and methane (CH_4 ; black dots). (B) Pore-water profiles of dissolved inorganic carbon (DIC; black dots) and its carbon isotopic composition ($\delta^{13}\text{C-DIC}$; grey dots). (C) Pore-water profile of dissolved calcium (Ca^{2+}). (D) Solid-phase profile of total organic carbon (C_{org}). All geochemical data except for $\delta^{13}\text{C-DIC}$ (this study) are from Heuer et al. (2017). Corresponding ages on the left-side y-axis are based on the age model by Hagino and the Expedition 370 Scientists (2018). Lithological units and temperature data on the right-side y-axis are from Heuer et al. (2017) and (2020), respectively.

3. Methods

3.1 Geochemical analyses

In this study, we use sulfate (SO_4^{2-}), dissolved inorganic carbon (DIC), methane (CH_4), calcium (Ca^{2+}) and total organic carbon (C_{org}) data from Site C0023 obtained during IODP Expedition 370 (Heuer et al., 2017). All pore-water, gas and sediment measurements were performed onboard *D/V Chikyu* according to IODP standard protocols (Morono et al., 2017).

The carbon isotopic composition of DIC ($\delta^{13}\text{C-DIC}$) was determined via isotopic ratio monitoring-gas chromatography mass spectrometry (irm-GC-C-MS; Thermo Finnigan Delta Plus XP isotope-ratio mass spectrometer (IRMS) connected to TRACE GC Ultra gas chromatograph) (Ijiri et al., 2012) at the Kochi Institute for Core Sample Research, JAMSTEC, Japan. The $\delta^{13}\text{C-DIC}$ values are expressed relative to VPDB (Vienna Pee Dee Belemnite). The standard deviation from repeated carbon isotope analysis of the laboratory standard (NaHCO_3 solution) was $< 0.2\%$.

3.2 Reactive transport modeling

A one-dimensional reactive transport model (e.g., Boudreau, 1997) was used to simulate the past evolution of the SO_4^{2-} and CH_4 profiles. The model comprises three dissolved (SO_4^{2-} , CH_4

and DIC) and one solid species (C_{org}) as well as three reactions (organoclastic sulfate reduction (SR), biogenic methanogenesis (MG), and anaerobic oxidation of methane (AOM)). Organic matter degradation is described using a 3-G model, which accounts for the differences in reactivity of organic matter, whereby the organic matter pool is classified into labile, metabolize and refractory fractions (Jørgensen, 1978). To assess the evolution of metabolic rates during progressive burial and heating, we integrated the temperature dependency of the rate constants and a temperature-limiting term for catabolic activity according to LaRowe et al. (2014). The diagenetic reaction network further includes the precipitation of calcium sulfate phases including gypsum ($\text{CaSO}_4 \cdot 2\text{H}_2\text{O}$) and anhydrite (CaSO_4). The precipitation rates were estimated from consumption rates of SO_4^{2-} and Ca^{2+} .

We simulated the profiles of SO_4^{2-} and CH_4 from 5.53 Ma to the present-day situation for seven different snapshots. These snapshots were defined based on the different sedimentation intervals according to the age model for Site C0023 (Tab. S1; Hagino and the Expedition 370 Scientists, 2018) with different C_{org} flux (F_{org1} , F_{org2} and F_{org3}) at the upper boundary at each sedimentation interval. A full description of model setup, parameters and boundary conditions is provided in the Supplemental Material.

4. Results and discussion

4.1 Past migration of the deep SMT

We simulated the evolution of the shallow and the deep inverse SMT over the past 5.5 Ma to quantitatively test the conceptual geochemical process model we presented in Köster et al. (2021) (Fig. 3). While we originally postulated that oxic degradation of organic matter dominated during the deposition of the Lower Shikoku Basin facies due to low C_{org} contents and sedimentation rates (Köster et al., 2021), our model now demonstrates that SO_4^{2-} in the deep deposits was at least partially consumed (Fig. 3). The SO_4^{2-} pool, however, was not completely exhausted, but to some extent, preserved in the bottom 400 m of the Lower Shikoku Basin facies. Increased C_{org} contents during deposition of the Upper Shikoku Basin facies possibly related to elevated marine productivity initiated the onset of biogenic methanogenesis at around 2.5 Ma. As a consequence, a shallow SMT formed, where the upward diffusing CH_4 reacted with SO_4^{2-} diffusing downwards from the overlying seawater. Due to the availability of the relict SO_4^{2-} pool in the Lower Shikoku Basin facies, a second deep inverse SMT formed, where the downward diffusing CH_4 was oxidized by the preserved SO_4^{2-} (Fig. 3; Köster et al., 2021).

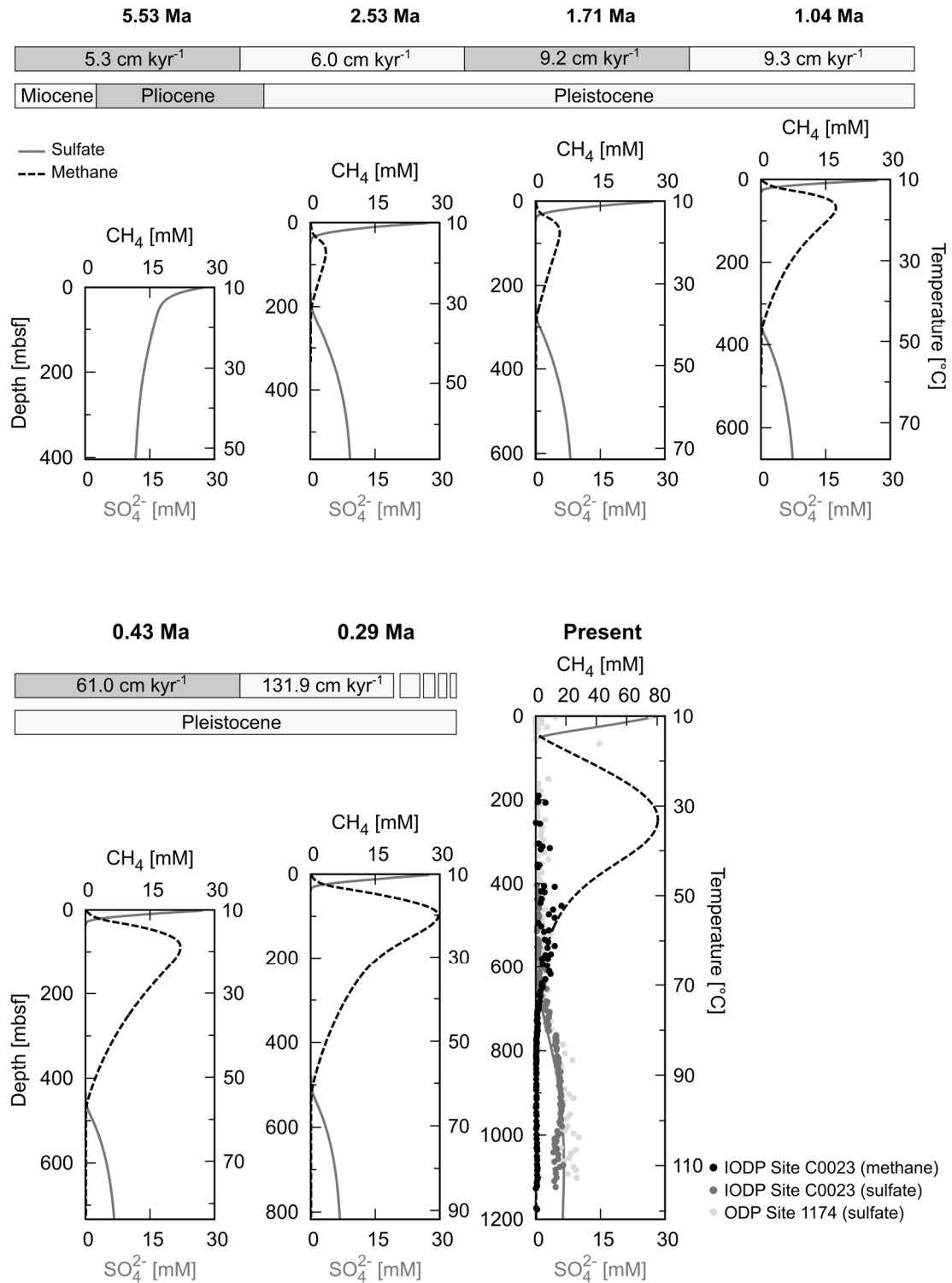


Figure 3. Snapshots of simulated depth-profiles of sulfate (grey line) and methane (black line) derived from the reactive transport model over the past ~5.5 Ma. The snapshots from 5.53 to 0.29 Ma correspond to the sedimentation intervals according to the age model for Site C0023 (Hagino and the Expedition 370 Scientists, 2018). *In situ* concentrations of sulfate (dark grey dots) and methane (black dots) from IODP Site C0023 (Heuer et al., 2017) as well as sulfate concentrations from ODP Site 1774 (light grey dots; Shipboard Science Party, 2001) are shown in the present-day situation. Temperature data on the y-axes are based on the steady-state temperature profile from Heuer et al. (2020).

Continuously increasing C_{org} burial during deposition of the Upper Shikoku Basin facies resulted in elevated methanogenesis. The increased CH_4 fluxes shifted the shallow and deep inverse SMTs up- and downwards, respectively (Fig. 3).

The model shows that the deep inverse SMT was fixed at a specific depth interval from 1.04 to 0.29 Ma, which corresponds to a present-day depth between 880 and 920 mbsf (Fig. 3). This past location is further indicated by the DIC profile and its carbon isotopic composition ($\delta^{13}\text{C-DIC}$) (Fig. 2B). While DIC concentrations remain low (< 2 mM) below 500 mbsf, they slightly increase up to 6 mM between 800 and 1000 mbsf. Concurrently, $\delta^{13}\text{C-DIC}$ values are constant around -5.0‰ , except for the interval between 900 and 930 mbsf where $\delta^{13}\text{C-DIC}$ values show a negative excursion down to -12.1‰ . Strongly ^{13}C -depleted DIC down to -30.0‰ is indicative of AOM (e.g., Alperin et al., 1988; Meister and Reyes, 2019). Even though the $\delta^{13}\text{C-DIC}$ values at Site C0023 are less negative, the preserved negative $\delta^{13}\text{C-DIC}$ signature and the concurrent maximum in DIC concentrations at around 900 mbsf could be the relic of a past SMT location, suggesting that the deep inverse SMT was stationary at this depth for almost one million years between ~ 1 and ~ 0.3 Ma (Fig. 3).

The onset of trench-style deposition at 0.43 Ma was accompanied by an increase in sedimentation rates by two orders of magnitudes compared to the basin-style sedimentation (Tab. S1; Hagino and the Expedition 370 Scientists, 2018) and an increase in temperature by $\sim 50^\circ\text{C}$ across the sediment column (Tsang et al., 2020). Heating of sediments due to ongoing burial might activate sedimentary organic matter that is recalcitrant at seafloor temperatures of $\sim 2\text{-}3^\circ\text{C}$, thus increasing its bioavailability (e.g., Wellsburry et al., 1997; Burdige, 2011). Therefore, the significant increase in temperature since ~ 0.4 Ma could have led to enhanced biogenic CH_4 production (Fig. 3; Köster et al., 2021).

4.2 Present-day sulfate and methane profiles and reaction rates

Our model reproduces the general shapes of the present-day SO_4^{2-} and CH_4 profiles (Fig. 3). Even though thermophilic methanogens can reach their optimal growth rate at temperatures above 45° , biogenic methanogenesis is known to be favored at moderate temperatures between 35° and 42°C (e.g., Zeikus and Winfrey, 1976). This temperature range is consistent with the present-day temperature of $\sim 35^\circ\text{C}$ at 250 mbsf, where simulated CH_4 concentrations reach maximum values of almost 80 mM. We argue that the offset between *in situ* and simulated CH_4 concentrations is likely related to an underestimation of *in situ* CH_4 concentrations, as the gas is known to escape during core recovery and sampling. Gas voids that occur when the total gas pressure exceeds the confining pressure within the core liner (e.g., Spivack et al., 2006) were

observed between 200 and 360 mbsf (Heuer et al., 2017), suggesting that *in situ* CH₄ concentrations are indeed higher than observed.

In this study, we derived present-day rates of organoclastic sulfate reduction (SR), biogenic methanogenesis (MG) and AOM from the reactive transport model (Fig. 4; Tab. S3). The modeled SR rates reach a maximum of almost 0.3 pmol cm⁻³ d⁻¹ in the upper 100 mbsf (Fig. 4A). The MG rates are elevated between 100 and 400 mbsf with a maximum of ~0.4 pmol cm⁻³ d⁻¹ at 190 mbsf (Fig. 4B). Potential SR and MG rates at Site C0023 were recently determined in radiotracer incubation experiments, which were performed at different temperature within the *in situ* range and the addition of different electron donors (Beulig et al., 2022). While potential SR and MG rates are extremely high (~10² to 10³ pmol cm⁻³ d⁻¹) in incubation experiments at a temperature of 40°C between 190 and 320 mbsf, they decrease to ~0.3 pmol cm⁻³ d⁻¹ further downcore, which is consistent with our modeled SR and MG rates (Fig. 4). The significant decrease in potential metabolic rates is accompanied by a drop in vegetative cell concentrations by two orders of magnitude from > 10⁴ to < 10² cells cm⁻³ at an *in situ* temperature between 40° and 50°C (Heuer et al., 2020). This temperature range reflects the upper temperature limit for mesophilic microbial community, suggesting that only (hyper-)thermophilic microorganisms survived burial into deeper and hotter sediments (Beulig et al., 2022).

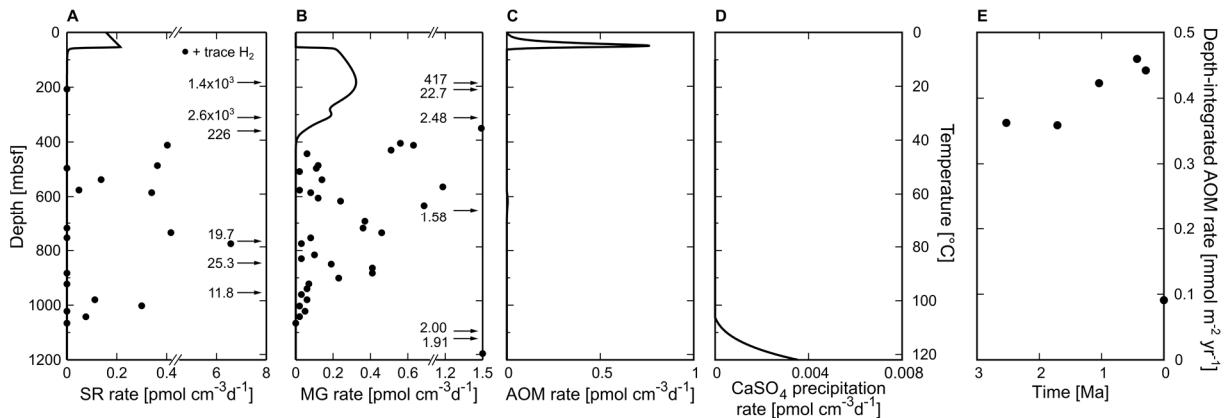


Figure 4. Metabolic reaction rates derived from the reactive transport model. (A) Simulated present-day organoclastic sulfate reduction (SR) rate (black line). Potential sulfate reduction rates (using ³⁵S-SO₄²⁻) with trace H₂ added (black dots) from Beulig et al. (2022) are shown for comparison. (B) Simulated present-day biogenic methanogenesis (MG) rate (black line). Potential rates of methanogenesis (using ¹⁴C-DIC) with trace H₂ added (black dots) are from Beulig et al. (2022). Note that some data points of potential SR and MG rates in (A) and (B), in particular between 190 and 360 mbsf, are off-scale. (C) Simulated present-day rate of anaerobic oxidation of methane (AOM). (D) Simulated present-day calcium sulfate (CaSO₄) precipitation rate. (E) Simulated evolution of the depth-integrated AOM rate since the onset of AOM at ~2.5 Ma.

Beulig et al. (2022) argued that organoclastic SR has started at ~0.4 Ma, following the onset of rapid sedimentation and associated heating of the sediments. Their argumentation refers to the observation that at Ocean Drilling Program (ODP) Site 1225 in the eastern equatorial Pacific, where sediment age and present-day C_{org} contents are similar to those at Site C0023, SO_4^{2-} is depleted by less than 2 mM compared to seawater values (Shipboard Scientific Party, 2003). However, thermal conditions at ODP Site 1225 are markedly different and the temperature only reaches 7°C at the sediment-basement interface. C_{org} contents in the bottom ~450 m of the sediment column at Site C0023 are ~0.25 wt% on average and, thus, similar to ODP Site 1225 (Fig. 2D), but it should be noted that these low contents represent the preserved refractory organic matter pool and that the initial C_{org} contents at Site C0023 were likely higher. Based on our model, organoclastic SR already occurred at 5.53 Ma (Fig. 3). During this time, the thermal regime was similar compared to the upper ~400 m of the present-day sediment column and the temperature increased up to 50°C at the sediment-basement interface. This temperature range is consistent with the temperature optimum (~35°C) of mesophilic sulfate-reducing bacteria (e.g., Isaksen and Jørgensen, 1996) and the maximum in potential SR rates in incubation experiments at 40°C (Fig. 4; Beulig et al., 2022). In addition, we observed pyrite enrichments accompanied by minima in the magnetic susceptibility even in the lower parts of the Lower Shikoku Basin facies, suggesting that iron (oxyhydr)oxides were diagenetically transformed into iron sulfides (Köster et al., 2021). The occurrence of pyrite between 900 and 1100 mbsf, ~200 m below the current inverse SMT, indicates that the sulfidization front was located deeper in the past. This in turn means that the inverse SMT was also located deeper and/or organoclastic SR already occurred during the deposition of the Lower Shikoku Basin facies. Thus, the onset of SR before 0.4 Ma is very likely (Fig. 3).

While a relict SO_4^{2-} pool with concentrations of up to 6 mM is still preserved below the current deep inverse SMT at ~730 mbsf, the measured concentrations scatter, but show an overall decreasing trend below 1000 mbsf at temperatures above 105°C, suggesting an additional sink of SO_4^{2-} (Fig. 2A). Concurrently, Ca^{2+} concentrations sharply increase from 50 to 170 mM at the sediment-basement interface (Fig. 3C). The release of Ca^{2+} is most likely caused by alteration of plagioclase in the underlying basement (Heuer et al., 2017). During this albitization, calcic plagioclase (e.g., anorthite [$CaAl_2Si_2O_8$]) is replaced by albite ($NaAl_2Si_3O_8$) and Ca^{2+} is released into the pore water (e.g., Humphris and Thompson, 1978). The overall decrease in SO_4^{2-} concentration below 1000 mbsf can be explained by the precipitation of anhydrite ($CaSO_4$), which is a major sink for SO_4^{2-} in hydrothermal systems (e.g., Alt et al., 1986). We integrated the precipitation of $CaSO_4$ phases in the reactive transport model (see

Supplemental Material) and derived the precipitation rate (Fig. 4D). The pore water is saturated with respect to anhydrite below 1000 mbsf at temperatures above 110°C. Consequently, the decreasing trend in *in situ* SO₄²⁻ concentrations in the deeper core part is well reproduced by the model (Fig. 3). The precipitation of anhydrite accounts for almost 1% of the total SO₄²⁻ consumption at Site C0023 (Fig. S3).

The current depth of the shallow SMT at Site C0023 could not be determined during IODP Expedition 370 since sediments shallower than ~200 mbsf were not recovered (Heuer et al., 2017). Based on SO₄²⁻ and CH₄ profiles from the adjacent ODP Site 1174 (Fig. 1; Shipboard Scientific Party, 2001), we assume that the shallow SMT is located at ~5 mbsf. The simulated shallow SMT, however, is located at around 50 mbsf (Fig. 3). This difference is related to the lack of geochemical and sedimentation rate data in the upper 200 m of the sediment column. Therefore, we used the sedimentation rate of the Trench-wedge facies and took C_{org} data as fitting parameter for the upper 200 m in the model. We performed a time series simulation for the upward migration of the shallow SMT (Fig. S4). If assuming a constant present-day sedimentation rate of ~130 cm kyr⁻¹ similar to the rate in the most recent Trench-wedge facies (Hagino and the Expedition 370 Scientists, 2018), an increase in C_{org} contents of up to 4 wt% in the upper 30 m of the sediment column is necessary to shift the shallow SMT to ~7 mbsf. This upward migration will take around 2,000 years (Fig. S4). An overall increase in C_{org} contents is reasonable due to the proximity to the Japanese Islands and, thus, a related higher input of organic-rich (terrigenous) material from the coast and the shelf off Shikoku Island. However, an increase of up to 4 wt% might be overestimated. Thus, we suspect that the shallow position of the SMT is likely the result of increasing C_{org} contents in the surface sediments, but at the same time, a decrease in present-day sedimentation rates compared to a rate of ~130 cm kyr⁻¹.

4.3 Decay of the deep inverse SMT

In marine shelf sediments, the SMT is commonly considered as a sharp boundary where SO₄²⁻ and CH₄ profiles intersect and the concentrations of both species decrease below detection limit (e.g., Niewöhner et al., 1998). However, the SO₄²⁻ and CH₄ profiles at Site C0023 overlap in a relatively broad zone between ~600 and 700 mbsf, whereby CH₄ only reaches near-zero concentrations (< 0.5 mM) at ~785 mbsf (Fig. 2A). This tailing of CH₄ into the SO₄²⁻-rich zone has been commonly observed in shallow sediments of the Black Sea and is explained by inefficient microbial CH₄ oxidation (Jørgensen et al., 2001; Knab et al., 2009).

A positive excursion in $\delta^{13}\text{C}\text{-CH}_4$ values up to -54‰ at ~ 730 mbsf, indicative of a biogenic CH_4 sink and the activity of AOM-performing organisms (Heuer et al., 2020), locates the current deep inverse SMT between the actual zone of overlapping pore-water SO_4^{2-} and CH_4 and the depth where CH_4 decreases to near-zero concentrations. This depth corresponds to a temperature range between 80° to 85°C (Fig. 2A; Heuer et al., 2020). As incubation experiments with hydrothermal sediments from the Guaymas Basin have shown that AOM is limited at temperatures $> 80^\circ\text{C}$ (e.g., Kallmeyer and Boetius, 2004; Holler et al., 2011), Köster et al. (2021) inferred that, at present, AOM only barely occurs at Site C0023.

Here, we assess the evolution of AOM activity by simulating AOM rates. Figure 4E shows the depth-integrated AOM rate for the deep inverse SMT since the onset at ~ 2.5 Ma. The AOM rates slightly increase from ~ 0.35 to ~ 0.45 $\text{mmol m}^{-2} \text{yr}^{-1}$ between 2.5 and 0.4 Ma. A significant drop in AOM rates to < 0.1 $\text{mmol m}^{-2} \text{yr}^{-1}$ can be observed since the beginning of the rapid burial and associated heating of sediments at around 0.4 Ma (Fig. 4E). Furthermore, $\delta^{13}\text{C}\text{-DIC}$ values do not show a negative excursion typically observed at the SMT (Fig. 2B). Accordingly, radiotracer experiments do not show elevated potential AOM and SR rates with the excess addition of CH_4 at the depth of the current deep inverse SMT (Beulig et al., 2022). These observations collectively suggest that AOM activity at the lower inverse SMT is at the threshold to cease or has already stopped and consequently, the deep inverse SMT gradually disappears. This is consistent with the findings by Beulig et al. (2022) that microorganisms at Site C0023 live within the narrow range between subsistence near the upper temperature limits for microbial life and a rich surplus of energy and bioavailable organic carbon. We suspect that with increasing time, the concentrations gradients of SO_4^{2-} and CH_4 likely equilibrate by diffusion, leading to an even broader sulfate-methane overlap zone.

5. Conclusions

In this study, we quantitatively tested the conceptual model we previously proposed (Köster et al., 2021) by using reactive transport modeling. Site C0023 has experienced significant changes in biogeochemical processes, which is ultimately the result of strongly changing depositional, and, in particular, thermal conditions that are driven by the tectonic migration of the ocean floor. Based on the reactive transport model, we demonstrated the evolution of the deep inverse SMT from its establishment at around 2.5 Ma, through the downward migration until ~ 0.5 Ma to its decay since the onset of the rapid heating at ~ 0.4 Ma. With progressive burial and associated heating, the AOM activity at the deeper inverse SMT gradually decreases and the SMT successively disappears. We refer to this process as a fading SMT. This is the first time

that such a decrease in microbial activity and the impact on geochemical conditions as a consequence of increasing temperatures can be observed *in situ*, which further underlines the unique biogeochemistry of Site C0023.

Acknowledgements

This research used samples and data provided by the International Ocean Discovery Program (IODP). We would like to thank all personnel involved in the operations onboard the *D/V Chikyu* during Expedition 370, especially Kira Homola and Justine Sauvage, as well as the support team at Kochi Core Center. This study is funded by the German Research Foundation (DFG) in the framework of the priority program 527 (Bereich Infrastruktur – International Ocean Discovery Program; project 388260220). We acknowledge further financial support from the Helmholtz Association (Alfred Wegener Institute Helmholtz Centre for Polar and Marine Research).

References

- Alperin, M.J., Reeburgh, W.S., and Whiticar, M.J., 1988. Carbon and hydrogen isotope fractionation resulting from anaerobic methane oxidation. *Global Biogeochemical Cycles*, **2**, 279-288. doi:10.1029/GB002i003p00279.
- Alt, J.C., Honnorez, J., Laverne, C., and Emmermann, R. 1986. Hydrothermal alteration of a 1 km section through the upper oceanic crust, Deep Sea Drilling Project Hole 504B: Mineralogy, chemistry and evolution of seawater-basalt interactions. *Journal of Geophysical Research: Solid Earth*, **91**, 10309-10355. doi:10.1029/JB091iB10p10309.
- Beulig, F., Schubert, F., Adhikari, R.R., Glombitza, C., Heuer, V.B., Hinrichs, K.-U., et al., 2022. Rapid metabolism fosters microbial survival in deep, hot subseafloor biosphere. *Nature Communications*, **13**, 312. doi:10.1038/s41467-021-27802-7.
- Blöchl, E., Rachel, R., Burggraf, S., Hafenbradl, D., Janasch, H.W., and Stetter, K.O., 1997. *Pyrolobus fumarii*, gen. and sp. nov., represents a novel group of archaea, extending the upper temperature limit for life to 113°C. *Extremophiles*, **1**, 14-21. doi:10.1007/s007920050010.
- Boudreau, B.P., 1997. *Diagenetic Models and Their Implementation: Modelling Transport and Reactions in Aquatic Sediments*. Springer, Berlin, Heidelberg, New York, 428 p.
- Burdige, D.J., 2011. Temperature dependence of organic matter remineralization in deeply-buried marine sediments. *Earth and Planetary Science Letters*, **311**, 396-410. doi:10.1016/j.epsl.2011.09.043.
- D'Hondt, S., Rutherford, S., and Spivack, A.J., 2002. Metabolic activity of subsurface life in deep-sea sediments. *Science*, **295**, 2067-2070. doi:10.1126/science.1064878.
- D'Hondt, S., Jørgensen, B.B., Miller, D.J., Batzke, A., Blake, R., Cragg, B.A., et al., 2004. Distributions of microbial activities in deep subseafloor sediments. *Science*, **306**, 2216-2221. doi:10.1126/science.1101155.

- Hagino, K., and the Expedition 370 Scientists, 2018. Data report: calcareous nannofossils from the middle Miocene to Pleistocene, IODP Expedition 370 Site C0023. In: *Proceedings of the International Ocean Discovery Program Volume 370* (eds. Heuer, V.B., Inagaki, F., Morono, Y., Kubo, Y., Maeda, L., and the Expedition 370 Scientists). College Station, TX (International Ocean Discovery Program). doi:10.14379/iodp.proc.370.201.2018.
- Head, I.M., Jones, D.M., and Larter, S.R., 2003. Biological activity in the deep subsurface and the origin of heavy oil. *Nature*, **426**, 344-352. doi:10.1038/nature02134.
- Heuer, V.B., Inagaki, F., Morono, Y., Kubo, Y., Maeda, L., and the Expedition 370 Scientists, 2017. Temperature limit of the deep biosphere off Muroto. *Proceedings of the International Ocean Discovery Program Volume 370*: College Station, TX (International Ocean Discovery Program). doi:10.14379/iodp.proc.370.2017.
- Heuer, V.B., Inagaki, F., Morono, Y., Kubo, Y., Spivack, A., Viehweger, B., et al., 2020. Temperature limits to deep seafloor life in the Nankai Trough subduction zone. *Science*, **370**, 1230-1234. doi:10.1126/science.abd7934.
- Holler, T., Widdel, F., Knittel, K., Amann, R., Kellermann, M.Y., Hinrichs, K.-U., et al., 2011. Thermophilic anaerobic oxidation of methane by marine microbial consortia. *The ISME Journal*, **5**, 1946-1956. doi:10.1038/ismej.2011.77.
- Hoshino, T., Doi, H., Uramoto, G.-I., Wörmer, L., Adhikari, R.R., Xiao, N., et al., 2020. Global diversity of microbial communities in marine sediment. *Proceedings of the National Academy of Sciences of the United States of America*, **117**, 27587-27597. doi:10.1073/pnas.1919139117.
- Horsfield, B., Schenk, H.J., Zink, K., Ondrak, R., Dieckmann, V., Kallmeyer, J., et al., 2006. Living microbial ecosystems within the active zone of catagenesis: Implications for feeding the deep biosphere. *Earth and Planetary Science Letters*, **246**, 55-69. doi:10.1016/j.epsl.2006.03.040.
- Humphris, S.E., and Thompson, G., 1978. Hydrothermal alteration of oceanic basalts by seawater. *Geochimica et Cosmochimica Acta*, **42**, 107-125. doi:10.1016/0016-7037(78)90221-1.
- Ijiri, A., Harada, N., Hirota, A., Tsunogai, U., Ogawa, N.O., Itaki, T., Khim, B.-K., and Uchida, M., 2012. Biogeochemical processes involving acetate in sub-seafloor sediments from the Bering Sea shelf break. *Organic Geochemistry*, **48**, 47-55. doi:10.1016/j.orggeochem.2012.04.004.
- Inagaki, F., Nunoura, T., Nakagawa, S., Teske, A., Lever, M., Lauer, A., et al., 2006. Biogeographical distribution and diversity of microbes in methane hydrate-bearing deep marine sediments on the Pacific Ocean Margin. *Proceedings of the National Academy of Sciences of the United States of America*, **103**, 2815-2820. doi:10.1073/pnas.0511033103.
- Inagaki, F., Hinrichs, K.-U., Kubo, Y., Bowles, M.W., Heuer, V.B., Hong, W.L., et al., 2015. Exploring deep microbial life in coal-bearing sediment down to ~2.5 km below the ocean floor. *Science*, **349**, 420-424. doi:10.1126/science.aaa6882.
- Isaksen, M.F., and Jørgensen, B.B., 1996. Adaptation of psychrophilic and psychrotrophic sulfate-reducing bacteria to permanently cold marine environments. *Applied and Environmental Microbiology*, **62**, 408-414. doi:10.1128/aem.62.2.408-414.1996.
- Jørgensen, B.B., 1978. A comparison of methods for the quantification of bacterial sulfate reduction in coastal marine sediments: II. Calculation from mathematical models. *Geomicrobiology Journal*, **1**, 11-27. doi:10.1080/01490457809377722.

- Jørgensen, B.B., Weber, A., and Zopfi, J., 2001. Sulfate reduction and anaerobic methane oxidation in Black Sea sediments. *Deep Sea Research Part I: Oceanographic Research Papers*, **48**, 2097-2120. doi:10.1016/S0967-0637(01)00007-3.
- Kallmeyer, J., and Boetius, A., 2004. Effects of temperature and pressure on sulfate reduction and anaerobic oxidation of methane in hydrothermal sediments of Guaymas Basin. *Applied and Environmental Microbiology*, **70**, 1231-1233. doi:10.1128/AEM.70.2.1231-1233.2004.
- Kallmeyer, J., Pockalny, R., Adhikari, R.R., Smith, D.C., and D'Hondt, S., 2012. Global distribution of microbial abundance and biomass in subseafloor sediment. *Proceedings of the National Academy of Sciences of the United States of America*, **109**, 16213-16216. doi:10.1073/pnas.1203849109.
- Kashefi, K., and Lovley, D.R., 2003. Extending the upper temperature limit for life. *Science*, **301**, 934-934. doi:10.1126/science.1086823.
- Knab, N.J., Cragg, B.A., Hornibrook, E.R.C., Holmkvist, L., Pancost, R.D., Borowski, C., Parkes, R.J., and Jørgensen, B.B., 2009. Regulation of anaerobic methane oxidation in sediments of the Black Sea. *Biogeosciences*, **6**, 1505-1518. doi:10.5194/bg-6-1505-2009.
- Köster, M., Kars, M., Schubotz, F., Tsang, M.-Y., Maisch, M., Kappler, A., et al., 2021a. Evolution of (bio-)geochemical processes and diagenetic alteration of sediments along the tectonic migration of ocean floor in the Shikoku Basin off Japan. *Geochemistry, Geophysics, Geosystems*, e2020GC009585. doi:10.1029/2020GC009585.
- LaRowe, D.E., Dale, A.W., Aguilera, D.R., L'Heureux, I., Amend, J.P., and Regnier, P., 2014. Modeling microbial reaction rates in a submarine hydrothermal vent chimney wall. *Geochimica et Cosmochimica Acta*, **124**, 72-97. doi:10.1016/j.gca.2013.09.005.
- Lever, M.A., Rogers, K.L., Lloyd, K.G., Overmann, J., Schink, B., Thauer, R.K., Hoehler, T.M., and Jørgensen, B.B., 2015. Life under extreme energy limitations: a synthesis of laboratory- and field-based investigations. *FEMS Microbiological Reviews*, **39**, 688-728. doi:10.1093/femsre/fuv020.
- Mahony, S.H., Wallace, L.M., Miyoshi, M., Villamor, P., Sparks, R.S.J., and Hasenaka, T., 2011. Volcano-tectonic interactions during rapid plate-boundary evolution in the Kyushu region, SW Japan. *GSA Bulletin*, **123**, 2201-2223. doi:10.1130/B30408.1.
- Meister, P., Brunner, B., Picard, A., Böttcher, M.E., and Jørgensen, B.B., 2019. Sulphur and carbon isotopes as tracers of past sub-seafloor microbial activity. *Scientific Reports*, **9**, 1-9. doi:10.1038/s41598-018-36943-7.
- Meister, P., and Reyes, C., 2019. The carbon-isotope record of the sub-seafloor biosphere. *Geosciences*, **9**, 507. doi:10.3390/geosciences9120507.
- Morono, Y., Inagaki, F., Heuer, V.B., Kubo, Y., Maeda, L., and the Expedition 370 Scientists, 2017. Expedition 370 methods. In: *Proceedings of the International Ocean Discovery Program Volume 370* (eds. Heuer, F. Inagaki, Y. Morono, Y. Kubo, L. Maeda, and the Expedition 370 Scientists). College Station, TX (International Ocean Discovery Program). doi:10.14379/iodp.proc.370.102.2017.
- Niewöhner, C., Hensen, C., Kasten, S., Zabel, M., and Schulz, H.D., 1998. Deep sulfate reduction completely mediated by anaerobic methane oxidation in sediments of the upwelling area off Namibia. *Geochimica et Cosmochimica Acta*, **62**, 455-464. doi:10.1016/S0016-7037(98)00055-6.

- Parkes, R.J., Wellsbury, P., Mather, I.D., Cobb, S.J., Cragg, B.A., Hornibrook, E.R.C., and Horsfield, B., 2007. Temperature activation of organic matter and minerals during burial has the potential to sustain the deep biosphere over geological timescales. *Organic Geochemistry*, **38**, 845-852. doi:10.1016/j.orggeochem.2006.12.011.
- Shipboard Science Party, 2001. Site 1174. In: *Proceedings of the Ocean Drilling Program, Initial Reports, 190* (eds. Moore, G.F., Taira, A., Klaus, A., et al.). College Station, TX (Ocean Drilling Program), 1-149. doi:10.2973/odp.proc.ir.190.105.2001.
- Shipboard Scientific Party, 2003. Site 1225. In: *Proceedings of Ocean Drilling Program, Initial Reports, 201*. (eds. D'Hondt, S., Jørgensen, B.B., Miller, D.J., et al.). College Station, TX (Ocean Drilling Program), 1-86. doi:10.2973/odp.proc.ir.201.106.2003.
- Spivack, A.J., McNeil, C., Holm, N.G., and Hinrichs, K.-U., 2006. Determination of in situ methane based on analysis of void gas. In: *Proceedings of Ocean Drilling Program, Scientific Results, Volume 201* (eds. Jørgensen, B.B., D'Hondt, S.L., Miller, D.J., et al.): http://www-odp.tamu.edu/publications/201_SR/119/119.htm. doi:10.2973/odp.proc.sr.201.119.2006.
- Taira, A., Hill, I., Firth, J., Berner, U., Brückmann, W., Byrne, T., et al., 1992. Sediment deformation and hydrogeology of the Nankai Trough accretionary prism: Synthesis of shipboard results of ODP Leg 131. *Earth and Planetary Science Letters*, **109**, 431-450. doi:10.1016/0012-821X(92)90104-4.
- Takai, K., Nakamura, K., Toki, T., Tsunogai, U., Miyazaki, M., Miyazaki, J., et al., 2008. Cell proliferation at 122°C and isotopically heavy CH₄ production by hyperthermophilic methanogen under high-pressure cultivation. *Proceedings of the National Academy of Sciences of the United States of America*, **105**, 10949-10954. doi:10.1073/pnas.0712334105.
- Tsang, M. Y., Bowden, S. A., Wang, Z., Mohammed, A., Tonai, S., Muirhead, D., et al., 2020. Hot fluids, burial metamorphism and thermal histories in the underthrust sediments at IODP 370 site C0023, Nankai Accretionary Complex. *Marine and Petroleum Geology*, **112**, 104080. doi:10.1016/j.marpetgeo.2019.104080.
- Wellsbury, P., Goodman, K., Barth, T., Cragg, B.A., Barnes, S.P., and Parkes, R.J., 1997. Deep marine biosphere fueled by increasing organic matter availability during burial and heating. *Nature*, **388**, 573-576. doi:10.1038/41544.
- Yamano, M., Kinoshita, M, Goto, S., and Matsubayashi, O., 1992. Extremely high heat flow anomaly in the middle part of the Nankai Trough. *Physics and Chemistry of the Earth, Parts A/B/C*, **28**, 487-497. doi:10.1016/S1474-7065(03)00068-8.
- Zeikus, J.G., and Winfrey, M.R., 1976. Temperature limitation of methanogenesis in aquatic sediments. *Applied and Environmental Microbiology*, **31**, 99-107. doi:10.1128/aem.31.1.99-107.1976.

CHAPTER VI:**Conclusions and outlook**

This cumulative doctoral thesis focused on (bio-)geochemical processes, in particular the cycling of Fe, in the 1.2-km-deep and hot subsurface sediments recovered at IODP Site C0023 in the Nankai Trough off Cape Muroto, Japan. Over the past 15 Ma, Site C0023 has moved ~750 km – relative to its present-day position – from the central Shikoku Basin to the Nankai Trough due to tectonic motion of the Philippine Sea plate (Fig. 1). Due to its complex geological and thermal history, Site C0023 offers a great opportunity to study biogeochemical processes under strongly changing environmental, geochemical and depositional conditions over geological timescales.

(1) By combining a large set of complementary geochemical and rock magnetic data with sedimentation rates and sediment ages as well as reactive transport modeling, we reconstructed the evolution of (bio-)geochemical processes and the diagenetic alteration of sediments along the tectonically induced migration of Site C0023 over the past 15 Ma. Our results demonstrate that aerobic respiration processes dominated during early deposition of the organic carbon-starved Lower Shikoku Basin facies and that sulfate could penetrate deeply into the sediments (Fig. 1a). With ongoing deposition, higher carbon burial initiated the onset of organoclastic sulfate reduction. The sulfate pool, however, was not completely exhausted, but to some extent preserved in the bottom of the Lower Shikoku Basin facies (Fig. 1b). An increase in sedimentation rates and organic carbon contents during deposition of the Upper Shikoku Basin facies, possibly related to elevated marine productivity, led to the transition from a carbon-starved to an elevated carbon burial environment and the onset of biogenic methanogenesis and the anaerobic oxidation of methane (AOM) at around 2.5 Ma. As a consequence, a shallow sulfate-methane transition (SMT) formed, where the upward diffusing methane reacted with sulfate diffusing downwards from the overlying seawater. Due to the availability of the relict sulfate pool in the Lower Shikoku Basin facies, the second deep inverse SMT formed, where downward diffusing methane was oxidized by the preserved sulfate. A continuous increase in carbon burial during the deposition of the Upper Shikoku Basin facies resulted in elevated biogenic methanogenesis. The increased flux of methane caused an up- and downward migration of the shallow and inverse SMT, respectively, which, in turn, was accompanied by shifts of the sulfidization fronts.

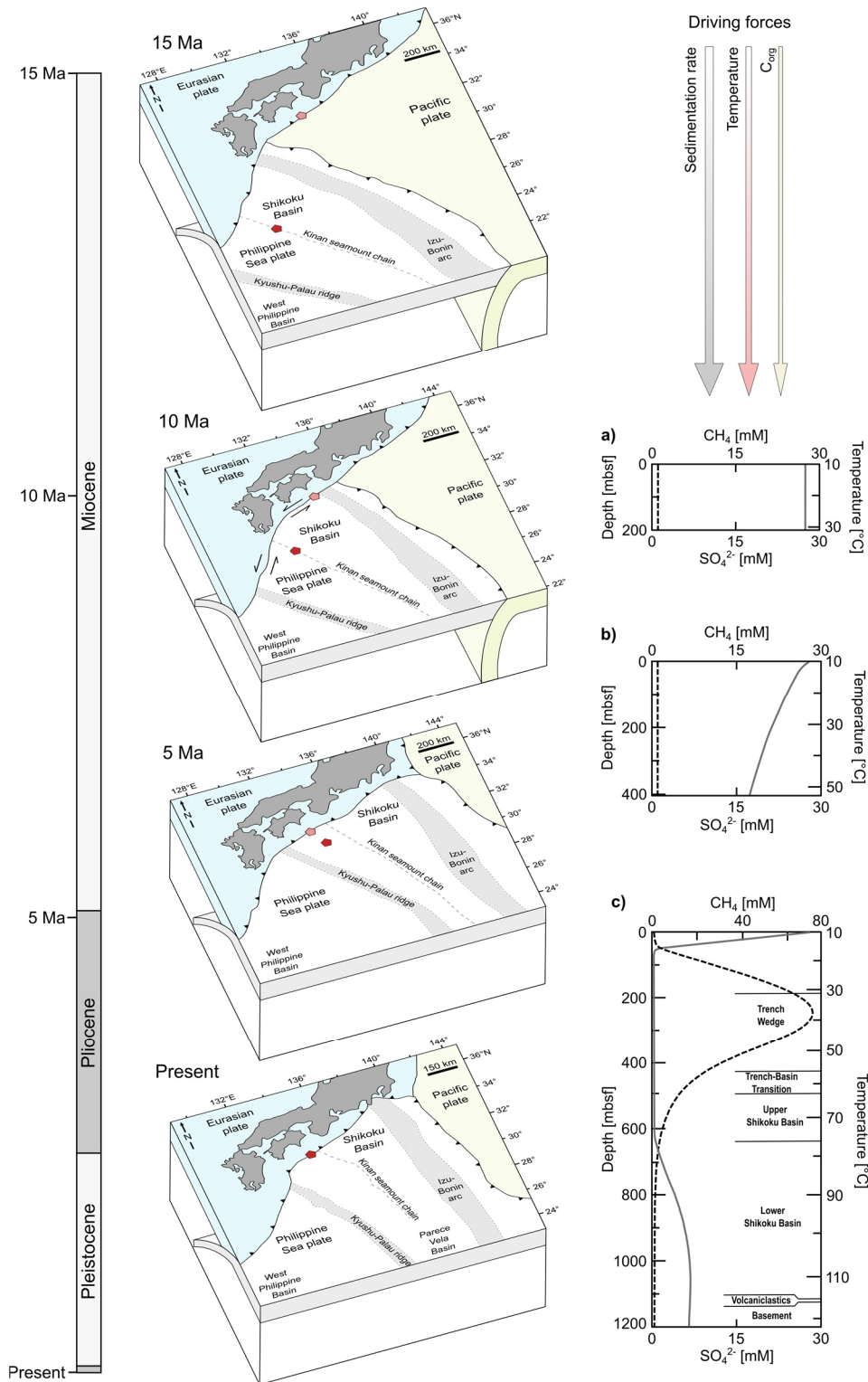


Figure 1. Left: Simplified schematic overview of the Nankai Trough subduction zone offshore Japan and the relative movement of Site C0023 during its tectonically induced migration over the past 15 Ma. Japan is held fixed at its current position. Light and dark red symbols represent the current position of Site C0023 and its former position during the tectonic migration, respectively. Modified after Lin et al. (2016), Heuer et al. (2017) and Underwood and Guo (2018). Right: Schematic illustration of the evolution of the sulfate (solid grey line) and methane (dotted black line) profiles at Site C0023 during its tectonic migration. The main driving force for the changes in biogeochemical processes is the significant increase in sedimentation rate, which in turn also affect the sediment temperature and the organic carbon burial.

Site C0023 entered the Nankai Trough at ~ 0.4 Ma. The associated transition from hemipelagic basin-style to trench-style deposition led to a pronounced increase in sedimentation rate and a temperature increase of about 50°C across the sediment column. This significant heating of the sediments could activate organic matter that is recalcitrant at seafloor temperatures, thereby enhancing biogenic methane production.

At present, the sulfate and methane profiles at the deep inverse SMT overlap in a relatively broad zone between 600 and 700 mbsf (Fig. 1c), suggesting inefficient microbial oxidation of methane. The depth of the sulfate-methane overlap zone corresponds to a temperature between 80° to 85°C . This temperature range coincides with the known temperature limit of anaerobic methane-oxidizing communities. Depth-integrated AOM rates derived from the reactive transport model indicate that the microbial activity of AOM-performing microbial communities at the deep inverse SMT has already started to cease and the SMT is about to further disappear.

The described non-steady state diagenesis and evolution of biogeochemical processes have also produced a complex sequence of diagenetic overprints of the magnetic mineral assemblage. The assessment of the diagenetic overprint has important implications for the interpretation of rock magnetic properties as they are widely used as paleoenvironmental proxy and for paleomagnetic recording. The downward migration of the deep inverse SMT due to elevated biogenic methane production shifted the lower sulfidization front into the Lower Shikoku Basin facies, leading to the alteration of the preserved sedimentary Fe pool and the formation of diagenetic pyrite several millions of years after the initial deposition. Extremely high sedimentation rates since the onset of trench-style deposition at ~ 0.4 Ma prevented a complete pyritization by decreasing the time the respective interval was located in the sulfidic zone and the preservation of greigite, which caused a secondary increase in the magnetic signal. In addition, increasing burial temperature and/or fault-related fluid circulation below the décollement could have led to the formation of authigenic magnetic Fe minerals including magnetite.

(2) To assess the availability of reactive Fe phases that might serve as potential energy substrate for microbially mediated processes in the deep and hot subseafloor sediments at Site C0023, we combined chemical sequential Fe extraction with ^{57}Fe -specific Mössbauer spectroscopy and rock magnetic end-member unmixing. Our results indicate that high amounts of reducible Fe(III) that could be used as electron acceptor for microbial Fe(III) reduction in the deep subseafloor sediments are still preserved as phyllosilicate-bound Fe throughout the sediment

column. In contrast to other marine settings, discrete ash layers at Site C0023 contain significantly lower contents of reactive Fe compared to the surrounding mud rock.

This study also demonstrates that Fe speciation data need to be interpreted with caution if applying chemical sequential Fe extraction on ancient sediments. Thus, as already proposed in recent studies, we highly recommend the application of a secondary independent Fe speciation technique such as ^{57}Fe -specific Mössbauer spectroscopy and/or rock magnetic techniques if the research question requires a specific Fe mineral characterization.

(3) By means of stable Fe isotope analyses ($\delta^{56}\text{Fe}$), another aim of this study was to investigate whether the isotopic composition of dissolved Fe ($\text{Fe(II)}_{\text{aq}}$) and reactive solid-phase Fe(III) is indicative of microbially mediated Fe cycling in the deep subseafloor sediments at Site C0023. Even though a growing number of studies were conducted within the last two decades to trace and decipher iron sources, transport and reaction pathways in the marine environment, the isotopic composition of dissolved and sequentially extracted Fe in sediments deeper than 5 m below the seafloor has not been determined so far. Thus, this study also served to assess the applicability of stable Fe isotopes as a proxy for microbially mediated processes in deep subseafloor sediments.

The isotopic composition of $\text{Fe(II)}_{\text{aq}}$ is generally low with $\delta^{56}\text{Fe} < -1\text{‰}$. In some samples, we found exceptionally low $\delta^{56}\text{Fe}$ values down to almost -5.9‰ , which have never been reported in the natural marine environment before. The overall light isotopic composition of $\text{Fe(II)}_{\text{aq}}$ does not rule out microbial Fe reduction as the main pathway releasing $\text{Fe(II)}_{\text{aq}}$. The extremely light values, however, cannot be solely explained by dissimilatory iron reduction (DIR), suggesting that additional processes are involved. The light $\delta^{56}\text{Fe}$ values are best explained by a Rayleigh distillation model in which $\text{Fe(II)}_{\text{aq}}$ is continuously removed from the pore water by diffusion and adsorption onto Fe (oxyhydr)oxide surfaces. We argue that DIR as well as diffusion and adsorption of $\text{Fe(II)}_{\text{aq}}$ initially co-occurred since the onset of DIR at around 2 Ma. While the significant increase in temperature beyond the temperature limit of mesophilic microorganisms since the onset of trench-style deposition at ~ 0.4 Ma might have stopped the DIR-related release of $\text{Fe(II)}_{\text{aq}}$, the diffusional and adsorptive $\text{Fe(II)}_{\text{aq}}$ removal continued. This decoupling of biotic and abiotic processes is ultimately driven by the depositional and thermal history of Site C0023. These findings expand the knowledge of processes controlling the isotopic composition of dissolved and solid-phase Fe in deep consolidated sediments.

The presented cumulative doctoral thesis is first of its kind that investigates the evolution of (bio-)geochemical processes in subseafloor sediments along the tectonically induced migration of ocean floor from its origin to the present-day position. The research conducted in this thesis considerably contributes to an improved understanding of the variability of (bio-)geochemical processes and microbial activity in deep subseafloor sediments over geological timescales. It further demonstrates that the geochemical patterns we observe today – including the pore-water profiles as well as the Fe isotope and sedimentary records – are a consequence of long-term variations in depositional conditions, the organic carbon availability and temperature conditions. Thus, this study emphasizes that the geological background and the (bio-)geochemical history of the sediments need to be considered for a reliable interpretation of the present-day geochemical profiles and the assessment of microbial activity in deep subseafloor sediments.

The findings of this study may also be relevant for other sedimentary settings that have experienced similar tectonically induced spatial migrations, such as deep subseafloor sediments that are nowadays located close to the subduction zone offshore South America in the South Pacific Ocean. In order to understand the past and future evolution of the (bio-)geochemical processes in more detail, it would be very interesting to study and drill further sites along the age transect of Site C0023.

References

- Heuer, V.B., Inagaki, F., Morono, Y., Kubo, Y., Maeda, L., and the Expedition 370 Scientists, 2017. Temperature limit of the deep biosphere off Muroto. *Proceedings of the International Ocean Discovery Program Volume 370*: College Station, TX (International Ocean Discovery Program). doi:10.14379/iodp.proc.370.2017.
- Lin, W., Byrne, T.B., Kinoshita, M., McNeill, L.C., Chang, C., Lewis, J.C., et al., 2016. Distribution of stress in the Nankai subduction zone, southwest Japan and a comparison with Japan Trench. *Tectonophysics*, **692**, 123-130. doi:10.1016/j.tecto.2015.05.008.
- Underwood, M.B., and Guo, J., 2018. Clay-mineral assemblages across the Nankai-Shikoku subduction system, offshore Japan: A synthesis of results from the NanTroSEIZE project. *Geosphere*, **14**, 2009-2043. doi:10.1130/GES01626.1.

APPENDIX

APPENDIX OF CHAPTER II

Supporting Material for

Evolution of (bio-)geochemical processes and diagenetic alteration of sediments along the tectonic migration of ocean floor in the Shikoku Basin off Japan

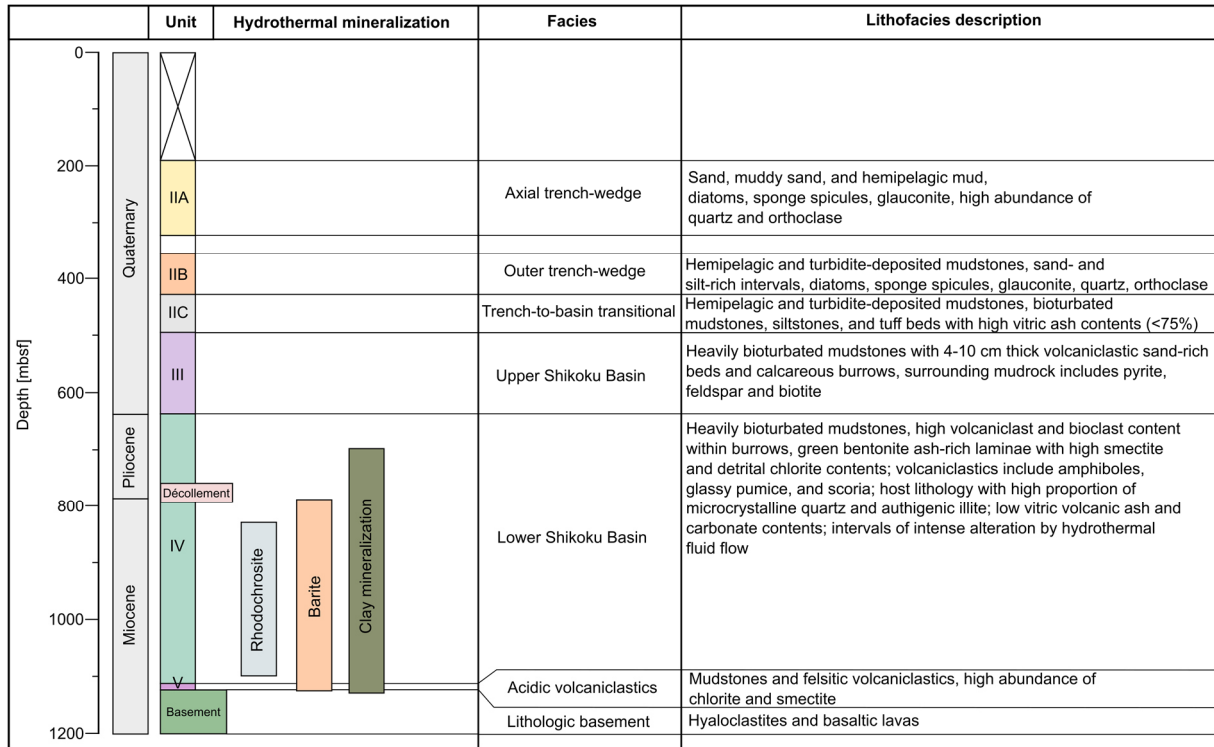


Figure S1. Geological log showing the lithological units, the corresponding depth and ages, horizons of hydrothermal mineralization, facies as well as lithofacies descriptions for Site C0023. The upper 189 meters were not recovered. Modified after Heuer et al. (2017a) and Tsang et al. (2020). (<https://creativecommons.org/licenses/by-nc/4.0/>).

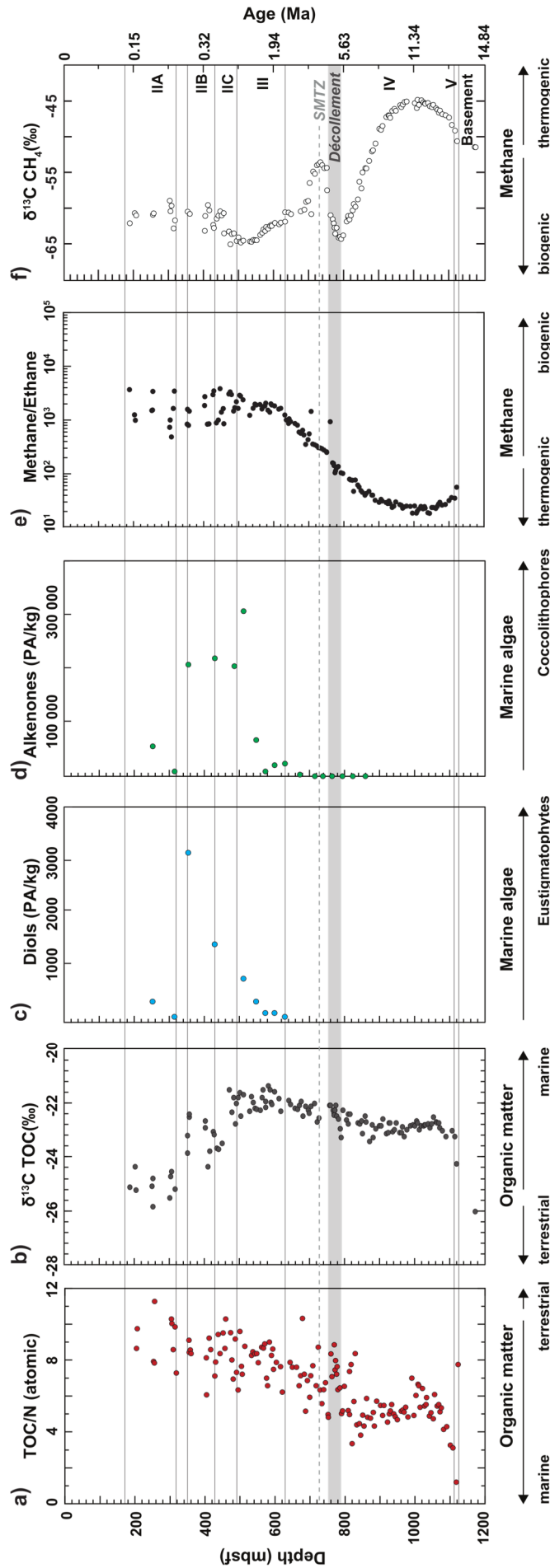


Figure S2. Down-core profiles of a) TOC/N ratios (from Heuer et al., 2017a), b) $\delta^{13}\text{C}$ -TOC, c) long-chain diols, d) alkenones, e) methane/ethane ratios (from Heuer et al., 2017a), and f) $\delta^{13}\text{C}$ - CH_4 (from Heuer et al., 2020). Lithological units (Heuer et al., 2017a) are indicated on the right. Corresponding ages on the right-side y-axis are based on the age model by Hagino and the Expedition 370 Scientists (2018). The gray dashed line and gray shading indicate the location of the present SMT and the décollement, respectively (Heuer et al., 2017a).

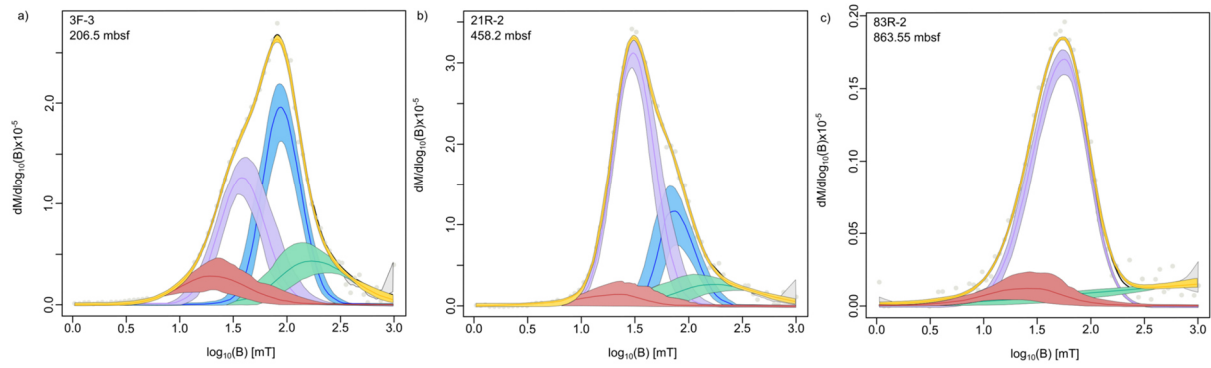


Figure S3. Coercivity distributions of three sediment samples (a) 370-C0023A-3F-3, 80.0-105.9 cm, (b) 370-C0023A-21R-2, 101.0-103.0 cm, and (c) 370-C0023A-83R-2, 56.0-58.0 cm) derived from IRM acquisition curves obtained by using the MAX UnMix application (Maxbauer et al., 2016), shown on a logarithmic field scale. Data are shown in grey circles and the black line (partially visible) is the spline fit. Yellow line = cumulative model fit, blue line = EM1 with B_h of 1.9 \log_{10} units, purple line = EM2 with B_h of 1.6 \log_{10} units, green line = EM3 with $B_h > 2 \log_{10}$ units, red line = EM4 with B_h of 1.3 \log_{10} units. The shaded areas represents error envelopes of 95% confidence intervals.

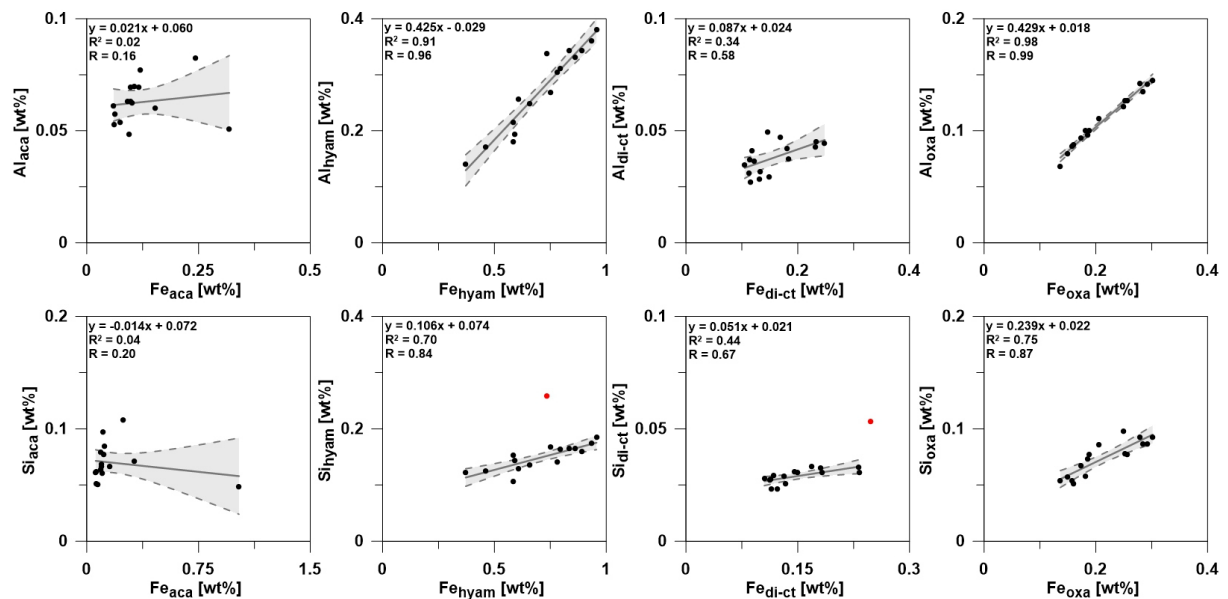


Figure S4. Correlation between Fe and Al (top) and Si (below) for the respective extracting solutions after Poulton and Canfield (2005). Red dots represent statistical outlier.

Table S1. Bulk element contents of Al, Fe, and S in wt% of duplicate samples and the relative differences in %.

Method	Sample	Depth [mbsf]	Al [wt%]	Relative difference [%]	Fe [wt%]	Relative difference [%]	S [wt%]	Relative difference [%]
Total acid digestion	370-C0023A-14X-1, 46.0-65.0 cm	403.555	8.11	1.25	3.91	0.71	0.116	0.79
			8.01		3.88		0.115	
	370-C0023A-49R-2, 90.0-123.5 cm	688.658	8.97	2.34	4.15	2.45	0.206	1.53
			8.76		4.05		0.203	
	370-C0023A-67R-2, 44.0-88.0 cm	776.870	8.66	0.44	4.35	0.41	0.164	1.69
			8.62		4.37		0.161	
	370-C0023A-86R-2, 85.0-123.0 cm	891.300	8.95	1.75	4.41	1.78	0.226	1.84
			8.80		4.33		0.230	
	370-C0023A-103R-4, 0.0-56.0 cm	1063.424	8.57	1.31	4.31	1.47	0.417	4.27
			8.69		4.25		0.400	

Table S2. Sequential extraction procedure after Poulton and Canfield (2005) applied to samples of Site C0023.

Step	Target mineral phase	Terminology	Extraction reagent	Extraction time	pH
I	Fe bound in carbonates and AVS	Fe _{aca}	1 M Na-acetate	24 h	4.5
II	Easily reducible Fe oxides (ferrihydrite, lepidocrocite)	Fe _{hyam}	1 M hydroxylamine-HCl in 25% v/v acetic acid	48 h	
III	Reducible Fe oxides (goethite, hematite)	Fe _{di-ct}	Na-dithionite (50 g L ⁻¹)/0.02 M Na-citrate*	2 h	4.8
IV	Magnetite	Fe _{oxa}	0.2 M ammonium oxalate/0.17 M oxalic acid	6 h	

*Na-citrate solution was modified to 0.02 M according to Henkel et al. (2016).

Table S3. Sequentially extracted Fe_{aca}, Fe_{hyam}, Fe_{di-ct}, and Fe_{oxa} contents in wt% of duplicate samples and the relative differences in %.

Method	Sample	Depth [mbsf]	Fe _{aca} [wt%]	Relative difference [%]	Fe _{hyam} [wt%]	Relative difference [%]	Fe _{di-ct} [wt%]	Relative difference [%]	Fe _{oxa} [wt%]	Relative difference [%]
Sequential extraction of Fe (oxyhydr)oxides	370-C0023A-86R-2, 85.0-123.0 cm	891.300	0.080	4.77	0.794	0.50	0.146	9.91	0.222	6.76
			0.084		0.790		0.132		0.237	
	370-C0023A-93R-4, 85.0-127.0 cm	960.901	0.069	0.87	0.698	15.58	0.103	9.55	0.275	5.92
			0.068		0.816		0.114		0.259	
	370-C0023A-96R-8, 0.0-43.0 cm	997.023	0.099	2.06	0.846	3.24	0.102	14.48	0.309	0.71
			0.097		0.874		0.117		0.311	
	370-C0023A-108R-1, 83.0-133.5 cm	1109.083	0.047	2.80	0.667	0.40	0.149	2.72	0.266	4.22
			0.045		0.669		0.145		0.255	
	370-C0023A-110R-2, 65.0-130.0 cm	1123.250	0.060	15.93	0.608	12.49	0.102	15.37	0.294	20.76
			0.052		0.536		0.087		0.239	

Table S4. Overview of Mössbauer spectra fitting parameters.

Sample	Temp. [K]	Phase	CS [mm s ⁻¹]	ΔE_Q [mm s ⁻¹]	ε [mm s ⁻¹]	B_{hf} [T]	Pop (\pm) [%]	χ^2	Fe phase
370-C0023A- 18R-1, 19.0-41.0 cm	295	Db1	1.24	2.64			61.0 (1.2)	0.92	Fe(II)
		Db2	0.37	0.64			39.0 (1.3)		Fe(III)
	77	Db1	1.26	2.87			57.7 (1.5)	0.81	Fe(II)
		Db2	0.45	0.72			42.3 (1.6)		Fe(III)
	5	Db1	1.27	2.87			48.5 (2.1)	2.70	Fe(II)
		Db2	0.44	0.79			38.4 (2.9)		Fe(III)
S1		0.31		0.03	49.5	13.1 (2.0)	Fe(III)*		
370-C0023A- 81R-7, 0.0-30.0 cm	295	Db1	1.13	2.67			63.8 (1.1)	0.85	Fe(II)
		Db2	0.35	0.59			36.2 (1.2)		Fe(III)
	77	Db1	1.26	2.88			54.3 (2.1)	0.81	Fe(II)
		Db2	0.47	0.63			40.0 (1.9)		Fe(III)
		S1	0.34		0.01	52.4	5.7 (0.0)		Fe(III)*
	5	Db1	1.26	2.92			55.9 (2.4)	0.87	Fe(II)
Db2		0.45	0.73			35.3 (1.6)	Fe(III)		
S1		0.47		-0.05	52.9	8.8 (0.9)	Fe(III)*		
370-C0023A- 105R-2, 0.0-45.0 cm	295	Db1	1.13	2.67			66.4 (1.7)	1.02	Fe(II)
		Db2	0.36	0.57			33.6 (1.5)		Fe(III)
	77	Db1	1.26	2.89			65.3 (2.1)	0.68	Fe(II)
		Db2	0.44	0.62			34.7 (1.9)		Fe(III)
	5	Db1	1.27	2.92			60.7 (1.5)	0.61	Fe(II)
		Db2	0.48	0.75			28.7 (1.9)		Fe(III)
S1		0.37		0.02	53.7	10.6 (0.7)	Fe(III)*		

Temp. – temperature during measurement; Phase – fitted compound, Db: doublet; S: sextet; center shift (CS in mm s⁻¹); quadrupole splitting (ΔE_Q in mm s⁻¹); quadrupole shift (ε in mm s⁻¹); hyperfine field (B_{hf} in T), Pop – relative abundance (in %), χ^2 as goodness of fit and identified Fe mineral phases: Fe(II), Fe(III).

*note: the identified sextet feature can be attributed to both a magnetically-ordered (e.g., poorly crystalline) Fe(III) phase or an artefact of paramagnetic relaxation of Fe atoms in phyllosilicates low in total Fe.

References

- Hagino, K., and the Expedition 370 Scientists, 2018. Data report: calcareous nannofossils from the middle Miocene to Pleistocene, IODP Expedition 370 Site C0023. In: *Proceedings of the International Ocean Discovery Program Volume 370* (eds. Heuer, V.B., Inagaki, F., Morono, Y., Kubo, Y., Maeda, L., and the Expedition 370 Scientists). College Station, TX (International Ocean Discovery Program). doi:10.14379/iodp.proc.370.201.2018.
- Henkel, S., Kasten, S., Poulton, S.W., and Staubwasser, M., 2016. Determination of the stable iron isotopic composition of sequentially leached iron phases in marine sediments. *Chemical Geology*, **421**, 93-102. doi:10.1016/j.chemgeo.2015.12.003.
- Heuer, V.B., Inagaki, F., Morono, Y., Kubo, Y., Maeda, L., and the Expedition 370 Scientists, 2017a. Temperature limit of the deep biosphere off Muroto. *Proceedings of the International Ocean Discovery Program Volume 370*: College Station, TX (International Ocean Discovery Program), doi:10.14379/iodp.proc.370.2017.
- Heuer, V.B., Inagaki, F., Morono, Y., Kubo, Y., Spivack, A., Viehweger, B., et al., 2020. Temperature limits to deep seafloor life in the Nankai Trough subduction zone. *Science*, **370**, 1230-1234. doi:10.1126/science.abd7934.
- Maxbauer, D.P., Feinberg, J.M., and Fox, D.L. (2016). MAX UnMix: A web application for unmixing magnetic coercivity distributions. *Computers & Geosciences*, **95**, 140-145. doi:10.1016/j.cageo.2016.07.009.
- Poulton, S.W., and Canfield, D.E. (2005). Development of a sequential extraction procedure for iron: implications for iron partitioning in continentally derived particulates. *Chemical Geology*, **214**, 209-221. doi:10.1016/j.chemgeo.2004.09.003.
- Tsang, M.-Y., Bowden, S. A., Wang, Z., Mohammed, A., Tonai, S., Muirhead, D., et al., 2020. Hot fluids, burial metamorphism and thermal histories in the underthrust sediments at IODP 370 site C0023, Nankai Accretionary Complex. *Marine and Petroleum Geology*, **112**, 104080. doi:10.1016/j.marpetgeo.2019.104080.

APPENDIX OF CHAPTER III

Supporting Material for

Influence of early low-temperature and later high-temperature diagenesis on magnetic mineral assemblages in marine sediments from the Nankai Trough

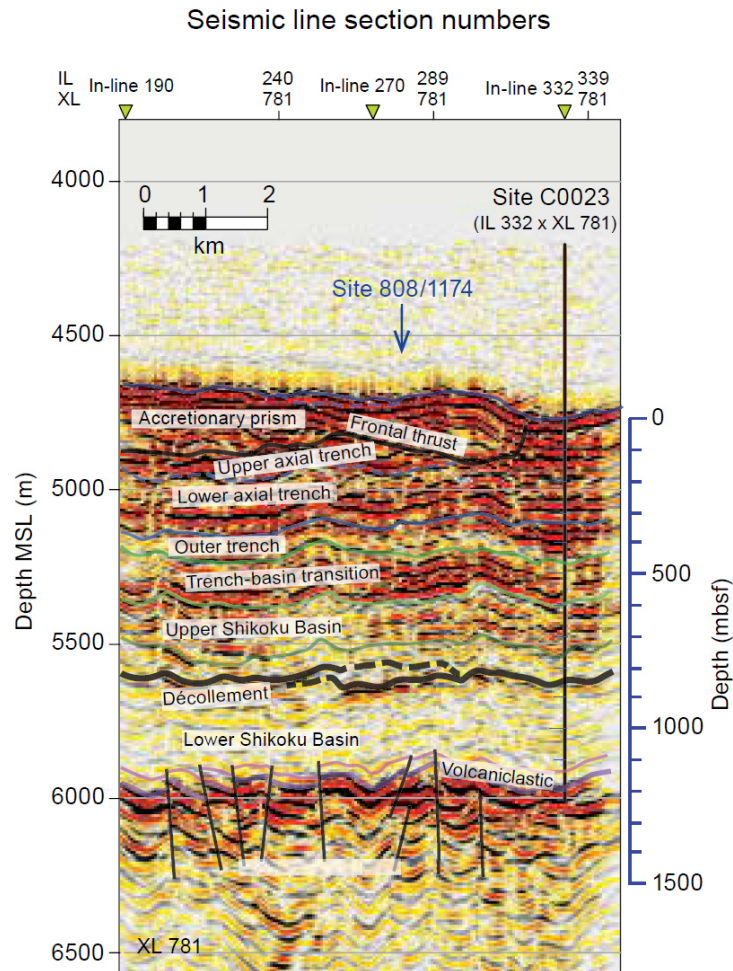


Figure S1. Depth-converted pre-stack time migrated seismic section IL 781 cropped into the region of interest with superimposed geological interpretation. Original data are available at <http://www-udc.ig.utexas.edu/sdc/cruise.php?cruiseIn=ew9907>. The blue arrow is the projected position of Sites 808 and 1174 (from Heuer et al. (2017)). The left-hand axis is depth in meters below mean sea level (MSL). The right-hand axis is depth in meters below sea floor (mbsf).

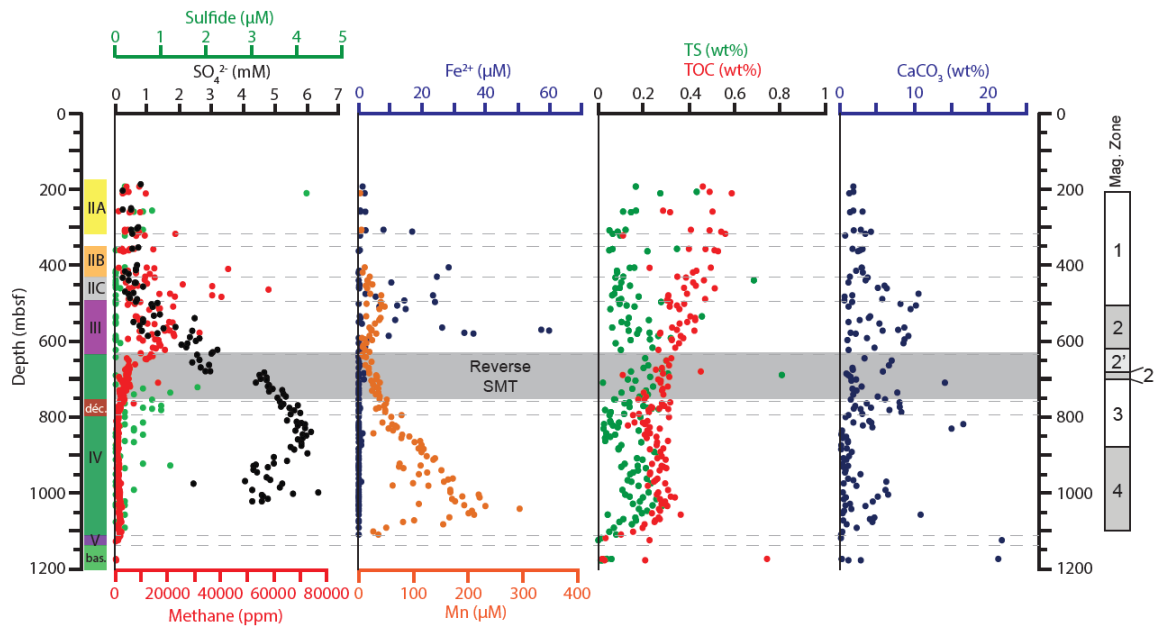
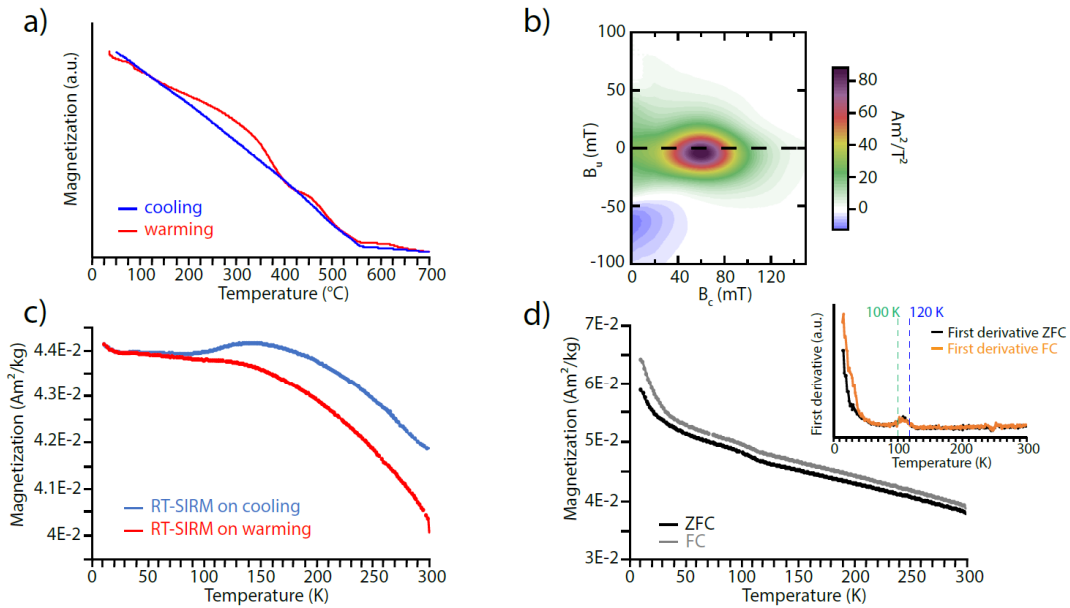


Figure S2. Selected shipboard geochemical data from Heuer et al. (2017). TS is total sulfur and TOC is total organic carbon. The magnetic zones identified here are indicated on the right. On the left, the lithologic units (IIA to V), décollement ('déc.'), and basement ('bas.') are from Heuer et al. (2017).

High coercivity sample

Spl. 370-C0023A-7X-1W, 32-34 cm depth: 305.32 mbsf



Low coercivity sample

Spl. 370-C0023A-25R-5W, 15-17 cm depth: 498.25 mbsf

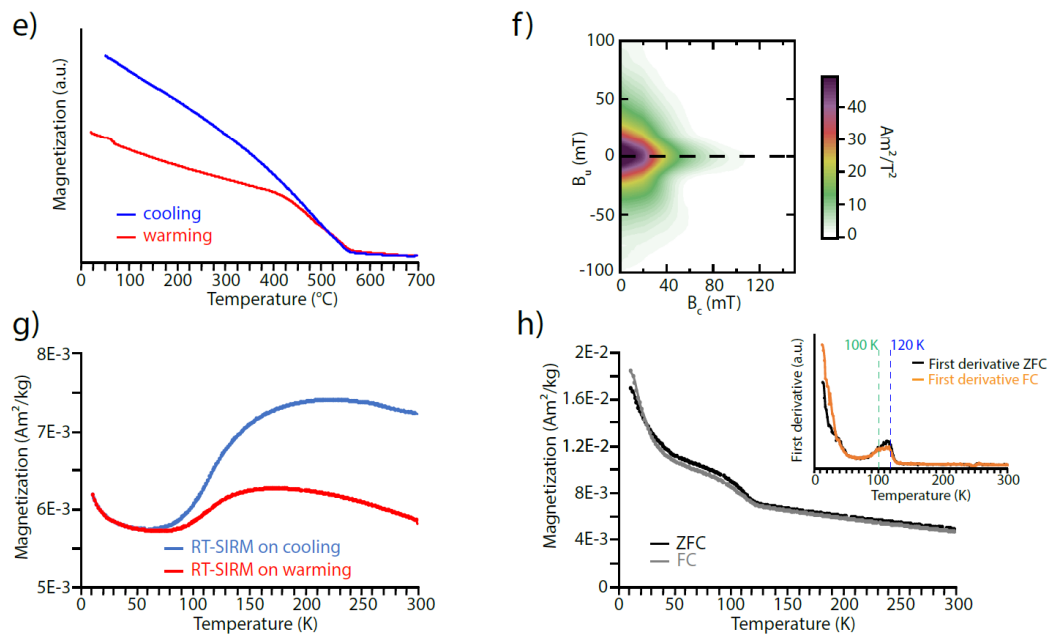


Figure S3. Magnetic measurements for two samples from Magnetic Zone 1 with high and low coercivities, respectively. (a, e) Thermomagnetic measurements (a.u.: arbitrary units), (b, f) conventional FORC diagrams (smoothing factor $\text{SF} = 10$), (c, g) RT-SIRM cycles, and (d, h) ZFC and FC curves with their first derivatives in the insets.

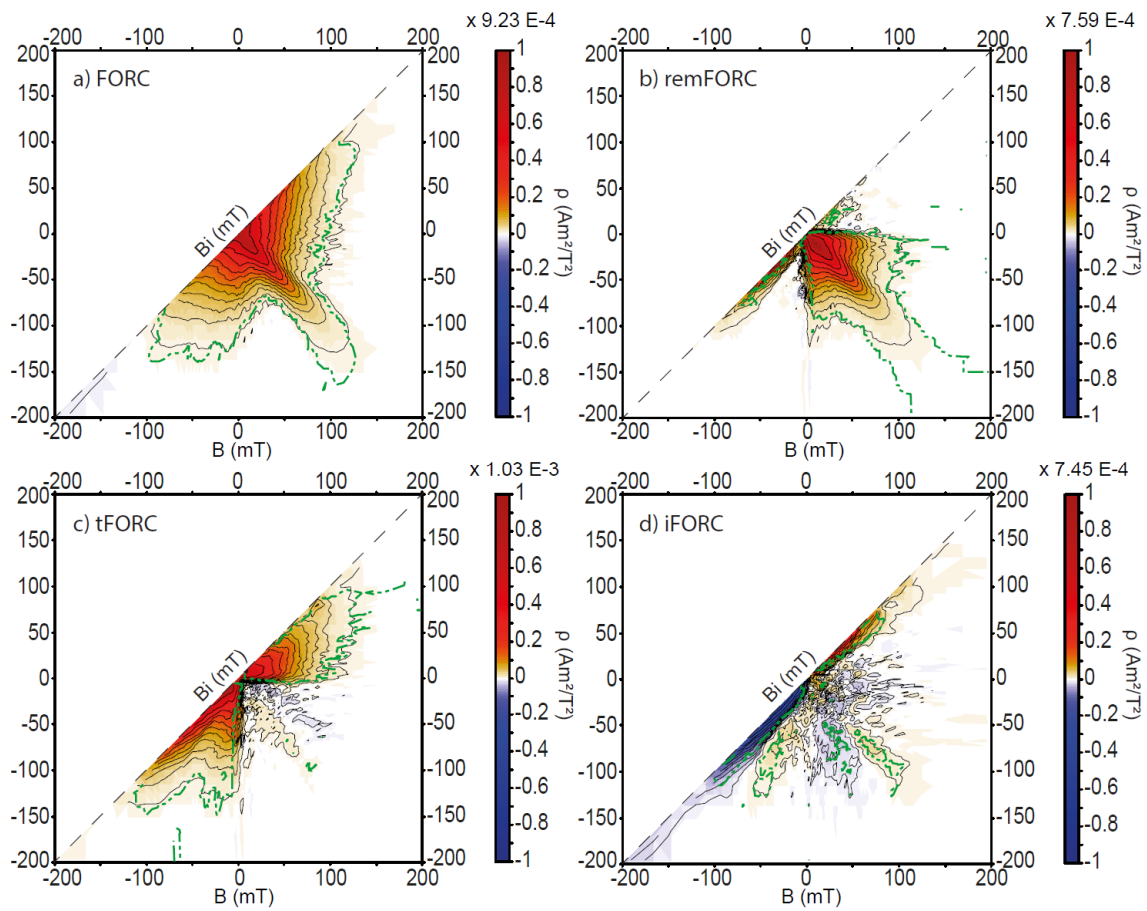


Figure S4. FORC diagrams for Sample 370-C0023A-22R-8W, 26-28 cm (depth: 472.305 mbsf) in Magnetic Zone 1. (a) Conventional FORC diagram, (b) remanent FORC (remFORC) diagram, (c) transient FORC (tFORC) diagram, and (d) induced FORC (iFORC) diagram. This sample has low coercivity ($B_{cr} \sim 28$ mT).

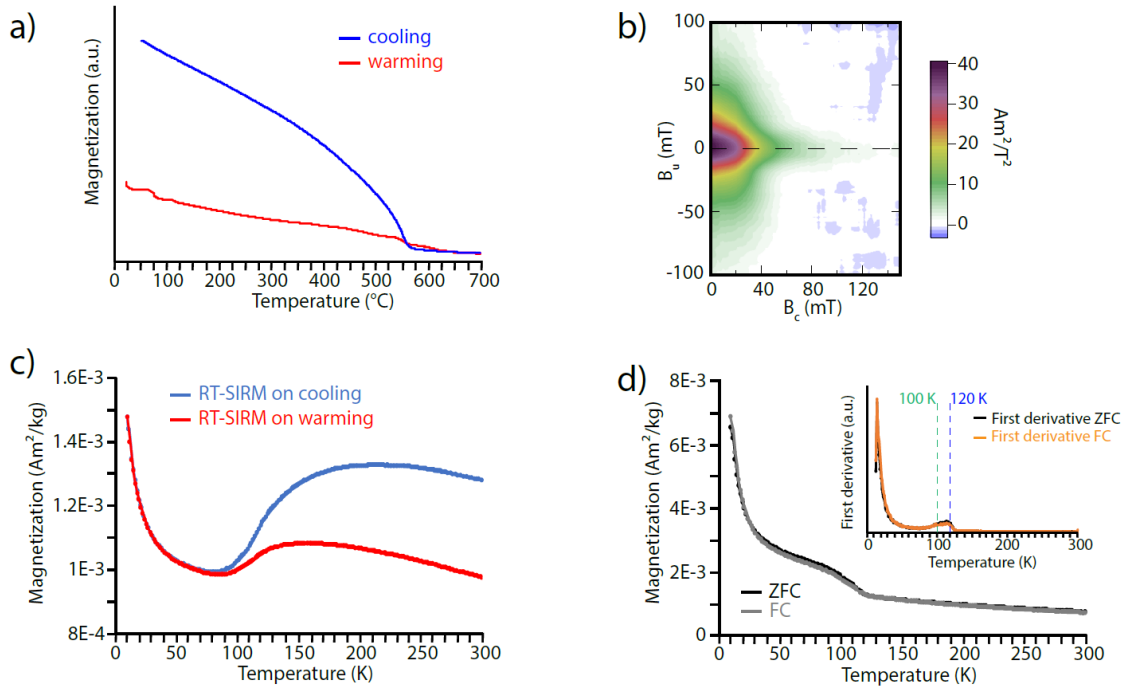


Figure S5. Magnetic measurements for Sample 370-C0023A-50R-5W, 42-44 cm (depth: 696.53 mbsf) from Magnetic Zone 2. (a) Thermomagnetic measurement (a.u.: arbitrary units), (b) conventional FORC diagram (smoothing factor SF = 10), (c) RT-SIRM cycle, and (d) ZFC and FC curves with their first derivatives in the inset.

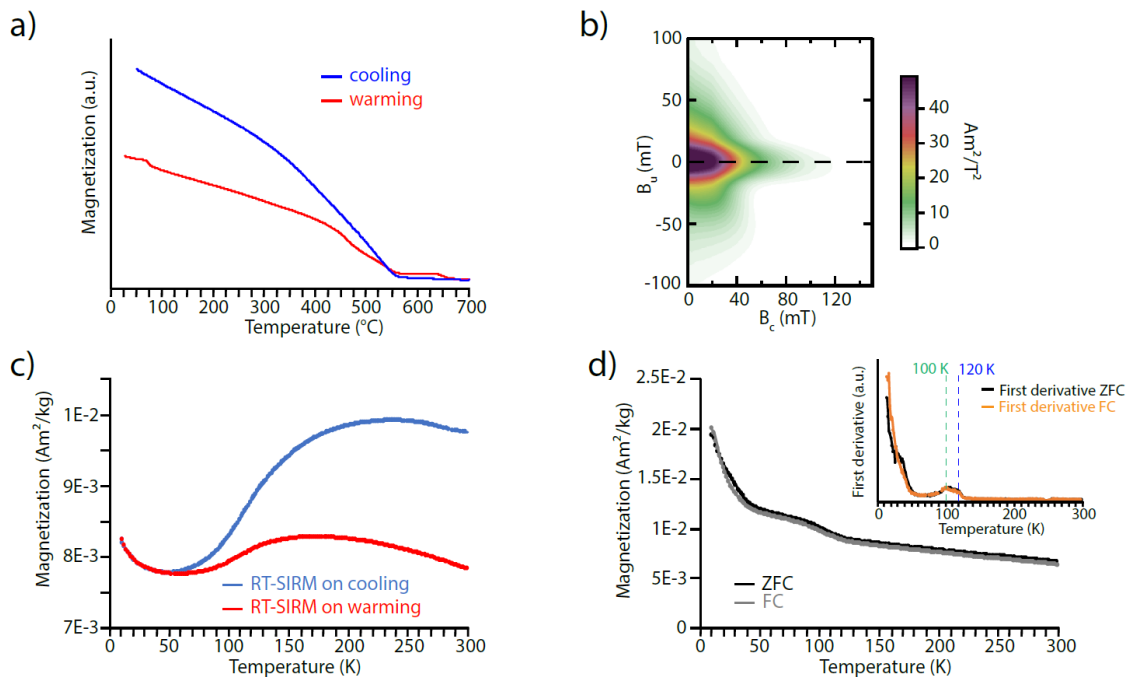


Figure S6. Magnetic measurements for Sample 370-C0023A-61R-3W, 70-72 cm (depth: 750.51 mbsf) from Magnetic Zone 3. (a) Thermomagnetic measurement (a.u.: arbitrary units), (b) conventional FORC diagram (smoothing factor SF = 10), (c) RT-SIRM cycle, and (d) ZFC and FC curves with their first derivatives in the inset.

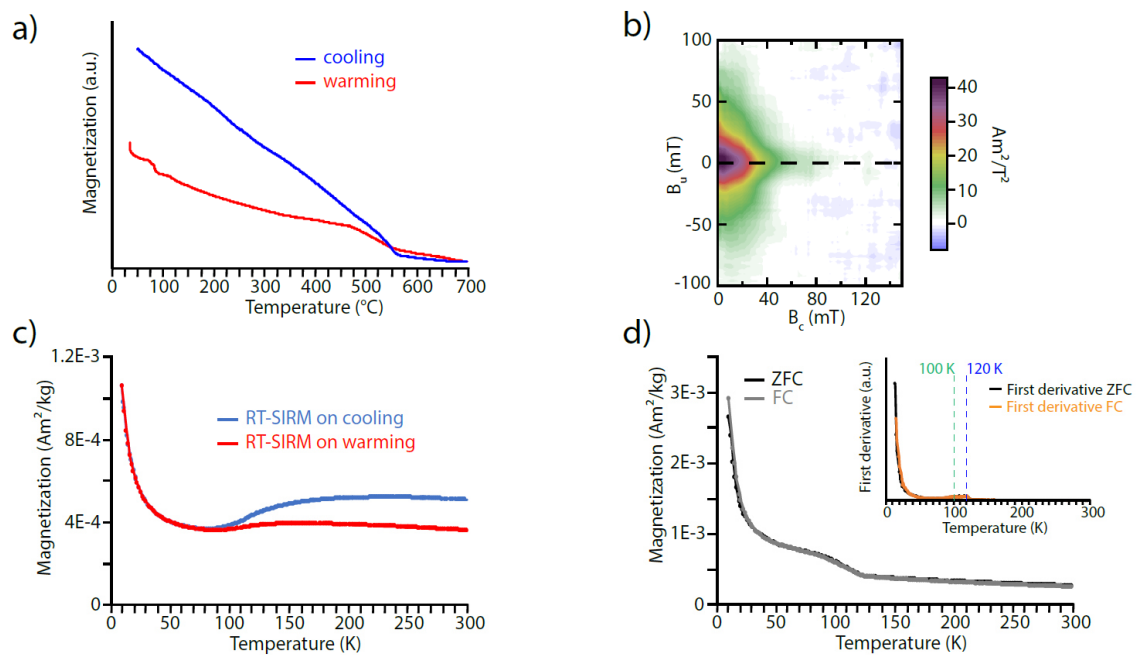


Figure S7. Magnetic measurements for Sample 370-C0023A-93R-6W, 48-50 cm (depth: 962.99 mbsf) from Magnetic Zone 4. (a) Thermomagnetic measurement (a.u.: arbitrary units), (b) conventional FORC diagram (smoothing factor = 10), (c) RT-SIRM cycle, and (d) ZFC and FC curves with their first derivatives in the inset.

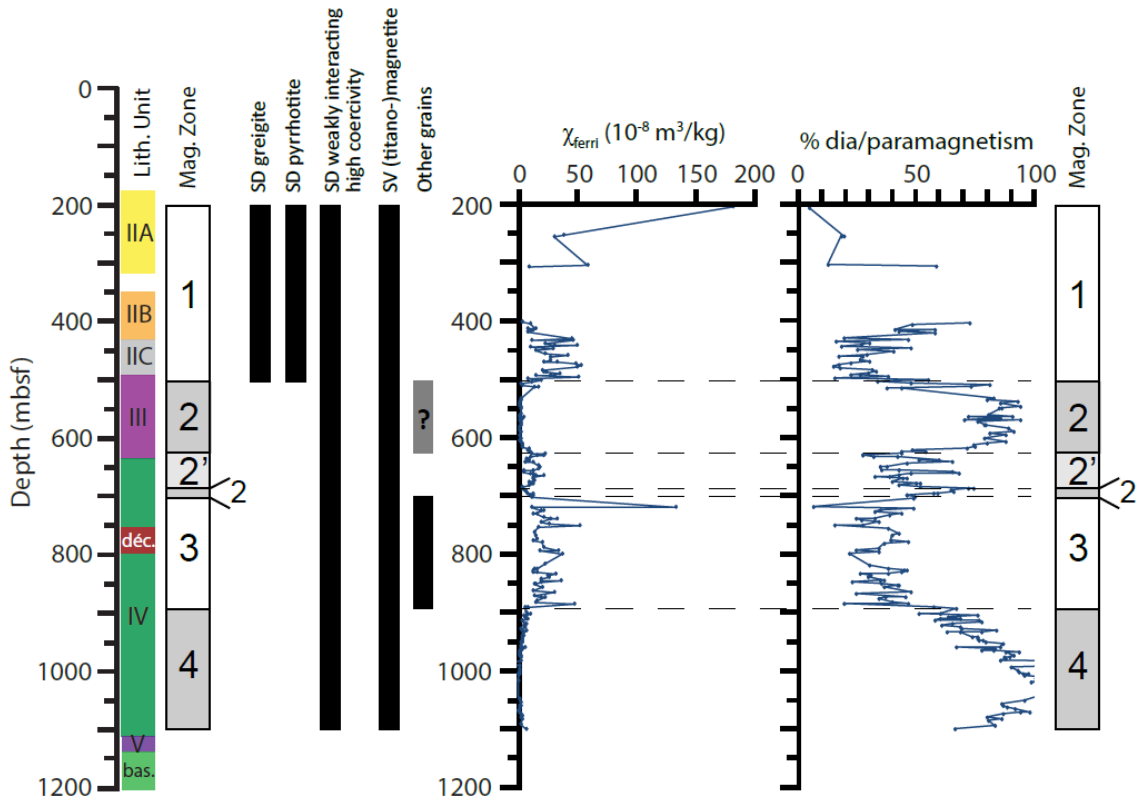


Figure S8. Summary of the magnetic mineral assemblage at Site C0023. The black and gray bars indicate the depth interval where magnetic minerals have been identified χ_{ferri} and %dia/paramagnetism were calculated from hysteresis measurements. $\chi_{\text{ferri}} = \chi_{\text{f}} - \chi_{\text{hfield}}$, where χ_{hfield} is the high-field magnetic susceptibility. %dia/paramagnetism = $(\chi_{\text{hfield}} / \chi_{\text{f}}) \times 100$. The high-field magnetic susceptibility calculated from hysteresis loops is complicated in MZs 2 and 4 because of the presence of paramagnetic (e.g., pyrite) and high coercivity (e.g. hematite) minerals. On the left-hand side, lithologic units (IIA to V), décollement ('déc.'), and basement ('bas.') are from Heuer et al. (2017).

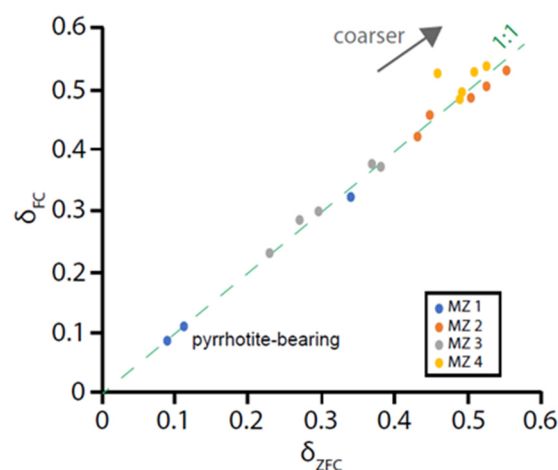


Figure S9. δ_{FC} versus δ_{ZFC} diagram. $\delta = (M_{80\text{K}} - M_{150\text{K}}) / M_{150\text{K}}$, where M is the magnetization at the stated temperatures (Moskowitz et al., 1993). Samples from Magnetic Zone (MZ) 2 (including MZ 2') and MZ 4 have higher δ values that are indicative of coarser magnetite grains in these zones.

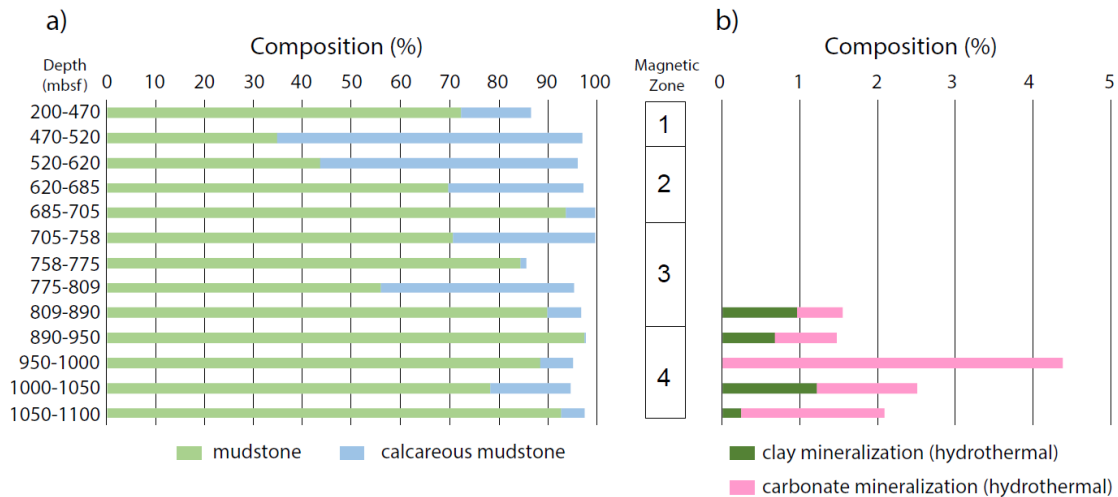


Figure S10. (a) Sediment compositions from core descriptions (Heuer et al., 2017), where compositions do not sum to 100%. Remaining lithologies include sand, volcanoclastic sediment, tuff, and breccia. (b) Hydrothermal mineralization is only present at the bottom of the hole. Depth intervals are based on magnetic variations. Magnetic Zone 2 in this figure includes MZ 2'.

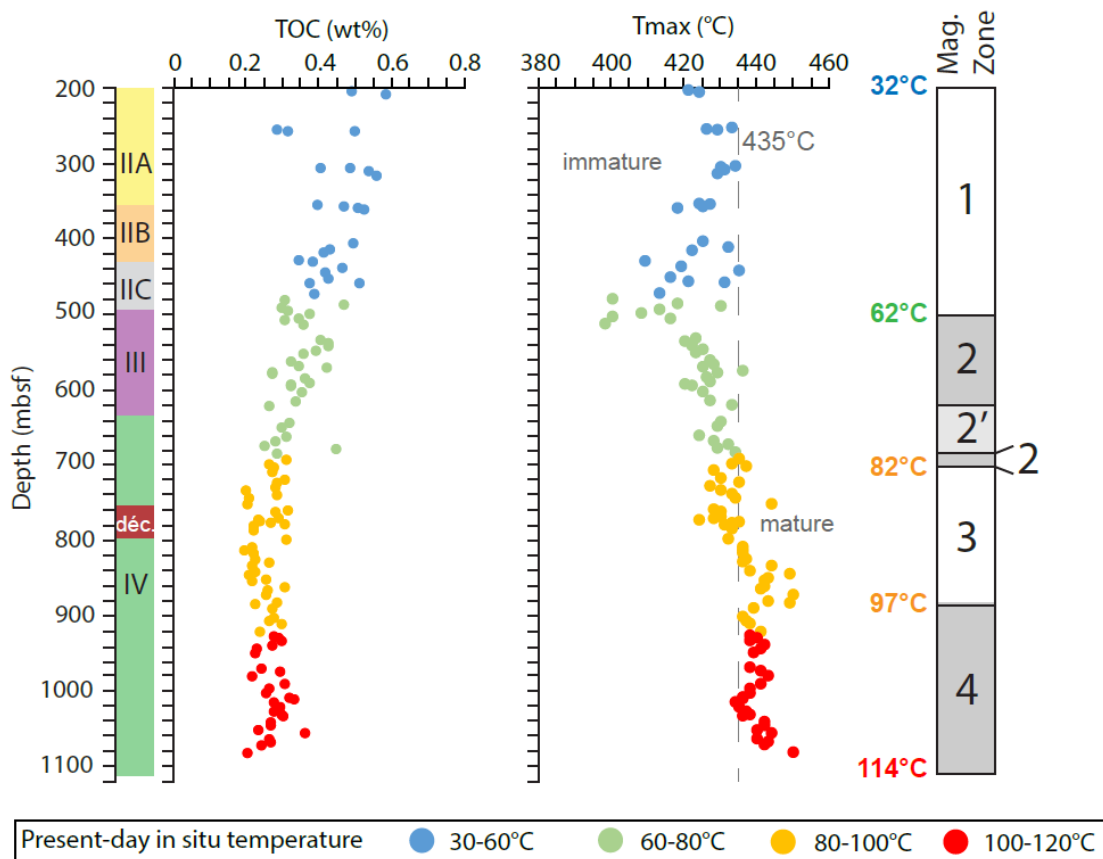


Figure S11. Total organic carbon (TOC; Heuer et al., 2017) and Rock-Eval pyrolysis parameters T_{max} (Stein, 2021). Present-day burial temperature is from shipboard results (Heuer et al., 2017). T_{max} of 435°C represents the boundary between immature and mature organic matter. The magnetic zones identified here are reported on the right-hand side with the present-day temperature at the boundary between each zone. On the left-hand side, the lithologic units (IIA to IV) and the décollement ('déc.') are from Heuer et al. (2017).

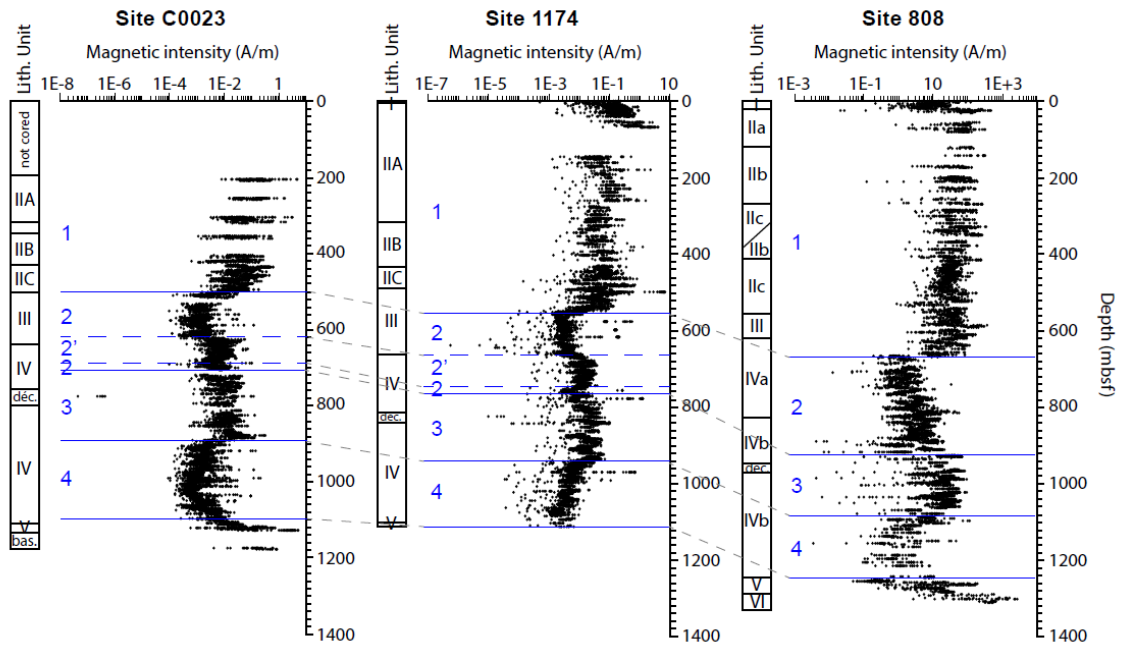


Figure S12. Down-core magnetic intensity measured on archive-half sections aboard *D/V Chikyu* at Site C0023 (Heuer et al., 2017) and *R/V JOIDES Resolution* at Site 1174 (Shipboard Scientific Party, 2001) and Site 808 (Shipboard Scientific Party, 1991). Lithologic units with the décollement (‘déc.’) are reported; the naming is site dependent. Magnetic zones identified here, in Shipboard Scientific Party (2001), and in Lu and Banerjee (1994) for Sites C0023, 1174, and 808, respectively, are indicated in blue.

Table S1. Average NRM, χ_{if} , ARM, and SIRM for the four magnetic zones identified at Site C0023.

Magnetic zone		1	2	2'	3	4
Depth interval [mbsf]		206.89-498-25	500.29-704.31	621.22-683.9	719.42-885.13	890.49-1099.12
NRM [Am ² kg ⁻¹]	Min. value	3.07E-06	1.86E-07	1.15E-06	1.58E-06	2.00E-07
	Max. value	3.37E-04	2.58E-05	1.45E-05	2.50E-05	7.45E-06
	Mean	3.79E-05	2.58E-06	5.59E-06	1.06E-05	1.32E-06
	Std. Dev.	5.89E-05	3.90E-06	2.94E-06	6.00E-06	1.24E-06
χ_{if} [1e ⁻⁸ m ³ kg ⁻¹]	Min. value	13.08	9.03	12.8	21.6	9.66
	Max. value	191.92	28.71	31.6	143.0	19.7
	Mean	41.58	13.82	21.3	33.9	13.4
	Std. Dev.	29.87	4.93	4.95	18.8	2.51
ARM [Am ² kg ⁻¹]	Min. value	1.17E-05	4.00E-06	6.89E-06	3.30E-05	1.56E-06
	Max. value	2.40E-04	2.36E-05	1.97E-05	1.16E-04	9.93E-06
	Mean	5.35E-05	8.02E-06	1.14E-05	7.73E-05	3.58E-06
	Std. Dev.	5.03E-05	4.36E-06	3.23E-06	2.20E-05	1.63E-06
SIRM [Am ² kg ⁻¹]	Min. value	1.21E-03	1.84E-04	3.95E-04	1.76E-03	4.66E-05
	Max. value	1.60E-02	1.64E-03	2.02E-03	7.02E-03	1.02E-03
	Mean	5.88E-03	5.81E-04	1.12E-03	3.23E-03	3.15E-04
	Std. Dev.	4.12E-03	4.33E-04	4.13E-04	1.28E-03	2.36E-04

Table S2. Average M_s , M_{rs} , B_c , and B_{cr} values for the four magnetic zones identified at Site C0023.

Magnetic zone		1	2	2'	3	4
Depth interval [mbsf]		206.89-498-25	500.29-704.31	621.22-683.9	719.42-885.13	890.49-1099.12
M_s [Am ² kg ⁻¹]	Min. value	6.51E-03	1.57E-03	5.36E-03	1.45E-02	5.89E-04
	Max. value	2.61E-01	2.00E-02	2.86E-02	7.64E-02	1.12E-02
	Mean	5.23E-02	6.04E-03	1.53E-02	2.76E-02	4.43E-03
	Std. Dev.	4.52E-02	5.40E-03	5.53E-03	1.40E-02	2.85E-03
M_{rs} [Am ² kg ⁻¹]	Min. value	1.69E-03	2.54E-04	5.26E-04	2.24E-03	7.66E-05
	Max. value	4.76E-02	2.13E-03	2.67E-03	9.98E-03	1.27E-03
	Mean	1.38E-02	7.32E-04	1.39E-03	3.99E-03	4.21E-04
	Std. Dev.	1.38E-02	5.21E-04	5.15E-04	1.73E-03	2.83E-04
B_c [T]	Min. value	7.48E-03	6.09E-03	5.11E-03	4.12E-03	7.45E-03
	Max. value	5.47E-02	1.83E-02	9.05E-03	1.42E-02	1.60E-02
	Mean	2.41E-02	1.18E-02	8.07E-03	1.20E-02	9.46E-03
	Std. Dev.	1.60E-02	2.98E-03	7.45E-04	1.51E-03	1.76E-03
B_{cr} [T]	Min. value	2.64E-02	2.55E-02	2.57E-02	2.28E-02	2.45E-02
	Max. value	7.10E-02	6.06E-02	3.13E-02	3.42E-02	3.68E-02
	Mean	4.71E-02	3.63E-02	2.87E-02	3.16E-02	2.89E-02
	Std. Dev.	1.60E-02	7.24E-03	1.24E-03	1.76E-03	2.78E-03

Table S3. Depths of magnetic zones at Sites C0023, 1174, and 808 with corresponding sedimentary facies.

Magnetic zone		1	2	2'	3	4
Site C0023 ^a	Depth [mbsf]	206.89-498-25	500.29-704.31	621.22-683.9	719.42-885.13	890.49-1099.12
	Lithological units	II and very top of III	III and top of IV	III + top of IV	IV (with décollement)	IV
	Sedimentary facies	Trench-wedge and Trench-to-basin, Upper Shikoku Basin	Upper and Lower Shikoku Basin	Upper and Lower Shikoku Basin	Lower Shikoku Basin	Lower Shikoku Basin
Site 1174 ^b	Depth [mbsf]	0-553.25	553.25-763.1	645.0-744.0	763.1-941.7	941.7-1111.3
	Lithological units	I, II and top of III	III and IV	III and IV	IV	IV
	Sedimentary facies	Slope-apron, Trench-wedge and Upper Shikoku Basin	Upper and Lower Shikoku Basin	Lower Shikoku Basin	Lower Shikoku Basin	Lower Shikoku Basin
Site 808 ^c	Depth [mbsf]	0-675.0	675.0-925.0	<i>not identified</i>	925.0-1080.0	1080.0-1243.0
	Lithological units	I, II, III and IVa	IVa and IVb		IVb (with décollement)	IVb
	Sedimentary facies	Slope-apron, Trench-wedge and Upper Shikoku Basin	Upper and Lower Shikoku Basin		Lower Shikoku Basin	Lower Shikoku Basin

^aHeuer et al. (2017); IODP Site C0023 drilled in 2016; latitude 32°22.00'N; longitude 134°57.98'E; water depth 4776 m

^bMoore et al. (2001); ODP Site 1174 drilled in 200; latitude 32°21'N; longitude 134°57'E; water depth 4751.2 m

^cHill et al. (1993); ODP Site 808 drilled in 1990; latitude 32°21'N; longitude 134°57'E; water depth 4676 m

References

- Heuer, V.B., Inagaki, F., Morono, Y., Kubo, Y., Maeda, L. and the Expedition 370 Scientists, 2017. Temperature limit of the deep biosphere off Muroto. *Proceedings of the International Ocean Discovery Program Volume 370*: College Station, TX (International Ocean Discovery Program), doi:10.14379/iodp.proc.370.2017.
- Hill, I.A., Taira, A., Firth, J.V., et al. (1993). *Proceedings of the Ocean Drilling Program, Initial Reports, 190*: College Station, TX (Ocean Drilling Program), doi:10.2973/odp.proc.sr.131.1993.
- Lu, R., and Banerjee, S.K., 1994. Magnetite dissolution in deep sediments and its hydrologic implication: A detailed study of sediments from Site 808, Leg 131. *Journal of Geophysical Research*, **99**, 9051–9059. doi:10.1029/93JB03204.
- Moore, G.F., Taira, A., Klaus, A., et al. (2001). *Proceedings of the Ocean Drilling Program, Scientific Results, 131*: College Station, TX (Ocean Drilling Program), doi:10.2973/odp.proc.ir.190.2001.

- Shipboard Science Party, 1991. Site 808. In: *Proceedings of the Ocean Drilling Program, Initial Reports, 131* (eds. Taira, A., Hill, I., Firth, J.V., et al.). College Station, TX (Ocean Drilling Program), 71-269. doi:10.2973/odp.proc.ir.131.106.1991.
- Shipboard Science Party, 2001. Site 1174. In: *Proceedings of the Ocean Drilling Program, Initial Reports, 190* (eds. Moore, G.F., Taira, A., Klaus, A., et al.). College Station, TX (Ocean Drilling Program), 1-149. doi:10.2973/odp.proc.ir.190.105.2001.

APPENDIX OF CHAPTER IV

Supporting Material for

Uniquely low iron isotopic signatures in deep marine sediments caused by Rayleigh distillation

Sedimentary setting and geological background

Pore-water and solid-phase samples analyzed in this study were taken from Hole C0023A (Supplementary Fig. 1) during International Ocean Discovery Program (IODP) Expedition 370 (Temperature Limit of the Deep Biosphere off Muroto) onboard *D/V Chikyu* in September–November 2016 (Heuer et al., 2017). IODP Site C0023 (32°22.00'N, 134°57.98'E; 4776 m water depth) is located in the Nankai Trough off Shikoku Island, Japan, where the Philippine Sea plate is subducting beneath the Eurasian plate at a current rate of 4–6 cm yr⁻¹ (Seno et al., 1993; DeMets et al., 2010). Due to off-scraping of sediment from the descending Philippine Sea plate, the Nankai accretionary prism has been formed (Le Pichon et al., 1987; Taira et al., 1992). Site C0023 is situated in the protothrust zone of the accretionary prism, where a ~1200 m thick sediment sequence accumulated on the ~16-million-year-old basaltic basement. The sediment sequence at Site C0023 is divided into the following lithostratigraphic units from bottom to top: the volcanoclastic facies (Unit V), the Lower Shikoku Basin facies (hemipelagic mudstone; Unit IV), the Upper Shikoku Basin facies (hemipelagic mudstone with abundant volcanic ash layers; Unit III), the basin-to-trench transitional facies (Subunit IIC), the outer trench-wedge facies (Subunit IIB), and the axial trench-wedge facies (Subunit IIA) (Heuer et al., 2017). A more detailed description including the diagenetic history of Site C0023 can be found in Köster et al. (2021).

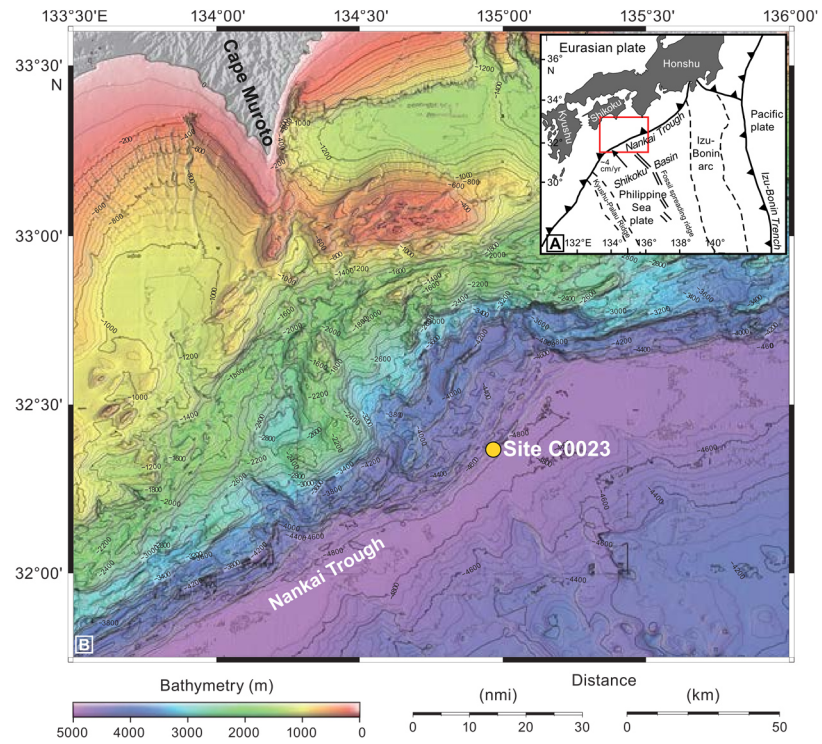


Figure S1. Location of IODP Site C0023 in the Nankai Trough offshore Japan. (A) Inset showing the general tectonic setting of the Nankai Trough, which marks the subduction boundary between the Philippine Sea plate and the Eurasian Plate. (B) Bathymetric map of the Nankai Trough off Cape Muroto. IODP Site C0023 is located in a water depth of 4776 m. Modified after Heuer et al. (2017).

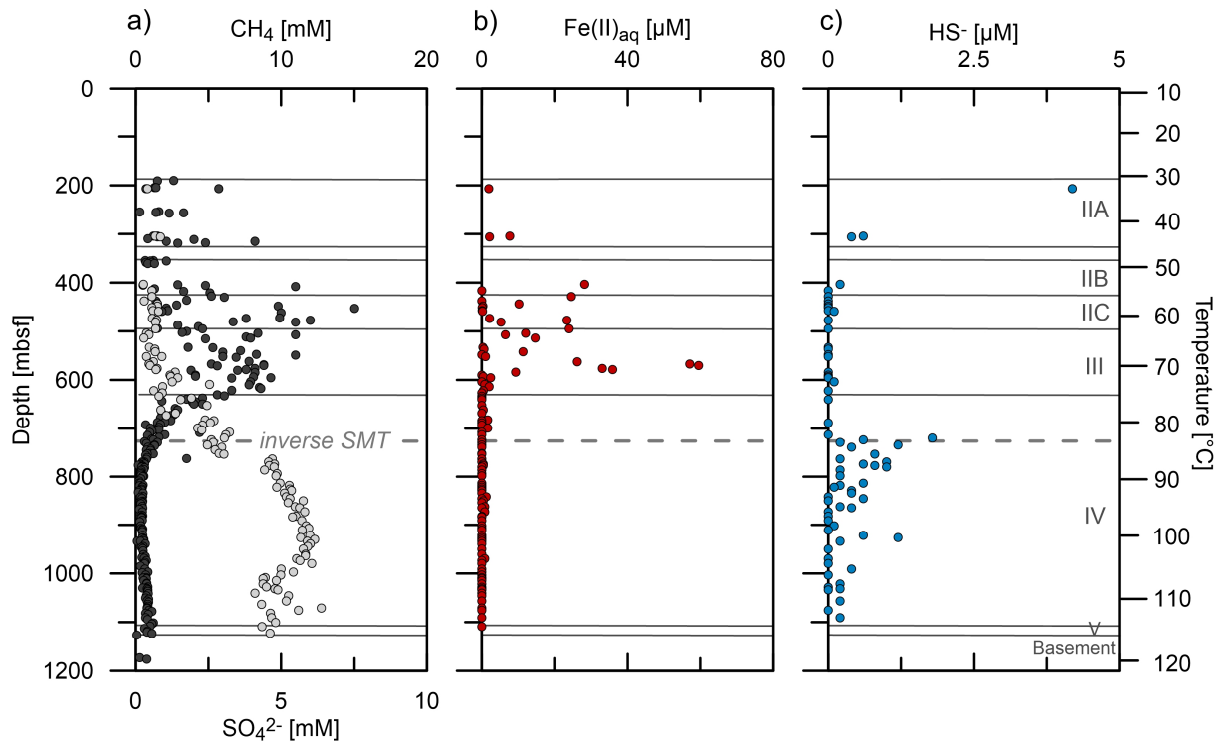


Figure S2. Down-core profiles of methane, sulfate, dissolved iron and hydrogen sulfide at Site C0023. Pore-water and gas concentrations of (a) methane (CH_4) (black dots) and sulfate (SO_4^{2-}) (gray dots), (b) dissolved iron ($\text{Fe(II)}_{\text{aq}}$) and (c) hydrogen sulfide (HS^-) (from Heuer et al., 2017). Lithological units (see Sedimentary setting and geological background) and temperature data are from Heuer et al. (2017) and Heuer et al. (2020), respectively. An inverse sulfate-methane transition (SMT) is located at ~730 mbsf.

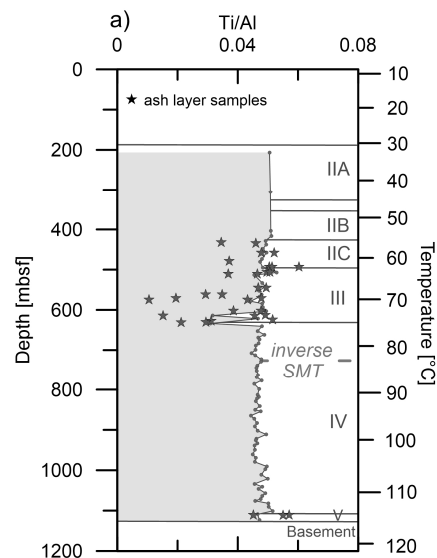


Figure S3. Down-core profile of the Ti/Al ratio in mud rock and discrete ash layers at Site C0023. While the Ti/Al ratios in the mud rock samples are relatively constant around 0.05 (gray shaded area), the Ti/Al ratios in the discrete ash layer samples (stars) vary between 0.01 and 0.06. Lithological units and temperature data as in Fig. 2.

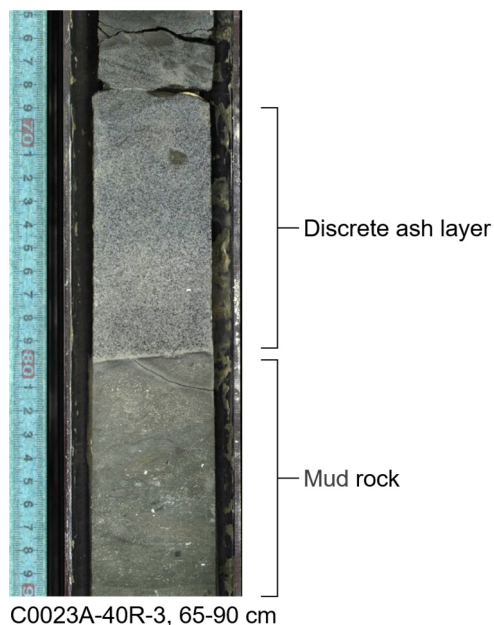


Figure S4. Core picture showing a discrete ash layer. The discrete ash layer in core C0023A-40R-3 is located in a depth of ~624 mbsf (from Heuer et al., 2017).

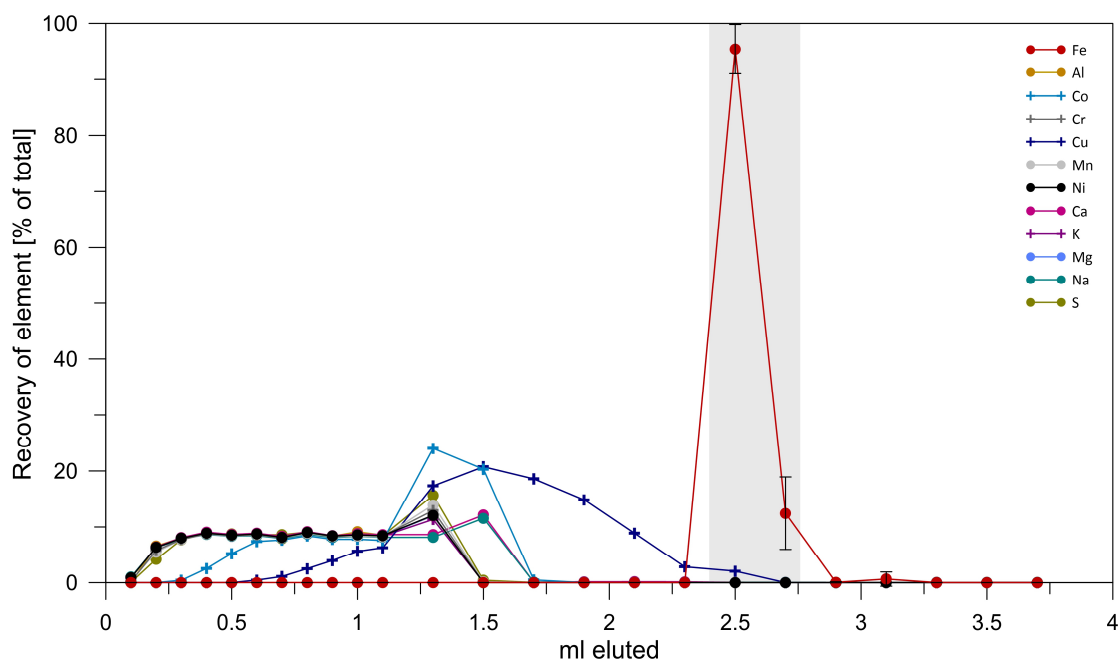


Figure S5. Column calibration using the AG-MP1 anion exchange resin. Column calibration confirmed the effective separation of Fe from the salt matrix (Na, K, Ca, Mg, S) and other trace metals (e.g., Ni, Cr, Mn, Co, Cu) by using the AG-MP1 anion exchange resin according to Homoky et al. (2013). The recovery of total Fe is 108% and can be attributed to a dilution effect before ICP-OES measurement. Error bars indicate the simple standard deviation (1SD; n=4).

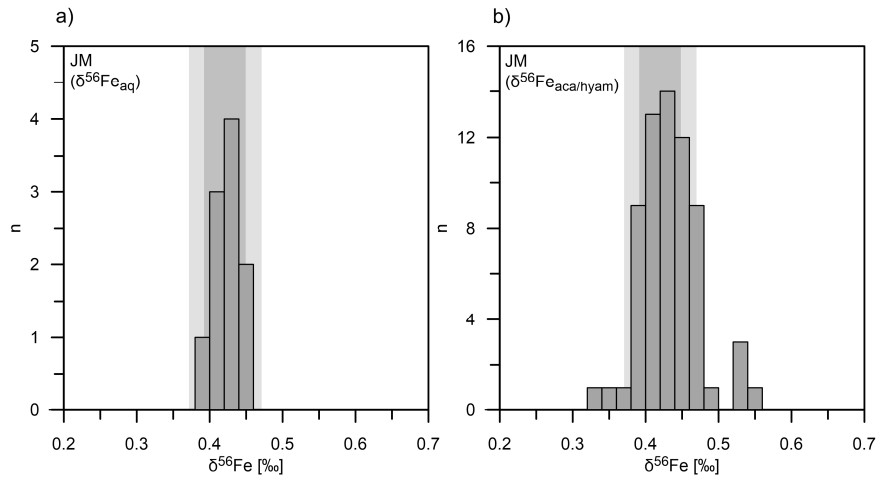


Figure S6. JM standard distribution. The internal laboratory RM JM (Johnson&Matthey, Fe puratronic wire) was measured every six samples to monitor the instrumental reproducibility. Only samples in between the JM samples that were within the analytical uncertainty of the target value ($0.42 \pm 0.05\text{‰}$, 2SD; Schoenberg and von Blanckenburg, 2005) were taken into account for further data evaluation. The measured $\delta^{56}\text{Fe}$ values for the RM JM were (a) $0.42 \pm 0.06\text{‰}$ (2SD, $n=19$) for the isotopic measurements of pore-water Fe ($\delta^{56}\text{Fe}_{\text{aq}}$) and (b) $0.43 \pm 0.08\text{‰}$ (2SD, $n=65$) for the isotopic measurement of the Na-acetate- and hydroxylamine-HCl-leached Fe pools ($\delta^{56}\text{Fe}_{\text{aca}}$ and $\delta^{56}\text{Fe}_{\text{hyam}}$). The dark and light grayish area represents 1SD and 2SD of target value of the RM JM (Schoenberg and von Blanckenburg, 2005), respectively.

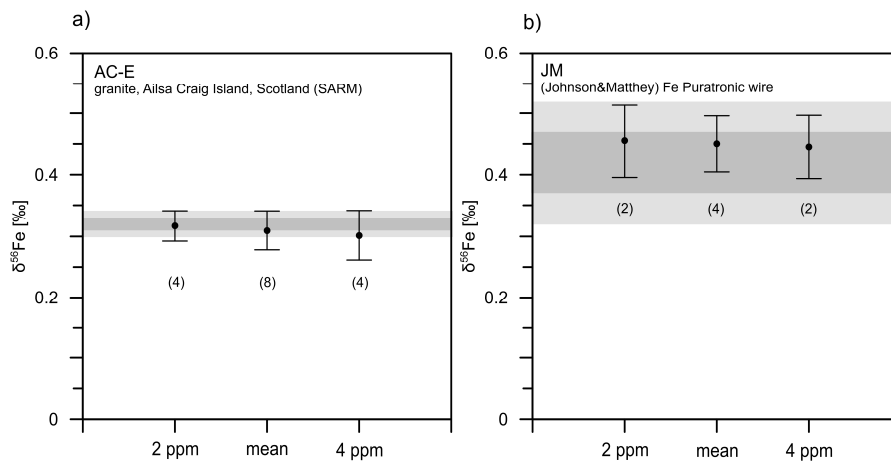


Figure S7. Column chromatography of the reference samples AC-E and JM. Isotopic composition of (a) the RM AC-E (granite rock; Ailsa Craig Island, Scotland (SARM)) and (b) the internal laboratory RM JM (Johnson&Matthey; Fe Puratronic wire) after column chromatography with AG-MP1 anion exchange resin. Error bars indicate the simple standard deviation (1SD). The dark and light grayish area represents 1SD and 2SD of the certified reference values, respectively. Numbers within parentheses refer to the number of processed reference samples for the respective concentration (2 and 4 ppm) and the resulting mean.

Table S1. Diffusion coefficients of Fe(II)_{aq} in free solution for seawater (D^{SW}) and corrected for sediment tortuosity (D_{sed}) at various temperatures and porosity values.

T [°C]	D^{SW} [$m^2 s^{-1}$] ^a	D_{sed} [$m^2 s^{-1}$] ^b	ϕ^c
5°C	$3.81 \cdot 10^{-10}$	$1.30 \cdot 10^{-10}$	0.7
25°C	$6.57 \cdot 10^{-10}$	$2.24 \cdot 10^{-10}$	
50°C	$9.98 \cdot 10^{-10}$	$3.40 \cdot 10^{-10}$	
75°C	$1.34 \cdot 10^{-9}$	$4.55 \cdot 10^{-10}$	
5°C	$3.81 \cdot 10^{-10}$	$6.68 \cdot 10^{-10}$	0.5
25°C	$6.57 \cdot 10^{-10}$	$1.15 \cdot 10^{-10}$	
50°C	$9.98 \cdot 10^{-10}$	$1.75 \cdot 10^{-10}$	
75°C	$1.34 \cdot 10^{-9}$	$2.35 \cdot 10^{-10}$	
5°C	$3.81 \cdot 10^{-10}$	$4.74 \cdot 10^{-11}$	0.4
25°C	$6.57 \cdot 10^{-10}$	$8.19 \cdot 10^{-11}$	
50°C	$9.98 \cdot 10^{-10}$	$1.24 \cdot 10^{-10}$	
75°C	$1.34 \cdot 10^{-9}$	$1.66 \cdot 10^{-10}$	

^aThe diffusion coefficients of Fe(II)_{aq} in free solution for seawater are corrected for the dynamic viscosity μ according to Li and Gregory (1979). The dynamic viscosity μ , which is a function of salinity and temperature, is calculated according to the algorithm from El-Dessouky and Ettouney (2002).

^bThe diffusion coefficients of Fe(II)_{aq} in free solution for seawater are corrected for sediment tortuosity after Boudreau (1997).

^cTypical values of porosity for unconsolidated near-surface sediments are around 0.7 (e.g., Berner, 1980). The present-day porosity values at Site C0023 in the ferruginous zone range between 0.4 and 0.5 (Heuer et al., 2017).

Table S2. Sequential extraction procedure after Poulton and Canfield (2005) applied to mud rock and volcanic ash layer samples of Site C0023.

Step	Target mineral phase	Terminology	Extraction reagent	Extraction time	pH
I	Carbonate-bound and sorbed Fe and AVS ^a Easily reducible Fe	Fe _{aca}	1 M Na-acetate	24 h	4.5
II	(oxyhydr)oxides (ferrihydrite, lepidocrocite)	Fe _{hyam}	1 M hydroxylamine-HCl in 25% v/v acetic acid	48 h	
III	Reducible Fe oxides (goethite, hematite)	Fe _{di-ct}	Na-dithionite (50 g L ⁻¹)/ 0.02 M Na-citrate ^b	2 h	4.8
IV	Magnetite	Fe _{oxa}	0.2 M ammonium oxalate/0.17 M oxalic acid	6 h	

^aAcid volatile sulfide

^bNa-citrate solution was modified to 0.02 M according to Henkel et al. (2016)

Table S3. Sequentially extracted Fe contents in the internal laboratory reference material (RM) HE443-077-cc (anoxic sediment from the Helgoland mud area, North Sea) and associated isotopic composition ($\delta^{56}Fe_{aca}$ and $\delta^{56}Fe_{hyam}$) determined over the past 5 years in comparison with Fe contents and isotopic composition determined in the framework of this study. Uncertainty is expressed as the twofold standard deviation (2SD).

Step	Terminology	Fe contents determined over the past 5 years [mg/g] (n=67)	Fe contents this study [mg/g] (n=6)	$\delta^{56}Fe$ determined over the past 5 years [‰] (n=4)	$\delta^{56}Fe$ this study [‰] (n=2)
I	Fe _{aca}	4.7 ± 0.6	4.8 ± 0.1	-0.07 ± 0.04	-0.06 ± 0.03
II	Fe _{hyam}	3.1 ± 0.7	2.8 ± 0.2	-0.33 ± 0.07	-0.28 ± 0.04
III	Fe _{di-ct}	2.6 ± 0.4	2.6 ± 0.1	-	-
IV	Fe _{oxa}	1.0 ± 0.2	1.2 ± 0.05	-	-

References

- Berner, R.A., 1980. *Early Diagenesis: A Theoretical Approach*. Princeton Univ. Press, Princeton, New Jersey.
- Boudreau, B.P., 1997. *Diagenetic Models and Their Implementation: Modelling Transport and Reactions in Aquatic Sediments*. Springer, Berlin, Heidelberg, New York, 428 p.
- DeMets, C., Gordon, R.G., and Argus, D.F., 2010. Geologically current plate motions. *Geophysical Journal International*, **181**, 1-80. doi:10.1111/j.1365-246X.2009.04491.x.
- El-Dessouky, H.T., and Ettouney, H.M., 2002. *Fundamentals of Salt Water Desalination*. Elsevier Science B.V., Amsterdam.
- Heuer, V.B., Inagaki, F., Morono, Y., Kubo, Y., Maeda, L., and the Expedition 370 Scientists, 2017. Temperature limit of the deep biosphere off Muroto. *Proceedings of the International Ocean Discovery Program Volume 370*: College Station, TX (International Ocean Discovery Program). doi:10.14379/iodp.proc.370.2017.
- Heuer, V.B., Inagaki, F., Morono, Y., Kubo, Y., Spivack, A., Viehweger, B., et al., 2020. Temperature limits to deep seafloor life in the Nankai Trough subduction zone. *Science*, **370**, 1230-1234. doi:10.1126/science.abd7934.
- Homoky, W.B., John, S.G., Conway, T.M., and Mills, R.A., 2013. Distinct iron isotopic signatures and supply from marine dissolution. *Nature Communications*, **4**, 2143. doi:10.1038/ncomms3143.
- Köster, M., Kars, M., Schubotz, F., Tsang, M.-Y., Maisch, M., Kappler, A., et al., 2021a. Evolution of (bio-)geochemical processes and diagenetic alteration of sediments along the tectonic migration of ocean floor in the Shikoku Basin off Japan. *Geochemistry, Geophysics, Geosystems*, e2020GC009585. doi:10.1029/2020GC009585.
- Le Pichon, X., Iiyama, T., Boulègue, J., Charvet, J., Faure, M., Kano, K., et al., 1987. Nankai Trough and Zenisu Ridge: a deep-sea submersible survey. *Earth and Planetary Science Letters*, **83**, 285-299. doi:10.1016/0012-821X(87)90072-0.
- Li, Y.-H., and Gregory, S., 1974. Diffusion of ions in sea water and in deep-sea sediments. *Geochimica et Cosmochimica Acta*, **38**, 703-714. doi:10.1016/0016-7037(74)90145-8.
- Poulton, S.W., and Canfield, D.E., 2005. Development of a sequential extraction procedure for iron: implications for iron partitioning in continentally derived particulates. *Chemical Geology*, **214**, 209-221. doi:10.1016/j.chemgeo.2004.09.003.
- Schoenberg, R., and von Blanckenburg, F., 2005. An assessment of the accuracy of stable Fe isotope ratio measurements on samples with organic and inorganic matrices by high-resolution multicollector ICP-MS. *International Journal of Mass Spectrometry*, **242**, 257-272 doi:10.1016/j.ijms.2004.11.025.
- Seno, T., Stein, S., and Gripp, A.E., 1993. A model for the motion of the Philippine Sea Plate consistent with NUVEL-1 and geological data. *Journal of Geophysical Research: Solid Earth*, **98**, 17941-17948. doi:10.1029/93JB00782.
- Taira, A., Hill, I., Firth, J., Berner, U., Brückmann, W., Byrne, T., et al., 1992. Sediment deformation and hydrogeology of the Nankai Trough accretionary prism: synthesis of shipboard results of ODP Leg 131, *Earth and Planetary Science Letters*, **109**, 431-450. doi:10.1016/0012-821X(92)90104-4.

APPENDIX OF CHAPTER V

Supporting Material for

Fading of a sulfate-methane transition in deep and hot sediments from the Nankai Trough

Model setup and parameterization

The reactive transport model consists of four species and three reactions and uses the one-dimensional (depth, z) advection-transport-reaction equations (Mogollón et al., 2016; Volz et al., 2020) for dissolved (Eq. S1) and solid species (Eq. S2):

$$\varphi_i \frac{\partial C_{i,j}}{\partial t} = \frac{\partial}{\partial z} \left(\frac{\varphi_i D_{i,j}}{\theta^2} \frac{\partial C_{i,j}}{\partial z} \right) - \frac{\partial \varphi_i v_i C_{i,j}}{\partial z} + \varphi_i \sum R_{i,j} \quad (\text{S1})$$

$$(1 - \varphi_i) \frac{\partial G_{i,j}}{\partial t} = - \frac{\partial (1 - \varphi_i) w_i G_{i,j}}{\partial z} + (1 - \varphi_i) \sum R_{i,j} \quad (\text{S2})$$

where t is time, z is sediment the depth in meter below seafloor (mbsf) and i,j represent subscripts depicting depth and species-dependence, respectively; φ is the porosity (Eq. S3); C, G are the species concentrations (dissolved (SO_4^{2-} , CH_4 , DIC) and solid (C_{org}) species, respectively); D is the tortuosity-corrected diffusion coefficient (θ^2), which was calculated according to Boudreau (1996) as $\theta^2 = 1 - 2\ln(\varphi)$; v, w are the burial velocity of the dissolved (Eq. S4) and the solid phase (Eq. S5), respectively; $\sum R_{i,j}$ is the sum of the reactions affecting the given species j . The effects of biological induced mixing (bioturbation and bioirrigation) is not considered in the model since biological induced mixing affects the upper 10 cm of sediment, which is not the focus of this study.

The porosity profile shows an exponential decrease with depth typical for compacting sediments (Fig. S1E). The data were fit with the following equation:

$$\varphi = \varphi_\infty + (\varphi_0 - \varphi_\infty) \exp(-\beta z) \quad (\text{S3})$$

where φ_∞ is the porosity at compaction; φ_0 is the porosity at the sediment-water interface (SWI), and β is the depth-attenuation coefficient.

Assuming steady state sediment compaction, the burial velocity of the dissolved phase (v) and solid phase (w) follows the conservation of mass:

$$v = \omega \frac{\varphi_{\infty}}{\varphi} \quad (\text{S4})$$

$$w = \omega \frac{1-\varphi_{\infty}}{1-\varphi} \quad (\text{S5})$$

where ω is the compacted velocity of the sedimentation.

The temperature-dependent diffusion coefficient D^0 is calculated in the R-package "marelac" (Soetaert et al., 2020). The diffusion coefficient D in seawater is generally corrected by viscosity:

$$D^{sw} = D^0 \frac{\mu_0}{\mu_{sw}}, \quad (\text{S6})$$

where μ is the dynamic viscosity, the script sw indicates a (saline) pore-water value and the script o indicates an infinite-dilution value (Li and Gregory, 1974). Values of the dynamic viscosity in Boudreau (1997) and the R-package "marelac" (Soetaert et al., 2020) are based on an empirical equation developed by Kukulka et al. (1987), which is claimed to be accurate for the temperature range between 0°C and 30°. Since the temperature within the sediments at Site C0023 increases up to 120°C (Heuer et al., 2020), we here use the algorithm from El-Dessouky and Ettouney (2002), which is valid up to 180°C, given by:

$$\mu = \mu_w \mu_R \times 10^{-3} \quad (\text{S7})$$

with

$$\mu_w = \exp(-3.79418 + 604.129/(139.18 + T)) \quad (\text{S8})$$

$$\mu_R = 1 + A \cdot S + B \cdot S^2 \quad (\text{S9})$$

$$A = 1.474 \times 10^{-3} + 1.5 \times 10^{-5} T - 3.927 \times 10^{-8} T^2 \quad (\text{S10})$$

$$B = 1.0734 \times 10^{-5} - 8.5 \times 10^{-8} T + 2.23 \times 10^{-10} T^2 \quad (\text{S11})$$

where viscosity μ is in $\text{kg m}^{-1}\text{s}^{-1}$, temperature T in °C, and salinity S in mg kg^{-1} . The temperature within the sediment is a function of depth (z) and fitted by a polynomial function with:

$$T = 10 + 0.1136635 \times 10^{-2} z - 1.69 \times 10^{-9} z^2. \quad (\text{S12})$$

The primary redox reactions include organoclastic sulfate reduction (SR; Eq. S13), methanogenesis (MG; Eq. S14), anaerobic oxidation of methane (AOM; Eq. S15) and the precipitation of gypsum and/or anhydrite ($CaSO_4 \cdot nH_2O$; Eq. S16):



The rate of organic matter degradation (R_{TOC}) was modeled using a 3-G model in which the heterogeneity of organic matter and its evolution during burial is considered (Jørgensen, 1978). In the 3-G model, the organic matter pool is classified into three discrete fractions (labile C_{org}^1 , metabolizable C_{org}^2 and refractory C_{org}^3), whereby each fraction is characterized by a specific degradability. Following this assumption, the rate of organic matter degradation was calculated as follows:

$$R_{TOC} = -\sum_{i=1}^3 \sigma_i C_{org}^i \quad (S17)$$

where C_{org}^i and σ_i are the concentrations of organic carbon and the specific first-order degradability of each fraction, respectively (Jørgensen, 1978).

The rate expressions for organoclastic sulfate reduction (R_1), methanogenesis (R_2), AOM (R_3) and the precipitation of anhydrite and/or gypsum (R_4) are given by:

$$R_1 = R_{TOC}(1 - f_s) \quad (S18)$$

$$R_2 = R_{TOC}f_s \quad (S19)$$

$$R_3 = k_{AOM} \times \frac{C_{CH_4}C_{SO_4}}{C_{SO_4} + k_{s,AOM}} \quad (S20)$$

$$R_4 = k_{pp} \times \left(\frac{C_{Ca}C_{SO_4}}{K_{sp}} - 1 \right). \quad (S21)$$

The factor f_s (S18 and S19) is a rate-limiting term that determine the extent to which organoclastic sulfate reduction and methanogenesis are inhibited by sulfate. It is based on the complementary error function (erfc) defined by:

$$f_s = 0.5 \times \operatorname{erfc}((C_{SO_4} - C_{SO_4}^*)/k_{in}), \quad \text{where } f_s \sim \begin{cases} 1 & \text{if } C_{SO_4} < C_{SO_4}^* \\ 0 & \text{if } C_{SO_4} > C_{SO_4}^* \end{cases} \quad (\text{S22})$$

The terms $C_{SO_4}^*$ and k_{in} are the threshold sulfate concentration for methanogenesis and a parameter controlling steepness, respectively (Burdige et al., 2016a; 2016b). The AOM rate depends on a Monod type kinetic function with an inhibition constant $k_{S,AOM}$ of 1 mM (Nauhaus et al., 1995) and the rate constant k_{AOM} (Arndt et al., 2006). The factor k_{pp} is the kinetic rate constant of the $CaSO_4 \cdot nH_2O$ precipitation and K_{sp} is the solubility product.

The temperature dependent rate constants k_{AOM} and $\sigma_{i=1-3}$ are defined as:

$$k_{AOM} = k_{AOM}^0 f(T) F_{in}(T), \quad (\text{S23})$$

and

$$\sigma_{i=1-3} = \sigma_{i=1-3}^0 f(T) F_{in}(T), \quad (\text{S24})$$

where k_{AOM}^0 and σ_i^0 are the AOM rate and organic matter degradation rate constants at the reference temperature, T_0 , respectively; $f(T)$ determines the temperature dependency of the rate constant and $F_{in}(T)$ is a temperature-limiting term (LaRowe et al., 2014).

The temperature dependence of rate constants $f(T)$ is calculated using a Q_{10} value of 1.7:

$$f(T) = Q_{10}^{\frac{T-T_0}{10}}. \quad (\text{S25})$$

A Q_{10} value of 1.7 means that the rate constants increase by a factor of 1.7 for every 10 degree increase in temperature relative to the reference temperature, T_0 , at the sediment surface (10°C). The temperature limiting term $F_{in}(T)$, which is based on the assumption that microbes grow or catalyse reactions over a finite temperature range, is defined as:

$$F_{in}(T) = 0.5 \cdot \operatorname{erfc}\left(\frac{T-T_c}{T_{in}}\right), \quad (\text{S26})$$

where T is the *in situ* temperature, T_c is the threshold temperature, T_{in} the steepness parameter, and erfc the complementary error function (LaRowe et al., 2014).

The observations from cultivation-based approaches in hydrothermally influenced sediment from the Guaymas Basin demonstrated activity of thermophilic anaerobic methane-oxidizing communities at temperatures between 5°C and 75°C with an apparent optimum between 45°C

and 60°C (Kallmeyer and Boetius, 2004; Holler et al., 2011). More recently, methane at Site C0023 was found to be biologically oxidized until sediments reach a temperature of 80°C to 85°C, while methanogenesis rates drop two orders of magnitude above 45°C (Heuer et al., 2020). Based on these studies, we set the threshold temperature $T_C=60^\circ\text{C}$ for AOM and $T_C=40^\circ$ for organic matter degradation (Fig. S1). The temperature limiting term $F_{in}(T)$ is 1 when $T < T_C$ and approaches 0 when $T \geq T_C$.

The sinks and sources of sulfate, methane and DIC are calculated according to the stoichiometries in Eqs. S13 – S16. The concentration of Ca^{2+} is fitted by a polynomial function:

$$C_{Ca} = 2.16845 + 0.0508293z - 5.13449 \times 10^{-5}z^2 + 3.64882 \times 10^{-8}z^3, \quad (\text{S27})$$

if the depth $z < 860$ mbsf and

$$C_{Ca} = -10175.5 + 33.3848z - 0.0364487z^2 + 1.32897 \times 10^{-5}z^3, \quad (\text{S28})$$

if $z > 860$ mbsf.

Gypsum ($\text{CaSO}_4 \cdot 2\text{H}_2\text{O}$) and anhydrite (CaSO_4) are the two stable calcium sulfate phases that can occur as geologic deposits (Rolnick, 1954). While gypsum is stable at temperatures below 40°C, anhydrite is the stable phase at temperature above 130°C. In a temperature range between 40 and 130°C, no clear indication of the stable phase can be established (Partridge and White, 1929; Rolnick, 1954; Serafeimidis and Anagnostou, 2015).

The precipitation of calcium sulfate phases depends on the saturation state Ω , which is defined as:

$$\Omega = \frac{\gamma_{Ca}C_{Ca}\gamma_{SO_4}C_{SO_4}(a_w)^n}{K_{Sp}}, \quad (\text{S29})$$

where γ_{Ca} and γ_{SO_4} are activity coefficients of Ca^{2+} and SO_4^{2-} , respectively and a_w is the activity of water. An Ω value < 1 is indicative of mineral dissolution while $\Omega > 1$ implies mineral precipitation.

The activity coefficients of species are calculated based on the Truesdell-Jones equation (Truesdell and Jones, 1974), which is an extended version of the Debye-Hückel equation (Debye and Hückel, 1923), as follows:

$$\log \gamma_i = -Az_i^2 \frac{I^{0.5}}{1+B \cdot a_i \cdot I^{0.5}} + b_i I, \quad (\text{S30})$$

where a_i and b_i are both empirical ion size parameters ($a_{Ca} = 4.86\text{\AA}$; $a_{SO4} = 5.31\text{\AA}$; $b_{Ca} = 0.15 \text{ mol L}^{-1}$; $b_{SO4} = -0.07 \text{ mol L}^{-1}$; from Parkhurst, 1990). These ion-specific ion size parameters allow the prediction of activity coefficients accurately up to 2.0 mol L^{-1} . z_i is the charge number of ion i and I is the ionic strength of the solution on a molality basis, defined by (Lewis and Randall, 1921), as follows:

$$I = \frac{1}{2} \sum_j m_j z_j^2. \quad (\text{S31})$$

The ionic strength is summed for all charged species in solution. The constants A and B are calculated from the dielectric constant, water density, and temperature (DeVoe, 2020):

$$A = \frac{1}{\ln 10} \frac{\sqrt{2} N_A^2 e^3 (\rho_w)^{0.5}}{(8\pi \epsilon_r \epsilon_0 R (T+273.15))^{1.5}} = \frac{1.82483 \times 10^6 (\rho_w)^{0.5}}{(\epsilon_r (T+273.15))^{1.5}} \quad \text{in } [\text{mol}^{-0.5} \text{kg}^{0.5}] \quad (\text{S32})$$

and

$$B = \frac{\sqrt{2} N_A e (\rho_w)^{0.5}}{(\epsilon_r \epsilon_0 R (T+273.15))^{0.5}} = \frac{50.29037 \times 10^8 (\rho_w)^{0.5}}{(\epsilon_r (T+273.15))^{0.5}} \quad \text{in } [\text{cm}^{-1} \text{mol}^{-0.5} \text{kg}^{0.5}] \quad (\text{S33})$$

where N_A is the Avogadro constant, e is the elementary charge (the charge of a proton), R is gas constant, ρ_w and ϵ_r are the density and relative dielectric constant of the seawater and ϵ_0 is the dielectric constant of vacuum. The denominator $\ln 10$ is used for the conversion of natural logarithm (base e) to scientific logarithm (base 10).

The ionic strength of seawater may be calculated from salinity by (DOE, 1994):

$$I = \frac{19.924S}{1000 - 1.005S}. \quad (\text{S34})$$

The seawater density ρ_w is calculated following the Nayar's expression, which is valid for temperatures between 0° and 180°C , salinities between 0 and 160 g kg^{-1} and pressures between 0 and 12 MPa (Nayar et al., 2016):

$$\rho_w(T, S, P) = \rho_w(T, S, P_0) \times F_P, \quad (\text{S35})$$

where

$$\rho_w(T, S, P_0) = a_1 + a_2T + a_3T^2 + a_4T^3 + a_5T^4 + b_1(S/1000) + b_2(S/1000)T + b_3(S/1000)T^2 + b_4(S/1000)T^3 + b_5(S/1000)^2T^2 \quad (\text{S36})$$

and

$$F_P = \exp \left[(P - P_0) \times (c_1 + c_2T + c_3T^2 + c_4T^3 + c_5T^4 + c_6T^5 + S \times (d_1 + d_2T + d_3T^2)) + \frac{(P^2 - P_0^2)}{2} \times (c_7 + c_8T + c_9T^3 + d_4S) \right] \quad (\text{S37})$$

with

$$\begin{aligned} a_1 &= 9.999 \times 10^2, a_2 = 2.034 \times 10^{-2}, a_3 = -6.162 \times 10^{-3}, a_4 = 2.261 \times 10^{-5}, a_5 = -4.657 \times 10^{-8} \\ b_1 &= 8.020 \times 10^2, b_2 = -2.001, b_3 = 1.677 \times 10^{-2}, b_4 = -3.060 \times 10^{-5}, b_5 = -1.613 \times 10^{-5}, \\ c_1 &= 5.0792 \times 10^{-4}, c_2 = -3.4168 \times 10^{-6}, c_3 = 5.6931 \times 10^{-8}, c_4 = -3.7263 \times 10^{-10}, c_5 = 1.4465 \times 10^{-12}, \\ c_6 &= -1.7058 \times 10^{-15}, c_7 = -1.3389 \times 10^{-6}, c_8 = 4.8603 \times 10^{-9}, c_9 = -6.8039 \times 10^{-13}, \\ d_1 &= -1.1077 \times 10^{-6}, d_2 = 5.5584 \times 10^{-9}, d_3 = -4.2539 \times 10^{-11}, d_4 = 8.3702 \times 10^{-9}, P_0 = 0.101 \text{ MP}. \end{aligned}$$

The dielectric constant of seawater is calculated following the expression (Liu et al. 2011; Lawrence et al., 2020):

$$\varepsilon_r(T, P, S) = \varepsilon_r(T, P, 0) \times F_S. \quad (\text{S38})$$

The dielectric constant of pure water ($\varepsilon_r(T, P, 0)$) at high temperature and pressure is calculated according to the equation (Bradley and Pitzer, 1979):

$$\varepsilon_r(T, P, 0) = u_1 \exp(u_2(T + 273.15) + u_3(T + 273.15)^2) + (u_4 + u_5/(u_6 + T + 273.15)) \ln \left(\frac{u_7 + u_8/(T + 273.15) + u_9(T + 273.15) + P}{u_7 + u_8/(T + 273.15) + u_9(T + 273.15) + 1000} \right) \quad (\text{S39})$$

which is valid for temperatures between 0 and 350°C and pressures between 0 and 5000 bar with

$$\begin{aligned} u_1 &= 3.4279 \times 10^2, u_2 = -5.0866 \times 10^{-3}, u_3 = 9.4690 \times 10^{-7}, u_4 = -2.0525, \\ u_5 &= 3.1159 \times 10^3, u_6 = -1.8289 \times 10^2, u_7 = -8.0325 \times 10^3, u_8 = 4.2142 \times 10^6, \\ u_9 &= 2.1417. \end{aligned}$$

Although there were several efforts to derive the salinity dependent F_S (e.g., Klein and Swift, 1977; Meissner and Wentz, 2004; Liu et al., 2011; Lawrence et al., 2020), all of these studies were limited to a temperature of 40°C. Since the expression of F_S at high temperature is missing, the model of Lawrence et al. (2020) has been adopted in this study:

$$F_S = 1 - 3.85142359 \times 10^{-3}S + 1.73819707 \times 10^{-5}S^2 - 8.86453805 \times 10^{-6}TS \quad (\text{S40})$$

The water activity (a_w) is calculated from osmotic coefficients according to the equation (Robinson and Stokes, 1970):

$$\ln a_w = -\frac{\phi_w \sum_i m_i}{1000/MW_w} \quad (\text{S41})$$

where MW_w is molecular weight of water ($MW_w=18.01534 \text{ g mol}^{-1}$) and ϕ_w is the osmotic coefficient of sea water. For the seawater composition, the stoichiometric molality is specified as:

$$\sum_i m_i = \frac{1000}{MW_s} \frac{S}{1000-S}, \quad (\text{S42})$$

where MW_s is the weighted average of the molecular weight of each dissolved solute in seawater ($MW_s=31.4038 \text{ g mol}^{-1}$) (Millero et al., 2008). Sharqawy et al. (2010) reviewed the osmotic coefficient data and derived a new relation based on the data of Bromley et al. (1974) due its wide parameter range of 0°–200°C in temperature and 10–120 g kg⁻¹ in salinity as:

$$\phi_w = a_1 + a_2T + a_3T^2 + a_4T^4 + a_5S + a_6ST + a_7ST^3 + a_8S^2 + a_9S^2T + a_{10}S^2T^2 \quad (\text{S43})$$

with

$$\begin{aligned} a_1 &= 8.9453233003 \times 10^{-1}, a_2 = 4.1560737424 \times 10^{-4}, a_3 = -4.6262121398 \times 10^{-6}, \\ a_4 &= 2.2211195897 \times 10^{-11}, a_5 = -1.1445456438 \times 10^{-4}, a_6 = -1.4783462366 \times \\ &10^{-6}, a_7 = -1.3526263499 \times 10^{-11}, a_8 = 7.0132355546 \times 10^{-6}, \\ a_9 &= 5.6960486681 \times 10^{-8}, a_{10} = -2.8624032584 \times 10^{-10}. \end{aligned}$$

The solubility product (K_{sp}) of minerals is generally a function of temperature and pressure (Helgeson and Kirkham, 1974). It can be expressed as the sum of the temperature dependency

part ($K_{sp,T}(T, P_0)$) at the reference pressure P_0 (i.e., 1 bar or water vapor pressure) and the pressure dependency part ($K_{sp,P}(T, P)$):

$$\begin{aligned}\log_{10} K_{sp} &= \log_{10} K_{sp,T}(T, P_0) + \log_{10} K_{sp,P}(T, P) \\ &= \log_{10} K_{sp,T}(T, P_0) - \frac{\Delta V_0}{RT}(P - P_0) + \frac{\Delta \kappa_0}{2RT}(P - P_0)^2\end{aligned}\quad (S44)$$

where ΔV_0 and $\Delta \kappa_0$ are the standard partial molar volume and the standard partial molar compressibility of the dissolution reaction, respectively (Culberson and Pytkowicz, 1968). R is the gas constant ($8.314 \text{ Jk}^{-1}\text{mol}^{-1}$) and T is temperature in Kelvin. The solubility products of gypsum and anhydrite at the reference pressure P_0 were fitted from 0° to 75°C and 75° to 250°C , respectively, according to Dai et al. (2017):

$$\begin{aligned}\log_{10} K_{T,sp,gypsum} &= 110.504 - 5040.336/(T + 273.15) \\ &- 39.689 \cdot \log_{10}(T + 273.15)\end{aligned}\quad (S45)$$

$$\begin{aligned}\log_{10} K_{T,sp,anhydrite} &= -762,806/(T + 273.15) + 11,600.95 \\ &- 4061.02 \cdot \log_{10}(T + 273.15) + 1.321 \cdot (T + 273.15) \\ &+ 5.42 \times 10^7/(T + 273.15)^2\end{aligned}\quad (S46)$$

where T is the temperature in $^\circ\text{C}$. The standard partial molar volume ΔV_0 and the standard partial molar compressibility of the dissolution reaction $\Delta \kappa_0$ can be expressed as temperature-dependent functions (Kaasa, 1998; Dai et al., 2017):

$$\Delta V_{0,gypsum} = -47.722 + 0.22247T - 1.82529 \times 10^{-3}T^2 - 2.12429 \times 10^{-6}T^3 \quad (S47)$$

$$\Delta \kappa_{0,gypsum} = -17.83 \times 10^{-3} + 1.543 \times 10^{-5}T + 1.601 \times 10^{-6}T^2 - 1.684 \times 10^{-8}T^3 \quad (S48)$$

$$\Delta V_{0,anhydrite} = -55.379 + 0.22423T - 1.9922 \times 10^{-3}T^2 - 2.0301 \times 10^{-6}T^3 \quad (S49)$$

$$\Delta \kappa_{0,anhydrite} = -15.89 \times 10^{-3} + 6.0247 \times 10^{-6}T - 1.673 \times 10^{-8}T^2, \quad (S50)$$

where the units of ΔV_0 and $\Delta \kappa_0$ are $\text{cm}^3 \text{ mole}^{-1}$ and $\text{cm}^3 \text{ mole}^{-1} \text{ bar}^{-1}$, respectively. Gypsum is assumed to precipitate below 75°C and anhydrite above 75°C if $\Omega > 1$.

The boundary conditions at the SWI are imposed concentrations and fluxes for the aqueous and solid species, respectively, while a no-gradient boundary condition is used for all species at the sediment-basement interface. Seven snapshots were constructed according to the age model for

Site C0023 (Hagino and the Expedition 370 Scientists, 2018) with different C_{org} flux (F_{org1} , F_{org2} and F_{org3}) at the upper boundary at each depositional environment.

The model was coded in R (version 3.2.4) using the ReacTran package (Soetaert and Meysman, 2012) to solve Eq. S1 to S2. The advective velocities of dissolved and solid species were solved using the compact grid function within the ReacTran package, which considers sediment compaction. All species, parameters and boundary conditions except those given in the text are listed in Table S2

Model limitations

The application of reactive transport models is a valuable tool to study and assess the temporal evolution of biogeochemical processes in deep subseafloor sediments on geological timescales as well as to infer past and present reaction rates (e.g., Arndt et al., 2009; Contreras et al., 2013; Wehrmann et al., 2013). However, the explanatory power of paleo-modeling studies is often limited by the lack of high-resolution data and knowledge of boundary conditions in the past (Arndt et al., 2009; Wehrmann et al., 2013). Thus, several parameters and constants in paleo-model studies typically represent fitting parameters. For instance, the C_{org} flux ($F_{\text{org1-3}}$) at each sedimentation interval in this study were adjusted according to the C_{org} contents and the sulfate concentration profiles. However, different combinations of F_{org1} , F_{org2} and F_{org3} at each sedimentation interval does not significantly change the general results. Dissolved calcium (Ca^{2+}) concentrations were not directly calculated and carbonate precipitation was neglected. Since this study focusses on the evolution of the deep inverse sulfate-methane transition (SMT), carbonate precipitation was not implemented in the reactive transport model. The implementation of carbonate precipitation will significantly alter the DIC profile (Fig. S1D). In addition, the re-activation of refractory organic matter at high temperature was not included in the model.

Since temperature is an important factor regulating metabolic reaction rates (e.g., Arndt et al., 2013), we integrated the temperature dependence of rate constants $f(T)$ and the temperature-limiting term ($F_{\text{in}}(T)$) for catabolic activity according to LaRowe et al. (2014). We are aware that the rate constants may have an even more complex function of temperature and, thus, this approach may be oversimplified. Nonetheless, the presented study is the first attempt to investigate the evolution of biogeochemical processes in deep subseafloor sediments under the influence of extremely increasing temperature. It can be constantly re-evaluated and tested in the light of the continuously improving understanding of the deep subseafloor biosphere. To

assess the influence of different values for Q_{10} , T_{in} and T_c on the concentration profiles of sulfate and methane, we performed a series of sensitivity tests (Fig. S2).

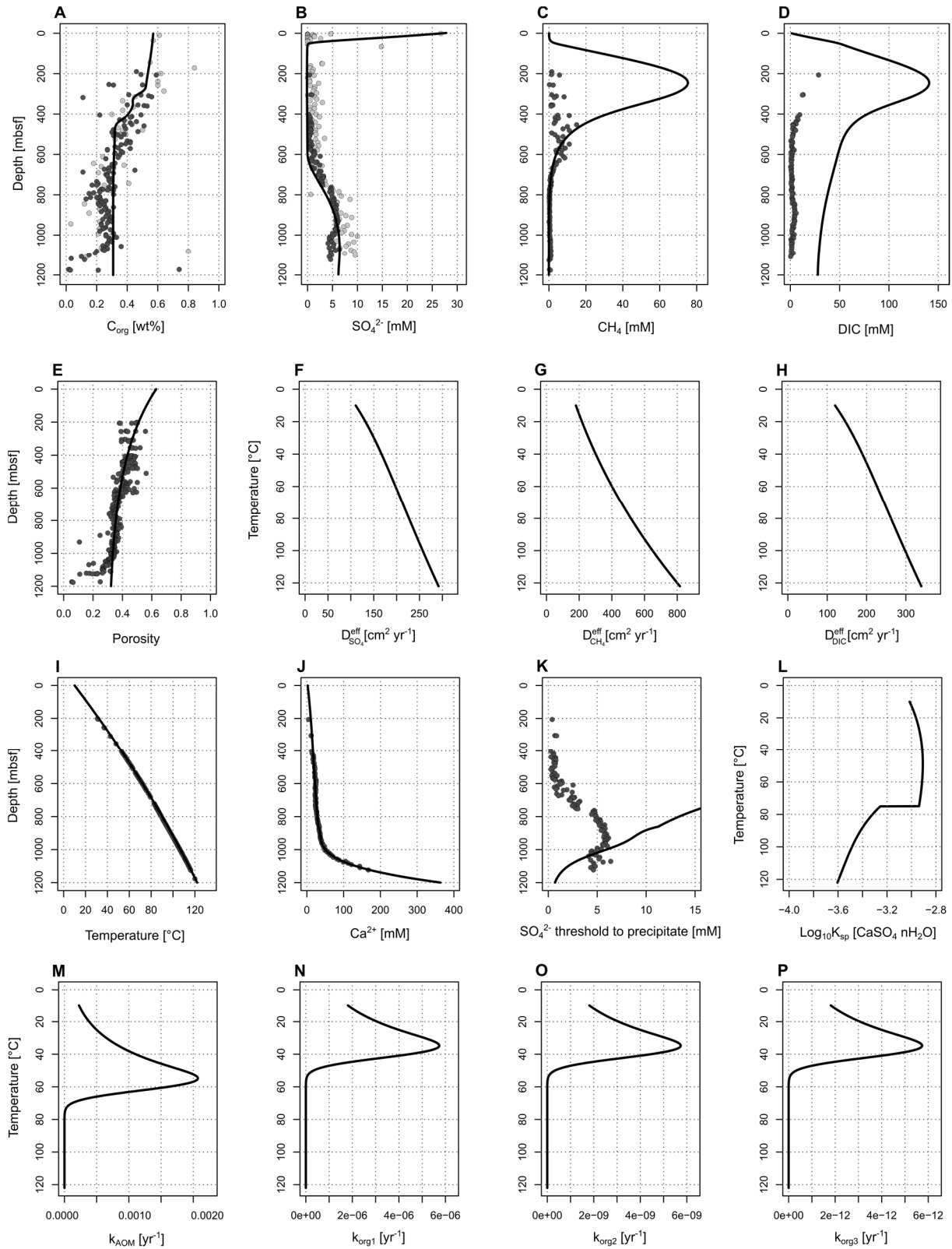


Figure S1. Model fits including (A) C_{org} , (B) sulfate, (C) methane, (D) DIC, (E) porosity, (F)-(H) Effective diffusion coefficient ($D^{\text{eff}} = D/\theta^2$) of sulfate, methane and DIC, (I) temperature, (J) dissolved calcium, (K) sulfate threshold to precipitate as gypsum/anhydrite, (L) Solubility product of gypsum and anhydrite, (M)-(P) rate constants k of AOM and organic matter degradation. Black and grey dots represent geochemical data of IODP Site C0023 (Heuer et al., 2017, 2020) and ODP Site 1174 (Shipboard Scientific Party, 2001), respectively.

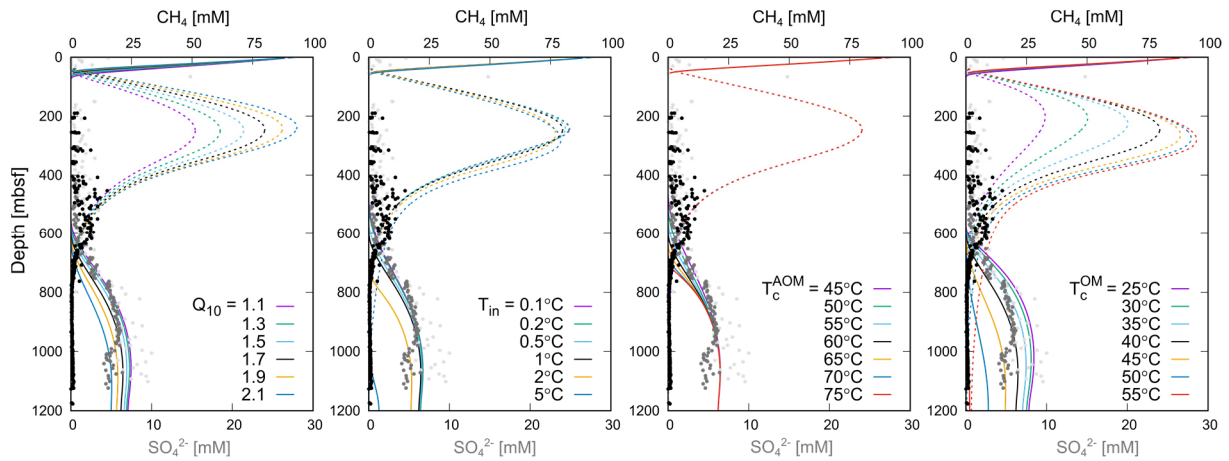


Figure S2. Sensitivity tests using different values for Q_{10} , the steepness parameter T_{in} and the threshold temperature T_c . In this study, we used $Q_{10} = 1.7$, $T_{in} = 1^\circ\text{C}$, $T_c = 60^\circ\text{C}$ for AOM and $T_c = 40^\circ\text{C}$ for organic matter degradation. Black and dark grey dots represent *in situ* methane and sulfate concentrations determined at IODP Site C0023, respectively (Heuer et al., 2017). Light grey dots represent sulfate concentrations determined at ODP Site 1174 (Shipboard Scientific Party, 2001).

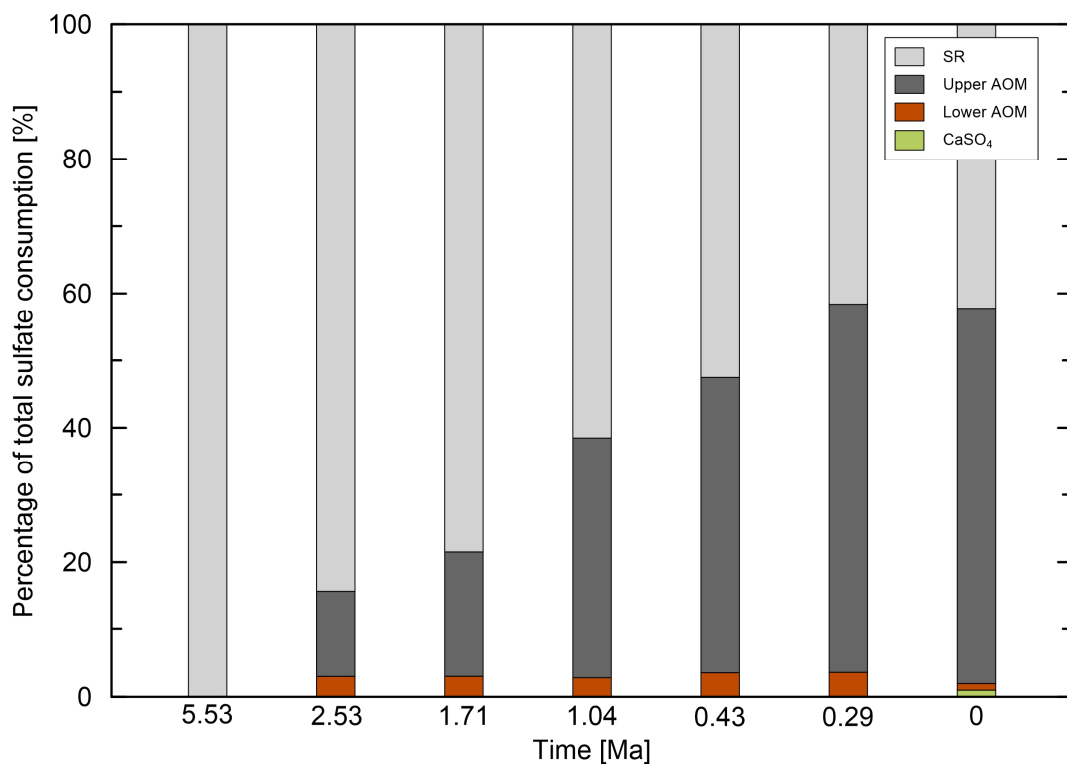


Figure S3. Percentage of organoclastic sulfate reduction (SR), anaerobic oxidation of methane (AOM) and anhydrite (CaSO_4) precipitation in the total sulfate consumption during the past ~ 5.5 Ma. Upper and lower AOM correspond to the consumption at the shallow and the deep inverse SMT, respectively.

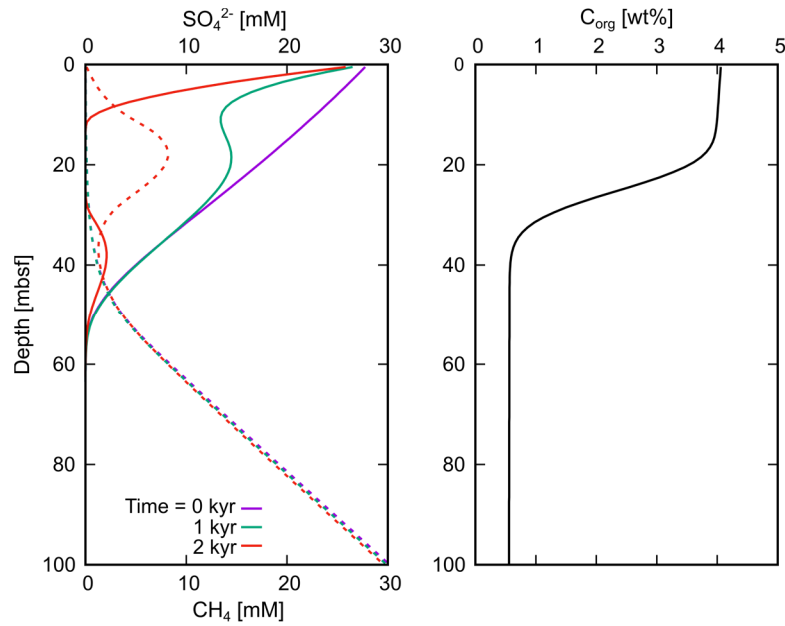


Figure S4. Time series for the evolution of the sulfate (solid lines) and methane (dashed lines) profiles if the C_{org} contents in the upper ~30 m of the sediment column are increased of up to 4 wt%. The sedimentation rate in this scenario is equal to the sedimentation rate of $\sim 130 \text{ cm kyr}^{-1}$ determined for the most recent Trench-wedge facies recovered at Site C0023.

Table S1. Lithological units and associated facies, lithology, depth range, age and sedimentation rates at Site C0023 (Heuer et al., 2017). Ages and sedimentation rates are based on biostratigraphy studies on calcereous nannofossil assemblages (Hagino and the Expedition 370 Scientists, 2018).

Unit	Facies	Lithology	Depth [mbsf]	Age [Ma]	Sedimentation rate [cm kyr ⁻¹]
IIA	Axial trench-wedge	Hemipelagic and pelagic sand, muddy sand, turbidite-deposited silt and sandstones	189–318.5		
IIB	Outer trench-wedge	Hemipelagic and pelagic mud, turbidite-deposited mudstones	353–428	0.29	131.9
IIC	Trench-to-basin transition	Turbidite-deposited silt and sand, tuffs and volcanoclastic sediments	428–494	0.29–0.43	61.0
III	Upper Shikoku Basin	Heavily bioturbated volcanoclastic mudstones	494–637.5	0.43–2.53	9.3–6.0
IV	Lower Shikoku Basin	Heavily bioturbated mudstones with green ash-rich laminae	637.5–1112	2.53–13.53	6.0–3.5
V	Acidic volcanoclastics	Mudstones and felsic ash	1112–1125.9		
	Basaltic basement	Hyaloclastites	1125.9		

Table S2. Species, parameter values and boundary conditions used in the one-dimensional transport-reaction model.

	Symbol	Unit	Value
<i>Species and fitting parameter</i>			
Sediment thickness		m	1200
Porosity at SWI	φ_0		0.63
Porosity at compaction	φ_∞		0.30
Depth-attenuation coefficient	B	m ⁻¹	1/445.8
1 st order deg. coeff. TOC ₁	σ_1^0	yr ⁻¹	2.0E-06
1 st order deg. coeff. TOC ₂	σ_2^0	yr ⁻¹	2.0E-09
1 st order deg. coeff. TOC ₃	σ_3^0	yr ⁻¹	2.0E-12
Threshold sulfate concentration for methanogenesis	$C_{SO_4}^*$	mM	0.1
Parameter controlling steepness of f_s	k_{in}	mM	0.08
Threshold temperature for AOM	T_c	°C	60
Threshold temperature for OM degradation	T_c	°C	40
Q ₁₀ temperature coefficient	Q ₁₀		1.7
Parameter controlling steepness of F_{in}	T_{in}	°C	7
AOM rate constant	k_{AOM}^0	yr ⁻¹	2.0E-4
Monod constant for AOM	$k_{S,AOM}$	mM	1.0
CaSO ₄ precipitation rate constant	k_{pp}	mM yr ⁻¹	5E-7
<i>Sedimentation interval 1</i>			
Sedimentation rate	Ω	m Myr ⁻¹	35
Sedimentation time		Myr	8.0
Sedimentation thickness		m	281
Flux of TOC ₁	F_{org1}	mol m ⁻² yr ⁻¹	0.008
Flux of TOC ₂	F_{org2}	mol m ⁻² yr ⁻¹	0.007
Flux of TOC ₃	F_{org3}	mol m ⁻² yr ⁻¹	0.002
<i>Sedimentation interval 2</i>			
Sedimentation rate	Ω	m Myr ⁻¹	53
Sedimentation time		Myr	3
Sedimentation thickness		m	161
Flux of TOC ₁	F_{org1}	mol m ⁻² yr ⁻¹	0.024
Flux of TOC ₂	F_{org2}	mol m ⁻² yr ⁻¹	0.008
Flux of TOC ₃	F_{org3}	mol m ⁻² yr ⁻¹	0.006

Table S2. (continued) Species, parameter values and boundary conditions used in the one-dimensional transport-reaction model.

	Symbol	Unit	Value
<i>Sedimentation interval 3</i>			
Sedimentation rate	Ω	m Myr ⁻¹	60
Sedimentation time		Myr	0.82
Sedimentation thickness		m	49
Flux of TOC ₁	F _{org1}	mol m ⁻² yr ⁻¹	0.024
Flux of TOC ₂	F _{org2}	mol m ⁻² yr ⁻¹	0.009
Flux of TOC ₃	F _{org3}	mol m ⁻² yr ⁻¹	0.007
<i>Sedimentation interval 4</i>			
Sedimentation rate	Ω	m Myr ⁻¹	92
Sedimentation time		Myr	0.67
Sedimentation thickness		m	62
Flux of TOC ₁	F _{org1}	mol m ⁻² yr ⁻¹	0.039
Flux of TOC ₂	F _{org2}	mol m ⁻² yr ⁻¹	0.013
Flux of TOC ₃	F _{org3}	mol m ⁻² yr ⁻¹	0.016
<i>Sedimentation interval 5</i>			
Sedimentation rate	Ω	m Myr ⁻¹	93
Sedimentation time		Myr	0.61
Sedimentation thickness		m	56
Flux of TOC ₁	F _{org1}	mol m ⁻² yr ⁻¹	0.027
Flux of TOC ₂	F _{org2}	mol m ⁻² yr ⁻¹	0.013
Flux of TOC ₃	F _{org3}	mol m ⁻² yr ⁻¹	0.016
<i>Sedimentation interval 6</i>			
Sedimentation rate	Ω	m Myr ⁻¹	610
Sedimentation time		Myr	0.14
Sedimentation thickness		m	86
Flux of TOC ₁	F _{org1}	mol m ⁻² yr ⁻¹	0.087
Flux of TOC ₂	F _{org2}	mol m ⁻² yr ⁻¹	0.087
Flux of TOC ₃	F _{org3}	mol m ⁻² yr ⁻¹	0.105
<i>Sedimentation interval 7</i>			
Sedimentation rate	Ω	m Myr ⁻¹	1319
Sedimentation time		Myr	0.29
Sedimentation thickness		m	382
Flux of TOC ₁	F _{org1}	mol m ⁻² yr ⁻¹	0.075
Flux of TOC ₂	F _{org2}	mol m ⁻² yr ⁻¹	0.226
Flux of TOC ₃	F _{org3}	mol m ⁻² yr ⁻¹	0.300

Table S3. Present-day depth-integrated rates of organoclastic sulfate reduction, biogenic methanogenesis, anaerobic oxidation of methane and anhydrite precipitation derived from the transport-reaction model.

Depth-integrated reaction rates	[mmol m ⁻² yr ⁻¹]
Organoclastic sulfate reduction (SR)	3.9
Biogenic methanogenesis (MG)	5.1
Anaerobic oxidation of methane (AOM)	5.2
AOM at the shallow SMT	5.1
AOM at the deep inverse SMT	0.1
Anhydrite (CaSO ₄) precipitation	0.1

References

- Arndt, S., Brumsack, H.-J., and Wirtz, K.W., 2006. Cretaceous black shales as active bioreactors: A biogeochemical model for the deep biosphere encountered during ODP Leg 207 (Demera Rise). *Geochimica et Cosmochimica Acta*, **70**, 408-425. doi:10.1016/j.gca.2005.09.010.
- Arndt, S., Hetzel, A., and Brumsack, H.-J., 2009. Evolution of organic matter degradation in Cretaceous black shales inferred from authigenic barite: A reaction-transport model. *Geochimica et Cosmochimica Acta*, **73**, 2000-2022. doi:10.1016/j.gca.2009.01.018.
- Arndt, S., Jørgensen, B.B., LaRowe, D.E., Middelburg, J.J., Pancost, R.D., and Regnier, P., 2013. Quantifying the degradation of organic matter in marine sediments: A review and synthesis. *Earth-Science Reviews*, **123**, 53-86. doi:10.1016/j.earscirev.2013.02.008.
- Boudreau, B.P., 1996. The diffusive tortuosity of fine-grained unlithified sediments: *Geochimica et Cosmochimica Acta*, **60**, 3139-3142. doi:10.1016/0016-7037(96)00158-5.
- Boudreau, B.P., 1997. *Diagenetic Models and Their Implementation: Modelling Transport and Reactions in Aquatic Sediments*. Springer, Berlin, Heidelberg, New York, 428 p.
- Bradley, D.J., and Pitzer, K.S., 1979. Thermodynamics of electrolytes. 12. Dielectric properties of water and Debye-Hueckel parameters to 350.degree.C and 1 kbar. *Journal of Physical Chemistry*, **83**, 1599-1603. doi:10.1021/j100475a009.
- Bromley, L.A., Singh, D., Ray, P., Sridhar, S., and Read, S.M., 1974. Thermodynamic properties of sea salt solution. *AIChE Journal*, **20**, 326-335. doi:10.1002/aic.690200218.
- Burdige, D.J., Komada, T., Magen, C., and Chanton, J.P., 2016a. Carbon cycling in Santa Barbara Basin sediments: A modeling study. *Journal of Marine Research*, **74**, 133-159. doi:10.1357/002224016819594818.
- Burdige, D.J., Komada, T., Magen, C., and Chanton, J.P., 2016b. Methane dynamics in Santa Barbara Basin (USA) sediments as examined with a reaction-transport model. *Journal of Marine Research*, **74**, 277-313. doi:10.1357/002224016821744151.
- Contreras, S., Meister, M., Liu, B., Prieto-Mollar, X., Hinrichs, K.-U, Khalili, A., Ferdelman, T.G., Kuypers, M.M.M., and Jørgensen, B.B., 2013. Cyclic 100-ka (glacial-interglacial) migration of seafloor redox zonation on the Peruvian shelf. *Proceedings of the National Academy of Sciences of the United States of America*, **110**, 18098-18103. doi:10.1073/pnas.1305981110.

- Culberson, C., and Pytkowicz, R.M., 1968. Effect of pressure on carbonic acid, boric acid, and the pH in seawater. *Limnology and Oceanography*, **13**, 403-417. doi:10.4319/LO.1968.13.3.0403.
- Dai, Z., Kan, A.T., Shi, W., Zhang, N., Zhang, F., Yan, F., et al., 2017. Solubility measurements and predictions of gypsum, anhydrite, and calcite over wide ranges of temperature, pressure, and ionic strength with mixed electrolytes. *Rock Mechanics and Rock Engineering*, **50**, 327-339. doi:10.1007/s00603-016-1123-9.
- Debye, P., and Hückel, E., 1923. De la theorie des electrolytes. I. abaissement du point de congelation et phenomenes associes. *Physikalische Zeitschrift*, **24**, 185-206.
- DeVoe, H., 2020. *Thermodynamics and chemistry*. Second Edition Version 10. University of Maryland, College Park, Maryland, USA.
- DOE, 1994. Handbook of methods for the analysis of the various parameters of the carbon dioxide system in sea water, version 2. (eds. Dickson, A.G., and Goyet, C.). ORNL/CDIAC-74.
- El-Dessouky, H.T., and Ettouney, H.M., 2002. *Fundamentals of Salt Water Desalination*. Elsevier Science B.V., Amsterdam.
- Hagino, K., and the Expedition 370 Scientists, 2018. Data report: calcareous nannofossils from the middle Miocene to Pleistocene, IODP Expedition 370 Site C0023. In: *Proceedings of the International Ocean Discovery Program Volume 370* (eds. Heuer, V.B., Inagaki, F., Morono, Y., Kubo, Y., Maeda, L., and the Expedition 370 Scientists). College Station, TX (International Ocean Discovery Program). doi:10.14379/iodp.proc.370.201.2018.
- Helgeson, H.C., and Kirkham, D.H., 1974. Theoretical prediction of the thermodynamic properties of aqueous electrolytes at high pressures and temperatures: I. Summary of the thermodynamic electrostatic properties of the solvent. *American Journal of Science*, **274**, 1089-1198. doi:10.2475/ajs.274.10.1089.
- Heuer, V.B., Inagaki, F., Morono, Y., Kubo, Y., Maeda, L., and the Expedition 370 Scientists, 2017. Temperature limit of the deep biosphere off Muroto. *Proceedings of the International Ocean Discovery Program Volume 370*: College Station, TX (International Ocean Discovery Program). doi:10.14379/iodp.proc.370.2017.
- Heuer, V.B., Inagaki, F., Morono, Y., Kubo, Y., Spivack, A., Viehweger, B., et al., 2020. Temperature limits to deep seafloor life in the Nankai Trough subduction zone. *Science*, **370**, 1230-1234. doi:10.1126/science.abd7934.
- Holler, T., Widdel, F., Knittel, K., Amann, R., Kellermann, M.Y., Hinrichs, K.-U., et al., 2011. Thermophilic anaerobic oxidation of methane by marine microbial consortia. *The ISME Journal*, **5**, 1946-1956. doi:10.1038/ismej.2011.77.
- Jørgensen, B.B., 1978. A comparison of methods for the quantification of bacterial sulfate reduction in coastal marine sediments: II. Calculation from mathematical models: *Geomicrobiology Journal*, **1**, 11-27. doi:10.1080/01490457809377722.
- Kaasa, B., 1998. Prediction of pH, mineral precipitations and multiphase equilibria during oil recovery. Ph.D. thesis, Norwegian University of Technology and Science-NTNU.
- Klein, L.A., and Swift, C.T., 1977. An improved model for the dielectric constant of sea water at microwave frequencies. *IEEE Transactions on Antennas and Propagation*, **25**, 104-111. doi:10.1109/TAP.1977.1141539.

- Kukulka, D.J., Gebhart, B., and Mollendorf, J.C., 1987. Thermodynamic and transport properties of pure and saline water. *Advances in Heat Transfer*, **18**, 325-363. doi:10.1016/S0065-2717(08)70121-7.
- Kallmeyer, J., and Boetius, A., 2004. Effects of temperature and pressure on sulfate reduction and anaerobic oxidation of methane in hydrothermal sediments of Guaymas Basin. *Applied and Environmental Microbiology*, **70**, 1231-1233. doi:10.1128/AEM.70.2.1231-1233.2004.
- LaRowe, D.E., Dale, A.W., Aguilera, D.R., L'Heureux, I., Amend, J.P., and Regnier, P., 2014. Modeling microbial reaction rates in a submarine hydrothermal vent chimney wall. *Geochimica et Cosmochimica Acta*, **124**, 72-97. doi:10.1016/j.gca.2013.09.005.
- Lawrence, H., Bormann, N., and English, S.J., 2020. Uncertainties in the permittivity model for seawater in FASTEM and implications for the calibration/validation of microwave imagers. *Journal of Quantitative Spectroscopy and radiative Transfer*, **243**, 106813. doi:10.1016/j.jqsrt.2019.106813.
- Lewis, G.N., and Randall, M., 1921. The activity coefficient of strong electrolytes. *Journal of the American Chemical Society*, **43**, 1112-1154. doi:10.1021/ja01438a014.
- Li, Y.-H., and Gregory, S., 1974. Diffusion of ions in sea water and in deep-sea sediments. *Geochimica et Cosmochimica Acta*, **38**, 703-714. doi:10.1016/0016-7037(74)90145-8.
- Liu, Q., Weng, F., and English, S.J., 2011. An improved fast microwave water emissivity model. *IEEE Transactions on Geoscience and Remote Sensing*, **49**, 1238-1250. doi:10.1109/TGRS.2010.2064779.
- Meissner, T., and Wentz, F.J., 2004. The complex dielectric constant of pure and sea water from microwave satellite observations. *IEEE Transactions on Geoscience and Remote Sensing*, **42**, 1836-1849. doi:10.1109/TGRS.2004.831888.
- Meister P., Liu B., Ferdelman T.G., Jørgensen B.B., and Khalili, A., 2013. Control of sulphate and methane distributions in marine sediments by organic matter reactivity. *Geochimica et Cosmochimica Acta*, **104**, 183-193. doi:10.1016/j.gca.2012.11.011.
- Millero, F.J., Feistel, R., Wright, D.G., and McDougall, T.J., 2008. The composition of standard seawater and the definition of the reference-composition salinity scale. *Deep Sea Research I: Oceanographic Research Papers*, **55**, 50-72. doi:10.1016/j.dsr.2007.10.001.
- Mogollón, J.M., Mewes, K., and Kasten, S., 2016. Quantifying manganese and nitrogen cycle coupling in manganese-rich, organic carbon-starved marine sediments: Examples from the Clarion-Clipperton fracture zone. *Geophysical Research Letters*, **43**, 7114-7123. doi:10.1002/2016GL069117.
- Nayar, K.G., Sharqawy, M.H., Banchik, L.D., Lienhard V, J.H., 2016. Thermophysical properties of seawater: A review and new correlations that include pressure dependence. *Desalination*, **390**, 1-24. doi:10.1016/j.desal.2016.02.024.
- Parkhurst, D.L., 1990. Ion-association models and mean activity coefficients of various salts. In: *Chemical modeling of aqueous systems II* (eds. Melchior, D.D., and Bassett, R.L.). ACS Symposium Series, Volume 416. Washington DC, 30-43. doi:10.1021/bk-1990-0416.ch003.
- Robinson, R.A., and Stokes, R.H., 1970. *Electrolyte Solutions*. Butterworth & Co., London, 29 p., (Reprinted by Dover Publications, Mineola, New York, in 2002.)
- Rolnick, L.S., 1954. The stability of gypsum and anhydrite in the geologic environment. Ph.D. thesis, Massachusetts Institute of Technology, 156 p.

- Serafeimidis K., and Anagnostou G., 2015. The solubilities and thermodynamic equilibrium of anhydrite and gypsum. *Rock Mechanics and Rock Engineering*, **48**, 15-31. doi:10.1007/s00603-014-0557-1.
- Sharqawy, M.H., Lienhard V, J.H., and Zubair, S.M., 2010. Thermophysical properties of seawater: a review of existing correlations and data. *Desalination and Water Treatment*, **16**, 354-380. doi:10.5004/dwt.2010.1079.
- Shipboard Science Party, 2001. Site 1174. In: *Proceedings of the Ocean Drilling Program, Initial Reports, 190* (eds. Moore, G.F., Taira, A., Klaus, A., et al.). College Station, TX (Ocean Drilling Program), 1-149. doi:10.2973/odp.proc.ir.190.105.2001.
- Soetaert, K., and Meysman, F., 2012. Reactive transport in aquatic ecosystems: Rapid model prototyping in the open source software R. *Environmental Modelling & Software*, **32**, 49-60. doi:10.1016/j.envsoft.2011.08.011.
- Soetaert K., Petzoldt T., and Meysman F., 2020. marelac: Tools for Aquatic Sciences. R package version 2.1.10. <http://CRAN.R-project.org/package=marelac>.
- Truesdell, A.H., and Jones, B.F., 1974. WATEQ, a computer program for calculating chemical equilibria of natural waters. *Journal of Research U.S. Geological Survey*, **2**, 233-248.
- Volz, J.B., Liu, B., Köster, M., Henkel, S., Koschinsky, A., and Kasten, S., 2019. Post-depositional manganese mobilization during the last glacial period in sediments of the eastern Clarion-Clipperton Zone, Pacific Ocean. *Earth and Planetary Science Letters*, **532**, 116012. doi:10.1016/j.epsl.2019.116012.
- Wehrmann, L.M., Arndt, S., März, C., Ferdelman, T.G., and Brunner, B., 2013. The evolution of early diagenetic signals in Bering Sea subseafloor sediments in response to varying organic carbon deposition over the last 4.3 Ma. *Geochimica et Cosmochimica Acta*, **109**, 175-196. doi:10.1016/j.gca.2013.01.025.

ACKNOWLEDGEMENTS

First and foremost, I would like to thank my supervisors Prof. Dr. Sabine Kasten and Dr. Susann Henkel for giving me the opportunity to conduct this PhD project. I am very grateful for your constant support, your patience and guidance during the last years. Thank you very much for the fruitful discussions, your enthusiasm about my data, your constructive feedback and comments on the manuscripts and your encouragement. I highly appreciate that Prof. Dr. Marta Torres agreed to be the external reviewer.

I would like to thank my Thesis Advisory Committee (TAC) members Dr. Verena Heuer and Prof. Dr. Wolfgang Bach for the support throughout this PhD project. The manuscripts benefited greatly from the productive and inspiring discussions. In this context, I would like to thank the Graduate School POLMAR for allowing me to participate in different training courses.

I am sincerely grateful to Dr. Myriam Kars, who gave me the opportunity for a research stay at the Center for Advanced Core Research at Kochi University. Thank you for introducing the Rock mag world to me. I had a great time in Japan not only at but also outside work and I enjoy looking back on our trips to all the beautiful places on Shikoku Island and in Kyoto. I also want to acknowledge the Japan Society for the Promotion of Science (JSPS) for funding my research stay at the Kochi University in the framework of the JSPS Summer Program 2019.

This study would not have been possible without the close collaboration with the IODP Expedition 370 Scientists. Special thanks to Dr. Verena Heuer, Prof. Dr. Fumio Inagaki, Dr. Yuki Morono, Prof. Dr. Arthur Spivack, Dr. Florence Schubotz and Dr. Man-Yin Tsang for sharing your knowledge and vast expertise on the deep seafloor biosphere and IODP Site C0023. I enjoyed the time during the IODP 370 Post-Cruise Meeting in Aberdeen and the field trip to the Highlands afterwards. I also would like to thank Dr. Bo Liu, Prof. Dr. Michael Staubwasser, Anette Meixner, Prof. Dr. Simone Kasemann, Dr. Markus Maisch, Prof. Dr. Andreas Kappler, Dr. Akira Ijiri and Dr. Hayley Manners for their valuable input and constructive ideas for improvements of the manuscripts.

Thanks to all colleagues of the Marine Geochemistry group at AWI for the pleasant working atmosphere. I am particularly thankful to Ingrid Stimac, Ingrid Dohrmann, Denise Bethke, Mirko Lange, Johann Hollop, Dr. Grit Steinhöfel and Anette Meixner for their active support with the laboratory work, analyses and measurements and to Petra Meyer for the administrative

help. I also thank Dr. Natascha Riedinger, Prof. Dr. Marta Torres, Christopher Jones and Dr. Anna Lichtschlag for the great teamwork and the fruitful scientific discussions onboard *R/V Polarstern* during cruise PS119.

I am grateful that my colleagues and friends Dr. Jessica Volz, Anni Melcher, Dr. Ole Valk, Dr. Josefa Verdugo, Julia Lofffield and Daniel Müller accompanied me on this journey. Thank you very much for your support, the numerous (virtual) coffee and lunch breaks and all the great moments we spent together at and outside work. Special thanks go to Jessi for the inspiring discussions in our office, the positive exchange of ideas, for all the helpful advices and for proofreading parts of this thesis.

Mein persönlicher Dank gilt meinen Freunden Becci H., Becci M., Kim, Lara, Pauli, Rieke, Sassi, Sina, Svea, Svenja und Vanessa sowie Christa, Gerd, Meike und Greta für ihre Motivation und die vielen schönen gemeinsam verbrachten Stunden, Abende und Urlaube in den vergangenen Jahren.

Vom ganzen Herzen danke ich meinen Eltern Marlies und Ewald sowie meiner Schwester Jantje und Fabian für die uneingeschränkte Hilfsbereitschaft, die Ermutigungen und das Vertrauen nicht nur während der Doktorandenzeit, sondern über all die Jahre. Mein größter Dank gilt meinem Freund Till für seine bedingungslose Unterstützung und den Halt. Vielen Dank, dass ihr immer für mich da seid.

Versicherung an Eides Statt / Affirmation in lieu of an oath

gem. § 5 Abs. 5 der Promotionsordnung vom 18.06.2018 /
according to § 5 (5) of the Doctoral Degree Rules and Regulations of 18 June, 2018

Ich / I,

Male Köster

versichere an Eides Statt durch meine Unterschrift, dass ich die vorliegende Dissertation selbständig und ohne fremde Hilfe angefertigt und alle Stellen, die ich wörtlich dem Sinne nach aus Veröffentlichungen entnommen habe, als solche kenntlich gemacht habe, mich auch keiner anderen als der angegebenen Literatur oder sonstiger Hilfsmittel bedient habe und die zu Prüfungszwecken beigelegte elektronische Version (PDF) der Dissertation mit der abgegebenen gedruckten Version identisch ist. / *With my signature I affirm in lieu of an oath that I prepared the submitted dissertation independently and without illicit assistance from third parties, that I appropriately referenced any text or content from other sources, that I used only literature and resources listed in the dissertation, and that the electronic (PDF) and printed versions of the dissertation are identical.*

Ich versichere an Eides Statt, dass ich die vorgenannten Angaben nach bestem Wissen und Gewissen gemacht habe und dass die Angaben der Wahrheit entsprechen und ich nichts verschwiegen habe. / *I affirm in lieu of an oath that the information provided herein to the best of my knowledge is true and complete.*

Die Strafbarkeit einer falschen eidesstattlichen Versicherung ist mir bekannt, namentlich die Strafandrohung gemäß § 156 StGB bis zu drei Jahren Freiheitsstrafe oder Geldstrafe bei vorsätzlicher Begehung der Tat bzw. gemäß § 161 Abs. 1 StGB bis zu einem Jahr Freiheitsstrafe oder Geldstrafe bei fahrlässiger Begehung. / *I am aware that a false affidavit is a criminal offence which is punishable by law in accordance with § 156 of the German Criminal Code (StGB) with up to three years imprisonment or a fine in case of intention, or in accordance with § 161 (1) of the German Criminal Code with up to one year imprisonment or a fine in case of negligence.*

Ort / Place, Datum / Date

Unterschrift / Signature

